The American Institute of Physics joins its Russian colleagues in celebration of the 70th Birthday of Academician Boris Petrovich Zakharchenya. We wish Boris Petrovich the best of health, happiness, and great success in his scientific endeavors. We are proud to know him for many years as a talented Physicist, dedicated Editor, and as our dear friend. We value our collaboration with Boris Petrovich, and we hope it will continue for many years to come.

PERSONALIA

Boris Petrovich Zakharchenya (on his 70th birthday)

Fiz. Tekh. Poluprovodn. **32**, 759–760 (June 1998)

[S1063-7826(98)02706-9]

Boris Petrovich Zakharchenya, member of the editorial board of the journal ''Semiconductors,'' Academician of the Russian Academy of Sciences, Director of the Division of Solid-State Physics at the A. F. Ioffe Physicotechnical Institute of the Russian Academy of Sciences, and a scientist who has made an outstanding contribution to the development of semiconductor physics, celebrated his 70th birthday on May 1, 1998.

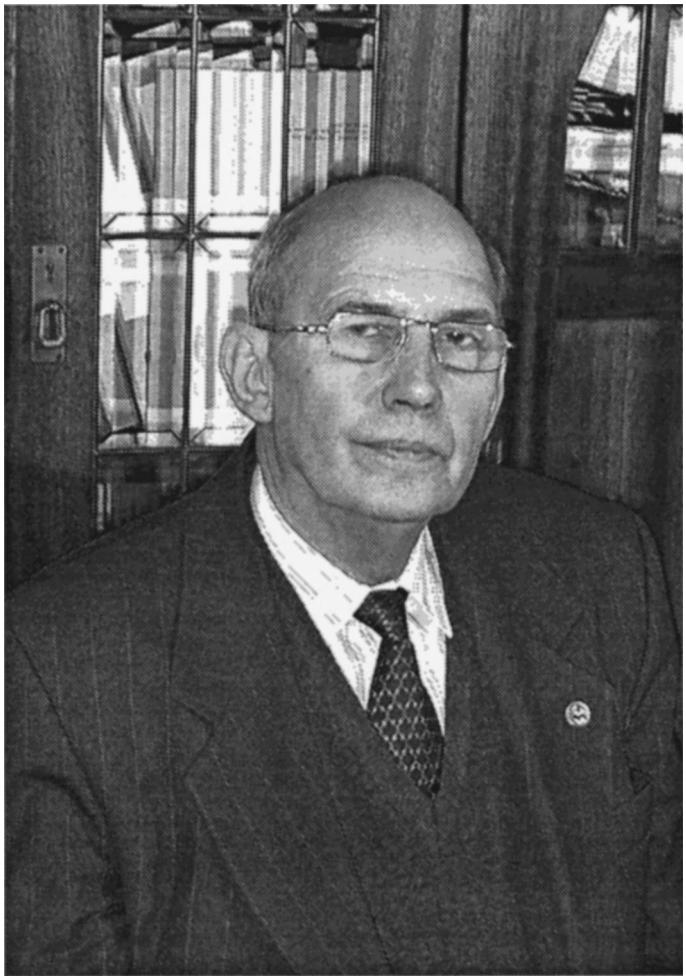

B. P. Zakharchenya was born in the city of Orsha in Byelorussia. He attended secondary school and university in Leningrad. In 1952 he graduated from the Department of Physics at Leningrad State University and entered the A. F. Ioffe Physicotechnical Institute, where he has been ever since.

The main direction of B. P. Zakharchenya's scientific research — optical spectroscopy and magnetooptics of semiconductors — was set while he was still a graduate student at the Physicotechnical Institute under the guidance of his teacher Corresponding Member of the Soviet Academy of Sciences E. F. Gross. B. P. Zakharchenya participated extremely productively in the pioneering investigations of the optical spectra of the exciton, a quasiparticle which was predicted by Ya. I. Frenkel' and whose hydrogen-like optical spectrum in cuprous oxide crystals was discovered shortly before (in 1951) by E. F. Gross and N. A. Karryev. The first observation of the Zeeman and Stark effects, the discovery of giant diamagnetic shifts of the energy levels of large-radius excitonic states, the observation of the main magnetooptic effect — magnetoabsorption oscillations associated with Landau levels — in the cuprous oxide spectrum, the observation (made independently and simultaneously by Thomas and Hopfield) of magnetic field reversal in the excitonic spectrum of cadmium sulfide is an incomplete list of the fundamental results obtained by B. P. Zakharchenya during the first ten years of his career. These results have made a large contribution to the development of the exciton physics and semiconductor magnetooptics. In 1966 B. P. Zakharchenya, together with other scientists, was awarded the Lenin Prize of the USSR for research on excitons.

In the beginning of the 1970s a remarkable series of investigations of the optical orientation of the spins of current carriers and atomic nuclei in semiconductors was conducted at the initiative and with the participation of B. P. Zakharchenya at the A. F. Ioffe Physicotechnical Institute. This work was awarded the 1976 State Prize of the USSR. B. P. Zakharchenya together with V. G. Fleĭsher were the first to achieve deep (down to 10^{-6} K) optical cooling of a system of nuclear spins and they discovered the optical manifestations of multiquantum nuclear resonances and optical orientation of holes. In the late 1970s B. P. Zakharchenya together with D. N. Mirlin conducted an extensive series of studies on the optics of hot carriers in semiconductors: They discovered the luminescence of hot photoelectrons and their momentum alignment under linearly polarized optical pumping. It was shown experimentally and theoretically (by M. I. D'yakonov and V. I. Perel') that ultrafast (femtosecond) dynamics of hot carriers and the particular features of the structure of semiconductors can be studied by investigating the hot luminescence of semiconductors and its behavior in a magnetic field. Important (from the standpoint of applications) investigations in the spectroscopy of semiconductors

doped with rare-earth elements (O. B. Gusev and M. S. Bresler) as well as investigations of semiconductor nanostructures have recently been successfully conducted in Zakharchenya's laboratory.

Zakharchenya's service in the development of optical spectroscopy and magnetooptics of semiconductors has been recognized by electing him Corresponding Member of the Soviet Academy of Sciences (1976) and active member of the Russian Academy of Sciences (1992) and by presenting him the 1996 P. N. Lebedev Bolshoi Gold Medal. As head of the Division of Solid-State Physics at the A. F. Ioffe Physicotechnical Institute B. P. Zakharchenya is a successful administrator, and as a professor at St. Petersburg State Electrical Engineering University he is devoting a great deal of energy and talent to pedagogical work. He is also devoting a great deal of attention to the journal ''Physics of the Solid State'' as chief editor.

We wish Boris Petrovich good health and great success in further scientific work.

Editorial Board of the journal ''Semiconductors''

Translated by M. E. Alferieff

ATOMIC STRUCTURE AND NON-ELECTRONIC PROPERTIES OF SEMICONDUCTORS

The role of macrodefects in electronic and ionic processes in wide-band II–VI semiconductors

B. R. Dzhumaev

Institute of Semiconductor Physics, Ukrainian Academy of Sciences, 252028 Kiev, Ukraine
(Submitted October 13, 1997; accepted for publication October 26, 1997)
Fiz. Tekh. Poluprovodn. **32**, 641–645 (June 1998)

This paper discusses the electrical, photoelectric, and photoluminescence characteristics and the ESR spectra of CdS crystals with various dislocation densities ($\gamma = 10^2 - 10^5$ cm^{-2}). It is found that the presence of mobile donors and of dislocations with density $\gamma > 10^3 - 10^4$ cm^{-2} has a number of specific effects: anisotropy of the electric-field-induced conductivity, athermal diffusion of donors under the action of ultrasound, distortion of the shape of the edge-luminescence spectrum, and photostimulated degradation of the photosensitivity and photoluminescence. The dependence of the type of macrodefects and the optical strength of the crystals on the fabrication process is studied. © *1998 American Institute of Physics.* [S1063-7826(98)00106-9]

The creation of LEDs and lasers based on wide-band II–VI semiconductors makes the problem of their degradation extremely crucial. An essential factor in the degradation is the presence of dislocation-generating heteroboundaries that penetrate the active layer.[1] Another important factor, as we established earlier, is the presence of highly mobile defects—shallow donors—for example Cd_i.[2] A significant role (in particular, in the degradation processes of lasers with electronic pumping) can also be played by other types of macrodefects: inclusions and grain boundaries.

This paper uses CdS as model crystals to study the interaction of a developed system of dislocations and mobile defects. The dislocation density γ in these crystals varied in the range $\gamma = 10^2 - 10^5$ cm^{-2}. Donors that are mobile at room temperature were present in them at the same time. Next follows a description of a series of specific effects that result from the indicated interaction. The limiting dislocation concentration, where these effects are no longer observed, is determined. Optical breakdown mechanisms of crystals used as the active elements of electronically pumped lasers are also studied.

EXPERIMENT AND DISCUSSION

High-resistance CdS crystals with a resistivity of $\rho > 10^8\ \Omega \cdot$cm were obtained by free growth from the vapor phase. The dislocation density was determined from etch pits on the (0001) plane. The method described in Ref.3 was used to obtain samples with small γ.

Crystals doped with Cu in a concentration range $10^{16} - 10^{18}$ cm^{-3} with $\gamma \leqslant 10^5$ cm^{-2} were used to study photostimulated degradation of the photocurrent and the photoluminescence (PL). Optical breakdown processes were studied in crystals grown under various ratios of the S and Cd vapor pressures by the method described in Ref. 4. Such crystals are often used as the working elements of electronically pumped lasers.

1. EFFECTS ASSOCIATED WITH THE PRESENCE OF DISLOCATIONS

The following specific effects associated with the presence of decorated dislocations were observed:

1) electric-field-induced conductivity anisotropy,
2) athermal diffusion of donors under the action of ultrasound,
3) distortion of the shape of the edge-luminescence spectrum,
4) photostimulated degradation of the photocurrent and the luminescence.

1.1. Electric-field-induced conductivity anisotropy

When an electric field E above some threshold value ($E_{th} \simeq 10 - 10^2$ V/cm) is applied at 300 K, an increase of several orders of magnitude in the dark current and the photocurrent with time was observed in a number of crystals with $\gamma > 10^3$ cm^{-2}. In other words, a conductive channel appeared along a direction parallel to **E**. However, the conductivity of the crystal in a direction perpendicular to the applied field showed virtually no change (the measurements were made by turning on the field for a short time). Thus, the conductivity showed induced anisotropy. The ratio $\sigma_\parallel / \sigma_\perp$ of the conductivities in the two directions could reach 10^3. The effect was independent of the crystallographic direction, and the channel could be formed either along the symmetry axis **c** or perpendicular to it. After the field was switched off, the state with increased conductivity decayed with time. Both processes—the formation and the breakdown of the conduc-

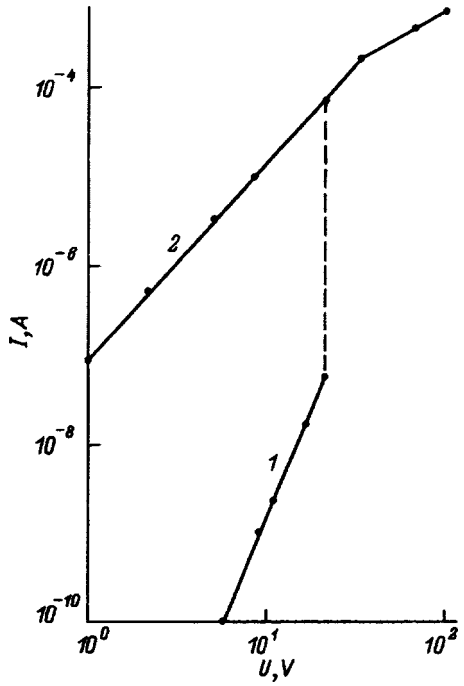

FIG. 1. The I–V characteristics of a sample before (*1*) and after (*2*) the formation of conductive channels in the dark. The dashed line shows the growth of current with time during the formation of conductive channels.

tive channel—were thermally active, with a activation energy of ε_a that virtually coincides with the diffusion activation energy $\varepsilon_{\text{diff}}$ of the mobile donors.[5]

A characteristic feature of crystals in which the formation of a conductive channel is observed is that they are initially inhomogeneous. This is evidenced by the form of the current-voltage characteristics of the dark current and the photocurrent (Fig. 1), as well as by the form of the amplitude–frequency characteristics (AFCs) of the photocurrent. To eliminate the effect of the contacts, the I–V characteristics were measured by a probe method. At small voltages U ($E<E_{\text{th}}$), they are nonlinear, and their slope $\alpha=2-6$ in the coordinates of Fig. 1 (curve *1*) is characteristic of space-charge limited currents (SCLCs), which are usually observed in CdS crystals at fields $E\gtrsim 10^3$ V/cm.[6] Since SCLCs are observed in the crystals studied here at fields of 1–10 V/cm, it can be assumed that the crystals are inhomogeneous and contain low-resistance regions separated by thin high-resistance intervals. This agrees with the form of the photocurrent AFC, which is characteristic of series-connected capacitors (the high-resistance intervals) and ohmic resistances (the low-resistance regions).

After a conductive channel is formed, the IVC changes slope and has a form characteristic of a IVC caused by double-injection currents (Fig. 1, curve *2*).[6] Green luminescence is then observed on the linear section in the high-field region at $T<100$ K, as usually occurs in CdS crystals in this case.

Thus, under the action of an electric field, a process occurs in these crystals which creates the conditions for double-injection currents to appear. In order for a double-injection current to appear in an n-type semiconductor, the contact with one of the electrodes (the cathode) must be ohmic, while the contact with the second electrode (the anode) must be a blocking contact capable of injecting holes.[7] The field applied to the sample must be fairly large in this case, so that the time of flight of the hole between the electrodes is shorter than its lifetime in the valence band. In our case, the role of the electrodes is played by the low-resistance regions. The low-resistance region adjacent to the high-resistance interval on the cathode side serves as the ohmic electrode. The blocking contact is formed in the near-anode region of the high-resistance interval by the formation in it of a thin insulating layer where mobile donors drift in the electric field.[8] When a static electric field is applied, positively charged donors migrate toward the cathode but do not come from the anode. Therefore, a high-resistance layer is formed close to the anode, the electric field in the sample is redistributed, its value at the anode increases until hole injection begins, and double injection appears in the sample, which stabilizes the situation. The current in this case is limited by the resistance of the low-resistance regions: the linear section of the I–V characteristic in the state with a conductive channel (Fig. 1, curve *2*). This mechanism of forming a blocking contact is confirmed by the coincidence of ε_a and $\varepsilon_{\text{diff}}$.

The conductivity in the state with a conductive channel depends on the dislocation density in the crystal, decreasing as γ decreases. The effect is not observed in crystals with $\gamma<10^3$ cm^{-2}, but appears when 10^4–10^5 cm^{-2} additional dislocations are introduced. Thus, it can be assumed that the low-resistance regions are dislocations decorated by donors.

1.2. Athermal donor diffusion under the action of ultrasound

A decrease of the steady-state photocurrent I_{ph} was observed in a number of the test crystals as a result of irradiation by ultrasound pulses (pulsewidth $\tau_i=10^{-5}$ sec) both at 300 K and at 77 K. In both cases, the process did not last longer than τ_i. An analysis of the thermally stimulated conductivity and I_{ph} spectra before and after irradiation, as well as of the lux–ampere characteristics, showed that the effect is caused by a decrease in the concentration of shallow mobile donors. With time, the initial characteristics of the crystal are restored. The activation energy of the restoration process is 0.4 eV, which coincides with the activation energy of Cd_i diffusion.[5] The effect is observed in crystals with a dislocation density of $\gamma>10^4$ cm^{-2}. The necessary dislocation densities, along with a number of other factors, show that the effect is caused by the accumulation of donors by dislocations under the action of ultrasound, as occurs in CdS crystals when they are processed for a long time by sinusoidal ultrasound.[9] A difference in the effect that we observed is the extremely short time that the process takes both at 300 K and at 77 K, which allows it to be regarded as having a very low activation barrier Q_a or even as athermal.

1.3. Shape distortion of the green-luminescence edge spectrum

It is well known that a zero-phonon line and its phonon sidebands with an intensity W_n that increases as n increases

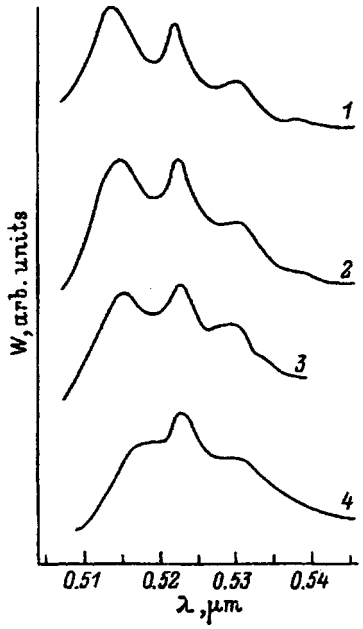

FIG. 2. Green luminescence spectra W of various CdS crystals. The absorptance increases from *1* to *4*.

(n is the number of emitted phonons) is observed in sufficiently perfect CdS single crystals in the green-luminescence edge spectrum.[10] In the most perfect CdS crystals, the ratio is $W_1/W_0=0.8$.[11] A feature of the crystals studied here (with $\gamma>10^4$ cm^{-2}) is that the intensity W_0 of the zero-phonon line is less than the intensity W_1 of the first phonon sideband (Fig. 2). Appreciable absorption in the 0.51 to 0.55-μm region is present in these crystals. The spectrum is distorted more strongly, the greater is the absorption in this region and the steeper is its spectral dependence. It can thus be concluded that the effect is associated with attenuation of the intensity of the emitted light because it is absorbed in the crystal. This is confirmed by the dependence of the shape of the spectrum on the path length of the emitted light in the crystal, which was deliberately varied in the experiments. As shown by studies of the AFCs, crystals with a distorted shape of the PL spectra are inhomogeneous in resistance and contain low-resistance regions. Dislocations decorated by donors are apparently responsible for the absorption in the 0.51 to 0.55-μm region. This assumption agrees with the results of a measurement of the currents induced by the electron probe, which show that the crystal contains linear defects, near which a decreased recombination rate is observed.

1.4. Photostimulated degradation of the photocurrent and photoluminescence

The action of visible and IR radiation on the CdS : Cu studied here at $T>300$ K reduced the photocurrent and the PL intensity (it caused photodegradation), because it coagulated the mobile donors and consequently formed fast-recombination centers.[12] Two thermally stimulated conductivity peaks caused by shallow donors were observed in our crystals: at $T_1=30$–35 K and at $T_2=45$–50 K, along with two components of the ESR signal, at $T<30$ K (D_1 and D_2) both in the dark and under illumination, differing in the half-width ΔH and the g factor. There are thus two types of donors in the crystals: D_1 and D_2. The fact that the crystals are initially inhomogeneous is evidenced by the contradiction between their low dc conductivity, corresponding to a carrier concentration of $n<10^5$ cm^{-3}, and the extremely low Q of a microwave cavity, corresponding to a mean free-carrier concentration of $n\gtrsim10^{16}$ cm^{-3} at $T>50$ K, as well as by the presence of the dark ESR signal from shallow donors (at $T<30$ K). It can thus be concluded that there are low-resistance inclusions in the high-resistance crystals studied here.

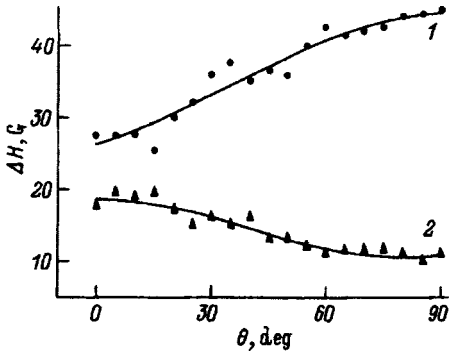

FIG. 3. Angular dependences $\Delta H(\theta)$. $N_d=2\times10^{17}$ (*1*) and 10^{15}–7×10^{16} cm^{-3} (*2*).

It is well known that the shallow-donor concentration can be judged from the angular dependence $\Delta H(\theta)$.[13] In the test samples, the angular dependences of both components of the ESR signal, measured in the dark, are described by the increasing curve *1* in Fig. 3, which corresponds to a donor concentration of $N_d>2\times10^{17}$ cm^{-3}. After illumination at $T<30$ K, the D_1 component of the ESR signal increases; its angular dependence $\Delta H(\theta)$ changes and is now described by the decreasing curve *2* in Fig. 3, which corresponds to $N_d=10^{15}$–7×10^{16} cm^{-3}.[13] The intensity of the D_2 component of the ESR signal and its angular dependence $\Delta H(\theta)$ show virtually no change in this case. The dark signal is thus determined by regions with a large concentration of D_1 and D_2 donors, while the photo-ESR signal is determined by high-resistance regions with a low concentration of D_1 donors (but with a large number of them) and a very low concentration of D_2 donors (no contribution of D_2 donors from the high-resistance regions is seen). The D_2 donors are thus concentrated mainly in the low-resistance regions, which are sinks for donors. After illumination at $T>30$ K, the intensity of the D_2 component of the ESR signal sharply falls, which corresponds to a decrease of the donor concentration in the low-resistance regions of the crystal. Thus, degradation mainly occurs close to sinks for donors. In the crystals studied here, the sinks are apparently Cu-decorated dislocations, since copper diffusion predominantly occurs along them.[14]

2. DEPENDENCE OF THE OPTICAL STRENGTH OF THE CRYSTALS ON THE RATIO OF THE SULFUR AND CADMIUM VAPOR PRESSURES DURING GROWTH

It is well known[15] that one of the main causes of the degradation of high-power, electronically pumped lasers

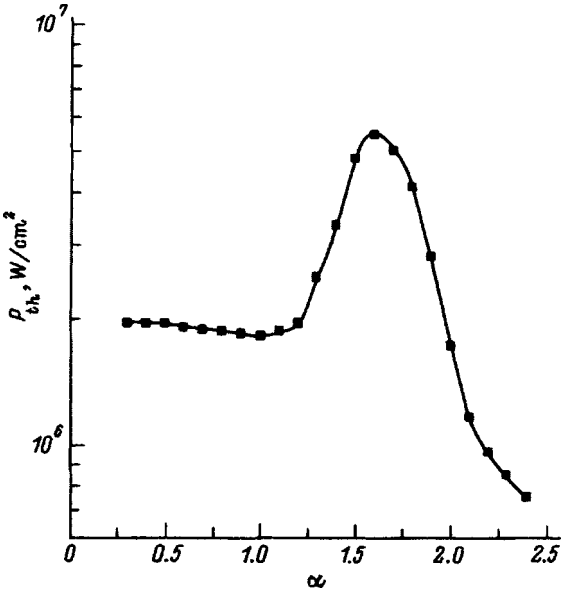

FIG. 4. Threshold power density of the optical breakdown of CdS single crystals grown with various ratios $\alpha = P_S/P_{CdS}$ of the vapor pressures.

based on II–VI semiconductors is that they break down under the action of their own radiation. The threshold of this breakdown depends on the processing conditions for obtaining the crystals. In particular, crystals with a rather high optical strength (11–13 MW/cm^2)[4] and the low dislocation density of $(0.6–1)\times10^4$ cm^{-2} can be obtained at some optimum ratio of the sulfur and cadmium vapor pressures $\alpha = P_S/P_{CdS} = 1.6$. At the same time, it is well known that it is possible to obtain an optical breakdown threshold that substantially exceeds the indicated values in crystals with a similar dislocation density.[3] Therefore, to explain the causes of the breakdown of crystals obtained with various ratios of the sulfur and cadmium vapor pressures, we measured their threshold optical breakdown powers and compared them with the results of a study of the macrodefects.

The threshold power density P_{th} for the optical breakdown of the crystals was determined by irradiating them with light pulses from a ruby laser with nanosecond pulsewidth by the technique described in Ref. 16. The results are shown in Fig. 4, from which it can be seen that the threshold depends only slightly on α in the region of excess cadmium vapor pressure. As the sulfur vapor pressure increases, the threshold power density increases, reaches a maximum at $\alpha = 1.6$, and then sharply decreases.

It turned out that, in the region with excess Cd vapor pressure ($\alpha = 0.5–1$), a significant number, $N = (5–7)\times10^4$ cm^{-2}, of Cd inclusions with a diameter of $d = 3–5$ μm is observed in the crystals. As the S vapor pressure increases, the number of inclusions decreases and their size increases, and, when $\alpha = 1.6$, $N \simeq 500$ cm^{-2} and $d \simeq 10$ μm. As the vapor pressure of S is increased further, the number of inclusions decreases further, until they completely disappear. However, the crystal becomes blocky in this case, with the number of block boundaries increasing as α increases. The increase of P_{th} as α increases from 0.5 to 1.6 correlates with the decrease of the number of Cd inclusions, while the decrease of P_{th} for $\alpha > 1.6$ correlates with the increase of the number of block boundaries. It can therefore be assumed that the breakdown of crystals grown with $\alpha < 1.6$ is caused by the absorption of optical radiation by Cd inclusions, while the breakdown of crystals obtained with $\alpha > 1.6$ is caused by absorption at block boundaries. This conclusion is confirmed by the different ways in which the optical breakdown of crystals occurs with $\alpha < 1.6$ and $\alpha > 1.6$. In the former case, it takes the form of spots that apparently are melted at the Cd inclusion sites, whereas the breakdown in the latter case corresponds to block boundaries. A similar picture appears when the working elements of lasers break down. Note that dislocations apparently do not play a substantial role in the optical breakdown processes of the crystals studied here, but the optimum crystal ($\alpha = 1.6$) is the one that contains the fewest inclusions with the minimum number of block boundaries.

A substantial role in the degradation processes of light-emitting devices is thus played not only by dislocations but also by other types of macrodefects.

CONCLUSIONS

As follows from the results presented above, the presence of a developed system of dislocations and donors that are mobile at room temperature has a number of specific effects. This is associated with the formation of low-resistance regions close to dislocations as a consequence of decoration processes and the possibility of redistributing the donors under the action of various external factors (light, ultrasound, electric field). The last factor destabilizes the characteristics of semiconductor materials. The effect with the greatest sensitivity to the dislocation density was the induced anisotropy of the conductivity. It was observed even for $\gamma > 10^3$ cm^{-2}. Shape distortion of the green band and the presence of athermal diffusion is recorded only when $\gamma > 10^4$ cm^{-2}.

It should be pointed out that some of the effects described here were also observed in other II–VI crystals (CdSe and CdTe), as well as in III–V crystals (GaP).

The enumerated effects make it possible to obtain additional information on degradation and aging processes in II–VI compounds. They can also be used as experimental evidence that dislocations are present simultaneously with mobile donors in crystals and layers.

One more degradation process of light-emitting devices, namely of high-power lasers, is their breakdown by optical radiation. Other types of macrodefects (inclusions, block boundaries) can play a substantial role in this case. As shown by the results presented above, not only the concentration but also the predominant type of macrodefects depends on the crystal-fabrication regimes (in particular, the ratio of the vapor pressure of the components). Cadmium inclusions are the macrodefects responsible for optical breakdown in the region of excess cadmium vapor pressure, whereas block boundaries are responsible in the region of excess sulfur vapor. This determines the form of the breakdown of the working elements of lasers and their optical strength.

[1] M. Ozawa *et al.*, Optoelectron., Devices Technol. **9**, 193 (1994).
[2] M. K. Sheinkman, N. E. Korsunskaya, I. V. Markevich, and T. V. Torchinskaya, J. Phys. Chem. Solids **43**, 475 (1982).
[3] N. V. Klimova, N. E. Korsunskaya, I. V. Markevich, G. S. Pekar, and A. F. Singaevsky, Mater. Sci. Eng., B **34**, 12 (1995).
[4] O. V. Bogdankevich, N. N. Kostin, E. M. Krasavina, I. V. Kryukova, E. V. Markov, E. V. Matvienko, and V. A. Teplitskiĭ, Izv. Akad. Nauk SSSR, Neorg. Mater. **23**, 1618 (1987).
[5] N. E. Korsunskaya, I. V. Markevich, T. V. Torchinskaya, and M. K. Sheinkman, J. Phys. C **13**, 2975 (1980).
[6] R. H. Bube, *Photoconductivity of Solids* (Wiley, New York, 1960).
[7] G. A. Marlos and J. Woods, Proc. Phys. Soc. **81**, 1013 (1963).
[8] C. H. Henry, K. Nassau, and J. W. Shiever, Phys. Rev. B **4**, 2453 (1971).
[9] A. P. Zdebskiĭ, N. V. Mironyuk, S. S. Ostapenko, A. U. Savchuk, and M. K. Sheĭnkman, Fiz. Tekh. Poluprovodn. **20**, 1861 (1986) [Sov. Phys. Semicond. **20**, 1167 (1986)].
[10] M. Aven and J. S. Prener [Eds.], *Physics and Chemistry of II–VI Compounds* (North-Holland, Amsterdam, 1977; Mir, Moscow, 1970).
[11] R. E. Halsted, M. Aven, and H. D. Coghill, J. Electrochem. Soc. **112**, 177 (1965).
[12] N. E. Korsunskaya, I. V. Markevich, T. V. Torchinskaya, and M. K. Sheinkman, Phys. Status Solidi A **60**, 565 (1980).
[13] K. Morigaki, S. Toyotomi, and J. Toyotomi, J. Phys. Soc. Jpn. **31**, 511 (1971).
[14] G. A. Sullivan, Phys. Rev. **184**, 796 (1969).
[15] V. I. Reshetov, G. V. Bushueva, G. M. Zinenkova, A. S. Nasibov, A. N. Pechenov, and N. A. Tyapunina, Kvant. Élektron. (Kiev) **14**, No. 1, 164 (1987).
[16] N. E. Korsunskaya, N. R. Kulish, G. S. Pekar', and A. F. Singaevskiĭ, Kvant. Élektron. (Kiev) No. 44, 74 (1993).

Translated by W. J. Manthey

One-dimensional structures formed by low-temperature slip of dislocations that act as sources of dislocation absorption and emission in II–VI semiconductor crystals

N. I. Tarbaev and G. A. Shepel'skiĭ

Institute of Semiconductor Physics, Ukrainian Academy of Sciences, 252650 Kiev, Ukraine
(Submitted July 28, 1997; accepted for publication November 17, 1997)
Fiz. Tekh. Poluprovodn. **32**, 646–653 (June 1998)

This paper presents and analyzes the results of measurements of characteristic narrow optical absorption and emission lines caused by low-temperature (at $T=1.8$–77 K) slip of dislocations in cadmium sulfide crystals. The optical absorption lines are characterized by giant oscillator strengths ($f\sim 1$). A model which explains the entire set of experimental results for cadmium sulfide and other II–VI compounds is proposed and substantiated. The proposed model associates the dislocation optical absorption and dislocation emission with the formation of one-dimensional chains of associates of point defects accompanying the slip of screw dislocations with jogs. The experimental data are used to calculate the linear density of jogs and the volume density of point defects in the chains, and the oscillator strengths of the corresponding optical transitions are also estimated. © *1998 American Institute of Physics.* [S1063-7826(98)00206-3]

It was shown earlier that characteristic emission lines appear in the edge photoluminescence (PL) spectra of cadmium sulfide crystals as a result of the low-temperature movement and generation of dislocations (at $T=1.8$–77 K).[1–3] These lines were subsequently called dislocation emission (DE). Dislocation emission consists of a group of narrow lines, which are located close to the fundamental absorption edge. Dislocation emission builds up as the degree of plastic deformation increases and, even for rather small residual deformation, can dominate the emission spectrum of CdS. Another feature of DE was ''low-temperature annealing:'' The DE lines virtually disappear from the PL spectrum after a crystal is held at room temperature for even a few hours, even though they are maintained for an indefinitely long time, for example, at 77 K. Thus, the electronic states associated with DE should be considered metastable.

Dislocation emission was also characteristic of crystals of other II–VI semiconductors—CdTe and CdSe. The very possibility that dislocations can be generated and can move in crystals of II–VI semiconductor compounds at temperatures virtually as low as you like, at least to $T=1.8$ K (low-temperature plastic deformation—LTPD), was first reported in Ref. 2. The detection of LTPD made it possible and was subsequently used to observe *in situ* elementary plastic-flow processes in cadmium sulfide crystals.[4–6] Heretofore, dislocations were generally introduced into semiconductor crystals only at temperatures significantly above 300 K. This was substantiated by the presence of high Peierls barriers, which prevented dislocations from moving in the periodic crystal-lattice potential. The detection of LTPD was possible because of the exceptionally high sensitivity of the PL method as used to record the initiation and evolution of plastic deformation.

The detection of the phenomenon of LTPD made it possible to establish several features that are, in our opinion, very important. It turned out that, even though macroscopic plastic deformation is very small at low temperatures ($\varepsilon\leqslant 10^{-4}$), it qualitatively transforms the optical, photoelectric, and radiative properties of the crystals. This is evidence that the electrical and optical activity of the electron states introduced when the dislocations move is extremely high.

As is well known, the movement of dislocations in a crystal lattice causes the generation of point defects. At high temperature, dislocations and the point defects formed by the dislocations already intensely interact when plastic deformation occurs. This does not makes it possible to separate the contributions of the dislocations themselves and the point defects to the variation of the physical properties of the crystals. It is evident that reducing the plastic-deformation temperature as low as possible suppresses the thermally activated interaction mechanisms of the dislocations and the point defects and gives a ''frozen'' or primary picture of the results of defect formation in crystals accompanying the movement of dislocations.

An important methodological remark can be made here. LTPD offers the rare opportunity of directly varying the concentration of introduced deformation defects in a controlled manner during a low-temperature experiment. It also offers the opportunity to visually observe the movement and generation of dislocations. These observations can be made because of the presence of intense DE in the PL and cathodoluminescence spectra.[3]

As far as the nature of the so-called dislocation states responsible for DE is concerned, different points of view have arisen here as new data have been accumulated. Based on a study of DE in CdS by means of spatially resolved spectroscopy, the authors of Refs. 5 and 7 have recently concluded that the electronic states of the dislocations directly participate in the transitions corresponding to DE. According

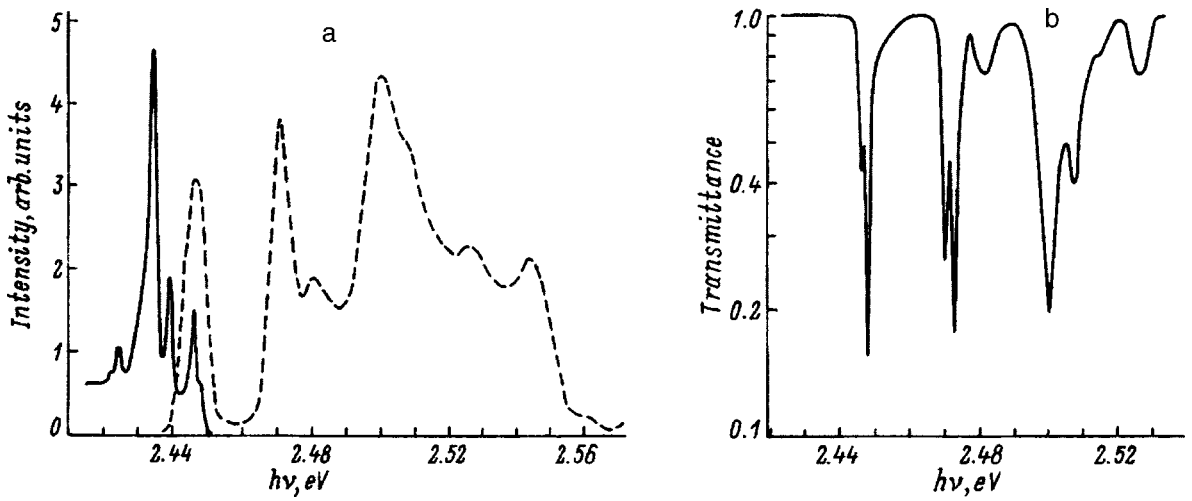

FIG. 1. Dislocation emission spectrum (a, solid curve), DE excitation spectrum (a, dashed curve), and optical transmission spectrum (b) as a result of LTPD of cadmium sulfide crystals.

to the conclusions of Ref. 7, radiative transitions occur via electronic states localized at the nuclei of screw dislocations. Versions in which point defects, located either in the tracks along which the dislocations move or even directly around the dislocations, participate in the DE are ruled out by Negriĭ.[7]

Here it is appropriate to emphasize that the authors of the cited papers confined their attention to the study of DE. In doing so, they ignored the fact that the dislocation states introduced at low temperatures, besides DE, cause radical changes in the optical absorption (OA) spectra, the PL excitation spectra, and the photoconductivity (PC) spectra. In our opinion, the interpretation of the OA spectra induced by LTPD and consisting of a group of narrow lines with a very high absorption coefficient α in them requires special attention (α can exceed 10^2 cm^{-1}). This is evidence that the corresponding optical transitions have a large oscillator strength. The total picture of the defect formation accompanying the movement of dislocations is thus far more complex than can be given by only the features of the DE. All the phenomena that result from LTPD must of course be taken into account in order to interpret the nature of the dislocation states under consideration. Note that the recorded DE and OA lines have no analogs in the original II–VI crystals and were not observed earlier. Moreover, they do not appear after plastic deformation is carried out at high temperatures ($T>300$ K). Finally, the indicated optical lines are not detected after intrinsic point defects are introduced into the crystal, including at low temperatures ($T<78$ K), for example, by irradiation with high-energy particles. In the latter case, the defect distribution can be uniform over volume but remains random.

This paper, besides the DE spectra, presents and analyzes the results of measurements of dislocation OA, the excitation spectra of DE and PC, and also the temperature quenching of DE. Based on these data, it is concluded that only a model of one-dimensional chains consisting of associates of point defects formed by moving dislocations can explain the entire set of experimental data most completely and without contradictions.

High-resistance, not specially doped bulk single crystals of CdS, as well as of CdSe and CdTe, were studied. The samples were fabricated in the form of rectangular parallelepipeds whose faces were oriented by x-ray diffraction. The samples were placed in a liquid-helium optical cryostat along with a uniaxial-strain device. The experimental methods and apparatus for spectroscopic measurements of PL, OA, and PC have been described in earlier articles.[8,9] Orientation of the faces of the samples made it possible to plastically deform them along prismatic or along mixed slip systems. The optical transmission along or normal to the crystal's **C** axis was measured using a wide beam that covered a significant volume of the sample and thus also a significant number of slip bands of the dislocations. Because of this circumstance, it is possible to speak of some average optical absorption coefficient α, even though the evolution of plastic flow in the crystal is fundamentally inhomogeneous. Determining α in this way gives underestimated values, which should be allowed for subsequently when estimating the density of dislocation defects. The PL was excited by the radiation of a He–Cd laser with a wavelength of 441.6 nm and a power of up to 5 mW. The excitation spectra of the DE was recorded using a DMR-4 monochromator and a radiation source consisting of a DKSSh-150 xenon lamp. The density N_d at which dislocations were produced on the (0001) face was determined from the number of etch pits, using the technique of Ref. 10.

The data shown in Fig. 1 correspond to the deformation of a CdS sample uniaxially compressed along the $\langle 10\bar{1}0\rangle$ direction at $T=4.2$ K. The PL, OA, and PL excitation spectra were recorded in the direction of the **C** crystallographic axis. The spectral distribution of the DE in cadmium sulfide crystals (Fig. 1a) can be obtained with virtually no background by using selective excitation in the characteristic lines that occur in the DE excitation spectrum (Fig. 1b). These lines

are detected in the impurity absorption region. The number of DE lines, their spectral position, and the intensity ratios in this case are independent of the power density of the exciting radiation. The entire DE spectrum can be obtained when PL is excited by radiation corresponding to any of the lines in the excitation spectrum.

The DE in Fig. 1a at $T=4.2$ K consists of a series of characteristic emission bands, which we shall call dislocation bands. In what follows, we shall consider three of the most distinct and intense bands, which for brevity we designate I, II, and III, with energies of 2.447, 2.440, and 2.435 eV, respectively. Bands II and III are quenched as the temperature is increased. In this case, band II virtually disappears already at $T=20$ K, while band III is quenched close to $T=40$ K. The intensity of band I, with the shortest wavelength, shows virtually no change in the range 4.2–40 K. As the temperature is increased further, the intensity begins to decrease, and only at $T=140$–150 K does band I become virtually insignificant in the PL spectrum. Note that the half-width of the dislocation bands in the temperature range 1.8–100 K is of the order of kT and is close to the half-width of the emission lines of bound excitons.

In the entire temperature range studied here, the dislocation bands are accompanied by a distinct LO phonon structure. The electron–phonon coupling factor is very similar for all the dislocation bands in this case and equals about 0.1. This can be evidence that all three types of radiative transitions go to the same final state, probably of the acceptor type. Actually, significant values of the electron–phonon coupling factor in CdS were found only for optical transitions to an acceptor, because of the large effective mass of the hole.[11]

Thus, if one starts only from the PL data, it is not particularly hard to interpret the radiative transitions in the DE. Actually, dislocation bands II and III should be attributed to radiative transitions from shallow donor levels, while band I is from a free energy band to the same acceptor state. This assumption agrees well with the presence of fine structure—the doubling of all three bands. The intensity redistribution of the lines in the doublet in favor of the lower-energy component is evidence that the upper of the doublet levels of the acceptor gradually fills with holes as the temperature is reduced.

As can be seen from the data of Fig. 1, the spectral positions of the bands in the OA completely coincide with those in the DE excitation spectrum. Such detailed coincidence of the absorption lines and the lines in the DE excitation spectrum indicates that the OA and DE lines correspond to optical transitions between electron states in the same system of energy levels. Note also that all the described features of the OA and the DE excitation spectra appear simultaneously with the DE lines as a result of LTPD and disappear simultaneously with the latter as a result of the low-temperature annealing described above (at temperatures of $\lesssim 300$ K).

Narrow bands also appear in the spectral distribution of the PC as a result of LTPD, with the new maxima of the photocurrent excitation coinciding in energy position with the maxima of the DE excitation spectrum. The PC bands are maintained all the way to the lowest temperatures in the experiment, about 1.8 K. This means that an internal photoelectric effect of electron type occurs in each of the dislocation absorption bands, since the photocurrent in CdS is determined by the majority current carriers—electrons. The photoelectric effect can be caused either directly by transitions of electrons into a band or by transitions accompanied by an Auger process. As a result, free electrons appear.

It should be pointed out that the described changes in the spectra are qualitatively independent of the observation direction. In samples oriented for mixed slip, bands induced by uniaxial compression in the spectra were not qualitatively distinctive, except for having significantly lower intensity and larger smearing. The latter circumstance is evidence that the dislocations slipping in the basal plane promote only broadening of the bands by their own elastic fields.

Piezooptical studies of DE band I and the OA band corresponding to it were used to determine the degree of orientation degeneracy (sixfold) and the symmetry of the electron states responsible for the DE—C_s.[12]

The quantitative data that we obtained from the optical absorption $\alpha(\nu)$ make it possible to estimate the mean density N of LTPD-generated, optically active centers by means of the standard equation[13]

$$fN=\frac{ncm}{\pi e^2\hbar}\int \alpha(\nu)d\nu, \tag{1}$$

where f is the oscillator strength, N is the concentration of oscillators, ν is the frequency, n is the refractive index, c is the velocity of light in vacuum, e and m are the charge and mass of the electron, and $\hbar=h/2\pi$ is Planck's constant. Substituting numerical values, we obtain

$$fN\simeq 1.13\times 10^{12}n\int \alpha(\nu)d\nu \tag{2}$$

(here α is measured in cm^{-1}, and N is measured in cm^{-3}). For the α values obtained from our experiment, we have $fN=2\times 10^{15}$ cm^{-3}. Negry and Osipyan[14] explained the luminescence spectrum of regions of the crystal locally plastically deformed at $T>300$ K by radiative recombination of electrons and holes directly at dislocations. However, even if it is assumed in the calculation that the number of states (oscillators) per unit length of the dislocation equals the number of atoms in which the coordination of the chemical bonds in the dislocation nucleus is disturbed, $\sim 10^7$ cm^{-1}, the large optical absorption observed in our experiment could only be explained by an oscillator strength of $f\sim 10^3$ for the optical transition. The estimate is made for a mean dislocation density of $N_d=10^5\mathrm{cm}^{-2}$ on the (0001) face of the deformed crystal, which corresponds to an absorption coefficient $\alpha=10$ cm^{-1}. Meanwhile, a value of $f\sim 10$ is already considered giant in semiconductors, is detected only in exciton–impurity complexes, and requires special theoretical substantiation.[15]

It is established in Ref. 16 that the screw component predominates in dislocations in CdS that slip according to the prismatic system, and this increases the actual length of the dislocation in the calculation for each observed etch pit in the (0001) plane. As can be judged from the dislocation con-

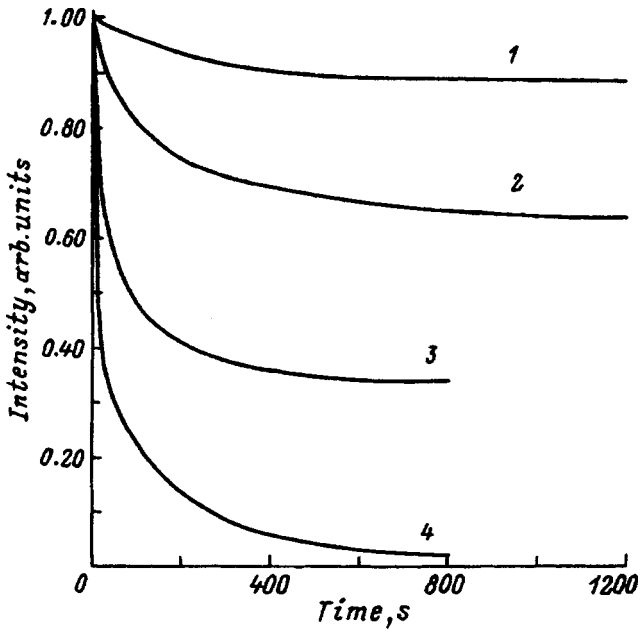

FIG. 2. Kinetic dependences of DE ''burnout'' vs temperature T, K: *1*—4.2, *2*—77, *3*—98, *4*—135.

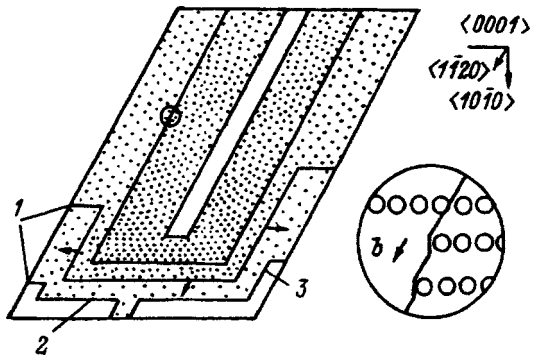

FIG. 3. Diagram of defect formation as a result of plastic deformation according to the $\langle 11\bar{2}0\rangle\{1\bar{1}00\}$ system because of the slip of screw dislocations with jogs (see the enlarged section) for compression along $[10\bar{1}0]$. *1*—slip dislocations emerging on the (0001) face; *2, 3*—edge and screw segments of dislocation loops, respectively. The variation of the density of the points conventionally reflects the increase of the mean density of associates of point defects after the passage of a successive screw segment. The arrows indicate the direction in which the dislocations move.

figuration given in Ref. 16, in a single slip band along a prismatic plane of type $\{1\bar{1}00\}$, the length of the dislocation (and, accordingly, the number of electron states) for one etch pit is increased in the calculation because of sharp bends, but in practice by no more than a factor of 3 or 4. Even if the probable differences in the energy spectrum of the electron states of the edge and screw sections of the dislocation are disregarded, this does not eliminate the fundamental quantitative divergences of the ''nuclear'' model from the data of the optical experiment.

It follows from the estimate given here that none of the models of the electron states responsible for DE which is associated directly with the dislocation nucleus, can explain the large values of the absorption coefficient that we observed.

Negry *et al.*[6] attributed the DE directly to the nuclei of the screw dislocations of the slip system $\langle 2\bar{1}10\rangle\{01\bar{1}0\}$ on the basis of the fact that the authors observe luminous spots that build up with time on the faces of the sample perpendicular to the basal plane. These spots are unambiguously interpreted as the moving tracks of screw dislocations. However, in our opinion, there is ambiguity here if one takes into account the experimentally observed fast quenching of the DE intensity by the exciting light when the optical excitation levels have comparatively low intensity (50 W/cm^2). Figure 2 shows the kinetic dependences of the DE intensity for various temperatures. Two sections can be distinguished in these curves: a section of rapid falloff and a section of relatively stable DE intensity. It can be seen that, as the temperature increases, the rate of the initial decay and its amplitude increase. Here the amplitude of the decay increases sharply and nonlinearly with increasing excitation intensity. Significant excitation intensities, up to 2×10^2 W/cm^2, which must result in strong quenching of the DE in the interval between the divergent screw dislocations, were used in Refs. 4, 6, and 7. In this case, apparently only not-yet-quenched sections in the immediate vicinity of the moving dislocations appeared. Thus, taking into account the limited spatial resolution and the background suppression during processing of the electronic television signal, instead of a continuous luminous strip between two divergent screw dislocations, only its ends were observed in Ref. 6 at 77 K. On this basis, the sources of the DE were assumed to be exclusively the regions of the dislocation nuclei. Our assumption was also confirmed by the fact that, at a temperature of 4.2 K, when the ''burnout'' of the DE is weak, what Negry *et al.*[6] see is an elongated continuous luminous band. Thus, the conclusions of this paper do not contradict the experimental data of the microluminescence analysis of Ref. 6.

On the other hand, besides linear defects, a significant number of point defects are formed by plastic deformation. Negry *et al.*[6] used direct observations to show that screw dislocations which slip in the $\{10\bar{1}0\}$ plane, generate dislocation PL. In this case, sources of dislocation luminescence are directly generated as the screw dislocations move. In our opinion, this is evidence that there is no participation of the mechanism in which defects are formed by the recombination of dislocations of the same type with oppositely directed Burgers vectors which slide in adjacent slip planes. At the same time, there is a well-known mechanism in which point defects are formed when screw dislocations move with jogs (see, for example, Ref. 17). When deformation occurs according to the prismatic slip system, the screw segments slip in parallel planes of type $\{1\bar{1}00\}$, while jogs with an edge component climb. Since diffusion can be ignored at low temperatures, the jogs generate either interstitial atoms or vacancies. As it moves along, the jog forms a continuous chain of defects (Fig. 3), which can be interrupted only when the jog shifts along a screw dislocation conservatively, for example, when it bends around a pinned quasi-one-dimensional defect.

One can attempt to consider what the structure of such a chain of vacancies is. The jog of the screw dislocation that we are interested in can be a segment of a dislocation of one

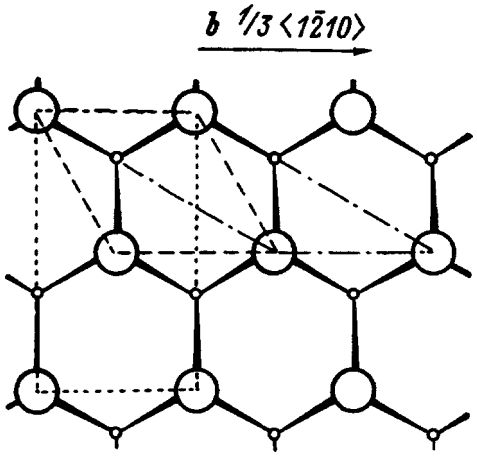

FIG. 4. Wurtzite lattice from the side of the basal plane and possible configurations of cavities in the continuum, formed by various jogs of a screw dislocation: The dotted, dashed, and dot–dashed curves indicate lines at 90°, 60°, and 30° dislocations, respectively.

of three types. According to Ref. 18, this can be a 90° (edge) dislocation or a mixed 60° or 30° dislocation.

For definiteness, we can consider a case in which vacancies are generated. Figure 4 conventionally shows, ignoring the width of the dislocations, the configurations of all three forms of jogs, imposed on a Wurtzite lattice in the basal plane. This shows the contours of the cross section of the cavity that would be formed in a continuum. The cavity would have the shape of a prism with generatrices **b** and **l**, where **l** is the unit section of the length of the corresponding jog. However, taking into account the discreteness of the crystal, the ''cavity'' will have the form of a chain of vacancies of type $V_{\mathrm{Cd}}-V_{\mathrm{S}}-V_{\mathrm{Cd}}-V_{\mathrm{S}}-\ldots$, etc., forming a one-dimensional structure (Fig. 5). In this case, for each elementary event, the climb of a single 60° or 30° jog will be formed along two pairs of vacancies. The climb of the jog of a 90° (edge) dislocation must create a cavity twice as large in volume and generate four pairs of vacancies each: $2(V_{\mathrm{Cd}}-V_{\mathrm{S}})$ on each step. It can be concluded from elementary energy considerations that the motion of a 90° jog will be

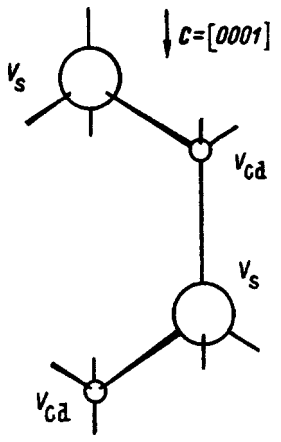

FIG. 5. Diagram of an associate of intrinsic point defects (a period of a one-dimensional chain), formed during the slip of a screw dislocation with jogs according to the $\langle 11\bar{2}0\rangle\{1\bar{1}00\}$ system.

hindered. Therefore, there is a basis for assuming that single jogs of 30° and 60° dislocations are the most probable source of point defects for the plastic deformation considered here.

The symmetry of each individual pair of vacancies $V_{\mathrm{Cd}}-V_{\mathrm{Cd}}$ belongs to group C_s; i.e., there is a first-order axis, at an angle to the (0001) axis, and a $\{1\bar{2}10\}$ mirror reflection plane. The $\{1\bar{2}10\}$ reflection plane can have the most symmetric configuration of the chain as a whole, but only when the axes of each alternate pair of vacancies $(V_{\mathrm{Cd}}-V_{\mathrm{S}})$, resulting from the pure climb of a jog, are located in the same plane. Such a configuration will apparently be energetically favorable, since it corresponds to the formation of the minimum dipole moment of the chain (the type of bonding in CdS is partially ionic). Chains that lie entirely in one plane will be triply orientationally degenerate. In the case of the formation of interstitial atoms, the difference is that a pair of Cd and S atoms in the region of a jog is displaced from their lattice sites into interstitial positions.

Thus, the collective electronic states of the chains of defects considered here cannot as a whole provide a higher degree of orientational degeneracy of the bands observed in absorption[12] and in emission[12,7] in the resonance dislocation band. At the same time, the symmetry of an individual pair of vacancies $(V_{\mathrm{Cd}}-V_{\mathrm{Cd}})$ and the degree of spatial degeneracy coincide with the symmetry of the electronic states corresponding to the DE.

Figure 3 schematically shows the formation mechanism of chains of intrinsic point defects by moving screw dislocations with jogs. The chain structure is shown only in the enlarged section.

Note to the diagram: We assume that (1) the number of closed half-loops equals the number of etch pits in the slip bands, (2) the loop initially penetrates the entire length of the slip plane because of the motion of the edge segment, (3) the mean linear density of jogs along the screw segments is N_d.

The number N of defect states assembled in a chain for a sample 1 cm thick can then be calculated from

$$N[\mathrm{cm}^{-3}]=0.5N_dN_j\times 10^7, \tag{3}$$

where 10^7 cm^{-1} is the linear density of point defects (the number of periods of complexes of defects per 1 cm of length), and 0.5 is a factor that averages the contribution to the generation of point defects of the first half-loops, which intersect virtually the entire sample, and of the last half-loops, whose contribution to the generation of the chain of defects is small.

The value obtained from Eq. (3) must be set equal to the value of N obtained experimentally from the data from optical absorption, estimated from Eq. (2): $N[\mathrm{cm}^{-3}]=2\times 10^{14}f$. We thus obtain

$$N_j=4\times 10^7/(N_df). \tag{4}$$

Taking a value of N_d equal to the mean of the dislocation density in slip planes per cm^2, 2×10^5, we obtain a relationship that connects N_j and f:

$$N_j[\mathrm{cm}^{-1}]=(1/f)2\times 10^2. \tag{5}$$

This makes it possible to estimate the mean linear density of the jogs on the screw segment on the basis of Eq. (4), after making some preliminary reasonable assumption concerning the oscillator strength f of the optical transitions. As is well known, the maximum oscillator strength is observed in optical transitions corresponding to bound excitons and ranges from 1 to 10 for II–VI crystals.[19] In our case, starting from the spectral position of the lines, it should be recalled that there is significant localization of the excitons. Therefore, $f=1$ should be chosen as the necessary limit of this quantity. We thus obtain $N_j=2\times10^2$ cm^{-1} as a lower estimate of N_j.

On the other hand, it is possible to give an upper estimate of N_j. Johnson and Gilman[20] proposed an estimate of the dislocation-braking stress t_d by single jogs with a density of N_j, caused by their nonconservative displacement, using the relationship

$$t_d=(N_jW)/b^2, \tag{6}$$

where W is the point-defect formation energy, and **b** is the Burgers vector. We shall start from the assumption that the slip mechanism of screw dislocations with jogs displaced nonconservatively and generating the defects responsible for DE is precisely the mechanism that controls the slip of dislocations in crystals at the given temperature. Using Eq. (6), we can estimate the value of N_j, starting from which the plastic flow of the crystal is controlled by the slip of screw dislocations with jogs: $N_j=t_db^2/W$. We use as t_d the mean value of the threshold stress t_{thr} of plastic deformation obtained from experiment for $T=77$ K: $t_d=(1/2)t_{\text{thr}}=0.5\times10^5$ kg/m^2 (the factor 1/2 takes into account the tilt of the slip plane with respect to the compression axis $[11\bar{2}0]$. We use as the point-defect formation energy the sum of the formation energies of two pairs of isolated vacancies, taken from Ref. 20: $W=2[W(V_{\text{Cd}})+W(V_{\text{S}})]=2(3.5+2)$ eV $=11$ eV. This value is undoubtedly overestimated, since it neglects the interaction of close-lying defects. For CdS we have $b=0.414\times10^{-8}$ m.

Thus, $N_j=t_db^2/W=4.8\times10^3$ cm^{-1}. This is the upper limit of N_j. For this value of N_j, starting from Eq. (5), a smaller oscillator strength of the optical transition should be used, namely $f=0.1$. We have thus established that N_d lies in the range 2×10^2–4.8×10^3 cm^{-1}. It thus follows [see Eq. (4)] that the mean bulk density of the point defects located in chains lies in the range 2×10^{15}–5×10^{16} cm^{-3}, which is a quite realistic value.

Starting from the above exposition, we present the following model of electronic transitions that explains the set of features of the absorption and emission spectra of cadmium sulfide crystals deformed plastically at low temperature. The transition responsible for the longest-wavelength optical absorption band and the shortest-wavelength PL band corresponds to the excitation of excitons coupled to the quasi-one-dimensional structure of vacancy (interstitial) type formed when jogs move on screw dislocations. Since the excitons are localized on a quasi-one-dimensional structure, the exciton level must be smeared into a band because of the overlap of the wave functions of the bound exciton states along the chain. The other OA bands represent absorption by excited states of the same system. Moreover, in the latter case, the excitation propagates along the chain of defects and quickly relaxes to the ground state; it therefore does not show up in the emission.

The large oscillator strengths f are thus explained by intrachain resonance interaction. This presents an appropriate analogy with molecular crystals, in which the molecules are stacked into one-dimensional oriented chains. The matrix element of the intrachain interaction in such crystals exceeds that of the interchain interaction by at least two orders of magnitude. Long-wavelength DE bands II and III, for which no resonance absorption is observed, represent emission associated with certain breakdowns of the translational symmetry of the chains of intrinsic or impurity origin, excited via the ''one-dimensional bound-exciton bands'' mentioned above. Because of low binding energy, the chain structure is unstable. Therefore, low temperature is a necessary factor to prevent the decay of the structures. The indicated model can be applied to other II–VI compounds, starting from the similarity of their DE.

There are other important facts in favor of the existence of one-dimensional structures and narrow free-energy bands associated with them. Thus, LTPD results in appreciable anisotropy in the longitudinal and transverse photocurrents with respect to the assumed orientation of the chains: The ratio $I_{\parallel}/I_{\perp}$ reaches 10. Moreover, the current-carrier mobility, estimated from PL measurements in the dislocation bands of the OA, has a value of $\mu\approx5\times10^5$cm^2/(V·s). This is at least an order of magnitude greater than the mobility of the conduction-band electrons in cadmium sulfide.

CONCLUSIONS

The low-temperature (in the interval 1.8–77 K) motion of dislocations results in the appearance in the optical and radiative spectra of II–VI crystals of characteristic narrow lines that have no analogs in the original crystals or in crystals subjected to any other form of processing. The optical transitions are characterized by giant oscillator strengths, while the corresponding electron states turn out to be metastable. Based on the experimental results and quantitative estimates, a model of defect formation by slipping screw dislocations with jogs has been proposed. In terms of this model all the features of the optical and radiative spectra of II–VI crystals subjected to LTPD are explained. The jogs form one-dimensional periodic electron structures consisting of associates of intrinsic point defects of the crystal lattice. It is just the low temperature that prevents the associates from decaying and makes the one-dimensional structures stable. The giant oscillator strengths of the optical transitions are explained by intense intrachain resonance interaction. The linear density of the jogs and the volume density of the point defects in the chains have been computed from the experimental data, and the oscillator strengths are estimated for the corresponding optical transitions. It is shown that it is incorrect to use a model of defect formation accompanying LTPD in which the OA data are disregarded.

We express our appreciation to F. T. Vas'ko for a useful discussion of the experimental results.

We wish to thank the State Fund for Fundamental Re-

search of the Ministry of Science of Ukraine, with whose support this work was carried out.

[1] V. F. Grin', E. V. Markov, E. A. Sal'kov, N. I. Tarbaev, and G. A. Shepel'skiĭ, Fiz. Tverd. Tela (Leningrad) **20**, 2188 (1978) [Sov. Phys. Solid State **20**, 1263 (1978)].
[2] E. A. Sal'kov, N. I. Tarbaev, and G. A. Shepel'skiĭ, Ukr. Fiz. Zh. **26**, 1570 (1981).
[3] N. I. Tarbaev, J. Schreiber, and G. A. Shepelskii, Phys. Status Solidi A **110**, 97 (1988).
[4] V. D. Negriĭ and Yu. A. Osip'yan, JETP Lett. **35**, 598 (1982).
[5] J. Appl. Phys. **74**, 7008 (1993).
[6] V. D. Negry, Yu. A. Osipyan, and N. V. Lomak, Phys. Status Solidi A **126**, 49 (1991).
[7] V. D. Negriĭ, Fiz. Tverd. Tela **34**, 2462 (1992) [Sov. Phys. Solid State **34**, 1320 (1992)].
[8] E. A. Sal'kov, N. I. Tarbaev, and G. A. Shepel'skiĭ, Fiz. Tverd. Tela (Leningrad) **22**, 1110 (1980) [Sov. Phys. Solid State **22**, 646 (1980)].
[9] E. A. Sal'kov, N. I. Tarbaev, and G. A. Shepel'skiĭ, Fiz. Tekh. Poluprovodn. **14**, 1540 (1980) [Sov. Phys. Semicond. **14**, 913 (1980)].
[10] Yu. A. Osip'yan, I. S. Smirnova, and G. K. Strukova, Fiz. Khim. Obrab. Mater. **6**, 145 (1974).
[11] I. I. Hopfield, Phys. Chem. **10**, 110 (1959).
[12] E. A. Sal'kov, N. I. Tarbaev, and G. A. Shepel'skiĭ, Fiz. Tekh. Poluprovodn. **15**, 1467 (1981) [Sov. Phys. Semicond. **15**, 851 (1981)].
[13] A. M. Stoneham, *Theory of Defects in Solids* (Clarendon Press, Oxford, 1975; Mir, Moscow, 1978), Vol. 1.
[14] V. D. Negry and Yu. A. Osipyan, Phys. Status Solidi A **55**, 583 (1979).
[15] É. I. Rashba, Fiz. Tekh. Poluprovodn. **8**, 1241 (1974) [Sov. Phys. Semicond. **8**, 807 (1974)].
[16] Yu. A. Osipyan, V. F. Petrenko, G. K. Strukova, I. I. Khodos, Phys. Status Solidi A **57**, 477 (1980).
[17] J. P. Hirth and J. Lothe, *Theory of Dislocations* (McGraw-Hill, New York, 1968; Atomizdat, Moscow, 1972).
[18] Yu. A. Osipyan and I. S. Smironova, Phys. Status Solidi **30**, 19 (1968).
[19] D. G. Thomas and J. J. Hopfield, Phys. Rev. **175**, 1021 (1968).
[20] W. G. Johnson and J. J. Gilman, J. Appl. Phys. **31**, 632 (1960).

Translated by W. J. Manthey

Study of the surface structure of tin dioxide layers for gas sensors by atomic-force microscopy

M. V. Bestaev, D. Ts. Dimitrov, A. Yu. Il'in, V. A. Moshnikov, F. Träger, and F. Steitz

St. Petersburg Electrical Engineering University, 197376 St. Petersburg, Russia Physics Department, Kassel University, D-34182 Kassel, Germany

(Submitted November 11, 1997; accepted for publication December 5, 1997)
Fiz. Tekh. Poluprovodn. **32**, 654–657 (June 1998)

This paper presents the results of a study by atomic-force microscopy of tin dioxide layers as a function of the conditions under which they are doped with iodine and tellurium during the production of the layers by thermal vacuum deposition of tin, followed by oxidation. Data concerning the atomic-force microscopy of layers fabricated in various processing regimes are presented and discussed. It is shown that introducing volatile impurities into the starting charge is an effective means of modifying the surface structure of the layers and of altering the character of its microsurface. The temperature dependence of the sensitivity of the layers to toluene vapor is studied and analyzed. © *1998 American Institute of Physics.* [S1063-7826(98)00306-8]

Semiconductor sorption sensors based on layers of tin dioxide SnO_2 possess a number of advantages and are promising for developing gas-analysis apparatus for various technical purposes.[1] The properties of the layers, especially the sensitivity and selectivity with respect to the gases to be detected, are determined by the processes for producing them and depend on the microstructure and surface topology,[2] deviations from stoichiometry,[3] the form and content of the dopants,[4–6] and effects at the grain boundaries associated with the microsegregation of impurities and the isolation of second-phase precipitates.[7]

In this paper we present the results of experimental studies of the surface topology and properties of tin dioxide layers as a function of the conditions under which they are doped during their production.

In obtaining tin dioxide layers, films of metallic tin are first formed by thermal vacuum deposition on substrates of 22KhS ceramic, as described in Ref. 8. The films were homogeneous in thickness and had a mirror-smooth surface. They were then oxidized while annealing them in two stages. The low-temperature stage (6 h at a temperature of 480 K) produced phase transitions according to the reaction $Sn \rightarrow SnO \rightarrow Sn_3O_4 \rightarrow SnO_2$ (amorphous). The high-temperature stage (6–30 h at 725 K) is necessary for forming the crystal structure SnO_2 (amorphous)$\rightarrow SnO_2$ (crystalline). Oxidative annealing was carried out in a controlled atmosphere with a partial pressure of oxygen in the range 0.10–0.35 atm.

Iodine and tellurium were used as impurities. Tin iodide SnI_2 and tin telluride SnTe served as sources and were introduced in a controlled concentration into the starting mix for depositing the metallic tin. When the impurities were present, a regime of explosive deposition of the mix was used.

Atomic-force microscopy (AFM) was used to investigate the surface topology of the layers. This made it possible to obtain data on the microrelief in the nanometer range and allowed the samples to be tested directly in air. The measurements were made on a Park Scientific Instrument scanning force microscope of type PSI-CP. The informational signal was recorded by reflecting the ray of a laser diode onto a coordinate-sensitive photodetector. Software from PSI was used in analyzing the results, making it possible to record and process data, to carry out filtering and smoothing, and also to statistically analyze the resulting pictures. The *ex situ* AFM regime was used. Images of the surface recorded in different sections of different samples of each of the series had an identical character, which is evidence that the results had rather good reproducibility and repeatability.

An analysis of the set of AFM data showed that introducing volatile impurities into the starting mix is an effective way to control the surface structure of the layers.

In the absence of impurities, SnO_2 layers are characterized by the surface topology shown in Fig. 1a. The AFM image shows hilly formations with comparatively smooth contours. The microsurface is relatively indistinct. X-ray diffraction using the technique of Ref. 9 showed that such layers have a homogeneous composition and possess a polycrystalline structure.

The surface topology typical of $SnO_2\langle I\rangle$ layers is shown in Fig. 1b. When iodine is introduced into the mix, the form of the surface changes and becomes more crumbly. The microsurface is more distinct than in the preceding case. The AFM image shows many domelike bumps. These changes can be associated with the self-doping effect that occurs when tin compounds are heat treated in an iodine medium.[10] Accordingly, under our conditions—with oxidative annealing—the reaction $2SnI_2 \rightarrow Sn + SnI_4$ is possible. In this case, the tin concentration increases in the material, while the volatile components are already removed at the stage of low-temperature oxidation, which results in crumbling of the surface. As the iodides escape, voids can be formed, including nanometer-size voids, and fine structure of the microsurface can appear.

The surface topology of the $SnO_2\langle I,Te\rangle$ layers is shown in Fig. 1c. As can be seen, introducing iodine and tellurium

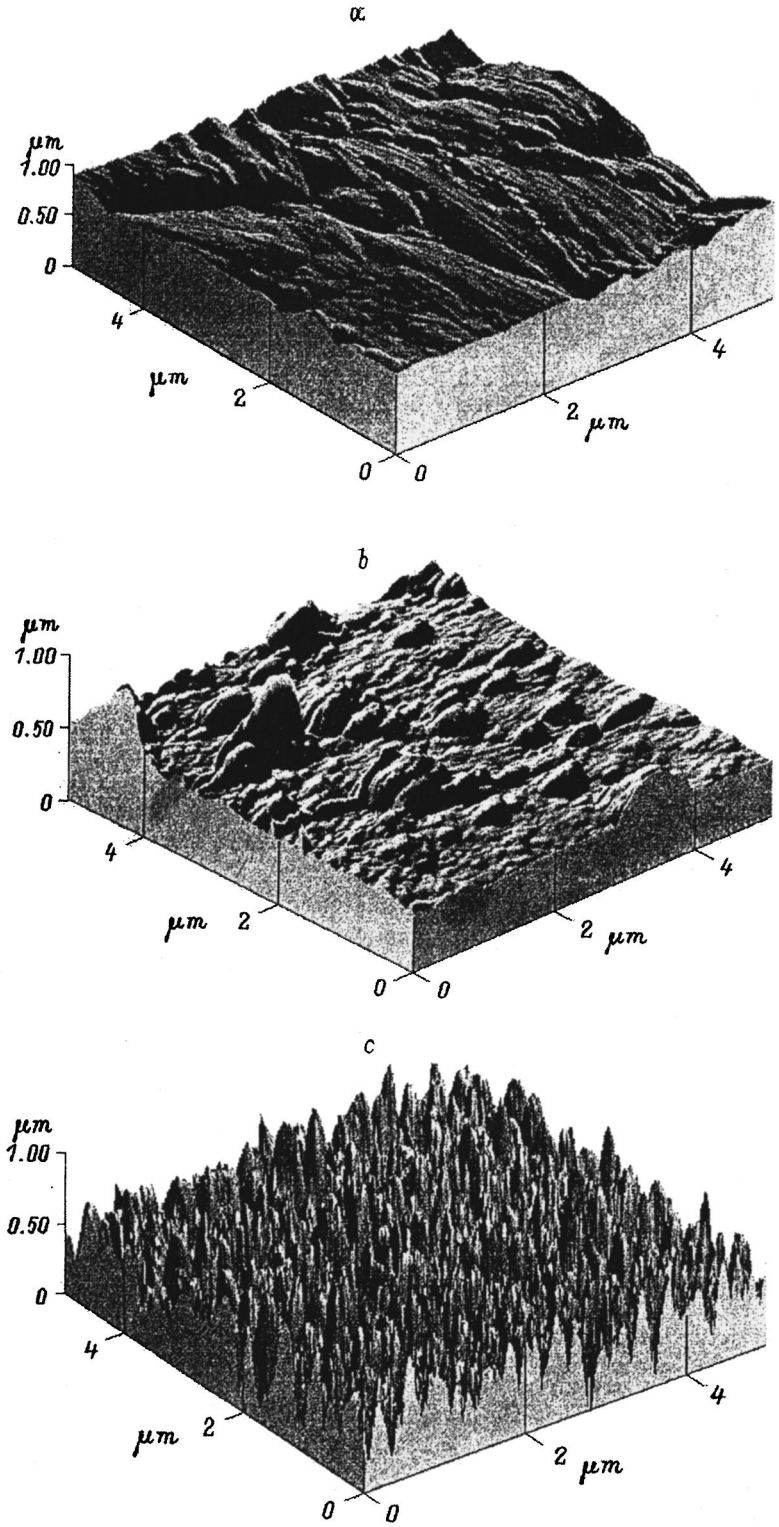

FIG. 1. Surface topology of layers of SnO_2 (a), SnO_2 ⟨I⟩ (b), and SnO_2 ⟨I,Te⟩ (c).

in combination substantially alters the surface structure and radically changes the character of the microsurface. The surface is strongly developed. A system of regular adjoining conical protrusions tight-packed against each other can be seen in the AFM image. The area of the adsorbing surface increases significantly. A statistical analysis of the AFM profile over a linear interval of 4.34 μm gives the following values of the characteristic microsurface parameters: the rms deviation of the height is $R_{rms}=399$ Å; the mean size of the roughness is $R_{ave}=239$ Å; the mean height is 0.216 μm, and the median distribution over height is 0.219 μm.

In our opinion, it is interesting to compare the AFM data from the SnO_2⟨I,Te⟩ layers with the results of investigating them by the method of internal etching.[1] The treatment of

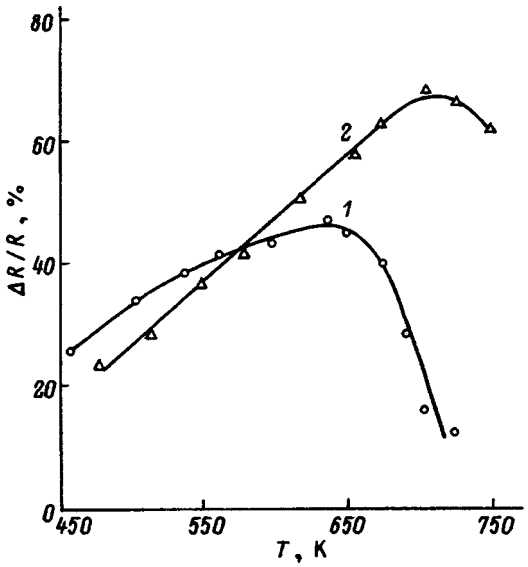

FIG. 2. Temperature dependence of the sensitivity under the action of toluene vapor for SnO_2 (*1*) and $SnO_2\langle I,Te\rangle$ layers (*2*).

these results provides evidence of the presence in the samples at the deposition stages of a tin film and of low-temperature annealing of the tellurium bonds that characterize tin telluride. Taking this factor into account in interpreting the features of the observed microsurface, it can be assumed that SnTe microinclusions and agglomerates of them, which are distributed in the surface region of the film and which influence the oxidation process, retard its flow at the sites where they occur, whereas an oxide layer freely forms on the other sections and predominantly grows upward.

In tests of tin dioxide layers in sensors for detecting the vapors of organic solvents, it was established that the introduction of volatile impurities that initiate the process of surface modification and influence the adsorption capability of the surface changes the properties of the layers. The temperature dependence of the sensitivity, expressed in terms of the relative change of the resistance of the sample ($\Delta R/R$) under the action of toluene vapor in a concentration of $C_t = 60\ \mathrm{mg/m^3}$, is shown in Fig. 2 for layers of SnO_2 and $SnO_2\langle I,Te\rangle$. As can be seen, the $SnO_2\langle I,Te\rangle$ layers have higher sensitivity. Its maximum value is attained at the optimum working temperature of $T \simeq 700\ \mathrm{K}$ and equals about 65%. In our opinion, the sensitivity increase is mainly associated with the increase of the total number of adsorption centers, because the area of the adsorbent has increased and because fine structure has formed on the microsurface. Effects at grain boundaries can also play a definite role. At the high-temperature annealing stage, tellurium is isolated on the surface of the grains in the form of second-phase precipitates.[11] Their presence can result in local changes of the surface potential to a depth of the Debye screening length, which amplifies (because of the additional polarizability) the interaction of polar molecules of toluene with oxygen in the form O_2^- and O^-, adsorbed by the tin dioxide. It should be pointed out that, for the $SnO_2\langle I,Te\rangle$ layers, one observes an increase of the temperature corresponding to the maximum sensitivity, and the desorption edge accordingly shifts into the higher-temperature region. In agreement with the concepts of the role of tellurium deposits, this is evidence of an increase in the relative fraction of adsorption centers that possess higher binding energy with the surface.

It is essential that the change of the sensitivity depends on the processing regimes for obtaining the layers and is not identical for different gases. This circumstance makes it possible to enhance the selectivity of sensor devices based on tin oxide by using active layers with different gas-sensitive properties. In this case, information concerning the concentration of each of the gases in the mixture to be analyzed (for example, CO/toluene) can be systematically distinguished.

The results of the studies reported here thus show that introducing volatile impurities into the starting mix when producing tin dioxide layers is an effective way to modify the surface structure and can be used to purposefully alter the gas-sensitive properties of layers for gas sensors.

[1] D. Kohl, Sens. Actuators **18**, 71 (1989).
[2] F. F. Vol'kenshteĭn, *Electronic Processes on the Surface of Semiconductors Accompanying Chemisorption* (Nauka, Moscow, 1987).
[3] D. E. Dyshel', Neorg. Mater. **32**, No. 1, 59 (1996).
[4] C. S. Rastomjee, R. S. Dale, R. J. Schaffer, F. H. Jones, R. G. Egdell, G. C. Georgiadis, M. J. Lee, T. J. Tate, and L. L. Cao, Thin Solid Films **279**, 98 (1996).
[5] A. S. Bakin, M. V. Bestaev, D. Tz. Dimitrov, V. A. Moshnikov, and Yu. M. Tairov, Thin Solid Films **296**, 168 (1997).
[6] B. A. Akimov, A. V. Albul, A. M. Gas'kov, V. Yu. Il'in, M. Labo, M. N. Rumyantseva, and L. I. Ryabova, Fiz. Tekh. Poluprovodn. **31**, 400 (1997) [Semiconductors **31**, 335 (1997)].
[7] R. S. Morrison, Sens. Actuators **12**, 425 (1987).
[8] E. V. Andreeva, A. B. Zil'berman, A. V. Makhin, V. A. Moshnikov, and D. A. Yas'kov, Fiz. Tekh. Poluprovodn. **27**, 1095 (1993) [Semiconductors **27**, 603 (1993)].
[9] N. I. Dolotov, A. B. Zil'berman, A. V. Makhin, V. A. Moshnikov, and D. A. Yas'kov, Neorg. Mater. **30**, No. 1, 83 (1994).
[10] R. Assenov, V. A. Moshnikov, and D. A. Yaskov, Cryst. Res. Technol. **21**, 1549 (1986).
[11] Yu. N. Andreev, M. V. Bestaev, D. Ts. Dimitrov, V. A. Moshnikov, Yu. M. Tairov, and N. P. Yaroslavtsev, Fiz. Tekh. Poluprovodn. **31**, 841 (1997) [Semiconductors **31**, 714 (1997)].

Translated by W. J. Manthey

Self-organizing nanoheterostructures in InGaAsP solid solutions

L. S. Vavilova, A. V. Ivanova, V. A. Kapitonov, A. V. Murashova, I. S. Tarasov, I. N. Arsent'ev, N. A. Bert, Yu. G. Musikhin, N. A. Pikhtin, and N. N. Faleev

A. F. Ioffe Physicotechnical Institute, Russian Academy of Sciences, 194021 St. Petersburg, Russia
(Submitted December 15, 1997; accepted for publication December 24, 1997)
Fiz. Tekh. Poluprovodn. **32**, 658–662 (June 1998)

This paper discusses the photoluminescence and x-ray microstructural properties of epitaxial layers of solid solutions of InGaAsP isoperiodic with InP (100) and GaAs (100) substrates, obtained in the region of immiscibility and spinodal decay. It shows that there is good agreement of the experimental results with the theoretical model of spinodal decay. The boundaries of the region in which two solid phases of different composition exist in epitaxial layers of solid solutions of InGaAsP isoperiodic with the InP and GaAs substrates are determined. A periodic nanoheterostructure is obtained in an epitaxial layer of InGaAsP solid solutions with a repetition period of 650 ± 30 Å in two mutually perpendicular directions. © *1998 American Institute of Physics.* [S1063-7826(98)00406-2]

Studies in the physics of semiconductor heterostructures have recently resulted in the appearance of a distinctive avenue of research—the physics of nanoheterostructures. Experimental and theoretical studies of physical phenomena that provide new possibilities for obtaining periodic nanoheterostructures are therefore crucial.

A number of theoretical papers have been devoted to the investigation of the spinodal decay effect in the immiscibility region of multicomponent solid solutions.[1–4] At the same time, it has been experimentally confirmed that the decay effect of multicomponent solid solutions exists in the immiscibility region[5–9] and that a compositionally modulated solid phase of semiconductor material has been formed.[10]

In this study, we have investigated experimentally the epitaxial quaternary solid solutions of InGaAsP produced in the immiscibility region and in the spinodal decay region, with the purpose of studying them and using them to obtain self-organizing periodic heterostructures.

In experimental papers devoted to the study of epitaxial deposition of quaternary solid solutions of InGaAsP, it was shown to be possible to obtain absolutely stable solid solutions isoperiodic with InP and GaAs[11,12] and to develop high-efficiency optoelectronic devices based on them.[13–15] At the same time, there are experimental data indicating that the solid solutions are unstable in the immiscibility region in a certain temperature and composition interval,[5–10] and this hinders the growth of homogeneous single-crystal epitaxial layers. The observed instability of the solid solutions is explained by the spinodal decay of the quaternary solid solution into two solid phases. This phenomenon has been studied in many theoretical papers,[1–4] where it was shown that the immiscibility and spinodal decay regions of quaternary solid solutions are bounded by curves of the type of concentric circles or ellipses whose shape and limits depend on the theoretical model, the approximations, and the boundary conditions used in the calculation. Beyond the limits of the immiscibility region lie absolutely stable solid solutions. Between the immiscibility and spinodal decay curves lie metastable solid solutions, and absolutely unstable solid solutions are found inside the spinodal decay region. The general tendency is for the immiscibility and spinodal decay regions to broaden with decreasing temperature. For the working temperatures of epitaxial deposition of InGaAsP solid solutions (900–1000 K), the spinodal decay region embraces a significant part of the solid solutions of InGaAsP that are isoperiodic with InP and GaAs. These theoretical prerequisites initiated our research into the properties of epitaxial quaternary solid solutions not only in order to eliminate the decay phenomena, but also in order to study the possibility of obtaining self-organizing periodic nanoheterostructures of InGaAsP solid solutions.[16–18]

In this work, we made a purposeful attempt to study the properties of quaternary solid solutions of InGaAsP isoperiodic with InP and GaAs substrates in the immiscibility and spinodal decay regions. Epitaxial layers of InGaAsP solid solutions were fabricated on InP (100) and GaAs (100) substrates by liquid-phase epitaxy at temperatures of 800–1000 K. We were mainly interested in searching for processing conditions that would promote unstable deposition of the epitaxial layers. The properties of the resulting epitaxial layers of InGaAsP solid solutions were studied by photoluminescence, x-ray diffraction, and transmission electron microscopy.

EXPERIMENTAL RESULTS

A. Photoluminescence properties

The photoluminescence properties of samples of quaternary solid solutions were studied by the standard technique on an synchronous-detection apparatus, with control and information output via a personal computer. The studies were carried out at temperatures of 300 and 77 K. The excitation level was varied from 10 to 10^4 W/cm^2, using He–Ne and Ar^+ lasers.

A characteristic photoluminescence spectrum of quaternary solid solutions of InGaAsP isoperiodic with InP and

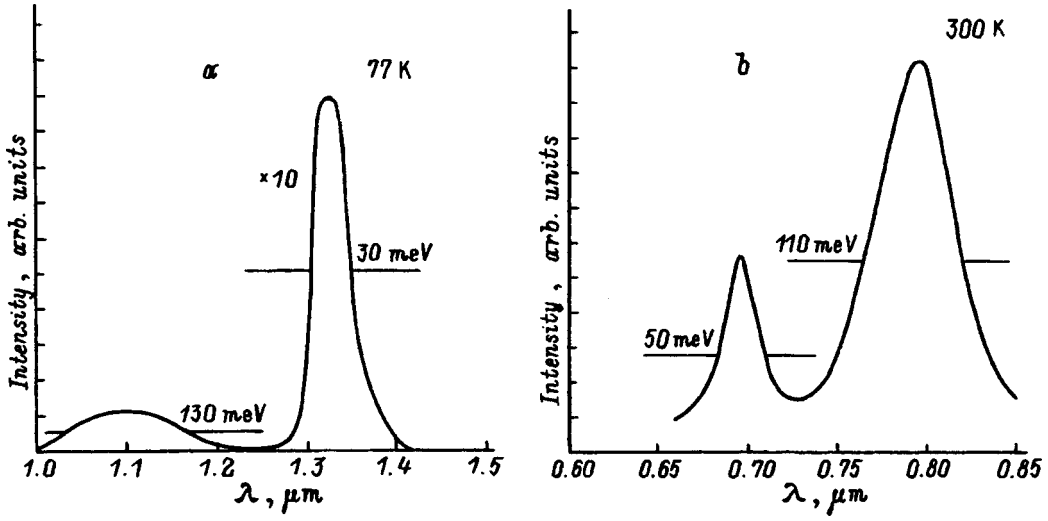

FIG. 1. Photoluminescence spectrum of an epitaxial layer of InGaAsP obtained in the immiscibility region of quaternary solid solutions on an InP (100) (a) and GaAs (100) (b) substrate.

GaAs, obtained in the immiscibility region, consisted of two luminescence bands (Figs. 1a and 1b). The band in the luminescence spectra that lies closer to the corresponding isoperiodic ternary solid solution ($In_{0.53}Ga_{0.47}As$ and $In_{0.47}Ga_{0.53}P$) was the main one in intensity and remained in the luminescence spectra, regardless of the chosen composition of the liquid (solid) phase of the calculated solid solution. Between the main band in the luminescence spectra and the corresponding binary compound (InP and GaAs) there usually was a second luminescence band with lower intensity and greater half-width. In this case, it was observed at temperatures of 300 and 77 K in samples obtained on GaAs substrates and only at a temperature of 77 K in samples obtained on InP substrates. This is associated with a feature that arises in the band structure of an epitaxial layer of a quaternary solid solution produced in the spinodal decay region: For samples on GaAs substrates, the additional emission band possesses the minimum band gap, which promotes its appearance during photoexcitation, in contrast with samples on InP substrates, where the main luminescence band possesses the minimum band gap.

Studies of the dependence of the band intensity in the photoluminescence spectra on the excitation level demonstrated a monotonic dependence that is identical for the main and additional luminescence bands, which strongly reduces the probability of an impurity origin of the additional emission band. Studies of the temperature dependences of the luminescence spectra also did not reveal any features that were not characteristic of photoluminescence spectra that contain one main luminescence band.

By studying the photoluminescence spectra of samples of quaternary solid solutions isoperiodic with the InP and GaAs substrates, we succeeded in obtaining the following dependences of the wavelengths of the maxima of the emission peaks for the main and additional luminescence bands (Fig. 2a and 2b). To describe the solid solutions InGaAsP/InP and InGaAsP/GaAs, it is inconvenient to use the composition of the solid phase to characterize them, as is done in a continuous series of solid solutions, since we have assumed that spinodal decay regions are present. As such a characteristic we therefore chose the composition of the liquid phase from which the epitaxial layers were grown. It can be seen from the data shown in Fig. 2 that there exist continuous regions of quaternary solid solutions that are characterized by the presence of two emission bands in the photoluminescence spectra. The limits of these regions (indicated by arrows) satisfactorily agree with the calculated regions of unstable solid solutions of InGaAsP in the temperature range 800–1000 K.

We have also studied the photoluminescence spectra of epitaxial layers of solid solutions of InGaAsP/GaAs as a function of their thickness. The test samples were grown on GaAs (100) substrates from the liquid phase of identical composition in the region of unstable solid solutions. The results of these studies are shown in Fig. 3. The epitaxial layers with a thickness of 100–1000 Å have one band in the photoluminescence spectra. The epitaxial layers with a thickness of 1000–4000 Å have two bands in the photoluminescence spectra. Increasing the thickness of the epitaxial layer further reduces the quantum efficiency. The resulting dependence is evidence that composition-destabilization effects of the solid solutions begin to show up from a certain thickness of the epitaxial layer and strengthen as it increases. For a thickness greater than 5000 Å, the surface quality deteriorates (the number of defects increases, specularity is absent, and the surface becomes dull), and it becomes partially or totally impossible to pull the solution–alloy off the surface of the grown epitaxial layer. Similar phenomena were observed in the photoluminescence spectra of quaternary solid solutions of InGaAsP of various thicknesses grown in the immiscibility region on InP (100) substrates and are phenomenologically described in Ref. 11.

B. X-ray structural analysis

We carried out an x-ray microstructural analysis of the properties of quaternary solid solutions of InGaAsP isoperi-

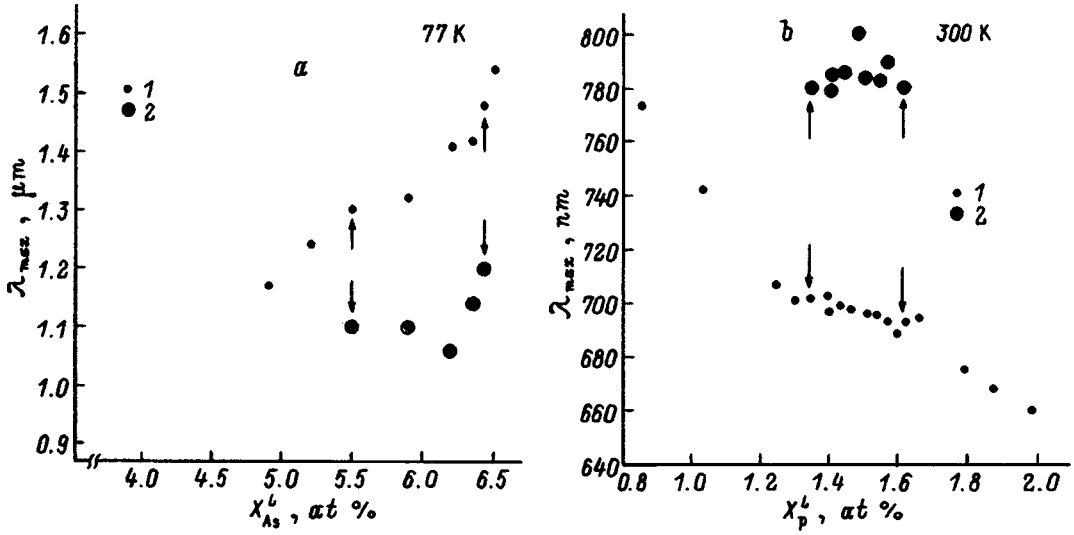

FIG. 2. Wavelength of the maximum of the main (*1*) and additional (*2*) photoluminescence bands of solid solutions of InGaAsP vs composition of the liquid phases from which solid solutions were grown on InP (100) (a) and GaAs (100) (b) substrates.

odic with InP and GaAs, whose photoluminescence spectra included two emission bands. The x-ray microstructural analysis of the samples was carried out on a two-crystal x-ray diffraction spectrometer by the standard technique. Characteristic features were detected in the x-ray diffraction spectra of test samples characterizing the mismatch of the lattice parameters of the epitaxial layer and the substrate. In contrast with the x-ray diffraction spectra of a layer of a stable solid solution, which has two peaks corresponding to the response from the substrate and the epitaxial layer, three peaks were observed in the x-ray diffraction spectra obtained here: one from the InP (or GaAs) substrate and two from the layer. This is evidence that two compositions that differ in the lattice constant are present in the solid phase in epitaxial layers of solid solutions of InGaAsP obtained in the immiscibility region.

C. Transmission electron microscopy

Samples of epitaxial layers of quaternary solid solutions of InGaAsP were studied by means of transmission electron microscopy on an EM-420 device operating with an accelerating voltage of 100 and 120 kV. The main method of investigation was the dark field regime in (200)-type reflection, which ensured the highest sensitivity to the chemical composition of the sample. The samples were prepared ''in planar cross section,'' using conventional procedures of mechanical grinding of a crater, followed by chemical etching in $HBr : K_2Cr_2O_7$ (1:1) until perforation occurred. Samples of quaternary solid solutions of InGaAsP/InP having the characteristic features in the photoluminescence and x-ray diffraction spectra were chosen for investigation on the transmission electron microscope. Figure 4 shows an electron micrograph of one of the test samples. The planar form of the sample revealed regions with different compositions of the solid phase that periodically repeated in mutually perpendicular [100] directions. The decay period, measured from a dark-field image using a (200) diffraction spot, was 650 ± 30 Å. At the same time, it was possible to observe regions with dimensions of up to 120 nm.

The absence of sharp, distinct boundaries between the dark and light regions is evidence of the presence of transition layers, which agrees with the wide additional band in the photoluminescence spectrum. A similar picture was obtained when such quaternary solid solutions of InGaAsP/GaAs were studied. It also showed the presence of a structure of alternating solid phases in epitaxial layers with additional bands in the photoluminescence and x-ray diffraction spectra.

CONCLUSIONS

As a result of the comprehensive studies that have been carried out on epitaxial layers of quaternary solid solutions

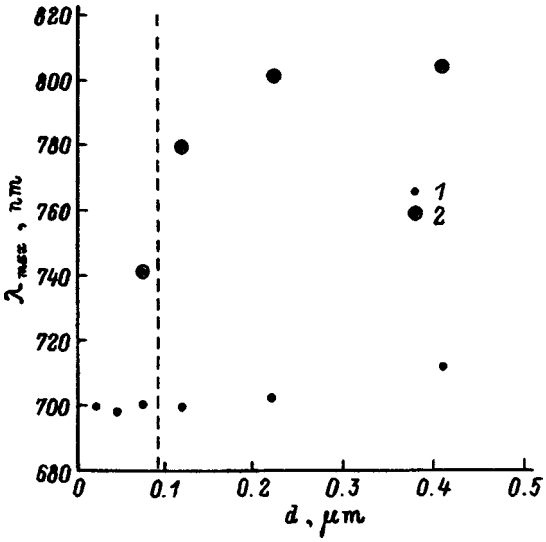

FIG. 3. Wavelength of the maximum of the main (*1*) and additional (*2*) photoluminescence bands of solid solutions of InGaAsP/GaAs vs the thickness of the epitaxial layer. $T = 300$ K.

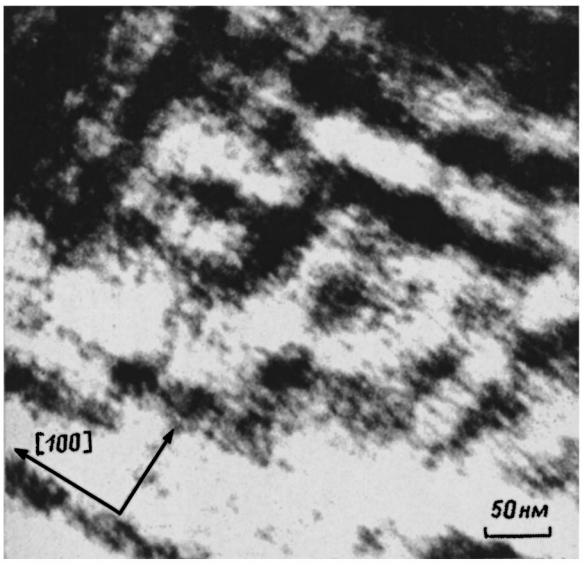

FIG. 4. Image of an InGaAsP/InP sample in planar cross section, obtained on an EM-420 transmission electron microscope.

of InGaAsP isoperiodic with InP and GaAs, obtained under processing conditions that stimulate the instability of the solid phase at growth temperatures of 800–1000 K, the following results were obtained:

(a) An additional luminescence band with a rather large half-width of $\Delta h\nu \approx 100-150$ meV is present in the photoluminescence spectra of samples of quaternary solid solutions of InGaAsP isoperiodic with InP and GaAs obtained in the immiscibility region.

(b) The regions of the solid solutions, whose photoluminescence spectra contain a second, additional band, satisfactorily agree with the calculated values of Refs. 3 and 4 for solid solutions isoperiodic with InP and GaAs.

(c) The x-ray diffraction spectra of epitaxial layers of InGaAsP solid solutions, which have an additional band in the photoluminescence spectra, always contain an additional peak, which indicates the presence of a second solid phase with a lattice parameter that differs from that of the main layer.

(d) The results of transmission electron microscopy revealed that periodic structure of solid phases of various compositions is present in the epitaxial layers in the planar section and in the cross-sectional view.

This set of experimental results indicates good agreement with the theoretical model for the appearance of the spinodal decay effect in multicomponent solid solutions and substantiates the possibility of obtaining periodic nanoheterostructures by using this effect.

We wish to thank A. V. Lyutetskiĭ and A. L. Stankevich for help. We also thank I. P. Ipatova, R. A. Suris, and V. A. Shchukin for fruitful discussions during the preparation of this article.

This work was carried out with the support of the Russian Fund for Fundamental Research (Grant 97-02-18105).

[1] B. de Cremoux, J. Phys. (Paris) **43**, C5-19 (1982).
[2] G. B. Stringfellow, J. Cryst. Growth **65**, 454 (1983).
[3] I. P. Ipatova, V. G. Malyshkin, A. Yu. Maslov, and V. A. Shchukin, Fiz. Tekh. Poluprovodn. **27**, 285 (1993) [Semiconductors **27**, 158 (1993)].
[4] I. P. Ipatova, V. G. Malyshin, and V. A. Shchukin, J. Appl. Phys. **74**, 7198 (1993).
[5] P. Henoc, A. Izrael, M. Quillec, and H. Launois, Appl. Phys. Lett. **40**, 963 (1982).
[6] O. Ueda, S. Isozumi, and S. Komiya, Jpn. J. Appl. Phys. **23**, L241 (1984).
[7] A. G. Norman and G. R. Booker, J. Appl. Phys. **57**, 4715 (1985).
[8] N. G. Chu, S. Nakahara, K. E. Strege, and W. D. Johnston, J. Appl. Phys. **57**, 4610 (1985).
[9] P. Roura, J. Bosch, S. A. Clark, F. Peiro, A. Cornet, J. R. Morante, and R. H. Williams, Semicond. Sci. Technol. **11**, 1310 (1996).
[10] S. K. Maksimov, L. A. Bondarenko, A. S. Petrov, and V. V. Kuznetsov, Fiz. Tverd. Tela **24**, 628 (1982) [Sov. Phys. Solid State **24**, 355 (1982)].
[11] E. Kuphal, J. Cryst. Growth **67**, 441 (1984).
[12] N. A. Bert, A. I. Gorelenok, A. G. Dzigasov, S. G. Konnikov, T. B. Popova, I. S. Tarasov, and V. K. Tibilov, J. Cryst. Growth **52**, 716 (1981).
[13] M. A. Ivanov, Yu. V. Il'in, N. D. Il'inskaya, Yu. A. Korsakova, A. Yu. Leshko, A. V. Lunev, A. V. Lyutetskiĭ, A. V. Murashova, N. A. Pikhtin, and I. S. Tarasov, Pisma Zh. Tekh. Fiz. **21**, 70 (1995) [Tech. Phys. Lett. **21**, 198 (1995)].
[14] R. J. Nelson, Appl. Phys. Lett. **35**, 654 (1979).
[15] Zh. I. Alfyorov, I. N. Arsent'ev, L. S. Vavalova, D. Z. Garbuzov, V. V. Krasovskiĭ, A. V. Tikunov, and V. P. Chalyĭ, Fiz. Tekh. Poluprovodn. **19**, 1115 (1985) [Sov. Phys. Semicond. **19**, 683 (1985)].
[16] I. S. Tarasov, N. A. Pikhtin, A. V. Murashova, A. V. Lyutetskiĭ, A. Yu. Leshko, M. A. Ivanov, N. A. Bert, and Zh. I. Alfyorov, in *Second Russian Conference on Semiconductor Physics RKFP'96*, Zelenogorsk, Feb. 26–March 1, 1996, Vol. 1, p. 40.
[17] I. S. Tarasov, L. S. Vavilova, N. I. Katsavets, A. V. Lyutetskiy, A. V. Murashova, N. A. Pikhtin, N. A. Bert, and Zh. I. Alferov, in *Abstracts of the International Symposium on Nanostructures: Physics and Technology*, St. Petersburg, Russia, June 24–28, 1996, p. 362.
[18] I. S. Tarasov, L. S. Vavilova, I. P. Ipatova, A. V. Lyutetskiy, A. V. Murashova, N. A. Pikhtin, V. A. Shchukin, and Zh. I. Alferov, in *Proceedings of the Twenty-third International Symposium on Compound Semiconductors ISCS-23*, St. Petersburg, Russia, September 23–27, 1996, p. 117.

Translated by W. J. Manthey

ELECTRONIC AND OPTICAL PROPERTIES OF SEMICONDUCTORS

Pressure-induced insulator–metal transition in electron-irradiated $Pb_{1-x}Sn_xSe$ ($x \leqslant 0.03$) alloys

E. P. Skipetrov, E. A. Zvereva, B. B. Kovalev, and L. A. Skipetrova

M. V. Lomonosov Moscow State University, 119899 Moscow, Russia
(Submitted August 11, 1997; accepted for publication October 16, 1997)
Fiz. Tekh. Poluprovodn. **32**, 663–667 (June 1998)

Galvanomagnetic effects ($B \leqslant 7$ T) in electron-irradiated *n*- and *p*-type $Pb_{1-x}Sn_xSe$ ($x \leqslant 0.03$) alloys ($T \approx 300$ K, $E = 6$ MeV, $\Phi \leqslant 5.7 \times 10^{17}$ cm^{-2}) in the neighborhood of a pressure-induced insulator–metal transition ($P \leqslant 18$ kbar) are discussed. The field dependences of the Hall coefficient calculated in terms of the two-band model are in satisfactory agreement with the experimental data, and the main parameters of the charge carriers in irradiated alloys are determined. It is shown that there is an increase in the hole concentration in the metallic phase under the action of pressure, associated with the motion of the energy bands at point *L* of the Brillouin zone, and that electrons overflow from the valence band into the band E_{t1} of resonance states induced by electron irradiation; the parameters of this band are estimated.
 [S1063-7826(98)00506-7]

1. INTRODUCTION

It is well known that electron irradiation of $Pb_{1-x}Sn_xSe$ alloys causes two radiative levels (radiative-defect bands) E_t and E_{t1}, apparently associated with two types of radiative defects, to appear in the energy spectrum of the alloys.[1,2] The main parameters of the E_t band (the defect-generation rate, the energy position, and the band structure) are well known for virtually the entire existence domain of the cubic phase of the alloys ($0.07 \leqslant x \leqslant 0.34$). At the same time, there is much less information on the E_{t1} level.

In particular, it has been established[3,4] that the position of the E_{t1} radiative level on an energy scale depends on the alloy composition and the pressure (Fig. 1). In PbSe, the E_{t1} level lies in the band gap close to the top of the valence band, L_6^+. As the Sn concentration in the alloy increases, the level almost does not change its position relative to the middle of the band gap, moving relative to the L_6^+ term approximately according to the linear law

$$E_{t1}[\text{meV}] = E(L_6^+) + 35 - 600x.$$

Thus, in alloys with a tin concentration of $x < 0.06$, the middle of the E_{t1} band is in the band gap, whereas, for $x > 0.06$, it falls within the valence band.

The E_{t1} band possesses donor–acceptor properties. Therefore, electron irradiation of crystals with $x < 0.06$ reduces the charge-carrier concentration both in *n*-type and in *p*-type samples. For sufficiently large irradiation fluxes, a transition occurs to the insulating state, in which the Fermi level is ''softly'' stabilized by a band of radiative defects partly filled with electrons. Hydrostatic compression of irradiated crystals causes the E_{t1} band to approach the top of the valence band and causes an insulator–metal transition associated with the overflow of electrons from the valence band into the radiative-defect band (Fig. 1).

The character of the dependences of the conductivity and the Hall coefficient of irradiated samples on pressure[3,4] is evidence that there are at least two conductivity mechanisms in the neighborhood of the insulator–metal transition. It should also be pointed out that, in the neighborhood of the transition, significant variations of the charge-carrier parameters occur in a rather wide range of pressures. This circumstance indicates that the E_{t1} band has a finite width. However, the width and structure of the radiative-defect band, as well as the radiative-defect generation rate during irradiation, is not yet known.

To obtain information on the conductivity mechanisms in electron-irradiated alloys and to determine the main parameters of the radiative-defect band E_{t1}, we analyzed the field dependences of the Hall coefficient of electron-irradiated $Pb_{1-x}Sn_xSe$ ($x \leqslant 0.03$) alloys in the neighborhood of the pressure-induced insulator–metal transition.

2. SAMPLES. MEASUREMENT TECHNIQUE

Single-crystal samples of $Pb_{1-x}Sn_xSe$ ($x = 0$, 0.03) with an initial electron or hole concentration of *n*, $p = (0.4\text{–}1.6) \times 10^{17}$ cm^{-3} were irradiated at room temperature on an ÉLU-6 linear electron accelerator ($E = 6$ MeV, $\Phi \leqslant 5.7 \times 10^{17}$ cm^{-2}). The conductivity and the field dependences of the Hall coefficient ($B \leqslant 7$ T) at $T = 4.2$ K in the irradiated crystals were studied at atmospheric pressure and under conditions of hydrostatic compression. The parameters of the samples, studied under pressure before and after irradiation by the maximum electron fluxes, are shown in Table I. Hydrostatic pressures of up to 18 kbar were obtained in a cham-

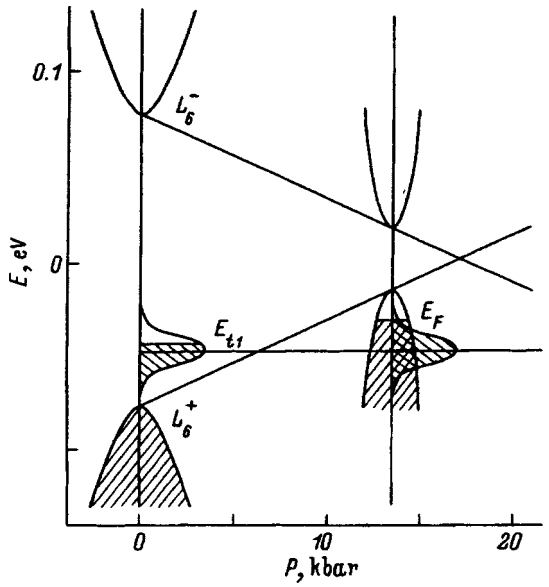

FIG. 1. Model of the reconstruction under pressure of the energy spectrum of electron-irradiated *n*-PbTe.

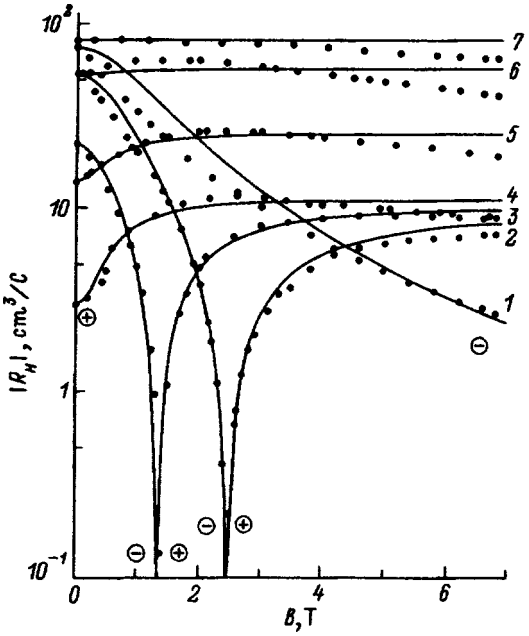

FIG. 2. Field dependences of Hall coefficient R_H at $T=4.2$ K for sample K-22 ($\Phi=2.8\times10^{17}$ cm^{-2}) in the neighborhood of the insulator–metal transition under the action of pressure: *P*, kbar: *1*—0.9, *2*—1.4, *3*—2.6, *4*—3.2, *5*—4.2, *6*—6.2, *7*—18.2. The solid curves show calculated results in accordance with Eqs. (1)–(3).

ber made from heat-treated beryllium bronze. A kerosine–oil–pentane mixture was used as the pressure-transmitting medium.

3. FIELD DEPENDENCES OF THE HALL COEFFICIENT IN THE NEIGHBORHOOD OF THE INSULATOR–METAL TRANSITION

It has been established that the Hall coefficient R_H of electron-irradiated samples strongly depends on the magnetic field even at atmospheric pressure, and that the absolute value of R_H decreases by more than an order of magnitude in the range of magnetic field studied here (Fig. 2). Hydrostatic compression reduces R_H more sharply and inverts the sign of the Hall coefficient as the magnetic field increases. As the pressure increases, the sign-inversion point of R_H shifts toward weaker magnetic fields, and, after the transition to the metallic phase ($P>P^*$), the Hall coefficient has a positive sign, increasing as the magnetic field increases. Finally, in the region of maximum pressures, the Hall coefficient is virtually independent of magnetic field.

The character of the field dependences of the Hall coefficient in the test samples confirms the assumption that at least two types of charge carriers of opposite sign coexist in electron-irradiated $Pb_{1-x}Sn_xSe$ ($x=0$; 0.03) alloys. The appearance of a sign-inversion point for R_H and the change in the form of the $R_H(B)$ dependences accompanying hydrostatic compression of irradiated crystals evidently indicates that the parameters of the charge carriers vary and that the main conduction mechanism changes when the insulator–metal transition occurs. To determine the main parameters of the charge carriers in the irradiated samples in terms of a two-band model, we calculated the field dependences of the Hall coefficient in the test samples:[5,6]

$$R_H=\frac{\sum \sigma_k\mu_k/(1+\mu_k^2B^2)}{\left[\sum \sigma_k/(1+\mu_k^2B^2)\right]^2+\left[\sum \sigma_k\mu_kB/(1+\mu_k^2B^2)\right]^2}, \tag{1}$$

$$1/\rho=\sum \sigma_k=\sum e_kn_k\mu_k, \tag{2}$$

where e_k, n_k, σ_k, and μ_k are the charge, concentration, conductivity, and mobility for each type of charge carrier, denoted by subscript *k*. In the limits of a weak magnetic field ($\mu_kB\ll1$), the expression for the Hall coefficient takes the form

TABLE I. Parameters of $Pb_{1-x}Sn_xSe$ samples studied under pressure at $T=4.2$ K.

Sample	x	Conductivity type	Irradiation flux Φ, 10^{17} cm^{-2}	Electron concentration n, 10^{17} cm^{-3}	Resistivity ρ, 10^{-4} Ω·cm	Mobility μ_H 10^5 cm^2/(V·s)
N8	0	*n*	0	1.06	7.3	0.81
		n	5.7	0.27	220.0	0.105
K-22	0.33	*p*	0	0.40	47.7	0.31
		n	2.8	0.82	269.0	0.028

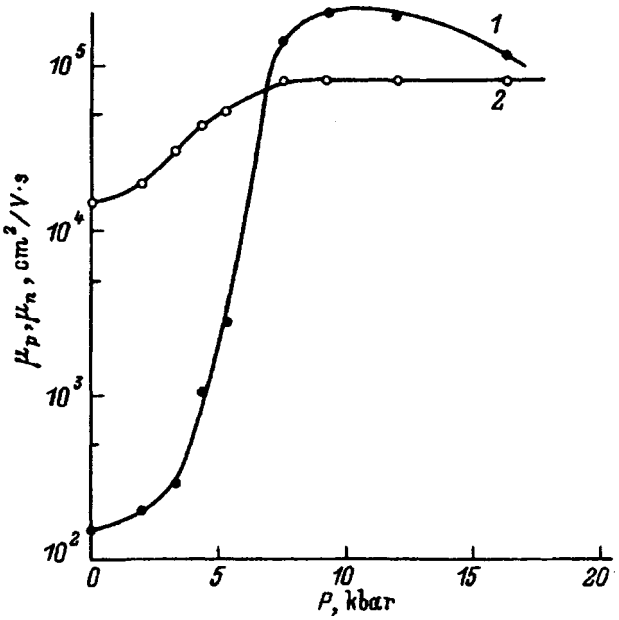

FIG. 3. Hole mobility μ_p (*1*) and electron mobility μ_n (*2*) in electron-irradiated sample N8 ($\Phi = 5.7\times10^{17}$ cm^{-2}) vs pressure.

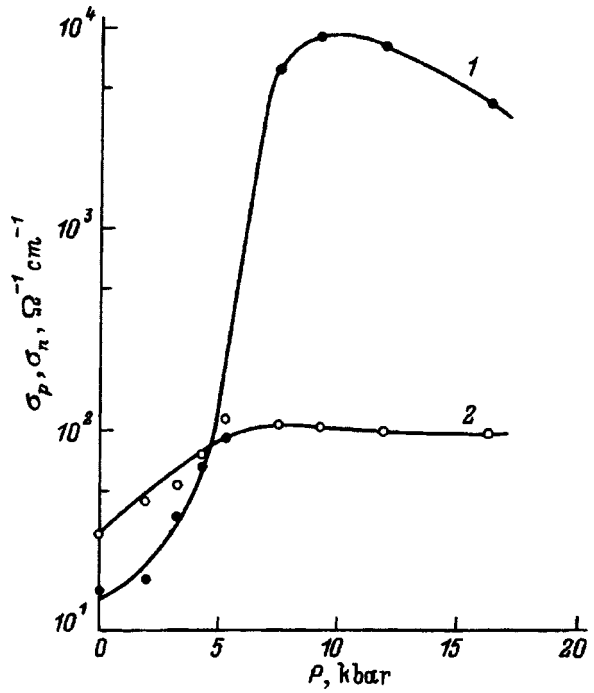

FIG. 4. Hole conductivity σ_p (*1*) and electron conductivity σ_n (*2*) in electron-irradiated sample N8 ($\Phi = 5.7\times10^{17}$ cm^{-2}) vs pressure.

$$R_H = \frac{\sum e_k n_k \mu_k^2}{\left(\sum e_k n_k \mu_k\right)^2}. \tag{3}$$

The parameters of the charge carriers were determined by adjusting the dependences given by Eq. (1) to the experimental data (Fig. 2). The program for doing the calculations involved the variation of only two parameters of the model (usually the charge-carrier mobilities). Two other parameters of the model (usually the conductivities σ_k) were determined by direct calculation from the Hall coefficients in a weak magnetic field, using Eq. (3), and from the conductivity at $T = 4.2$ K, using Eq. (2). The $R_H(B)$ dependences thus calculated are in satisfactory agreement with the experimental data in the entire range of pressures and magnetic fields studied here (see Fig. 2).

The results of calculating the charge-carrier parameters for one of the test samples are shown in Figs. 3 and 4. An analysis of these dependences shows that, as the pressure increases, the electron mobility in the irradiated samples increases appreciably and reaches values of $\mu_n = (1.5\text{–}8)\times10^4$ cm^2/(V·s). These mobilities are about an order of magnitude lower than values characteristic of band conductivity; nevertheless they are too large for conductivity via local states and most likely correspond to electron-type surface conductivity. The behavior of the electron conductivity σ_n under pressure apparently shows an appreciable reduction of the electron concentration in the surface layer of the irradiated crystals under the action of pressure. The variations of the electron parameters occur mainly in the insulator phase, whereas the $\mu_n(P)$ and $\sigma_n(P)$ dependences go to saturation after the transition to the metallic phase. This circumstance makes it possible to assume that the variations of the electron parameters in the surface layer are caused by a change in the position of the Fermi level relative to the top of the valence band.

The hole conductivity and mobility vary under the action of pressure in a consistent way, rapidly increasing by several orders of magnitude in the neighborhood of the insulator–metal transition. In the region of maximum pressures, the hole mobility reaches values typical of band conductivity in $Pb_{1-x}Sn_xSe$ alloys, $\mu_p = (1\text{–}2.5)\times10^5$ cm^2/(V·s). At the same time, the hole mobility is only $\mu_p \simeq 2\times10^2$ cm^2/(V·s) at atmospheric pressure. Such low values of the hole mobility were observed earlier in the insulator phase of electron-irradiated $Pb_{1-x}Sn_xSe$ ($x = 0.125$, 0.25) alloys[6] with conductivity along radiative-defect band E_t lying within the band gap. The μ_p and σ_p values calculated from Eqs. (1) and (2) are therefore evidently effective values and take into account both the contribution of the hole conductivity along the band E_{t1} of localized states and the contribution of conductivity along the valence band.

Thus, in electron-irradiated $Pb_{1-x}Sn_xSe$ ($x = 0$; 0.03) alloys, it is apparently necessary to take into account the existence of three conductivity mechanisms when the energy spectrum is reconstructed under the action of pressure. In low-pressure regions (in the insulator phase), the dominant mechanisms are electron-type surface conductivity and hole conductivity via the radiative-defect band, whereas, in the neighborhood of the insulator–metal transition, they are hole band conductivity and electron conductivity over the surface.

4. DEPENDENCES OF THE HOLE CONCENTRATION ON PRESSURE IN THE NEIGHBORHOOD OF THE INSULATOR–METAL TRANSITION AND THE PARAMETERS OF THE E_{t1} BAND

The results presented above make it possible to construct the dependence of the hole concentration on pressure after

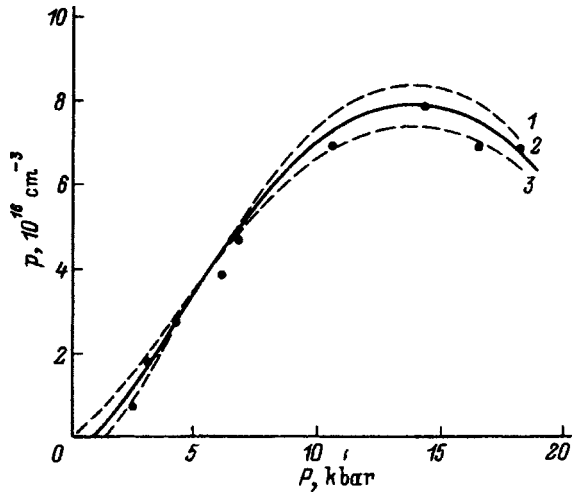

FIG. 5. Hole concentration at $T=4.2$ K in electron-irradiated sample K-22 ($\Phi=2.8\times10^{17}$ cm^{-2}) vs pressure. Curves *1–3* show calculated results from the model given by Eqs. (4)–(6), with $\Delta E_{t1}=17$ meV, $\sigma=15$ meV, and variation of the concentration of radiative defects: *1*—$N_{t1}=1.45\times10^{17}$ cm^{-3}, *2*—$N_{t1}=1.25\times10^{17}$ cm^{-3}, *3*—$N_{t1}=1.05\times10^{17}$ cm^{-3}.

the transition of irradiated alloys to the metallic phase, using the two-band model. Such a dependence can be obtained in several ways. First, the hole concentration can be calculated in terms of the two-band model, using the $\rho(P)$ and $R_H(P)$ dependences in a weak magnetic field given by Eqs. (2) and (3). For simplicity, fixed values (for example, the limiting mobilities and conductivities for each sample at atmospheric pressure) or the $\mu_n(P)$ and $\sigma_n(P)$ dependences calculated above (Figs. 3 and 4) can be chosen in this case as the electron conductivity and mobility in the surface layer. Second, it is possible to directly calculate the hole concentration from

$$p(P)=\sigma_p(P)/e\mu_p(P),$$

using data concerning the variation of the conductivity $\sigma_p(P)$ and hole mobility $\mu_p(P)$ under pressure obtained from the field dependences of the Hall coefficients (Figs. 3 and 4).

Analysis showed that, regardless of the method of calculation, after the transition to the metallic phase, the hole concentration rapidly increases, passes through a maximum, and monotonically decreases with increasing pressure (Fig. 5). Such behavior qualitatively agrees with theoretical concepts concerning the reconstruction of the energy spectrum under pressure (Fig. 1) and makes it possible to estimate the parameters of radiative-defect band E_{t1} by comparing the experimental and theoretical dependences of the hole concentration on pressure.

It was assumed in constructing the theoretical dependences that the generation of radiative defects during irradiation results in the appearance of half-filled states in the radiative-defect band; the position of the middle of the E_{t1} band relative to the middle of the band gap does not change under the action of pressure:[3,4]

$$E_{t1}-E_v=\Delta E_{t1}[\text{meV}]=35-600x-4.25P[\text{kbar}];$$

the density-of-states function $g_{t1}(E)$ in the radiative-defect zone is described by a Gaussian curve, while the defect-generation rate $dN_{t1}/d\Phi$ is independent of the radiation flux. Since it follows from the experimental data that, with hydrostatic compression, the hole concentration increases because electrons overflow from the valence band into the radiative-defect band, it was also assumed that, at any pressures P, the sum of the hole concentrations in the valence band, $p(P)$, and in the radiative-defect band, $p_{t1}(P)$, equals the starting concentration $p_{t1}(0)$ of unfilled states in the E_{t1} band at atmospheric pressure:

$$p_{t1}(0)=p(P)+p_{t1}(P), \tag{4}$$

$$p_{t1}(P)=\int_{E_F}^{\infty} g_{t1}(E)dE, \tag{5}$$

$$g_{t1}(E)=(N_{t1}/\sigma\sqrt{2\pi})\exp[-(E-E_{t1})^2/2\sigma^2], \tag{6}$$

where $N_{t1}=(dN_{t1}/d\Phi)\Phi$ is the total capacity of the radiative-defect band with hole concentrations of

$$p_{t1}(0)=(N_{t1}/2)-n_0$$

or

$$p_{t1}(0)=(N_{t1}/2)+p_0$$

for *n*-type and *p*-type samples, respectively; E_F is the Fermi level, calculated in terms of Dimmock's six-band model,[7] with parameters given in Ref. 8; and σ is the width of the E_{t1} band.

The parameters $dN_{t1}/d\Phi$ and σ of the resonance band were optimized by computer. To estimate the accuracy with which the generation rate $dN_{t1}/d\Phi$ of radiative defects and the width σ of the resonance band are determined, the values of N_{t1} and σ were varied for each sample (dashed curves in Fig. 5). The best agreement of the experimental and theoretical results was achieved for the following values of the parameters of the model:

$$dN_{t1}/d\Phi=(0.45\pm0.1)\times10^{17}\ \text{cm}^{-1},\quad \sigma=(15\pm5)\text{meV}.$$

Thus, the parameters of radiative-defect band E_{t1} turned out to be quite comparable with the analogous parameters of the E_t band, obtained in Ref. 2. However, the accuracy of determining the parameters of the model is extremely low. This circumstance, in particular, makes it impossible to estimate how the generation rate $dN_{t1}/d\Phi$ of radiative defects changes as the radiation flux increases and to determine the degree of deviation of the density-of-states function in the E_{t1} band from a Gaussian form.

5. CONCLUSIONS

The experimental results obtained in this paper indicate that, in electron-irradiated $Pb_{1-x}Sn_xSe$ ($x\leqslant0.03$) alloys in the neighborhood of the pressure-induced insulator–metal transition, it is necessary to take into account the existence of three conduction mechanisms: electron-type surface conduction, band hole conduction, and hole conduction along the radiative-defect band E_{t1}. The field dependences of the Hall coefficient, calculated in terms of the two-band model, satisfactorily agree with the experimental data in the entire range of pressures and magnetic fields considered here and make it

possible to determine the charge-carrier parameters in the irradiated samples. In such alloys, the insulator–metal transition under the action of pressure is accompanied by an overflow of electrons from the valence band to the E_{t1} band and by an increase of the free-hole concentration. The experimental dependences of the hole concentration on pressure are in satisfactory agreement with the theoretical values obtained in terms of the model proposed earlier for the reconstruction of the energy spectrum by the electrons of alloys under pressure. An analysis of these dependences is evidence that the radiative-defect band E_{t1} has a significant width ($\simeq 10$ meV) and makes it possible to estimate its main parameters.

The authors are grateful to A. M. Musalitin for irradiating the test samples with fast electrons.

This work was carried out with the financial support of the Russian Fund for Fundamental Research (Grants 96-02-18325, 96-02-16275, 96-15-96500).

[1] N. B. Brandt, V. N. Doropeĭ, V. P. Dubkov, and E. P. Skipetrov, Fiz. Tekh. Poluprovodn. **22**, 1462 (1988) [Sov. Phys. Semicond. **22**, 925 (1988)].
[2] N. B. Brandt and E. P. Skipetrov, Fiz. Nizk. Temp. **22**, 870 (1996) [Low Temp. Phys. **22**, 665 (1996)].
[3] N. B. Brandt, B. B. Kovalev, and E. P. Skipetrov, in *Proceedings of the Fourth International Conference on High Pressure in Semiconductor Physics* (Thessaloniki, Greece, 1990), p. 170.
[4] N. B. Brandt, B. B. Kovalev, and E. P. Skipetrov, Semicond. Sol. Technol. **6**, 487 (1991).
[5] P. S. Kireev, *Semiconductor Physics* (Vysshaya Shkola, Moscow, 1975), Chap. 4, p. 274.
[6] E. P. Skipetrov, V. P. Dubkov, A. M. Musalitin, and I. N. Podskakalov, Fiz. Tekh. Poluprovodn. **22**, 1785 (1988) [Sov. Phys. Semicond. **22**, 1129 (1988)].
[7] J. O. Dimmock, in *The Physics of Semimetals and Narrow Gap Semiconductors*, edited by D. L. Carter and R. T. Bate (Pergamon Press, New York, 1971) p. 319.
[8] N. B. Brandt, Ya. G. Ponomarev, and E. P. Skipetrov, Fiz. Tverd. Tela (Leningrad) **29**, 3233 (1987) [Sov. Phys. Solid State **29**, 1856 (1987)].

Translated by W. J. Manthey

Identifying the parameters of impurity levels in high-resistance semiconductor crystals by means of thermally stimulated currents with dosed illumination of the samples

P. G. Kasherininov and D. G. Matyukhin

A. F. Ioffe Physicotechnical Institute, Russian Academy of Sciences, 194021 St. Petersburg, Russia
(Submitted October 13, 1997; accepted for publication October 20, 1997)
Fiz. Tekh. Poluprovodn. **32**, 668–672 (June 1998)

A method is proposed for identifying the parameters of impurity levels in high-resistance (insulating) semiconductor crystals that makes it possible to use thermally stimulated currents with dosed illumination of the samples to simultaneously determine the depth of the impurity levels in the band gap of the crystal (ΔE) and to establish from which of the allowed band's edge should the depth of the levels be measured. The widely used ordinary method of thermally stimulated currents does not allow this to be done. © *1998 American Institute of Physics.* [S1063-7826(98)00606-1]

The method of thermally stimulated currents (TSC) is based on filling traps in a crystal with electrons and holes under the action of irradiation at low temperatures and then emptying them by heating. After recharging the impurity levels with carriers of different signs (electrons and holes), it is possible to determine the depths ΔE of these recharged levels in the band gap of the crystal from the activation energy of the carriers captured at the impurity levels into the corresponding allowed bands of the crystal from the temperature dependence of the TSC as the sample is heated. However, it is impossible in this case to establish from the edge of which of the allowed bands this depth ΔE of the levels should be measured.[1] When the impurity levels are filled with carriers of only one known sign of the conductivity (electrons or holes) during irradiation, there is no difficulty in identifying the parameters of the charge-exchange impurity levels from the TSC curves. Therefore, to identify the parameters of impurity levels in a crystal, it is sufficient to choose conditions that provide the directed filling of the impurity levels in a special type of structures during illumination by carriers of one (known) sign of the conductivity and by carriers of both signs, to measure the TSC spectra after the corresponding types of filling of the impurity levels in the crystal, and to identify the parameters of these levels by comparing the spectra.

The method is based on measuring the TSC in metal–semiconductor–metal (MSM) structures on high-resistance crystals after the structures are illuminated from the side of optically transparent metallic electrodes (M) with a dosed energy of ''intrinsic'' light ($h\nu > E_g$) ($h\nu$ is the energy of a light quantum, and E_g is the band gap of the crystal).

It has been established that actual MSM structures created by cold deposition of metal electrodes on the surface of a crystal (by sputtering, by chemical deposition of the metal, and by other means) contain a thin film of natural oxide (NO), which is located on the surface of the crystal between the metal and the semiconductor (20–50 Å thick).[2–4] Such structures are actually of type M(NO)S(NO)M with noninjecting electrodes when the electric fields in the contact regions are on the order of $E < 10^4$ V/cm and injecting electrodes when the fields in these regions are larger, $E > 10^4$ V/cm.[5,6] The flow of photocurrent through the layers of the tunnel-thin insulator (the NO) in such structures is accompanied by the accumulation of photoinduced charges of the carriers of the corresponding signs in the crystal at the boundary with these NO layers.[3–10] When such structures are illuminated with strongly absorbed intrinsic light from the side of the electrodes, photocurrent caused by photocarriers with the same sign as that of the illuminated electrode flows through the crystal. These photocarriers accumulate in the crystal at the boundary with the layers of tunnel-thin insulator (the NO) around the ''dark'' electrode opposite the illuminated one, are captured at impurity levels, and form in the crystal at this electrode monopolar electric charge with the same sign as that of the illuminated electrode. As the value of this charge is varied, the electric field in the crystal varies with time from a uniformly distributed field over the thickness of the crystal (in the absence of illumination) to a strongly nonuniform field over the thickness of the crystal, with the strong-field region localized in the crystal close to the dark electrode. When the electric field in the crystal at the dark electrode exceeds a critical value ($E > E_{cr}$), electric charge of the same sign as the polarity of the dark electrode begins to be injected from the dark electrode into the bulk of the crystal. From this instant, the corresponding impurity levels (traps) in the bulk of the crystal are filled with carriers of both signs (electrons and holes).[5,6]

The TSC curves in such structures, measured after various exposures, will give information on the depth of the impurity levels of charge-exchange carriers of only one (known) sign of conductivity (after short exposures), or by carriers of both signs (electrons and holes, after long exposures). The exposure time that provides charging of the impurity levels in the crystal with carriers of only one sign can be determined from the shape of the photocurrent relaxation of the MSM structure. The shape of the photocurrent relaxation in the MSM structure upon exposure to light of constant intensity is completely determined by the features of

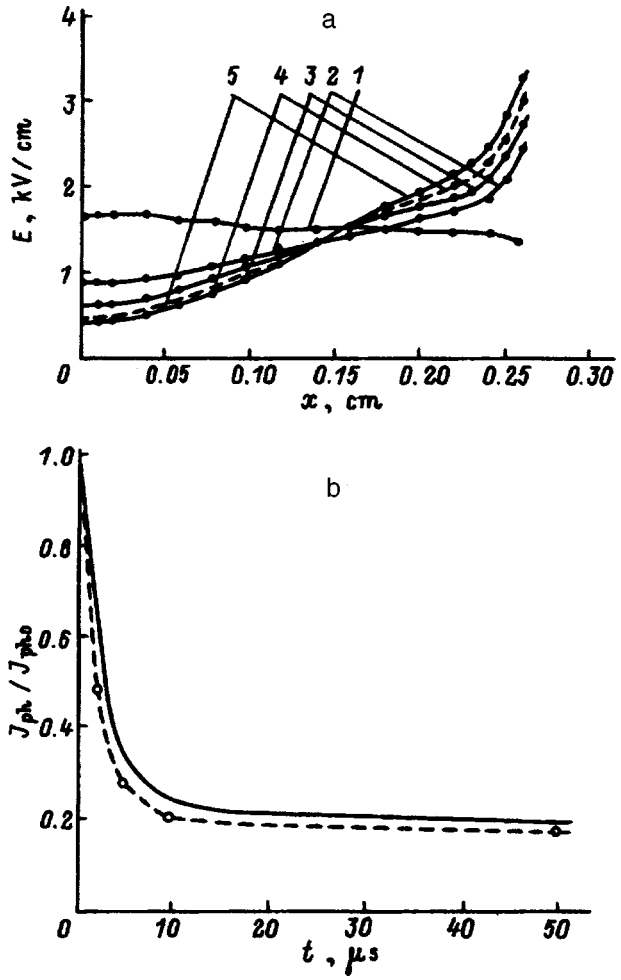

FIG. 1. Photocurrent relaxation in MSM structures on pure CdTe crystals ($N_t < 10^{14}$cm^{-3}) after turning on the illumination (applied voltage $V = 400$ V, $T = 300$ K). (a) electric field distribution in the crystal at various instants after beginning to illuminate the structure from the side of the positive electrode ($\lambda = 0.82$ μm, $I = 50$ mW/cm^2). Time t, sec: *1*—0, *2*—2×10^{-3}, *3*—5×10^{-3}, *4*—10×10^{-3}, *5*—50×10^{-3}. (b) variation of photocurrent J_{ph} with time (in relative units, where J_{ph0} is the initial photocurrent for a homogeneous electric field in the crystal). The solid curve shows the experimental values, and the dashed curve shows the values calculated from measured electric field distributions in the crystals at various instants after turning on the illumination (assuming that there is no injection from the side of the electrodes). The applied voltage is $V_0 = 400$ V, and $T = 300$ K.

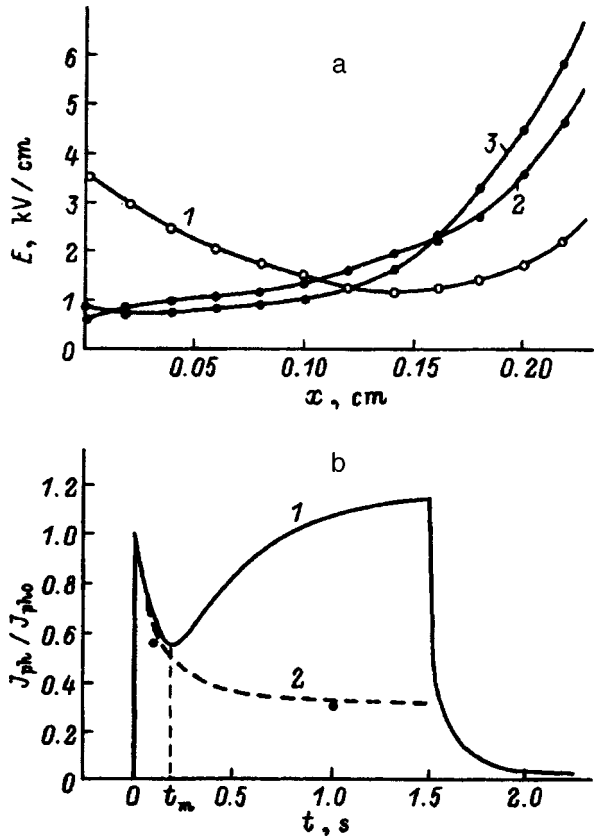

FIG. 2. Photocurrent relaxation in MSM structures on compensated CdTe crystals after turning on the illumination (applied voltage $V_0 = 400$ V, $T = 300$ K). (a) electric field distribution in the crystal at various instants after beginning to illuminate the structure from the side of the positive electrode ($\lambda = 0.82$ μm, $I = 10$ mW/cm^2). Time t,sec: *1*—0, *2*—0.1, *3*—1.0. (b) photocurrent relaxation in MSM structures after turning on the illumination (in relative units, where J_{ph0} is the initial photocurrent). *1* shows the experimental values, *2* shows the values calculated from the measured electric field distributions in the crystal at different instants after turning on the illumination (assuming that there is no injection from the side of the electrodes.

the photoinduced reconstruction of the electric field in the bulk of the structure with time.

In this case, the reconstruction of the electric field in the crystal with time, as shown in Refs. 5,6, and 8–10, has a monotonic character and is accompanied by the growth of the electric field at the dark electrode with time and by its decrease at the illuminated electrode. However, this reconstruction of the field in the crystal has an ambiguous effect on the value of the photocurrent that flows through the structure.

Such a reconstruction of the field in the crystal during illumination is accompanied by a change (a decrease) of the charge collected at the electrodes from each electron–hole pair created by the light at the illuminated electrode.[5,10–12] This process must result in a decrease of the photocurrent with time relative to its value for homogeneous distribution of the field in the crystal (when illumination is absent).

At the same time, this reconstruction of the field can change the injection properties of the dark electrode when the electric field close to this electrode in the crystal is increased above a definite critical value, and this must cause a sharp increase of the photocurrent flowing through the structure. The decisive effect of one or the other of these mechanisms on the current is determined by the character of the electric field distribution in the crystal and by its value at the electrodes of the structure.

The studies for this paper involved determining the parameters of the impurity levels in electrooptic insulating crystals of CdTe ($\rho = 10^7$–10^8 $\Omega\cdot$cm) with various impurity-level concentrations N_t: 1—$N_t < 10^{14}$ cm^{-3} (''pure'' crystals) and 2—$N_t > 10^{15}$ cm^{-3} (''compensated'' crystals). MSM structures were created on these crystals by chemically depositing optically transparent gold electrodes on etched surfaces of plane-parallel plates 0.25 cm thick and 0.25 cm^2 in area. The electrooptic technique of Ref. 10 was used to make measurements at $T = 300$ K of the shape of the current relaxation when the MSM structures are illuminated with intrinsic light ($\lambda = 0.63$ μm, 0.82 μm) from the side of

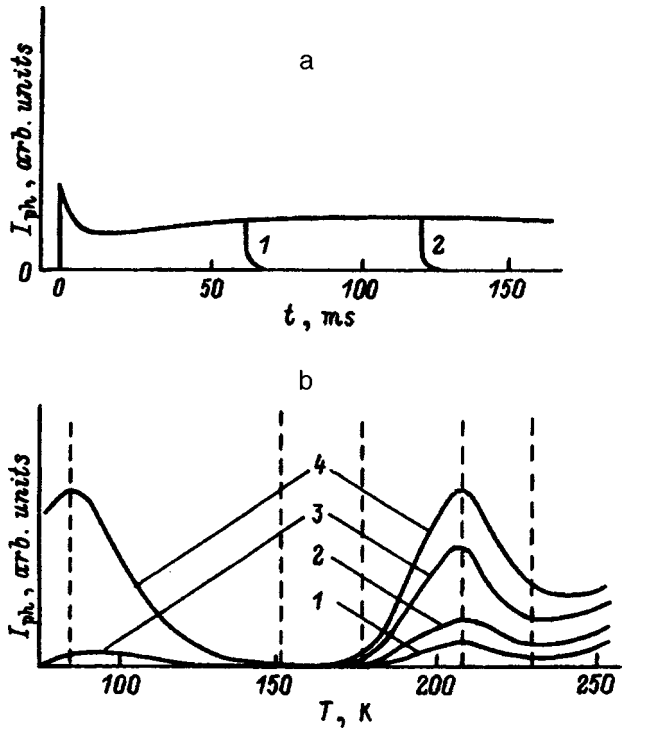

FIG. 3. TSCs after illumination of an MSM structure based on CdTe from the side of the positive electrode (at $T=77$ K, $V_0=20$ V, $I=3$ mW/cm^2, $\lambda=0.63\mu$m): (a) shape of the photocurrent relaxation of the structure after turning on the illumination ($V_0=20$ V, $T=77$ K, $I=3$ mW/cm^2, $\lambda=0.63$ μm). (b) TSCs after illuminating an MSM structure for various time intervals t,sec: *1*—6×10^{-2}, *2*—12×10^{-2}, *3*—25×10^{-2}, *4*—200.

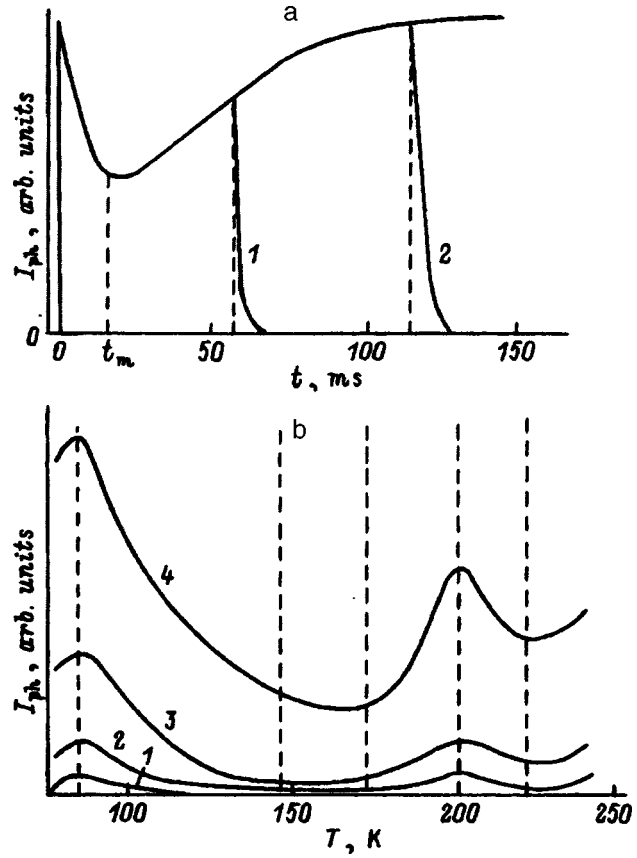

FIG. 4. TSCs after illumination of an MSM structure based on CdTe from the side of the negative electrode (at $T=77$ K, $V_0=20$ V, $I=3$ mW/cm^2, $\lambda=0.63\mu$m): (a) shape of the photocurrent relaxation of the structure after turning on the illumination ($V_0=20$ V, $T=77$ K, $I=3$ mW/cm^2, $\lambda=0.63$ μm). (b) TSCs after illuminating an MSM structure for various time intervals t,sec: *1*—6×10^{-2}, *2*—12×10^{-2}, *3*—25×10^{-2}, *4*—200.

the electrodes and measurements of the spatial distribution of the electric field $E(x,t)$ in the crystal between the electrodes of the structure at different times after beginning this illumination.

Based on the measured field distribution $E(x,t)$ and assuming that there is no injection of carriers from the side of the electrodes, the shape of the photocurrent relaxation in the structure when the illumination was turned on was calculated by the technique of Ref. 10, and the results of the calculations were compared with the experimentally measured shapes of the current relaxations in these structures.

The TSC spectra were studied after dosed illumination of the structures from the side of different electrodes at $T=77$ K.

Figures 1 and 2 show the electric field distribution in the volume of the crystal of the MSM structures (between the electrodes) at various times after beginning the illumination and the shape of the photocurrent relaxation in the structures, experimentally measured and calculated on the basis of the measured electric-field distribution in various types of crystals at $T=300$ K. As can be seen from Figs. 1a and 2a, the electric field at the dark electrode ($x=d$, where x is the thickness of the crystal, $0<x<d$, and d is the distance between the electrodes of the structure) under conditions of steady-state illumination in similar regimes is significantly higher in structures based on compensated crystals ($N_t>10^{15}$ cm^{-3}). As can be seen from Fig. 1b, the shape of the photocurrent relaxation in structures based on pure crystals ($N_t<10^{14}$ cm^{-3}) coincides with the calculated value and is determined only by the photoinduced reconstruction of the electric field in the crystal when the injection properties of the contacts remain unchanged. In the case of compensated crystals (Fig. 2b), the calculated and experimental values of the photocurrent coincide only at the initial instant; subsequently the experimentally measured values of the photocurrent significantly exceed the calculated values because carriers begin to be injected into the crystal from the side of the dark electrode. The minimum value of the experimentally measured photocurrent in structures based on compensated crystals ($N_t>10^{15}$ /cm^{-3}) is observed at $t=t_m$. During this time ($0-t_m$), only a monopolar electric charge of the same sign as that of the illuminated electrode is present in the crystal.

This work involved studying the TSC spectra on the high-resistance pure crystals ($N_t<10^{14}$ cm^{-3}) described above. During the recording of the TSC, the structure was cooled in the dark to $T=77$ K, and a constant voltage $U_0=20$ V was applied to the electrodes while they were held in the dark for $t=1$ min. The structure was illuminated from the side of different electrodes with constant-intensity flux of the intrinsic light ($\lambda=0.63$ μm, $I=10^{-2}$ W/cm^2), and the shape of the photocurrent relaxation was recorded (Figs. 3a and 4a). It can be seen that, at $T=77$ K the shape of the photocurrent relaxation in structures based on pure crystals

($N_t < 10^{14}$ cm^{-3}) has a form similar to Fig. 2b, with $t_m = 10$ ms. Dosed illumination of the structure by this light flux from the side of different electrodes is carried out through an optical shutter, with an exposure time of $t_e = 10^{-2}$–10^2 sec. After the illumination was switched off, the sample was held in the dark for $t = 1$ min, and then the structure was heated at a rate of $S = 0.3$ K/sec from $T = 77$ to 300 K while the temperature dependence of the transmitted current (the TSC) was recorded. The energy position of the impurity levels in the crystal (ΔE) was estimated from this, temperature dependence using the relationship $\Delta E = 23kT_m$,[1] where T_m is the temperature corresponding to the transmission peak, and k is Boltzmann's constant.

Figures 3b and 4b show the temperature dependences of the TSC; it can be seen that the form of the TSC curves is virtually identical after the sample has been illuminated for a long time from the side of different electrodes. As the exposure time t_e is decreased, a change of the ratio of the amplitudes of these peaks is observed on the TSC curves when the structure is illuminated from the side of different electrodes (Figs. 3b and 4b, curves *1*–*3*). Thus, after the structure is illuminated from the side of the negative electrode for a time $t_e = 2 \times 10^{-2}$ sec, only one peak at $T_m = 85$ K is observed on the TSC curves ($\Delta E = 0.17$ eV; see Fig. 4b, curve *1*), whereas, after it is illuminated from the side of the positive electrode for the same time, only one peak remains on the TSC curves at $T_m = 205$ K ($\Delta E = 0.41$ eV; see Fig. 3b, curve *1*). The energy positions of the impurity levels corresponding to the TSC peaks at $T_m = 85$ and 205 K are, respectively: $E_c - 0.17$ eV and $E_v + 0.41$ eV.

Thus, to completely determine the parameters of the impurity levels in a test crystal by means of the TSC method, it is necessary to create on it an MSM structure, to measure the shape of the photocurrent relaxation at the chosen illumination intensity ($T = 77$ K), to determine t_m, to measure the TSC after the structure is illuminated from the side of one of the electrodes for times of $t_e < t_m$ and $t_e \gg t_m$, and to determine the depth of the level in the crystal of these spectra in accordance with Ref. 1. The parameters of all the observed levels can be determined by comparing the TSC spectra after these exposures.

[1] A. G. Milnes, *Deep Impurities in Semiconductors* (Wiley, New York, 1963).
[2] V. I. Strikha, E. V. Buzaneva, and I. A. Radzievskaya, *Semiconductor Devices with a Schottky Barrier* (Sov. Radio, Moscow, 1974).
[3] M. A. Green and J. Shewchun, Solid-State Electron. **17**, 349 (1974).
[4] M. A. Green, V. A. K. Temple, and J. Shewchun, Solid-State Electron. **18**, 745 (1975).
[5] P. G. Kasherininov, A. V. Kichaev, A. A. Tomasov, and I. D. Yaroshetskiĭ, Pis'ma Zh. Tekh. Fiz. **20**, No. 18, 16 (1994) [Tech. Phys. Lett. **20**, 730 (1994)].
[6] P. G. Kasherininov, A. V. Kichaev, and I. D. Yaroshetskiĭ, Zh. Tekh. Fiz. **65**, No. 9, 193 (1995) [Tech. Phys. **40**, 970 (1995)].
[7] A. A. Gutkin, V. E. Sedov, Fiz. Tekh. Poluprovodn **9**, 1761 (1975) [Sov. Phys. Semicond. **9**, 1155 (1975)].
[8] P. G. Kasherininov, A. V. Kichaev, and I. D. Yaroshetskiĭ, Pis'ma Zh. Tekh. Fiz. **19**, 49 (1993) [Tech. Phys. Lett. **19**, 550 (1993)].
[9] P. G. Kasherininov, D. G. Matyukhin, and I. D. Yaroshetskiĭ, Pis'ma Zh. Tekh. Fiz. **21**, No. 7, 44 (1995) [Tech. Phys. Lett. **21**, 260 (1995)].
[10] P. G. Kasherininov, A. V. Kichaev, and A. A. Tomasov, Fiz. Tekh. Poluprovodn. **29**, 2092 (1995) [Semiconductors **29**, 1092 (1995)].
[11] G. Cavalleri, E. Gatti, G. Fabri, and V. Svelto, Nucl. Instrum. Methods **92**, 137 (1971).
[12] G. Fabri and V. Svelto, Nucl. Instrum. Methods **35**, 33 (1965).

Translated by W. J. Manthey

The nature of manganese luminescence centers in zinc sulfide single crystals

M. F. Bulanyĭ, B. A. Polezhaev, and T. A. Prokof'ev

Dnepropetrovsk State University, 320625 Dnepropetrovsk, Ukraine
(Submitted August 6, 1997; accepted for publication October 26, 1997)
Fiz. Tekh. Poluprovodn. **32**, 673–675 (June 1998)

This paper discusses how the luminescence-excitation method affects the spectral content of the emission in ZnS : Mn single crystals. It shows that the nearest neighborhood of the Mn^{2+} ions is associated with the elementary emission bands having maxima at the wavelengths $\lambda_m = 557$, 578, 600, 616, and 638 ± 2 nm in zinc sulfide crystals with different manganese concentrations. © *1998 American Institute of Physics.* [S1063-7826(98)00706-6]

Zinc sulfide doped with manganese has wide technical use in creating light sources with radiation in the yellow–orange region. Manganese has received much attention as a dopant of zinc sulfide. It received such attention because the material ZnS : Mn possesses bright and stable electroluminescence (EL) with a long service life when it is excited by either ac or dc voltage. However, despite many studies, the nature of the manganese luminescence centers formed by Mn^{2+} ions at various sites of the actual zinc sulfide crystal lattice and the mechanism of exciting them is still an open question.

The goal of this work was to study how the luminescence-excitation method affects the spectral composition of the radiation caused by the manganese ions.

The studies were carried out on single crystals of ZnS : Mn grown from the melt under argon pressure. α-MnS salt was used as a dopant. Crystals with a dopant concentration of C_{Mn} in the starting mix of $(10^{-4}–5\times10^{-2})$ g MnS per 1 g ZnS were studied with various luminescence-excitation methods. Photoluminescence (PL) spectra were studied with excitation by light at a wavelength of $\lambda = 365$ nm, which corresponds to impurity absorption of zinc sulfide, and with wavelengths corresponding to absorption at Mn^{2+} ions in zinc sulfide.[1] EL was studied with excitation by ac voltage corresponding to mean electric fields in the crystal of about $\sim(10^3–10^5)$ V/cm. Cathodoluminescence (CL) of the crystals was excited by electrons having an energy of about ~40 keV in a near-surface layer 1.5–2 μm thick.[2]

The luminescence spectrum depends on the manganese concentration for all forms of excitation. With small manganese concentrations $C_{\mathrm{Mn}} < 10^{-3}$ g/g, the emission spectrum contains bands associated with self-activated luminescence centers of zinc sulfide, having a maximum in the blue and green regions, and with manganese centers. Crystals with a large manganese concentration $C_{\mathrm{Mn}} \geqslant 10^{-3}$ g/g usually contain only the radiation of manganese ions, which is a wide band with a maximum in the region 580–590 nm. As the manganese concentration increases, the position of the emission maximum shifts toward shorter wavelengths by 5–8 nm. Moreover, the position of the maximum depends on the method and conditions of the luminescence excitation.[3] The observed features of the emission spectrum of Mn^{2+} ions in zinc sulfide are explained by the complex structure of the emission band. An analysis of the spectral content of the characteristics, carried out by means of the generalized method of Alentsev,[4] showed that elementary bands with emission maxima are present at wavelengths of $\lambda_m = 557 \pm 2$, 578 ± 2, 600 ± 2, 616 ± 2, and 638 ± 2 nm, which are associated with different locations of the Mn^{2+} ions in the actual zinc sulfide crystal lattice.[5,6] The most intense bands are those with $\lambda = 557$, 578, and 600 nm, which determine the position of the total maximum of the emission band of manganese.

The intensity of the elementary bands depends on the luminescence-excitation conditions. This is because, when the Mn^{2+} ions are located at different sites of the ZnS crystal lattice, there are differences in the probabilities of the radiative transitions in the manganese ion itself (reducing the symmetry of the crystal field increases the radiative transition probability[1]) and in the excitation mechanism: resonance from the sensitization centers[7,8] or as a direct consequence of impact with hot electrons during EL or as a result of the absorption of a light quantum from the characteristic absorption region of manganese in zinc sulfide during PL.

Studies of the PL showed that the emission of manganese centers with $\lambda_m = 557$ nm has virtually identical relative radiance both with excitation via sensitization centers by means of a resonance excitation mechanism (the wavelength of the exciting radiation is $\lambda_{\mathrm{exc}} = 365$ nm) and directly with absorption of light quanta from the absorption region ($\lambda_{\mathrm{exc}} = 390$, 430, 465, or 498 nm). The band with $\lambda_m = 578$ nm has the maximum radiance for excitation by light with $\lambda_{\mathrm{exc}} = 365$ nm. The long-wavelength elementary bands with $\lambda_m = 600$, 616, and 637 nm have the maximum radiance for excitation by light from the characteristic absorption region of manganese in zinc sulfide. These results can apparently be explained as follows: The manganese centers responsible for the $\lambda_m = 578$-nm line are mainly excited by a resonance mechanism from impurity point defects playing the role of sensitization centers. This means that these Mn^{2+} ions are located at sites where point defects pile up—for example, close to dislocations or the surface[9] at spacings of about ~(1–1.2) nm, which is the necessary condition for resonance interaction of the centers.

The centers that radiate at $\lambda_m = 600$, 616, and 637 nm are

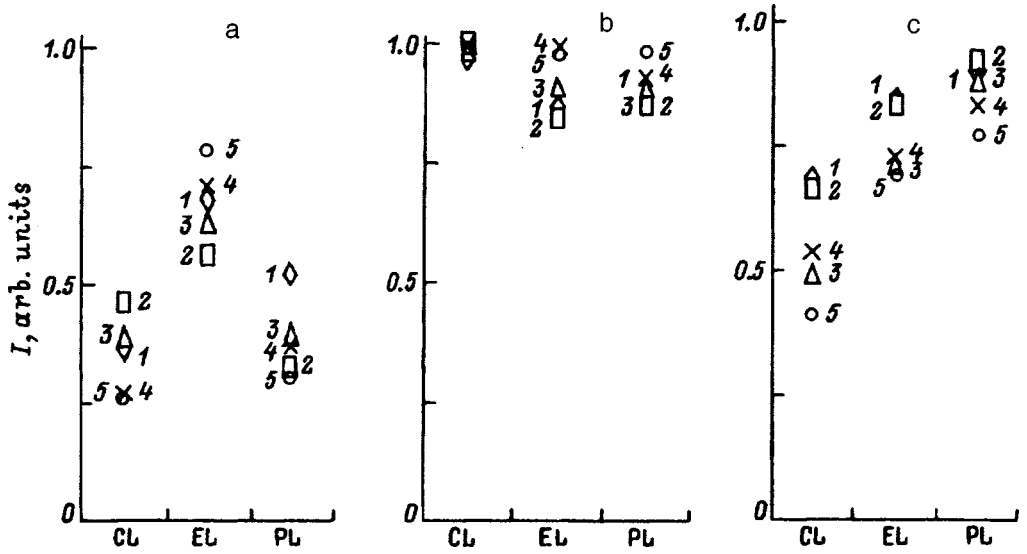

FIG. 1. Variation of the relative intensity I of bands with $\lambda_m = 557$ (a), 578 (b), and 600 (c) for various forms of luminescence excitation: PL, EL, CL. The manganese concentration is C_{Mn}, g/g: *1*—5×10^{-4}, *2*—10^{-3}, *3*—5×10^{-3}, *4*—10^{-2}, *5*—5×10^{-2}.

most likely located in the bulk of the crystal at those sites where the concentration of sensitization centers close to the Mn^{2+} ions is small. As a result, the radiance of these bands is greater when the excitation is produced by light from the characteristic absorption region.

The radiance of the band with $\lambda_m = 557$ nm, which is virtually independent of the method for exciting the PL, indicates that the mechanisms of resonance and nonresonance absorption of light have identical probability. In this case, the distances between the manganese centers and the sensitizer are critical for resonance interaction. This is indicated by the significant decrease of the amplitude of the band as the temperature is reduced, whereas the other elementary bands show little variation (reducing the temperature decreases the probability of the resonance excitation mechanism).

In order to study the location of the manganese centers over the volume of the crystal in more detail, the composition of the emission spectrum was studied as the luminescence was excited by various means: PL, EL, and CL. The results obtained for the three brightest elementary bands with different manganese concentration in ZnS : Mn crystals are shown in Fig. 1. It can be seen from this figure that the radiance of the band with $\lambda_m = 557$ nm is maximal for EL, while it is less for PL and CL. The intensity of the band with $\lambda_m = 600$ nm is maximal for PL and minimal for CL (when these results were obtained, the PL was excited by light with a wavelength of $\lambda_{\mathrm{exc}} = 365$ nm).

As far as the brightest band with $\lambda_m = 578$ nm is concerned, the greatest radiance of the emission was observed in CL.

In turn, these results can be explained as follows: The PL has a volume character when it is excited by light with $\lambda_m = 365$ nm, since the light penetrates to a significant depth.[10] With EL, the luminescence does not occur in the entire volume, but only in the part of it where the electric field is concentrated (the observed EL has a prebreakdown character in the test crystals[11]). At the same time, the CL can be considered surface luminescence: the luminescence involves the surface region with a depth of 1.5–2 μm.

By analyzing the results shown in Fig. 1, it can be concluded that the manganese centers with an emission of $\lambda_m = 557$ nm are located in the regions where the electric field is concentrated in the volume of the crystal when EL occurs. The centers that emit at $\lambda_m = 600$ nm are mainly located in the bulk part of the crystal, so that only part of them fall into the region of strong electric field.

The maximum intensity of the band with $\lambda_m = 578$ nm and the complete absence of circular symmetry on the polarization diagram for this band can be associated with the placement of these centers at sites where point defects accumulate and with distortion of the crystal lattice. Such sites can be both the surface itself and defects between blocks of the crystal. At the same time, the high intensity cannot be caused simply by a large number of these centers by comparison with the others. Actually, starting from the fact that the manganese ions are uniformly distributed over the volume of the crystal,[12] it can be assumed that the defects under consideration occupy only an insignificant part of the volume of the entire crystal. Therefore, their number will be minimal by comparison with the other defects. At the same time, the location of these centers in a distorted crystal field must increase the radiative transition probability in the Mn^{2+} ion itself[1] by comparison with the other types of manganese luminescence centers. Moreover, the close placement of the sensitization centers strengthens the resonance excitation mechanism, which has a greater probability than the other excitation mechanisms accompanying PL, EL, and CL. Moreover, when an electric field is applied (in EL), dislocations and surface defects can be sites of concentration of the electric field.[13] The enumerated causes make it possible to understand the maximum intensity of this band by comparison with the others for all forms and methods of luminescence excitation.

As far as the other types of manganese centers are con-

cerned, the centers responsible for the band with $\lambda_m = 600$ nm are most likely the most numerous. This is supported by the following facts: First, this band has significant intensity, even though it is caused by Mn^{2+} ions in a cubic lattice with high-symmetry crystal fields (this is indicated by the circular symmetry of the polarization diagrams[14]) and these centers consequently have a smaller radiative transition probability than the other centers. Second, the significant increase observed in this band by comparison with the others in PL when it is excited by light whose energy corresponds to the intrinsic absorption of manganese, as well as in EL in electric fields, where the excitation mechanism is predominant,[8] indicates that there are more of these centers than of the others.

[1] M. Aven and J. S. Prener [Eds.], *Physics and Chemistry of II–VI Compounds* (North Holland, Amsterdam, 1967; Mir, Moscow, 1970).
[2] N. D. Borisenko, V. I. Klimenko, and B. A. Polezhaev, Zh. Prikl. Spektrosk. **48**, 1012 (1988).
[3] N. D. Borisenko, V. I. Klimenko, and B. A. Polezhaev, Zh. Prikl. Spektrosk. **50**, 475 (1989).
[4] M. V. Fok, Trudy Fiz. Inst. Akad. Nauk SSSR **59**, 3 (1972).
[5] N. D. Borisenko, M. F. Bulanyi, F. F. Kodzhespirov, and B. A. Polezhaev, Zh. Prikl. Spektrosk. **55**, 452 (1991).
[6] N. D. Borisenko and B. A. Polezhaev, Zh. Prikl. Spektrosk. **53**, 1020 (1990).
[7] N. D. Borisenko, F. F. Kodzhespirov, E. G. Kuchukov, and B. A. Polezhaev, in *Questions on the Physics of Electroluminescence* (Dnepropetrovsk, 1979).
[8] N. D. Borisenko, M. F. Bulanyi, F. F. Kodzhespirov, and B. A. Polezhaev, Zh. Prikl. Spektrosk. **52**, 36 (1990).
[9] N. N. Novikov, *Structure and Structure-Sensitive Properties of Real Crystals* (Kiev, 1983).
[10] A. I. Vikhorev, in *Materials and Devices of Electronics* (Dnepropetrovsk, 1982).
[11] N. D. Borisenko, F. F. Kodzhespirov, and B. A. Polezhaev, Izv. Vyssh. Uchebn. Zaved. Fiz. No. **9**, 205 (1985).
[12] A. Ya. Yakunin, I. V. Shtambur, A. S. Kushnir, and S. A. Omel'chenko, Izv. Vyssh. Uchebn. Zaved. Fiz. No. **10**, 44 (1973).
[13] G. Matare, *Defect Electronics in Semiconductors* (Wiley, New York, 1971; Mir, Moscow, 1974).
[14] A. A. Andreev, N. D. Borisenko, A. I. Vikhorev, F. F. Kodzhespirov, E. G. Kuchukov, and B. A. Polezhaev, in *Abstracts of Reports of the Twenty-Sixth All-Union Conference on Luminescence* (Crystallography), Riga, 1980.

Translated by W. J. Manthey

Defect-formation processes in silicon doped with manganese and germanium

K. P. Abdurakhmanov, Sh. B. Utamuradova, Kh. S. Daliev, S. G. Tadjy-Aglaeva, and R. M. Ergashev

Mirzo Ulugbek Scientific Research Institute of Applied Physics, 700095 Tashkent, Uzbekistan
(Submitted October 9, 1997; accepted for publication November 3, 1997)
Fiz. Tekh. Poluprovodn. **32**, 676–678 (June 1998)

Deep-level transient spectroscopy has been used to study the effect of Ge atoms on the behavior of Mn in Si. It is shown that Ge atoms introduced into Si during growth manifest no electrical activity, even though their concentration is rather high: 10^{16}–10^{19} cm^{-3}. It is established that the presence of Ge atoms in the Si lattice enhances the efficiency of the formation of the deep levels $E_c-0.42$ eV and $E_c-0.54$ eV, which are associated with Mn in the Si lattice: the concentration of these deep levels in Si⟨Ge, Mn⟩ samples is a factor of 3–4 greater than in Si⟨Mn⟩. It is found that the presence of Ge atoms stabilizes the properties of the Mn levels in Si: They anneal more slowly than in Si⟨Mn⟩ by a factor of 5–6. It is assumed that the detected effects are associated with the features of the defect structure of Si doped with Ge and Mn.
 [S1063-7826(98)00806-0]

It is well known[1] that atoms of the transition elements possess mobility in Si because of a large diffusion constant. The capability of these atoms to migrate in the Si lattice makes them thermally unstable. Moreover, it is known that the presence of isovalent impurities (IVIs) in the volume of Si increases its thermal stability and radiation strength.[2,3] Therefore, we have studied the influence of IVI atoms (Ge) on the energy spectrum of deep levels (DLs) created by Mn and on the behavior of its atoms by means of deep-level transient spectroscopy (DLTS).

Samples of *n*- and *p*-type Si, doped with Ge during growth, with a resistivity of 5–100 $\Omega\cdot$cm and with orientation in the [111] direction, were used for the experiments. Samples of *n*- and *p*-Si grown by the Czochralski method were used as control samples, with a concentration of optically active oxygen of 6×10^{17} cm^{-3} and with resistivity ρ close to the ρ values of the Si⟨Ge⟩ samples.

To study the intra-impurity interactions of Mn and Ge atoms, Si samples doped with Ge during growth were also doped with Mn by diffusion. We have explained in detail in Refs. 4 and 5 the technology of introducing Mn into Si by diffusion. To make the capacitance measurements, diode structures were created by depositing Au in vacuum to create a Schottky barrier to the *n*-type Si and by depositing Sb as an ohmic contact. A Schottky barrier to the *p*-type Si was provided by Sb, and Au was used as an ohmic contact.

The DLTS spectra were measured in the dc voltage regime in the interval 77–300 K, with the emission-rate windows related by $t_2=3t_1$. We have described the technique for measuring and processing the DLTS spectra in a number of articles.[5,6] The DLTS spectra were premeasured (before introducing Mn atoms) in samples of *n*- and *p*-Si doped with Ge during growth. An analysis of the results of these measurements showed that DLs were not detected in an appreciable concentration in the Si⟨Ge⟩ samples. Supplementary experiments carried out by means of neutron-activation analysis showed that Ge atoms were present in the Si lattice in rather high concentrations of 10^{16}–10^{19} cm^{-3}. These data show that Ge atoms in the Si lattice manifest no electrical activity.

Measurements of the DLTS spectra of *p*-Si⟨Ge⟩ and *n*-Si⟨Ge⟩ samples diffusion-doped with Mn showed that the presence of Ge atoms in the Si lattice strongly affects the defect-formation processes. An analysis of the DLTS spectra (Fig. 1) shows that the efficiency of formation of DLs associated with Mn atoms in the Si lattice increases when Ge atoms are present. We showed earlier[4,5] that the diffusion introduction of Mn into Si results in the formation of a series of DLs with the following energies: $E_c-0.20$ eV, $E_c-0.42$ eV, and $E_c-0.54$ eV (Fig. 1, curve *1*). It was established that two of the latter levels are associated with Mn in silicon, namely, the DL with $E_c-0.42$ eV, caused by isolated Mn atoms in the state Mn^0, and the DL with $E_c-0.54$ eV, associated with paramagnetic $(Mn^0)_4$ clusters. The $E_c-0.20$-eV level is probably associated with a heat-treatment defect, since a DL with similar parameters is observed in the control samples (heat-treated in the absence of Mn).

An analysis and comparison of the results of measurements of the DLTS spectra in Si⟨Mn⟩ and Si⟨Ge, Mn⟩ samples show that the efficiency with which DLs with energies of $E_c-0.42$ eV and $E_c-0.54$ eV are formed is significantly higher in the presence of Ge atoms: the concentration of these levels in the Si⟨Ge, Mn⟩ samples is a factor of 3–4 higher than in the Si⟨Mn⟩ samples.

Note that the presence of Ge in the Si lattice has no substantial effect on the parameters of the Mn levels in Si (the ionization energy of the DLs and the carrier-capture cross section at the level). In this case, the energy spectrum of the DLs in the Si⟨Ge, Mn⟩ samples does not differ from that in the Si⟨Mn⟩ samples (Figs. 1 and 2).

The detected increase of the DL concentration associated with Mn in Si can probably be explained by the fact that Ge

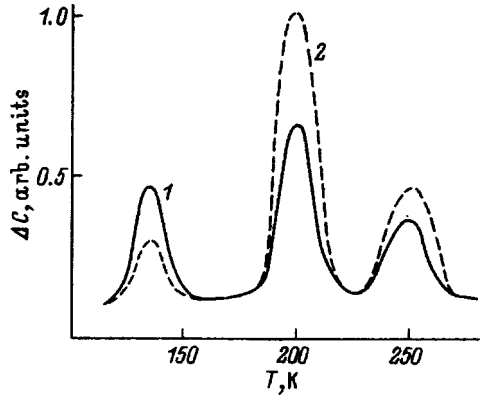

FIG. 1. Typical DLTS spectra of the following samples: *1*—*n*-Si⟨Mn⟩, *2*—*n*-Si⟨Ge,Mn⟩.

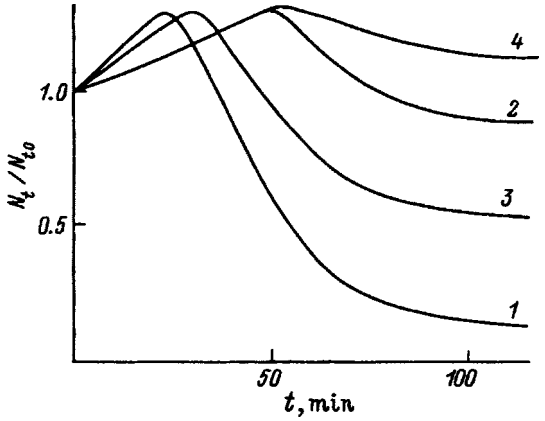

FIG. 3. Kinetics of low-temperature annealing ($T=130$ °C) of DLs in the following samples: *1, 2*—*n*-Si⟨Mn⟩, *3, 4*—*n*-Si⟨Ge,Mn⟩.

atoms introduced into Si in a rather high concentration occupy all the sinks and other imperfections of the Si lattice. It is well known[6] that there is a difference of 1.5–2 orders of magnitude between the solubility limit of Mn in Si and the concentration of electrically active Mn atoms. It is assumed that this difference is associated with the precipitation of a certain part of the introduced Mn atoms at some inactive sinks or with the coupling of the Mn into neutral complexes. The presence of Ge atoms occupying these sinks, however, increases the fraction of electrically active Mn atoms in Si. Note that the presence of Ge atoms in the Si lattice prevents the formation of thermal defects. It follows from a comparison of curves *2* and *3* in Fig. 1 that the formation efficiency of the level with an energy of $E_c-0.20$ eV, caused by heat treatment, is far lower in the *n*-Si⟨Ge⟩ samples than in the control *n*-Si. This fact confirms the data of Refs. 2 and 3.

The DLs created by Mn in Si, as we established earlier,[7] are unstable even at room temperature. It was therefore interesting to investigate the kinetics of low-temperature annealing of the DLs associated with Mn atoms when Ge impurities in various concentrations were present in the Si lattice. With this purpose, we studied the effect of isothermal annealing in the temperature interval 100–200 °C on the behavior of the Mn atoms in the *n*-Si⟨Ge, Mn⟩ samples.

Typical DLTS spectra of *n*-Si⟨Mn⟩ and *n*-Si⟨Ge, Mn⟩ samples submitted to isothermal annealing at 130 °C are shown in Fig. 3 (curves *1–4*). It follows from this figure that the DLs with an energy of $E_c-0.42$ eV, associated with isolated Mn^0 atoms (curve *1*), anneal rather rapidly, and that the DLs are almost completely annealed in the course of 1 h. The $E_c-0.54$ eV level (curve *2*), associated with clusters of four neutral Mn atoms, is characterized by greater stability, and it anneals significantly more slowly. An analysis of the kinetic curves in Fig. 3 shows that low-temperature annealing of the deep centers of Mn in the presence of Ge atoms in the volume of the Si (curves *3* and *4*) occurs more slowly than with the Si⟨Mn⟩ samples (curves *1* and *2*) by a factor of 5–6.

Thus, Ge atoms that manifest no electrical activity in Si enhance the formation efficiency of deep centers associated with Mn in Si and stabilize the properties of these centers.

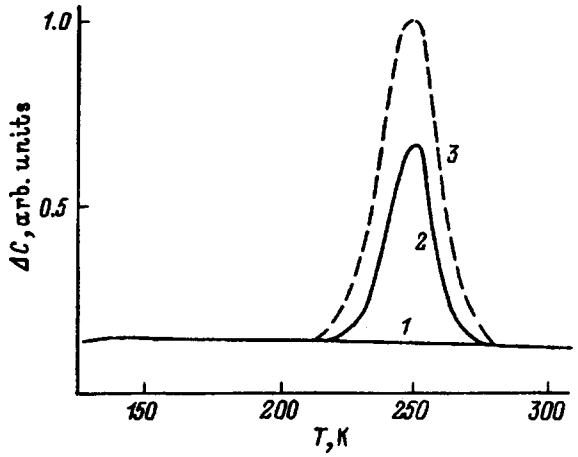

FIG. 2. DLTS spectra in the following samples: *1*—*p*-Si⟨Ge⟩, *2*—*p*-Si⟨Mn⟩, *3*—*p*-Si⟨Ge,Mn⟩.

[1] É. M. Omel'yanovskiĭ and V. I. Fistul', *Impurities of Transition Metals in Semiconductors* (Metallurgiya, Moscow, 1983).
[2] Yu. M. Babitskiĭ *et al.*, Fiz. Tekh. Poluprovodn. **18**, 1242 (1984) [Sov. Phys. Semicond. **18**, 775 (1984)].
[3] M. Ya. Dashevskiĭ *et al.*, Neorg. Mater. **24**, No. 9 (1988).
[4] K. P. Abdurakhmanov, Sh. B. Utamuradova *et al.*, Fiz. Tekh. Poluprovodn. **19**, 213 (1985) [Sov. Phys. Semicond. **19**, 133 (1985)].
[5] K. P. Abdurakhmanov, R. F. Vitman, Sh. B. Utamuradova *et al.*, Fiz. Tekh. Poluprovodn. **23**, 2227 (1989) [Sov. Phys. Semicond. **23**, 1379 (1989)].
[6] K. P. Abdurakhmanov, A. A. Lebedev *et al.*, Fiz. Tekh. Poluprovodn. **19**, 1158 (1985) [Sov. Phys. Semicond. **19**, 711 (1985)].
[7] A. A. Lebedev, K. P. Abdurakhmanov *et al.*, in *Properties of Doped Semiconductor Materials* (Nauka, Moscow, 1990).

Translated by W. J. Manthey

Structure of *DX*-like centers in narrow-band IV–VI semiconductors doped with group-III elements

I. I. Ivanchik and D. R. Khokhlov

M. V. Lomonosov Moscow State University, Physics Dependent, 119899 Moscow, Russia

A. I. Belogorokhov

State Institute of Rare Metals, Moscow, Russia

Z. Popović and N. Romćević

Physics Institute, Belgrade University, Belgrade, Yugoslavia

(Submitted October 13, 1997; accepted for publication November 11, 1997)
Fiz. Tekh. Poluprovodn. **32**, 679–683 (June 1998)

This paper presents a study of the structure of the IR reflectance spectra in the sub-gap region of lead telluride doped with indium and gallium and the Raman spectra in PbTe(In). In the Raman and reflectance spectra of PbTe(In), features are observed at a frequency of $\omega_0 \simeq 120\ \mathrm{cm}^{-1}$, whose amplitude sharply increases at temperatures T below the temperature where delayed photoconductivity appears, $T_c \simeq 25$ K. A similar feature at a frequency of $\omega_0 \simeq 155\ \mathrm{cm}^{-1}$ is also observed in PbTe(Ga), with the amplitude of the feature sharply increasing for $T > T_c \simeq 80$ K. An analysis of the resulting data makes it possible to conclude that, in contrast with classical *DX* centers in III–V semiconductors, the microscopic structure of the impurity centers in the two-electron (*DX*-like) ground state does not correspond to an impurity atom shifted from a lattice site, whereas the impurity atom is shifted from a lattice site for the metastable one-electron impurity state. © *1998 American Institute of Physics.* [S1063-7826(98)00906-5]

INTRODUCTION

The problem of *DX* centers in semiconductors has been an object of intense experimental and theoretical research for more than twenty years. The main characteristic of these impurity centers is strong electron–phonon interaction, resulting in the appearance of barriers in configuration space between states of the system with different numbers of localized electrons. In addition, strong polarization of the crystal lattice in the neighborhood of an impurity atom in certain cases produces a state with negative correlation energy (negative-*U* centers). Such a combination of properties leads to the appearance of an entire series of unusual effects, in particular, delayed photoconductivity at low temperatures. The microscopic structure of classical *DX* centers, observed in semiconductors of classes III–V and II–VI, has been studied in fairly great detail, both experimentally and theoretically.[1]

In semiconductors of group IV–VI, which are mostly narrow-band semiconductors, impurity states have a very specific nature. Because of the large permittivity and small effective mass of the charge carriers, the hydrogen-like impurity states have negligible energy, and all the observed impurity and defect levels are strongly localized and deep. It was assumed until recently that there are no *DX* centers in semiconductors with a narrow band gap, in particular, in IV–VI materials. However, it turned out that the properties of the impurity centers that appear when certain IV–VI semiconductors are doped with group-III impurities are largely analogous to the properties of *DX* centers. In particular, stabilization of the Fermi level, delayed photoconductivity, and long-term photomemory have been detected.[2]

At the same time, in contrast with the classical centers, the microscopic structure of ''*DX*-like'' impurity centers was unknown until recently. The results of a study of the IR reflectance and Raman spectra obtained in this paper allow us to make a series of important conclusions concerning this matter.

SAMPLES AND EXPERIMENTAL PROCEDURE

Single crystals of PbTe doped with In were grown by the Bridgman method, while single crystals of PbTe(Ga) were grown by the Czochralski method. The quantity of impurity in the samples corresponded to the condition of stabilization of the Fermi level 70 meV above the bottom of the conduction band in PbTe(In) (Ref. 3) and 70 meV below the bottom of the conduction band in PbTe(Ga).[4] The surface of the samples was subjected to chemical–mechanical polishing.

In this paper we present measurements of the Raman spectra of PbTe(In) at temperatures from 5 to 300 K and IR reflectance spectra of PbTe(In) and PbTe(Ga) in the temperature range 10–300 K.

Raman scattering was excited by unpolarized radiation from an argon laser with a wavelength of 488 nm (mean power about 100 mW). A U-1000 Jobin Yvon monochromator with a conventional photon-counting system and a Dilor monochromator equipped with a charge-coupled detector were used to measure the Raman spectra. When the classical photon-counting system was used, averaging was car-

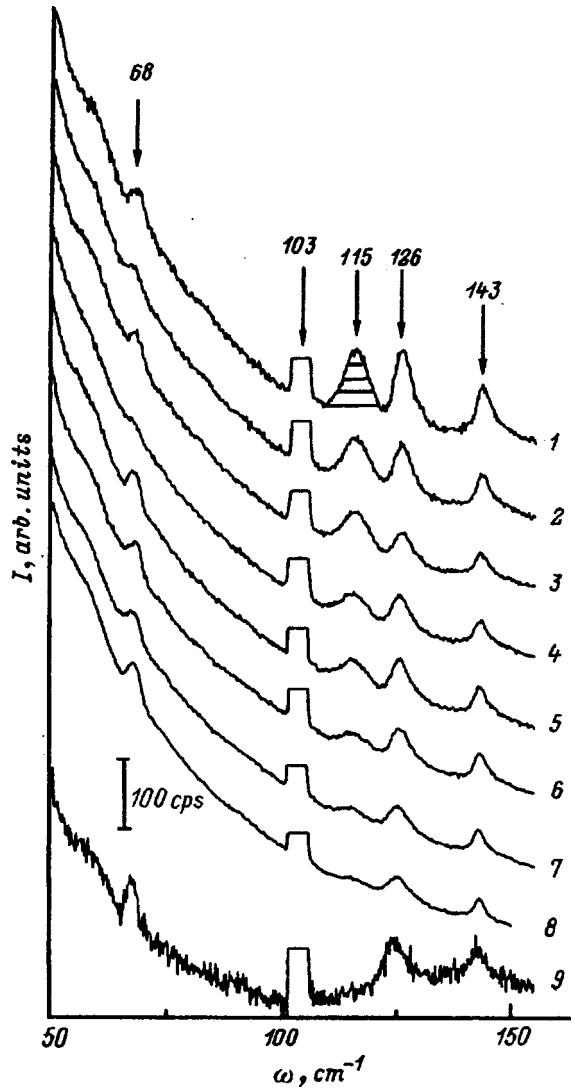

FIG. 1. Form of the Raman spectra of PbTe + 0.4 at.% In. Temperature T, K: *1*—10, *2*—15, *3*—20, *4*—25, *5*—30, *6*—50, *7*—65, *8*—100, *9*—300. The numbers with arrows on the curves denote the frequency of the corresponding lines in cm^{-1}.

ried out over approximately forty spectra for each temperature. The samples were placed in a closed-cycle cryostat with a temperature regulator that makes it possible to cool the samples to 10 K.

The IR reflectance spectra were measured in the wavenumber range 30–650 cm^{-1} at temperatures of 10–300 K, using a Bruker IFS-113v spectrometer equipped with an Oxford Instruments cryostat.

EXPERIMENTAL RESULTS

The Raman spectra of a single crystal of PbTe+0.4 at.% In at temperatures from 10 to 300 K are shown in Fig. 1. In general, first-order Raman modes are not active in the fcc lattice of lead telluride. The modes observed at 68, 126, and 143 cm^{-1} at all temperatures from 10 to 300 K are associated with the effect of the thin layer of TeO_2 on the surface of the sample. These modes are well known in other tellurides.[5,6] The powerful Raman line at 103 cm^{-1} is caused by plasma vibrations.

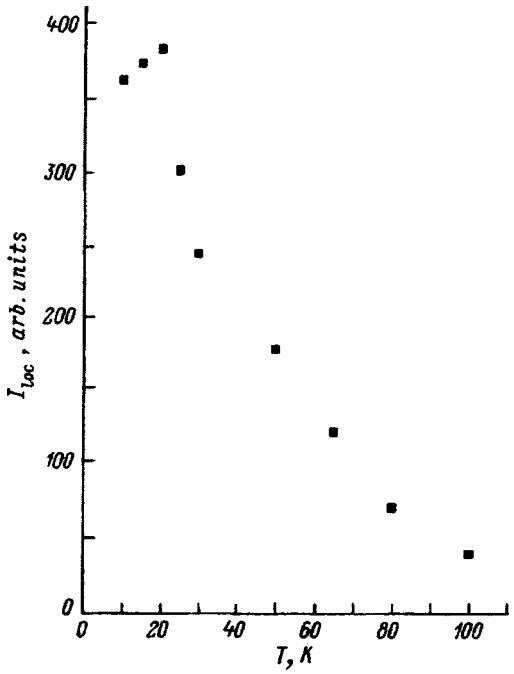

FIG. 2. Intensity I_{loc} of the Raman line at frequency $\omega_0 = 115\ cm^{-1}$ vs temperature.

The most interesting mode is that at $\omega_0 \simeq 115\ cm^{-1}$, which can be distinguished from the background only for temperatures below 100 K. As the temperature is reduced further, the mean intensity I_{loc} of the line increases, with the sharpest rise being observed at a temperature $T_c \simeq 25$ K (Fig. 2). It is important to note that the value of T_c coincides with the critical temperature below which the delayed photoconductivity effect is observed in PbTe(In).[7]

The IR reflectance spectra (R) of a single crystal of PbTe + 0.4 at. % In in the far IR is shown in Fig. 3. The experimental data are indicated by points. The procedure of numerical optimization of the parameters, using the standard plasmon–phonon dispersion relation for the permittivity of the form[8]

$$\varepsilon(\omega) = \varepsilon_\infty \left[1 - \frac{\omega_p^2}{\omega(\omega + i\gamma_p)} - \frac{\omega_{LO}^2 - \omega_{TO}^2}{\omega_{TO}^2 - \omega^2 - i\gamma_{TO}\omega} \right], \quad (1)$$

(where ω_{TO} and ω_{LO} are the frequencies of the transverse and longitudinal optical phonons, respectively; ω_p is the plasma frequency; γ_{TO} and γ_p are the phonon and plasmon damping factors, respectively; and ε_∞ is the high-frequency permittivity), does not make it possible to describe the additional structure in the reflectance spectra observed in the frequency region around 120 cm^{-1} at temperatures below 200 K. To obtain satisfactory agreement with the experimental data we must introduce in the dispersion relation an additional oscillator of the form

$$\frac{\omega_{loc}^2}{\omega_0^2 - \omega^2 - iG\omega}, \quad (2)$$

where ω_0 is the characteristic frequency of the oscillator, ω_{loc} is a quantity proportional to the oscillator strength, and G is the damping factor (the solid curves in Fig. 3). The

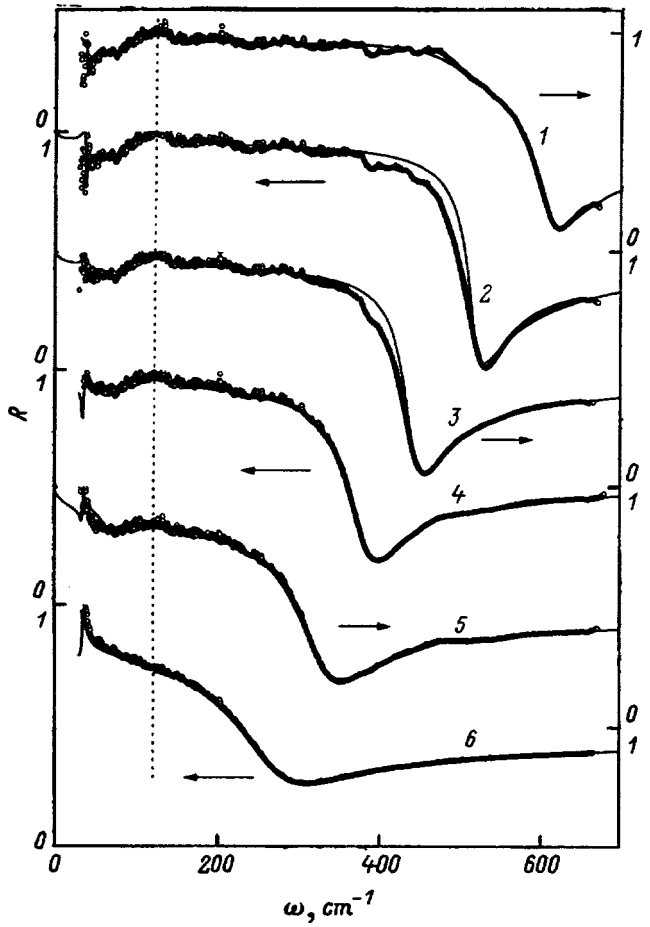

FIG. 3. IR reflectance spectra of PbTe+0.4 at.% In. *T*, K: *1*—10, *2*—50, *3*—100, *4*—150, *5*—200, *6*—300. The points show experimental values, and the solid curves show the results of a procedure of numerical optimization of the parameters, using the dispersion relations (1) and (2).

value $\omega_0 = 122\ \text{cm}^{-1}$ is virtually constant with temperature, whereas ω_{loc} (the oscillator strength) sharply increases as temperatures decrease below 50 K (Fig. 4). A similar structure is observed in the far-IR reflectance spectra of $Pb_{0.75}Sn_{0.25}Te$(In) (Refs. 9 and 10) and $Pb_{0.9}Mn_{0.1}Te$(In) (Ref. 11) at the same frequency.

An analogous additional structure is detected in the IR reflectance spectra of PbTe(Ga) (Fig. 5). The only difference from the PbTe(In) case is numerical: The frequency is $\omega_0 = 155\ \text{cm}^{-1}$, and ω_{loc} (the oscillator strength) sharply increases with decreasing temperature below $T_c = 80$ K—the critical temperature for the appearance of delayed photoconductivity in PbTe(Ga) (Fig. 6).

DISCUSSION OF RESULTS

It is easy to see that the temperature dependence of the intensity of the Raman mode at a frequency of ω_0 in PbTe(In), shown in Fig. 2, is very similar to the dependence of the oscillator strength on temperature for the IR-active mode at $122\ \text{cm}^{-1}$ (see Fig. 4). Moreover, an analogous structure at frequency $155\ \text{cm}^{-1}$ is recorded in the IR reflectance spectra of gallium-doped lead telluride.

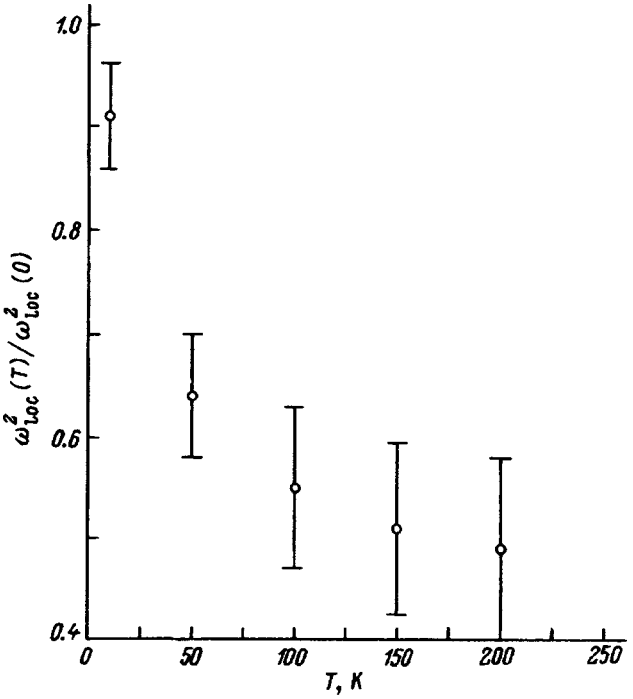

FIG. 4. Reduced oscillator strength in the form $\omega^2_{\text{loc}}(T)/\omega^2_{\text{loc}}(0)$ [see Eq. (2)] vs temperature for PbTe(In).

In our opinion, the nature of the additional oscillators that appear in the IR reflectance and Raman spectra, as well as in the photoconductivity spectra[12] of lead telluride doped with group-III elements—indium and gallium—is associated with the excitation of local phonon modes close to the impurity atoms. Actually, most importantly, the frequencies at which oscillators are observed are close to the frequency of the longitudinal optical phonon in PbTe, $\omega_{\text{LO}} = 110\ \text{cm}^{-1}$. In addition, the ratio

$$\frac{\omega_0^2(\text{In})}{\omega_0^2(\text{Ga})} = \frac{m_{\text{Ga}}}{m_{\text{In}}} \tag{3}$$

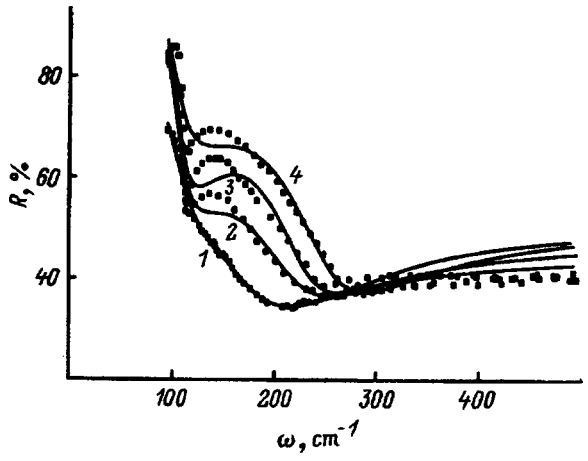

FIG. 5. Form of the IR reflectance spectra of PbTe+0.4 at.% Ga. *T*, K: *1*—300, *2*—150, *3*—70, *4*—50. The points show experimental values, and the solid curves show the result of a procedure of numerical optimization of the parameters, using the dispersion relations (1) and (2).

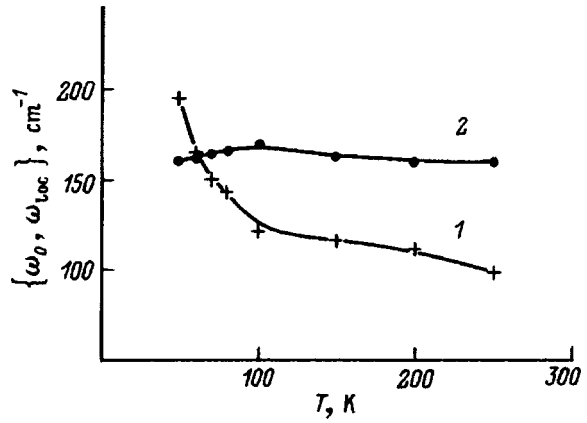

FIG. 6. Oscillator strength ($\omega_{\rm loc}$) (*1*) and frequency (*2*) vs temperature for PbTe(Ga).

for the frequencies of the local modes in terms of a simple model, which takes into account only the difference in the masses $m_{\rm In,Ga}$ of the indium and gallium impurity atoms, is satisfied with surprising accuracy.

What charge state of the indium and gallium impurity atoms corresponds to the observed local mode of the vibrations? It is well known[13] that group-III elements mainly replace the metal atoms in alloys based on lead telluride. However, the 2+ charge state of impurity atoms neutral relative to the lattice is metastable and decays to donor–acceptor pairs according to the reaction

$$2A^{2+} \rightarrow A^{+} \rightarrow A^{3+},$$

i.e., the effective interaction energy of the electrons at the impurity center is negative (negative-U centers).[13,14] This circumstance leads to the effect of stabilizing the Fermi level at a position corresponding to equality of the total multielectron energy of the A^+ and A^{3+} states.[14] Additional doping with other donors or acceptors in such a situation affects only the change of the impurity concentration in the univalent and trivalent states, but not the position of the Fermi level. Thus, the number of impurity atoms in the A^+ and A^{3+} states corresponds in order of magnitude to the total impurity concentration in the sample, about $10^{20}\,{\rm cm}^{-3}$. The delayed photoconductivity observed in the indicated materials at low temperatures $T<T_c$ cannot substantially change the ratio between A^+ and A^{3+}, since the concentration of nonuniform charge carriers does not exceed[3,4] $10^{18}\,{\rm cm}^{-3}$. At the same time, the experimental data indicate that the oscillator strength corresponding to the local phonon mode increases with decreasing temperature by a factor of more than 10. Thus, the observed local mode most likely corresponds to impurity centers observed in the metastable state A^{2+}, when only one electron is localized at the impurity. Temperature T_c is determined by the barrier height W in configuration space that separates the metastable impurity state from the two-electron ground state A^+; therefore, at low temperatures, when $kT<W$, the population of A^{2+} centers sharply increases under conditions of IR photoexcitation.

The resulting experimental data provide a basis for certain conclusions concerning the microscopic structure of the impurity centers in various charge states. Most importantly, despite the sharp increase in the amplitude $I_{\rm loc}$ of the Raman mode at a frequency $\omega_0=115\,{\rm cm}^{-1}$ as the temperature decreases below $T_c=25$ K, the value of $I_{\rm loc}$ is still much lower than the characteristic values corresponding to breakdown of the symmetry inversion over the entire volume of the crystal. Consequently, the appearance of the Raman mode is in all probability caused by local breakdown of the inversion symmetry. At the same time, at high temperatures $T>100$ K, the Raman mode at frequency $\omega_0=115\,{\rm cm}^{-1}$ is indistinguishable at the background level. Virtually all the impurity centers are found in the In^+ and In^{3+} states at these temperatures, from which it follows that local breakdowns of the inversion symmetry are absent for the indicated charge states of the impurity.

The following is yet another argument which shows that the impurity atom is displaced from the centrally symmetric position for the metastable charge state A^{2+}: Equation (1) is valid for the local modes associated with the indium and gallium impurity atoms. Therefore, since indium replaces lead in the crystal lattice, it could be expected that

$$\omega_0^2({\rm In})/\omega_{\rm LO}^2 = m_{\rm Pb}/m_{\rm In}. \tag{4}$$

However, the simplest computations show that Eq. (4) is not satisfied. The indicated contradiction is explained if it is recalled that impurity atoms in a metastable state shift from the centrally symmetric position. This in turn can result in a certain change in the force constants of the crystal lattice in the neighborhood of the impurity center and can cause Eq. (4) to break down.

Thus, these results are evidence that the A^+ and A^{3+} impurity states, which correspond to two electrons localized at the impurity and to the empty center, respectively, correspond to a centrally symmetric position of the impurity atom, whereas, for the metastable state A^{2+}, which corresponds to one localized electron, the impurity atom is displaced from the inversion center. Consequently, the ionization of each of the electrons from the two-electron impurity ground state results in a displacement of the impurity atom, first to an interstitial position, and then back into a substitutional center. As a result, barriers are formed in configuration space between all the states of the system with different numbers of localized electrons.

For classical *DX* centers in III–V and II–VI semiconductors, on the other hand, the two-electron ground state of the impurity corresponds to a noncentral position of the atom, whereas, in the one-electron and completely ionized state, the impurity atom is in a centrally symmetric position. The metastable one-electron state is shallow and is not separated by a barrier from the completely ionized impurity state.

The indicated difference is of fundamental importance. For *DX*-like centers in IV–VI compounds, it allows nonequilibrium charge carriers to accumulate in a metastable impurity state at low temperatures and produces a whole series of strong nonequilibrium effects: giant negative magnetoresistance,[15] stimulation of the quantum efficiency,[16] and other effects.[2]

This work was carried out with the partial support of the Russian Fund for Fundamental Research Grants Nos. 95-02-

04658-a and 96-02-16275-a, and Grant RFFI-Intas No. 95-1136.

[1] P. M. Mooney, J. Appl. Phys. **67**, R1 (1990).
[2] B. A. Akimov, A. V. Dmitriev, D. R. Khokhlov, and L. I. Ryabova, Phys. Status Solidi A **137**, 9 (1993).
[3] B. A. Akimov, N. B. Brandt, K. R. Kurbanov, L. I. Ryabova, A. T. Khasanov, and D. R. Khokhlov, Fiz. Tekh. Poluprovodn. **17**, 1604 (1983) [Sov. Phys. Semicond. **17**, 1021 (1983)].
[4] B. A. Akimov, N. B. Brandt, A. M. Gas'kov, V. P. Zlomanov, L. I. Ryabova, and D. R. Khokhlov, Fiz. Tekh. Poluprovodn. **17**, 87 (1983) [Sov. Phys. Semicond. **17**, 53 (1983)].
[5] A. S. Pine and G. Dresselhaus, Phys. Rev. B **4**, 356 (1971).
[6] J. A. Cape, L. G. Hale, and W. E. Tennant, Surf. Sci. **62**, 639 (1977).
[7] B. M. Vul, I. D. Voronova, G. A. Kalyuzhnaya, A. T. Mamedov, and T. Sh. Ragimova, JETP Lett. **29**, 21 (1979)].
[8] S. W. McKnight and M. K. El-Rayess, Solid State Commun. **49**, 1001 (1984).
[9] N. Romcevic, Z. V. Popovic, D. R. Khokhlov, A. V. Nikorich, and W. Koenig, Phys. Rev. B **43**, 6712 (1991).
[10] N. Romcevic, Z. V. Popovic, and D. R. Khokhlov, J. Phys.: Condens. Matter **4**, 4323 (1992).
[11] N. Romcevic, Z. V. Popovic, D. R. Khokhlov, and W. Koenig, Infrared Phys. Technol. **38**, 117 (1997).
[12] A. I. Belogorokhov, I. I. Ivanchik, S. V. Ponomarev, E. I. Slyn'ko, and D. R. Khokhlov, JETP Lett. **63**, 353 (1996).
[13] I. A. Drabkin and B. Ya. Moĭzhes, Fiz. Tekh. Poluprovodn. **15**, 625 (1981) [Sov. Phys. Semicond. **15**, 357 (1981)].
[14] D. R. Khokhlov and B. A. Volkov, in *Proceedings of the Twenty-Third International Conference on the Physics of Semiconductors* (Berlin, Germany, July 21–26, 1996) edited by M. Scheffer and R. Zimmermann [World Sci. **4**, 2941 (1996)].
[15] B. A. Akimov, A. V. Nikorich, D. R. Khokhlov, and S. N. Chesnokov, Fiz. Tekh. Poluprovodn. **23**, 668 (1989) [Sov. Phys. Semicond. **23**, 418 (1989)].
[16] B. A. Akimov and D. R. Khokhlov, Semicond. Sci. Technol. **8**, S349 (1993).

Translated by W. J. Manthey

Infrared reflectance spectra and Raman spectra of $Cu_xAg_{1-x}GaS_2$ solid solutions

I. V. Bodnar'

Belarus State University of Informatics and Radio Electronics, 220069 Minsk, Belarus
(Submitted September 9, 1997; accepted for publication November 18, 1997)
Fiz. Tekh. Poluprovodn. **32**, 684–687 (June 1998)

Using crystals of the compounds $CuGaS_2$ and $AgGaS_2$ and solid solutions based on them, the IR reflectance spectra and the Raman spectra have been studied in polarized light. Values have been determined for the frequencies of the longitudinal and transverse optical phonons, the damping coefficients, the IR intensity, and ε_0, and ε_∞. The concentration dependences of the indicated parameters have been constructed, and the character of the behavior of the optical vibrations in the solid solutions has been established. © *1998 American Institute of Physics.* [S1063-7826(98)01006-0]

The ternary compounds $CuGaS_2$ and $AgGaS_2$ belong to the family of I–III–VI semiconductors and possess interesting optical properties: a significant nonlinearity, strong birefringence, and a wide transparency range.[1–3] The presence of an isotropic point makes it possible to use these crystals as narrow-band filters in the visible and near-IR ranges.[4,5]

This paper presents the results of studies of the vibrational spectra of solid solutions of $Cu_xAg_{1-x}GaS_2$, formed from the compounds $CuGaS_2$ and $AgGaS_2$ crystallized in the chalcopyrite structure (space group $D_{2d}^{12}-I\bar{4}2d$). The primitive cell of the structure of such crystals contains two formula units, which results in the appearance of twenty-one optical and three acoustic phonon branches.[6] In this case, the optical vibrations are classified as

$$\Gamma^{\text{opt}}=1A_1(\Gamma_1)+2A_2+3B_1(\Gamma_3)+3B_2(\Gamma_4)+6E(\Gamma_5).$$

The two A_2 modes are inactive. The three B_2 and six E modes are IR active and appear in polarization fields $\mathbf{E}\|\mathbf{C}$ and $\mathbf{E}\perp\mathbf{C}$, respectively. The other modes are active in the Raman spectra.

We studied the vibrational spectra of these materials by means of IR reflectance spectra and Raman spectra. The indicated measurements were made on crystals grown by the method of directed crystallization of the melt (horizontal version) by the technique described in Ref. 7. The composition of the crystals was determined by an x-ray method, starting from the assumption that Vegard's law was satisfied in the system, while the homogeneity was monitored by means of x-ray microprobe analysis.

The IR reflectance spectra were recorded on a Perkin-Elmer 180 spectrophotometer in the frequency range 150–450 cm^{-1} at room temperature from the (112) surface of single crystals in polarized light. The Raman spectra were recorded on a Spex-Romolog 4 spectrometer with an adapter that made it possible to observe the Raman scattering at an angle of 180°. A Spectra Physics model 165 argon laser served as the excitation source. The polarization measurements were made at $\lambda_{exc}=5145$ Å in ($\perp$, $\perp$) and ($\|$, $\|$) geometries, in which the E and B_2 modes must appear according to the selection rules. To enhance the accuracy of the

TABLE I. Frequencies of TO/LO phonons (cm^{-1}) for compounds $CuGaS_2$ and $AgGaS_2$.

Symmetry (chalcopyrite)	$CuGaS_2$					$AgGaS_2$					Symmetry (sphalerite)
	IR reflectance		Raman scattering			IR reflectance		Raman scattering			
	Ref. 12	our data	Ref. 13	Ref. 14	our data	Ref. 12	our data	Ref. 12	Ref. 14	our data	
E (TO/LO)	–	–	75/76	75/76	75	65	–	34/34	36/36	33	X_5
B_2 (TO/LO)	–	–	259/284	95/95	95	–	–	65/66	65/65	65	W_4
B_1	–	–	138	116	–	–	–	54	125	–	W_2
E (TO/LO)	–	–	95/98	147/147	145/145	92	–	95/95	96	96	W_4
E (TO/LO)	156/160	158/160	147/167	167/167	166/166	161/166	160/164	157/160	160/161	160	W_3
B_1	–	–	203	238	–	–	–	190	–	190	X_3
E (TO/LO)	262/276	256/276	260/278	273/283	260/277	226/232	224/230	226/232	213/224	214/224	X_5
B_2 (TO/LO)	262/281	260/280	339/369	286/288	262/278	222/237	215/236	212/238	213/215	212/220	W_2
A_1	–	–	312	312	312	–	–	295	293	294	W_1
E (TO/LO)	332/352	330/350	335/352	332/352	332/352	325/349	324/346	324/349	–	325/348	W_4
B_1	–	–	243	401	–	–	–	334	–	–	W_2
B_2 (TO/LO)	363/384	362/390	371/402	367/393	366/393	370/396	368/292	367/399	367	366/398	Γ_{15}
E (TO/LO)	368/401	366/401	365/387	367/385	365/386	367/399	365/397	368/398	392	365/392	Γ_{15}

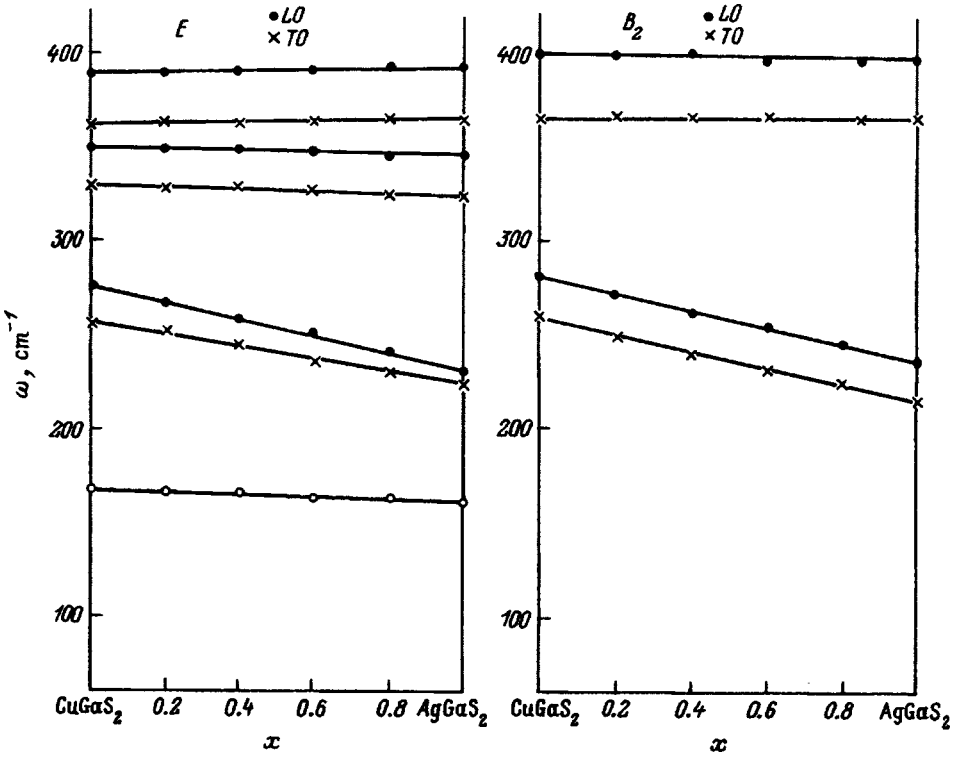

FIG. 1. Concentration dependences of the optical phonon frequencies for solid solutions of $Cu_xAg_{1-x}GaS_2$, determined from the IR reflectance spectra.

polarization measurements, a Glan prism was placed directly in front of the sample. The direction of the plane of polarization was varied by means of a half-wave plate. The spectral slit width during the measurements did not exceed 2 cm^{-1}.

Four reflectance bands are present in the reflectance spectra in the $\mathbf{E}\perp\mathbf{C}$ polarization for both the compounds and the solid solutions. At the same time, five bands (with three being possible according to the selection rules) are present in the $\mathbf{E}\|\mathbf{C}$ spectra. The appearance of ''superfluous'' bands in this polarization is associated with the fact that the reflectance spectra are recorded (as indicated above) from the (112) plane, which makes an angle of 35.3° with the optical axis. This has the result that the $\mathbf{E}\|\mathbf{C}$ polarization is only partially accomplished (about 66%), and therefore attenuated bands from the $\mathbf{E}\perp\mathbf{C}$ polarization spectra can be present in the spectra of this polarization.[8–10] The frequencies of the optical phonons and their symmetry for the ternary compounds are given in Table I.

The recorded spectra were processed by the method of sequential DA–K–K analysis, which possesses smaller errors than the dispersion analysis (DA) method or the Kramers–Kronig (K–K) method separately. In the DA–K–K method, Kramers–Kronig analysis is applied not to the function $R(\omega)$ itself, but to a function whose values are close to zero beyond the limits of the experimental interval.[11] Such a function is obtained after processing the reflectance spectra by the DA method, in which $\varepsilon(\omega)$ is obtained from

$$\varepsilon(\omega)=\frac{\varepsilon_\infty\Pi(\omega_{l,n}-\omega^2+i\omega\cdot g_{l,n})}{(\omega_{t,n}^2-\omega^2+i\omega g_{t,n})}. \tag{1}$$

This equation was used to determine the frequencies of the longitudinal ($\omega_{l,n}$) and transverse ($\omega_{t,n}$) phonons and the damping coefficients ($g_{l,n}$;$g_{t,n}$), as well as ε_∞.

The relations

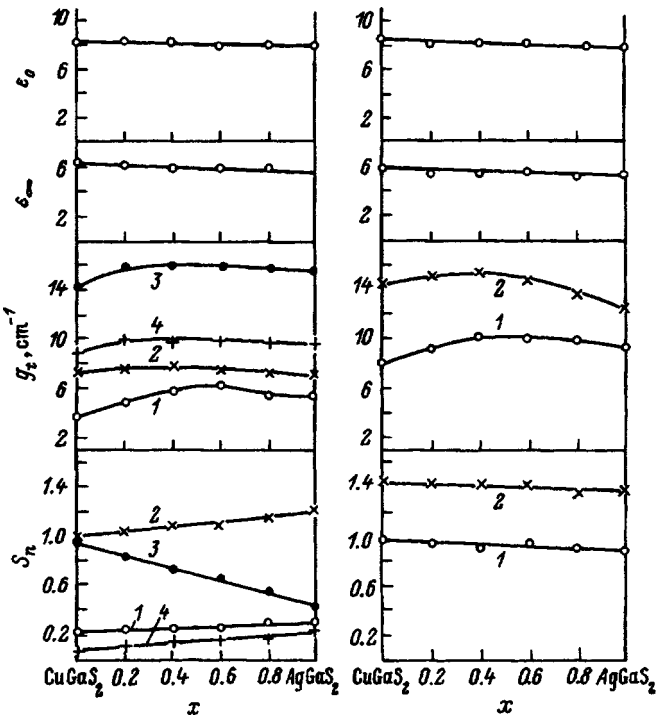

FIG. 2. Concentration dependences of the IR intensity S_2, the damping coefficients g_t, and the permittivities ε_∞ and ε_0.

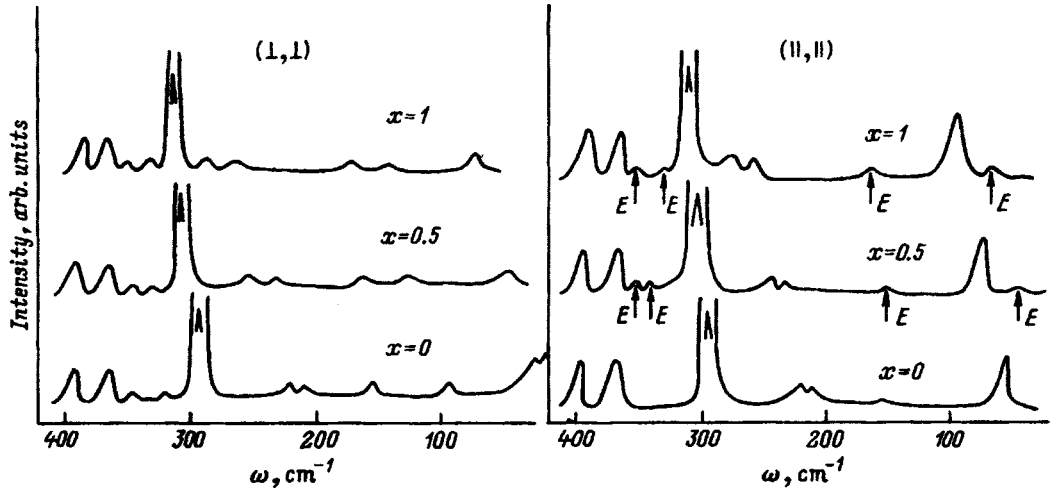

FIG. 3. Raman spectra of the compounds $CuGaS_2$ and $AgGaS_2$ and the solid solution $Cu_{0.5}Ag_{0.5}GaS_2$ in the $(\perp,\perp)$ and $(\parallel,\parallel)$ polarizations.

$$S_n=\frac{\varepsilon_\infty}{4\pi(\omega_{l,n}^2/\omega_{t,n}-1)}, \tag{2}$$

$$\varepsilon_0=\varepsilon_\infty+\sum_n 4\pi S_n \tag{3}$$

were used to calculate the IR intensities S_n and the permittivity ε_0.

Figures 1 and 2 show how the values of the parameters obtained by means of DA, combined with K–K analysis, depend on the composition of the solid solutions. It can be seen from Fig. 1 that, as the concentration of silver atoms in the $Cu_xAg_{1-x}GaS_2$ solid solutions increases, the variations of the frequencies of the optical phonons for both polarizations have a monotonic character—they smoothly shift toward lower frequencies. Parameters S_n, ε_0, and ε_∞ exhibit a similar character. The concentration dependence of the damping coefficients g_t for all the reflectance bands has a nonadditive character.

The Raman spectra of the compounds $CuGaS_2$ and $AgGaS_2$ and the solid solution $Cu_{0.5}Ag_{0.5}GaS_2$ are shown in Fig. 3, and the frequencies of the optical phonons and their symmetry for the ternary compounds are listed in Table I. The presence of superfluous bands in the $(\parallel,\parallel)$ geometry is associated with the causes indicated above. The most intense bands, with $\omega=312\ \mathrm{cm}^{-1}$ for $CuGaS_2$ and $\omega=294\ \mathrm{cm}^{-1}$ for

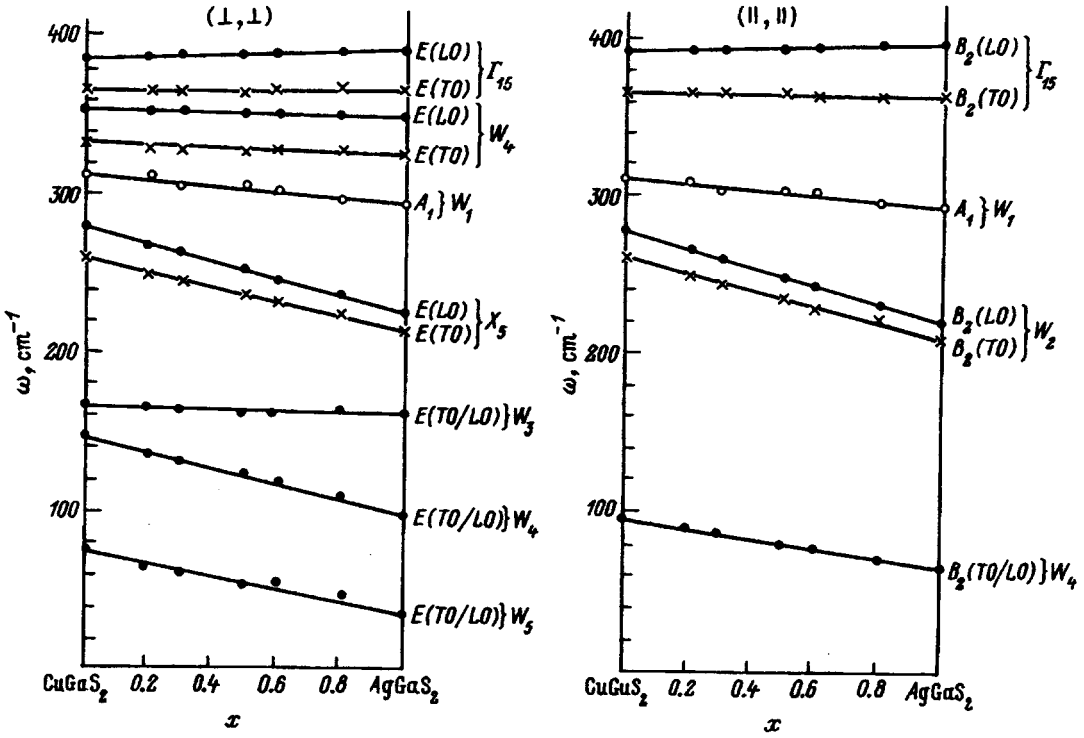

FIG. 4. Concentration dependences of the optical phonon frequencies for the solid solutions $Cu_xAg_{1-x}GaS_2$, determined from the Raman spectra.

$AgGaS_2$, which correspond to vibrations with A_1 symmetry, are present in both polarizations, which is attributable to the causes described above and to the very large scattering cross section of phonons of the given symmetry. Similar bands appear in the $Cu_xAg_{1-x}GaS_2$ solid solutions.

The bands for the solid solutions were identified by comparing them with the IR reflectance spectra and the Raman spectra of the ternary compounds $CuGaS_2$ and $AgGaS_2$. The most intense band in the solid solutions (as in the compounds $CuGaS_2$ and $AgGaS_2$) is the band corresponding to the vibration of symmetry A_1. This purely anionic band corresponds to vibrations of the sulfur atoms, with the other atoms fixed. As the composition varies, its frequency smoothly varies from $312\,cm^{-1}$ in $CuGaS_2$ to $294\,cm^{-1}$ in $AgGaS_2$, while the intensity remains virtually constant (Fig. 4).

A comparison of the IR reflectance spectra and the Raman spectra of the solid solutions with the spectra of the II–VI binary analogs and the frequency position of the corresponding bands makes it possible to conclude that the high-frequency E and B_2 modes, corresponding to the Γ_{15} modes of the sphalerite structure, are determined by the vibrations of the Ga–S bond, since their frequency position varies weakly with increasing concentration of the silver atom in the solid solutions. The intensity of these bands does not change in this case.

The low-frequency bands of the E and B_2 modes, which correspond to the X_5, W_4, and W_2 modes of the sphalerite structure, are the most sensitive to the substitution of silver atoms for copper atoms. Their frequencies vary smoothly with composition x from frequencies characteristic of $CuGaS_2$ to frequencies characteristic of the compound $AgGaS_2$, with constant intensity. It follows from what has been said that the indicated modes correspond to vibrations of the Cu–(Ag)–S bond. The other modes $E(X_s)$ and $B_2(W_4)$ are caused by vibrations of the S, Cu, and Ag atoms.

Thus, the studies presented here have shown that the optical vibrations in solid solutions of $Cu_xAg_{1-x}GaS_2$ manifest a single-mode behavior.

[1] J. L. Shay and J. H. Wernick, *Ternary Chalcopyrite Semiconductors: Growth, Electronic Structure and Applications* (New York, 1975).
[2] I. T. Bodnar and I. V. Bodnar, Phys. Status Solidi A **121**, K247 (1990).
[3] V. Yu. Rud', Yu. V. Rud', I. V. Bodnar', and L. G. Berezutskiĭ, Fiz. Tekh. Poluprovodn. **28**, 2014 (1994) [Semiconductors **28**, 1109 (1994)].
[4] V. V. Badikov, I. N. Matveev, S. M. Pshenichnikov *et al.*, Kristallografiya, **26**, 537 (1981) [Sov. Phys. Crystallogr. **26**, 304 (1981)].
[5] J. P. Laurenti, J. Appl. Phys. **56**, 2479 (1984).
[6] J. P. Kaminov, E. Buchler, and J. H. Wernick, Phys. Rev. B **2**, 960 (1970).
[7] I. V. Bodnar' and E. A. Kudritskaya, Neorg. Mater. **33**, 408 (1997).
[8] N. Yamamoto and T. Miyauchi, Bull. Univ. Osaka Prefect. A **23**, 147 (1974).
[9] I. V. Bodnar', A. G. Karoza, G. F. Smirnova, and T. V. Smirnova, Zh. Prikl. Spektrosk. **53**, 677 (1990).
[10] I. V. Bodnar', Fiz. Tekh. Poluprovodn. **31**, 49 (1997) [Semiconductors **31**, 41, (1997)].
[11] V. M. Burlakov, D. F. Rzaev and V. N. Pyrkov, Preprint, Institute of Spectroscopy, Acad. Sci. USSR (Troitsk, 1984).
[12] W. H. Koschel, F. Sorger, and Y. Baars, J. Phys. (Paris) **36**, 177 (1975).
[13] J. P. Van der Zeil, A. E. Meixner, H. M. Kasper, and J. A. Ditzenberger, Phys. Rev. B **9**, 4286 (1974).
[14] C. Carlone, D. Olego, A. Yayarama, and M. Cardona, Phys. Rev. B **22**, 3877 (1980).

Translated by W. J. Manthey

Analysis of capacitance-relaxation signals consisting of several exponentials

L. S. Berman

A. F. Ioffe Physicotechnical Institute, Russian Academy of Sciences, 194021 St. Petersburg, Russia
(Submitted November 17, 1997; accepted for publication November 18, 1997)
Fiz. Tekh. Poluprovodn. **32**, 688–689 (June 1998)

A new method has been developed for separating a signal consisting of several exponentials into its separate components. Modeling has been carried out for two exponentials with close-lying time constants and with amplitudes of the same order of magnitude. The method possesses high resolution. © *1998 American Institute of Physics.* [S1063-7826(98)01106-5]

Capacitance spectroscopy, in particular, the deep level transient spectroscopy (DLTS) method of Ref. 1, is currently widely used to determine the parameters of deep-level centers (DLCs) in semiconductors. This method has been developed in detail for the case of exponential time dependence of capacitance relaxation $\Delta C(t)$; however, this dependence can differ from exponential dependence for several reasons.[2] Thus, when several DLCs with close-lying thermal emission rates are present, the $\Delta C(t)$ dependence is described by a sum of exponentials with close-lying time constants, while the DLTS peaks blend into one peak. A number of methods for processing the results of the measurements have been proposed to separate this sum into separate components.

a) Measurement of the DLTS spectra at different time and/or temperature intervals and the approximation of these spectra by the optimal choice of the parameters.[3–6] When these methods are used, it is possible for the parameters to be determined ambiguously because of their large number. The multipoint correlation method of Ref. 7 is very sensitive even to small noise and measurement errors.

b) Methods based on recording and analyzing the time dependences of the capacitance at different temperatures, $C(t,T)$. They are more informative and reliable. The method of direct search[8,9] and iterative methods[8,10] can be used to obtain the correct results if the starting parameters are close to the true ones; otherwise, it is possible to determine a local minimum of the variance that corresponds to values of the parameters far from the true ones, or the series of iterations can diverge. The Fourier transformation for two exponentials[11,12] gives significant error even for a small noise level.

In this paper, we model a $\Delta C(t)$ dependence that consists of two exponentials with close-lying time constants and amplitudes of the same order of magnitude for the case of two DLCs with identical ionization energies and with majority-carrier capture cross sections of the same order of magnitude, with these capture cross sections having the same temperature dependence. The ratio of the thermal emission rates for these DLCs is independent of temperature, and therefore the choice of the measurement temperature does not make it possible to improve the resolution. Both experimental error and noise are taken into account in the modeling. The capacitance relaxation is modeled by

$$\Delta C_m(t)=[A_{1m}\exp(-e_{1m}t)+A_{2m}\exp(-e_{2m}t)](1-k_3)+(A_{1m}+A_{2m})[k_2\pm k_1+2k_4(RND-0.5)], \quad (1)$$

where A_{1m}, A_{2m}, e_{1m}, and e_{2m} are, respectively, the amplitude and rate of the thermal emission for the first and second transition processes, and the subscripts m correspond to the parameters of the model.

The error in measuring the capacitance relaxation is modeled by factor k_1. The capacitance can be measured with high accuracy, but the relative error in measuring the amplitude of the capacitance relaxation $\Delta C(0)$ exceeds the relative error of measuring the capacitance itself by a factor of $2N_d/(N_{t1}+N_{t2})$. Here N_d, N_{t1}, and N_{t2} are, respectively, the concentrations of the dopant and of the two DLCs.

For several exponentials with close-lying time constants, it is possible to choose a measurement regime (temperature, period of the filling pulses) for which steady-state filling of the DLCs is established in a time of the order of several time constants of the process. Multiple measurement and averaging of the results makes it possible to eliminate the constant component of the capacitance, and therefore it is modeled by the factor $k_2 \gtrless 0$; the value k_2 is chosen from the same considerations as is the value of k_1 [the capacitance-measurement error, multiplied by the ratio $2N_d/(N_{t1}+N_{t2})$].

Moreover, the measured capacitance of the diode is less than the barrier capacitance of the p–n transition because of the presence of resistance in the base of the diode. With $\tan\delta<0.1$, this methodological error is of the order of $(\tan\delta)^2$, where $\tan\delta$ is the tangent of the loss angle,[13] and it is modeled by the factor $(1-k_3)$. The white noise is modeled by the factor $2k_4(RND-0.5)$, where RND is a random set of numbers in the interval from 0 to 1. The smoothing of the errors and the noise (but not of the constant part of the capacitance) is modeled by multiple repetition of the transition process and averaging.

The $\Delta C(t)$ dependence is approximated by

$$\Delta C_a(t)=A_{1a}\exp(-e_{1a}t)+A_{2a}\exp(-e_{2a}t), \quad (2)$$

where the subscript a corresponds to the approximation parameters.

We used the recursive sequence method (RSM),[14] which is a modification of the method of moments (MM).[15,16] Both methods use a sequence of values of the transition process

TABLE I.

I. $k_1=2\times10^{-4}$, $k_2=2\times10^{-4}$, $k_3=10^{-2}$, $k_4=10^{-3}$

A_{1m}	A_{1a}		e_{1m}	e_{1a}		A_{2m}	A_{2a}		e_{2m}	e_{2a}	
	1	2		1	2		1	2		1	2
5	4.997	5.006	2	1.994	1.995	10	9.856	9.851	1	0.997	0.997
5	5.390	5.386	2	1.974	1.974	10	9.462	9.466	1.4	1.386	1.386
5	4.950	4.968	2	2.000	2.000	10	9.899	9.901	0.5	0.499	0.500

II. $k_1=2\times10^{-3}$, $k_2=2\times10^{-3}$, $k_3=10^{-2}$, $k_4=10^{-2}$

A_{1m}	A_{1a}		e_{1m}	e_{1a}		A_{2m}	A_{2a}		e_{2m}	e_{2a}	
	1	2		1	2		1	2		1	2
5	5.355	5.312	2	1.970	1.972	10	9.526	9.574	1	0.976	0.979
5	4.955	4.990	2	2.007	1.994	10	9.927	9.981	0.5	0.496	0.498

III. $k_1=2\times10^{-2}$, $k_2=2\times10^{-2}$, $k_3=10^{-2}$, $k_4=0.1$

A_{1m}	A_{1a}		e_{1m}	e_{1a}		A_{2m}	A_{2a}		e_{2m}	e_{2a}	
	1	2		1	2		1	2		1	2
5	5.456	5.218	2	2.094	2.090	10	9.734	10.134	0.5	0.462	0.469

Note: 1—The recursive-sequence method; 2—the Newton–Raphson method.

equally spaced in time, but RSM starts from a finite number of these values; this eliminates the error of the MM caused by cutting out the slow part of the process. In the absence of measurement errors and noise, the RSM makes it possible to determine the parameters with an error of only the computer itself. An automatic program has been written for the calculations. From 120 to 160 $\Delta C_m(t)$ values were used in the interval $0\leqslant t\leqslant t_1$, where t_1 was determined from the condition $\Delta C_m(t_1)\simeq 0.4\Delta C(0)$. The results obtained by the RSM were refined by the Newton–Raphson method.[9–11] Typical results of the modeling are shown in Table I. An analysis of these results makes it possible to make the following conclusions:

(1) The recursive sequence method has high resolution.
(2) For the given sensitivity of the measurement apparatus and when the inequality $N_{t1}+N_{t2}\ll N_d$ is satisfied, the resolution of the method is improved as the ratio $(N_{t1}+N_{t2})/N_d$ and/or the ratio e_1/e_2 increases.
(3) Refining the results by the Newton–Raphson method does not substantially improve the approximation. In some cases, the approximation is degraded (although not significantly). The minimum variance does not always exactly correspond to the best approximation.

[1] D. V. Lang, J. Appl. Phys. **45**, 3023 (1974).
[2] L. S. Berman and A. A. Lebedev, *Deep-Level Capacitance Spectroscopy in Semiconductors* (Nauka, Leningrad, 1981).
[3] R. Langfeld, Appl. Phys. A **44**, 107 (1987).
[4] I. Thurzo, D. Pogany, and K. Gmucova, Solid-State Electron. **35**, 1737 (1992).
[5] T. R. Hanak, R. K. Ahrenkiel, and M. L. Timmons, J. Appl. Phys. **67**, 4126 (1990).
[6] H. K. Kim, T. E. Schlesinger, and A. G. Milnes, J. Electron. Mater. **17**, 187 (1988).
[7] K. Dmowski, J. Appl. Phys. **71**, 2259 (1992).
[8] D. M. Himmelblau, *Process Analysis by Statistical Methods* (Wiley, New York, 1970; Mir, Moscow, 1973).
[9] B. Bandi, *Optimization Methods* (Mir, Moscow, 1988).
[10] E. N. L'vovskiĭ, *Statistical Methods of Constructing Empirical Formulas* (Vysshaya Shkola, Moscow, 1988).
[11] M. Okuyama and H. Tanakura, and Y. Hamakawa, Solid-State Electron. **26**, 689 (1983).
[12] S. Weiss and R. Kassing, Solid-State Electron. **31**, 1733 (1988).
[13] L. S. Berman, *Purity control of semiconductors by the method of capacitance transient spectroscopy* (ELIS, St. Petersburg, 1995), p. 114.
[14] A. I. Makushevich, *Recursive Sequences* (Nauka, Moscow, 1975), p. 46.
[15] P. D. Kirchner, V. J. Schaff, G. N. Naracas, L. F. Eastmen, T. J. Chappel, and C. M. Ransom, J. Appl. Phys. **52**, 6462 (1981).
[16] K. Ikossi-Anastasiou and K. P. Roenker, J. Appl. Phys. **61**, 182 (1987).

Translated by W. J. Manthey

Charge-transfer theory in polycrystalline semiconductors with deep impurity centers

K. M. Doshchanov

Physicotechnical Institute, Fizika–Solntse Scientific Manufacturing Organization, Uzbekistan Academy of Sciences, 700084 Tashkent, Uzbekistan

(Submitted June 11, 1996; accepted for publication December 16, 1997)
Fiz. Tekh. Poluprovodn. **32**, 690–696 (June 1998)

This paper discusses the static and dynamic properties of charge transfer through electrically active grain boundaries in polycrystalline semiconductors with deep impurity centers in the bulk of the grains. The admittance of the grain boundary is computed as a function of frequency and applied dc bias U_b. When $U_b \neq 0$, the admittance is mainly controlled by charge-exchange processes of the intergrain boundary states and to an insignificant extent by the charge exchange of deep traps in the bulk of the semiconductor. The application of this theory to the spectroscopy of intergrain boundary states is considered. © *1998 American Institute of Physics.* [S1063-7826(98)01206-X]

INTRODUCTION

The theory of charge transfer in polycrystalline semiconductors has been developed in a number of papers.[1–14] It follows from the results obtained in Ref. 12 that deep levels (deep traps) in the bulk of the grains have an appreciable effect on the static and dynamic characteristics of the conductivity. However, the theory of Ref. 12 is based on a thermoelectron-emission model[2,3] with a rather limited region of application (see Refs. 6–8). The generalized theory of Ref. 13 on the conductivity of polycrystals, which combined earlier models[1–8] based on successively taking into account the effect of grain boundaries on charge transfer, has a significantly broader region of application. Based on the theory of Ref. 13, this paper develops a new approach to the calculation of the static and dynamic characteristics of the conductivity of polycrystalline semiconductors with deep impurity centers.

As is well known, the spectroscopy of intergrain boundary states (BSs), based on measurement of the admittance, is an effective way to study the electronic properties of grain boundaries.[12] The theoretical basis of this method was developed in Refs. 9–12 in terms of a model of thermoelectron emission was proposed in Ref. 14. Another method of calculating the admittance of a polycrystal. In our opinion, it provides a more effective way to solve the problem of BS spectroscopy. The deep levels associated with background impurities in the bulk of the grains were disregarded in Ref. 14, and this substantially limits the possibility of using the results obtained there. One of the goals of this paper is to eliminate this limitation.

1. BASIC RELATIONS

Let us consider a one-dimensional model of a polycrystalline semiconductor—a chain of identical bicrystals with *n*-type conductivity of the grains and acceptor BSs. Along with shallow donors, let there be deep centers of both donor and acceptor type in the bulk of the grains, forming *n* levels of energy E_ν ($\nu = 1, 2, 3, \ldots, n$; $E_c - E_\nu < E_c - E_{\nu+1}$) in the band gap. Electron capture on the BS levels results in band bending close to the grain boundaries (which causes the formation of intercrystallite barriers). As in Ref. 12, we assume that the grain size significantly exceeds the width of the intercrystallite barrier; i.e., we exclude the possibility of complete consolidation of the grains.[1,13] Figure 1 shows the energy diagram of one of the bicrystals of the chain.

In what follows, we shall study the regularities of charge transfer in the model polycrystal described above when an ac voltage of

$$U(t) = U_0 + \tilde{U}\exp(i\omega t) \tag{1}$$

is applied to each of its grains, where U_0 is the dc bias, and $\tilde{U}$ and ω are the small-signal amplitude and frequency ($e\tilde{U} \ll kT$, where e is the absolute magnitude of the charge of the electron, T is the absolute temperature, and k is Boltzmann's constant). We assume that $\omega\tau_M \ll 1$, where $\tau_M = \varepsilon_0\varepsilon/(e\mu_m n_0)$ is the Maxwell relaxation time in the quasi-neutral regions of the crystal, n_0 and μ_n are the electron concentration and mobility in the bulk of the grains, and $\varepsilon_0\varepsilon$ is the absolute permeability. This condition makes it possible to determine Poisson's equation in the Schottky approximation:

$$\frac{\partial \mathcal{E}(x,t)}{\partial x} = \frac{\rho(x,t)}{\varepsilon_0\varepsilon}, \tag{2}$$

$$\rho(x,t) = \begin{cases} eN_0 + \sum_{\nu=1}^{n} eN_\nu\,[1 - f_\nu(x,t)], & \\ -l_2(t) < x + \delta < 0, & 0 < x < l_1(t), \\ 0, \quad x + \delta \leqslant -l_2(t), & x \geqslant l_1(t), \end{cases}$$

where $\rho(x,t)$ is the variable density of the volume charge in the bicrystals; $N_0 = N_d - N_A$, N_d is the concentration of totally ionized shallow donors, N_A is the total density of deep levels of acceptor type; N_ν is the density of energy level E_ν; $f_\nu(x,t)$ is the nonsteady-state distribution function of electrons on level E_ν; $l_1(t)$ is the variable width of the depletion

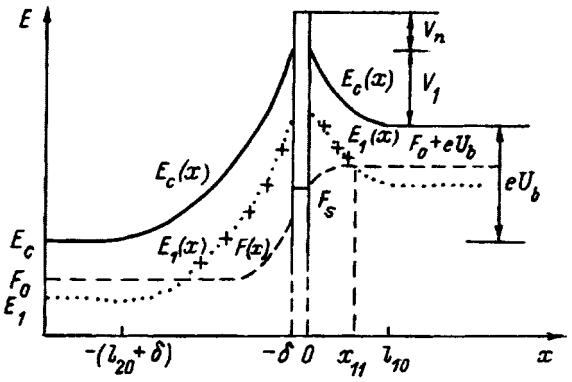

FIG. 1. Energy level diagram of a bicrystal. E_1 is a deep energy level of donor type, V_n is the height of the scattering barrier of the grain boundary,[13] and V_1 is the height of the intercrystal barrier when dc bias U_b is applied to it.

layer to the right of the boundary, $l_2(t)$ is that to the left of the boundary; and δ is the width of the grain boundary.

The field $\mathcal{E}(x,t)$ satisfies the following boundary conditions: $\mathcal{E}(x,t)=j(t)/(e\mu_n n_0)$ when $x\geqslant l_1(t)$, $x+\delta\leqslant -l_2(t)$,

$$\int_{-l_2(t)-\delta}^{l_1(t)} \mathcal{E}(x,t)dx = U_b(t), \tag{3}$$

$$\mathcal{E}(0,t)-\mathcal{E}(-\delta,t) = -\frac{en_s(t)}{\varepsilon_0\varepsilon}, \tag{4}$$

where $j(t)=j_{dc}+\tilde{j}\exp(i\omega t)$ is the ac current density, (j_{dc} and $\tilde{j}$ will be defined below); $U_b(t)=U(t)-j(t)d/(e\mu_n n_0)$ is the voltage falloff at the intercrystallite barrier; d is grain size, $d\gg l_1(t)+l_2(t)$; and $n_s(t)$ is the variable density of the electrons localized at the grain boundary.

The distribution function $f_\nu(x,t)$ and the conduction-electron concentration $n(x,t)$ in the depletion layers are determined from

$$\frac{\partial f_v(x,t)}{\partial t} = v_0 S_v\left\{ n(x,t)[1-f_v(x,t)] - g_v\, N_c\exp\left(-\frac{E_c-E_v}{kT}\right) f_v(x,t)\right\}, \tag{5}$$

$$\frac{\partial n(x,t)}{\partial x} + \frac{e\mathcal{E}(x,t)}{kT} n(x,t) = \frac{j(t)}{\mu_n kT}, \tag{6}$$

where v_0 is the mean thermal velocity of the conduction electrons, S_v is the electron-capture cross section at the E_v level, g_v is the degeneracy factor of level E_ν, and N_c is the effective density of states in the conduction band.

Solutions of Eqs. (1), (5), and (6) are sought in the form

$$\mathcal{E}(x,t)=\mathcal{E}(x)+\tilde{\mathcal{E}}(x)\exp(i\omega t),$$

$$f_\nu(x,t)=f_\nu(x)+\tilde{f}_\nu(x)\exp(i\omega t),$$

$$n(x,t)=n(x)+\tilde{n}(x)\exp(i\omega t).$$

We introduce the notation $n(0,t)+n(-\delta,t)=2N_c[\Phi_0+\tilde{\Phi}\exp(i\omega t)]$. The nonsteady-state distribution function of electrons at the BS levels is determined by[14]

$$f_s(E,t)=f(E-F_s) + \frac{\tilde{\Phi} f(E-F_s)[1-f(E-F_s)]\exp(i\omega t)}{\Phi_0[1+i\omega\tau f(E-F_s)]},$$

where $f(E-F_s)$ is the Fermi–Dirac distribution function, $F_s=E_c(0)+kT\ln\Phi_0$ is the position of the Fermi quasilevel at the grain boundary, $\tau=[2v_0S_nN_c\Phi_0]^{-1}$, and S_n is the capture cross section of an electron on a BS level. For $n_s(t)$ we have

$$n_s(t)=\int_{E_v(0)}^{E_c(0)} N(E)f_s(E,t)dE = n_s+\tilde{n}_s\exp(i\omega t), \tag{7}$$

where $N(E)$ is the BS density.

The relations given above make it possible to calculate the admittance of the polycrystal. However, it is first necessary to determine the static characteristics of the conductivity.

2. STATIC CONDUCTIVITY

When a constant voltage U_0 is applied to each grain of the polycrystal, the value of the band bending close to the grain boundaries is determined by

$$V(x)=\begin{cases} e\int_{-l_{20}-\delta}^{x}\mathcal{E}(x')dx', & -l_{20}<x+\delta<0,\\ -e\int_{x}^{l_{10}}\mathcal{E}(x')dx', & 0<x<l_{10}, \end{cases}$$

where l_{10} is the steady-state width of the depletion layer to the right of the boundary, and l_{20} is that to the left of the boundary. It follows from Eq. (3) that $V_2-V_1=eU_b$, where $V_1=V(0)$ is the height of the intercrystal barrier to the right of the boundary, $V_2=V(-\delta)$ is that to the left of the boundary; $U_b=U_0-j_{dc}d/(e\mu_n n_0)$, and j_{dc} is the density of the direct current.

When $\partial f_v(x,t)/\partial t=0$, we find the following expression from Eq. (5):

$$f_v(x)=\frac{n(x)}{n(x)+g_v N_c\exp[-(E_c-E_v)/kT]}. \tag{8}$$

The steady-state electron concentration $n(x)$ is approximated within a sufficient approximation by

$$\frac{n(x)}{n_0}=\begin{cases}(1-b_2)\exp[-z(x)]+b_2, & -l_{20}<x+\delta<0,\\ (1+b_1)\exp[-z(x)]-b_1, & 0<x<l_{10},\end{cases} \tag{9}$$

where $b_{1,2}=j_{dc}/(ev_{d\,1,2}n_0)$; $v_{d1}=-\mu_n\mathcal{E}(0)$ is the effective carrier diffusion rate to the right of the grain boundary, $v_{d2}=\mu_n\mathcal{E}(-\delta)$ is that to the left of the boundary,[13] and $z(x)=V(x)/kT$.

Using Eqs. (8) and (9), the solution of Eq. (2) leads to the expressions

$$\mathcal{E}(0)=\frac{j_{dc}}{e\mu_n n_0}-\frac{kT}{eL_D}[2z_1+2\Psi_1(z_1)]^{1/2}, \tag{10}$$

$$\mathcal{E}(-\delta)=\frac{j_{dc}}{e\mu_n n_0}+\frac{kT}{eL_D}[2z_2+2\Psi_2(z_2)]^{1/2}, \tag{11}$$

$$\Psi_{1,2}(z)=\sum_{v=1}^{n}\frac{a_v\,N_v}{(a_v\mp b_{1,2})N_0}\ln\left[\frac{1\pm b_{1,2}+(a_v\mp b_{1,2})e^z}{1+a_v}\right], \tag{12}$$

where $L_D=\sqrt{\varepsilon_0\varepsilon kT/e^2N_0}$ is the Debye screening length, $z_{1,2}=V_{1,2}/kT$, $a_v=g_v\exp(-\xi_v)$, $\xi_v=(F_0-E_v)/kT$, and $F_0=E_c-kT\ln(N_c/n_0)$. Using the boundary condition given by Eq. (4), we obtain

$$\sqrt{z_1+\Psi_1(z_1)}+\sqrt{z_2+\Psi_2(z_2)}=2\sqrt{z_b}, \tag{13}$$

where $z_b=V_b/kT$, and $V_b=e^2n_s^2/(8\varepsilon_0\varepsilon N_0)$.

In the particular case in which the conditions $b_1\ll a_v\ll 1$ and $a_v\exp(z_1)\gg 1$ are satisfied, we have from Eq. (13) that

$$V_1=\frac{V_b}{1+p_0}\left[1-(1+p_0)\frac{eU_b}{4V_b}\right]^2+\frac{pkT}{1+p_0}, \tag{14}$$

$$p_0=\sum_{v=1}^{n}\frac{N_v}{N_0},\quad p=\sum_{v=1}^{n}\frac{N_v\xi_v}{N_0}.$$

We should point out that Eq. (14) in other notation was obtained in Ref. 12 as a result of rather complex calculations and was regarded as the main formula for the height of the intercrystallite barriers.

For the current density, we have[13]

$$j_{dc}=\frac{ev_0n_0\theta_0}{1+\gamma}e^{-z_1}\left[1-\exp\left(-\frac{eU_b}{kT}\right)\right], \tag{15}$$

where $\theta_0=\overline{D}_n+S_n(N_s-n_s)/2$, $\overline{D}_n$ is the overall transparency of the grain boundary for electrons, N_s is the total BS density, and $\gamma=v_0(1/v_{d1}+1/v_{d2})\theta_0$.

The steady-state electron density on the BS levels is

$$n_s=\int_{E_v(0)}^{E_c(0)}N(E)f(E-F_s)dE. \tag{16}$$

The value of Φ_0 in the expression for quasilevel F_s is determined from Eqs. (9) and (15). Its value is

$$\Phi_0=\frac{j_{dc}(1+\gamma)}{2ev_0\theta_0N_c}\left[\coth\left(\frac{eU_b}{2kT}\right)-\frac{\beta\gamma}{1+\gamma}\right], \tag{17}$$

where $\beta=(v_{d2}-v_{d1})/(v_{d2}+v_{d1})$.

We introduce the function

$$\mathcal{L}_m(z)=L_D\int_0^z[2z'+2\Psi_m(z')]^{-1/2}dz', \tag{18}$$

where $m=0, 1, 2$; functions $\Psi_1(z)$ and $\Psi_2(z)$ are determined by Eq. (12),

$$\Psi_0(z)=\sum_{v=1}^{n}\frac{N_v}{N_0}\ln\left(\frac{1+a_ve^z}{1+a_v}\right).$$

Then $l_{m0}=\mathcal{L}_m(z_m)$, where $m=0, 1, 2$; l_0 is the width of the depletion layer for zero bias, $z_0=V_0/kT$, and V_0 is the equilibrium height of the intercrystal barrier. The quantities l_0, l_{10}, and l_{20} will be needed below in calculating the admittance of a polycrystal.

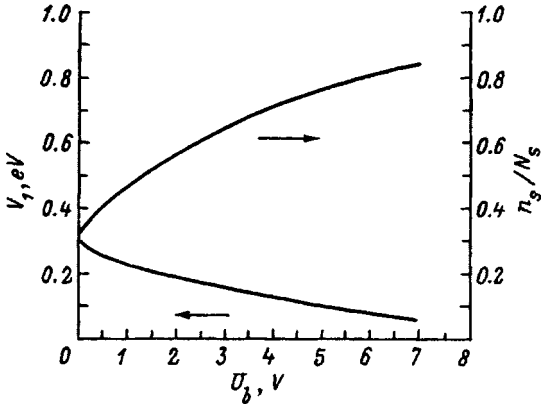

FIG. 2. Height of the intercrystal barrier and the ratio n_s/N_s vs U_b. n_s is the electron density at the grain boundary and N_s is the total BS density.

Equations (13), (15), and (16) form a system of self-consistent equations from which n_s, V_1, and j_{dc} are determined as functions of U_b. Figures 2 and 3 show the results of a numerical calculation of these values in polycrystalline silicon with an oxygen impurity which forms in the band gap two deep levels: $E_c-E_1=0.31$ eV (a donor) and $E_c-E_2=0.38$ eV (an acceptor).[15] The BS density was assumed to have a Gaussian distribution:

$$N(E)=\frac{N_s}{\sqrt{2\pi}\Delta E}\exp\left[-\frac{1}{2}\left(\frac{E-F_s}{\Delta E}\right)^2\right]. \tag{19}$$

The following values were used for the parameters: $\varepsilon=11.8$, $E_g=1.12$ eV, $v_0=10^7$ cm/sec, $\mu_n=521$ cm^2/$(V\cdot s)$, $N_d=6\times10^{15}$ cm^{-2}, $N_s=10^{12}$ cm^{-2}, $\Delta E=0.15$ eV, $F_s-E_v=0.66$ eV, $S_n=10^{-15}$ cm^2, $N_1=N_2=10^{15}$ cm^{-3}, $\overline{D}_n=0.1$, $T=300$ K, and $N_c=2.8\times10^{19}$ cm^{-3}. The electron concentration in the quasi-neutral regions is $n_0\approx N_0=N_d-N_2$.

It can be seen from Fig. 2 that, as the voltage falloff increases, the electron density at the grain boundary increases at the intercrystal barrier. This additional capture of electrons at the BS levels weakens the dependence of barrier

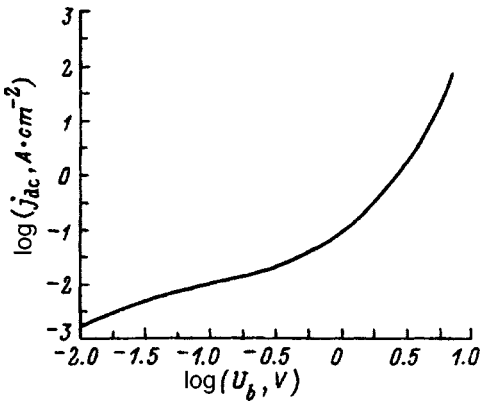

FIG. 3. The I–V characteristic of the grain boundary.

height V_1 on U_b. To completely remove the intercrystal barrier, it is necessary to apply a rather significant voltage to it.

The volt–ampere characteristic (Fig. 3) has three sections: linear, sublinear, and superlinear. The sublinear section corresponds to the compensation regime,[5,13] in which the decrease of the intercrystal barrier by the longitudinal electric field is partly compensated for by additional trapping of electrons on the BS levels. As the BSs fill up, the increase of the electron density at the grain boundary slows down, so that the sublinear dependence transforms to superlinear.

3. ADMITTANCE OF A POLYCRYSTAL

We now consider the solution of the system of Eqs. (2), (5), and (6) for the ac voltage given by Eq. (1). In order to avoid unwieldy expressions, we shall restrict the discussion to the case of $\gamma \ll 1$. It can then be assumed that the quasi-Fermi level $F(x)$ is constant when $z(x)<z_1$, whereas it tracks the bottom of the conduction band when $z_1<z(x)<z_2$ (Fig. 1). In this approximation, we have from Eq. (6) that

$$\tilde{n}(x)=-\frac{\tilde{V}(x)}{kT}n_0\exp[-z(x)], \tag{20}$$

where $\tilde{V}(x)$ is determined by

$$\tilde{V}(x)=\begin{cases} e\int_{-l_{20}-\delta}^{x}\tilde{\mathcal{E}}(x')dx', & -l_{20}<x+\delta<0, \\ -e\int_{x}^{l_{10}}\tilde{\mathcal{E}}(x')dx', & 0<x<l_{10}. \end{cases}$$

Using Eq. (20), we find from Eqs. (2) and (5) that

$$\frac{d\tilde{\mathcal{E}}(x)}{dx}=\begin{cases} \dfrac{e}{\varepsilon_0\varepsilon}\displaystyle\sum_{v=1}^{n}\frac{N_v\delta[z(x)-\xi_v]}{1+i\omega\tau_v}\frac{\tilde{V}(x_v)}{kT}, & z(x)<z_1, \\ 0, & z_1<z(x)<z_2, \end{cases} \tag{21}$$

where $\tau_v=\exp(\xi_v)/[(1+g_v)v_0n_0S_v]$ is the relaxation time of the part of the volume charge associated with the electrons on level E_v, and x_v satisfies the equation $z(x_v)=\xi_v$. Note that τ_v is independent of dc bias U_b. In deriving Eq. (21), we used the approximation $f_v(x)[1-f_v(x)]=\delta[z(x)-\xi_v]$. We have from the boundary conditions given by Eqs. (3) and (4) that

$$\tilde{U}_2-\tilde{U}_1=e\tilde{U}_b, \quad \tilde{\mathcal{E}}_1-\tilde{\mathcal{E}}_1-\tilde{\mathcal{E}}_2=-\frac{e\tilde{n}_s}{\varepsilon_0\varepsilon}, \tag{22}$$

where $\tilde{U}_1=\tilde{U}(0)$, $\tilde{U}_2=\tilde{U}(-\delta)$, $\tilde{U}_b=\tilde{U}-\tilde{j}d/(e\mu_n n_0)$, $\tilde{\mathcal{E}}_1=\tilde{\mathcal{E}}(0)$, and $\tilde{\mathcal{E}}_2=\tilde{\mathcal{E}}(-\delta)$; $\tilde{n}_s$ is the complex amplitude of the vibrations of the electron density on the BS levels [See Eq. (7)].

Solving Eq. (21) with the boundary conditions given by Eq. (22), we find

$$\tilde{\mathcal{E}}_m=\frac{\tilde{U}_b}{L}+(-1)^m\frac{e\tilde{n}_sL_m}{\varepsilon_0\varepsilon L}, \tag{23}$$

$$\tilde{V}_m=(-1)^m\frac{e\tilde{U}_bL_m}{L}+kTA\frac{\tilde{n}_s}{n_s}. \tag{24}$$

Here $m=1,2$; $L=L_1+L_2$; $A=e^2n_sL_1L_2/(\varepsilon_0\varepsilon kTL)$. For complex values of L_1 and L_2 with the dimension of length, we have

$$L_m=l_{m0}-\frac{1}{1+\varkappa}\sum_{v=1}^{n}\frac{r_vl_v\theta(z_1-\xi_v)}{R_v(1+i\omega\tau_v)}, \tag{25}$$

$$\varkappa=\sum_{v=1}^{n}\frac{r_v\theta(z_1-\xi_v)}{R_v(1+i\omega\tau_v)}, \tag{26}$$

where $l_v=\mathcal{L}_0(\xi_v)$, $R_v=L_D\sqrt{2\xi_v+2\Psi_0(\xi_v)}N_0/N_v$, $\theta(\xi)$ is the step function, and the value of r_v satisfies the recursion relation

$$r_v=l_v+\sum_{\mu=1}^{v-1}\frac{r_\mu(l_v-l_\mu)}{R_\mu(1+i\omega\tau_\mu)}.$$

Using Eqs. (20) and (24), it is easy to calculate $\tilde{\Phi}=[\tilde{n}(0)+\tilde{n}(-\delta)]/2N_c$ and then to determine $\tilde{n}_s$ from Eq. (7). As a result, we have

$$\frac{\tilde{n}_s}{n_s}=\frac{\alpha L_1}{(1+\alpha A)L}\frac{e\tilde{U}_b}{kT}\tanh\left(\frac{eU_b}{2kT}\right), \tag{27}$$

$$\alpha=\frac{1}{n_s}\int_{E_v(0)}^{E_c(0)}\frac{N(E)f(E-F_s)[1-f(E-F_s)]dE}{1+i\omega\tau f(E-F_s)}. \tag{28}$$

The complex amplitude of the vibrations of the current density is determined by[14]

$$\tilde{j}=ev_0\theta_0[\tilde{n}(0)-\tilde{n}(-\delta)]+\frac{i\omega\varepsilon_0\varepsilon}{2}(\tilde{\mathcal{E}}_1+\tilde{\mathcal{E}}_2). \tag{29}$$

It can be seen that the resulting relations can be used to determine the admittance $Y_b=\tilde{j}/\tilde{U}_b$ of the grain boundary. The calculations lead to the expressions

$$Y_b=G_1+\frac{i\omega\varepsilon_0\varepsilon}{L}-\frac{ej_{dc}}{kT}\frac{\alpha AL_1}{(1+\alpha A)L}\tanh\left(\frac{eU_b}{2kT}\right), \tag{30}$$

$$G_1=\frac{ej_{dc}}{kT}\frac{L_1}{L}\coth\left(\frac{eU_b}{2kT}\right). \tag{31}$$

The admittance of a polycrystal, calculated per unit area of cross section, is determined by

$$Y=\frac{Y_bd}{(1+Y_bd/e\mu_nn_0)D}, \tag{32}$$

where D is the length of the polycrystal.

As illustrations of the relations obtained here, Figs. 4–6 show the results of a numerical calculation of the conductivity $G(\omega,U_b)=\mathrm{Re}Y_b$ and capacitance $C(\omega,U_b)=\mathrm{Im}Y_b/\omega$ of the grain boundary in polycrystalline silicon with two deep levels in the bulk of the grains. The following values were used for the electron-capture cross sections at deep levels: $S_1=10^{-14}\,\mathrm{cm}^2$ and $S_2=10^{-15}\,\mathrm{cm}^2$. The values of the other parameters are given above.

Figures 4 and 5 show the dependences of the conductivity and capacitance on frequency for various U_b values. It

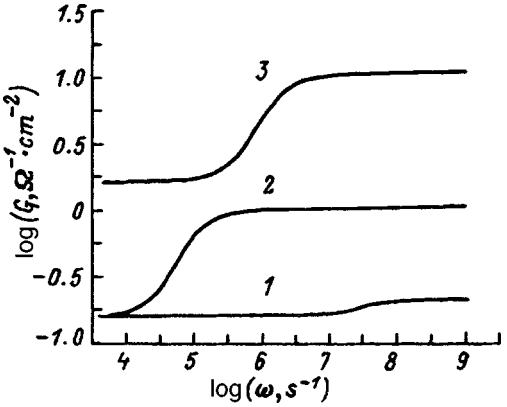

FIG. 4. Conductivity G of the grain boundary vs frequency ω for various U_b, V: *1*—0, *2*—1, *3*—3.

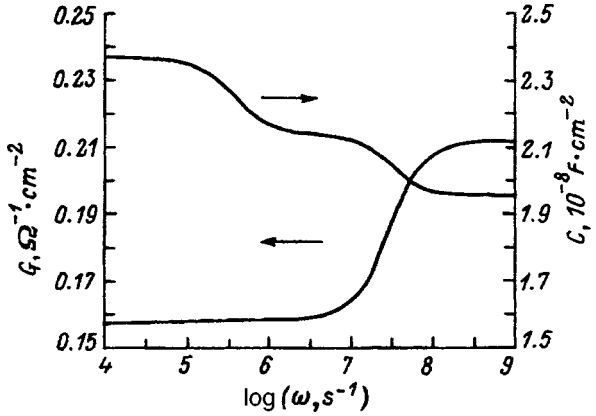

FIG. 6. Conductivity G and capacitance C of the grain boundary vs frequency ω when $U_b=0$ (on an enlarged scale).

can be seen that dispersion caused by relaxation of the charge density at the grain boundary predominates when $U_b\neq 0$. Against the background of this effect, the dispersion associated with the charge exchange of deep impurity centers is barely noticeable.

Figure 6 shows the $G(\omega,0)$ and $C(\omega,0)$ dependences on an enlarged scale. Two resonance frequencies can be clearly distinguished on the curve of the $C(\omega,0)$ dependence: $\omega_1=\tau_1^{-1}\simeq 3\times 10^7\ \mathrm{sec}^{-1}$ and $\omega_2=\tau_2^{-1}\simeq 3\times 10^5\ \mathrm{sec}^{-1}$. However, only one resonance frequency ω_1 can be distinguished on the curve of the $G(\omega,0)$ dependence. This stems from the fact that, when $\omega<10^7\ \mathrm{sec}^{-1}$, the static conductivity is $G_1(U_b=0)\gg\omega\mathrm{Im}(\varepsilon_0\varepsilon/L)$.

It thus follows from these results that, when $U_b\neq 0$, the admittance of the grain boundary is controlled mainly by charge-exchange processes of the BSs. Effects associated with the charge exchange of the deep levels in the bulk of the grains are relatively small and become appreciable only for $U_b=0$, when charge exchange of the BSs is absent. However, one important circumstance should be pointed out. The last term in Eq. (30), which determines the influence of charge exchange of the BSs on the admittance of the grain boundary, itself depends (via the value of A) on the charge exchange of the deep traps in the bulk of the grains; i.e., ''mixing'' of these processes occurs.[12] Therefore, in determining the BS spectrum from admittance measurements, it is necessary to take into account both the charge exchange of the BSs and the charge exchange of the deep traps in the bulk of the grains.

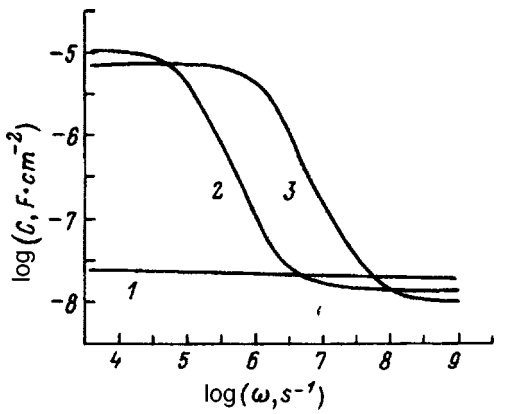

FIG. 5. Capacitance C of the grain boundary vs frequency ω for various U_b, V: *1*—0, *2*—1, *3*—3.

4. SPECTROSCOPY OF THE BOUNDARY STATES

Let us find relations that allow us to determine the density of the BSs from the measured static and dynamic characteristics of the conductivity of a polycrystalline semiconductor with deep impurity centers in the bulk of the grains. We assume in this case that the values of the parameters d, n_0 and μ_n are known. Then, using Eq. (32), it is easy to calculate the conductivity and capacitance of the grain boundary from the measured values of $\mathrm{Re}\,Y$ and $\mathrm{Im}\,Y$. Therefore, it is sufficient to find relations that determine the explicit dependence of $N(E)$ on $G(\omega,U_b)$, $C(\omega,U_b)$, j_{dc}, and $U_b=U_0-j_{dc}d/(e\mu_n n_0)$.

As in Ref. 14, we use the approximation $f(E-F_s)\times[1-f(E-F_s)]=kT\delta(E-F_s)$ to compute the integral in Eq. (28). Then

$$\alpha=\frac{N(F_s)kT}{n_s}\frac{2}{2+i\omega\tau},$$

where $N(F_s)$ is the density of BSs at the Fermi quasilevel.

It follows from Eqs. (25) and (26) that, when $\omega\tau_v\ll 1$, it is possible to set $L_1=l_{10}-\Delta l$ and $L_2=l_{20}-\Delta l$, where Δl is a real quantity. If the number of deep levels intersecting the Fermi quasilevel $F(x)$ is conserved as U_b varies, then Δl is independent of the dc bias. When $U_b=0$, the low-frequency capacitance of the grain boundary is $C_0=\varepsilon_0\varepsilon/2(l_0-\Delta l)$. We thus find

$$\Delta l=\frac{\varepsilon_0\varepsilon}{2}\left[\frac{1}{C_{HF}(0)}-\frac{1}{C_0}\right], \tag{33}$$

where $C_{HF}(0)=\varepsilon_0\varepsilon/2l_0$ is the high-frequency capacitance of the grain boundary when $U_b=0$.

Assuming in Eq. (30) that $\omega=0$, we find

$$P_{dc}=\frac{l_{10}-\Delta l}{l_{10}+l_{20}-2\Delta l}\left[\coth\left(\frac{eU_b}{2kT}\right)-\frac{A_1}{1+A_1}\tanh\left(\frac{eU_b}{2kT}\right)\right], \tag{34}$$

$$A_1=\frac{e^2N(F_s)}{\varepsilon_0\varepsilon}\frac{(l_{10}-\Delta l)(l_{20}-\Delta l)}{l_{10}+l_{20}-2\Delta l}, \tag{35}$$

where $P_{dc}=kTG_{dc}(U_b)/ej_{dc}$; $G_{dc}(U_b)$ is the low-frequency ($\omega\tau_v\ll 1$, $\omega\tau\ll 1$) conductivity of the grain boundary.

We introduce the notation

$$P_{HF}=\frac{kT}{ej_{dc}}\left\{G_{HF}(U_b)-\frac{C_{HF}^2(U_b)}{C_{HF}^2(0)}[G_{HF}(0)f-G_{dc}(0)]\right\},$$

where $G_{HF}(U_b)$ is the high-frequency conductivity of the grain boundary, and $C_{HF}(U_b)=\varepsilon_0\varepsilon/(l_{10}+l_{20})$ is the high-frequency capacitance of the grain boundary. When $\omega\tau_v\gg 1$ and $\omega\tau\gg 1$, we find from (30) that

$$P_{HF}=\frac{l_{10}}{l_{10}+l_{20}}\coth\left(\frac{eU_b}{2kT}\right).$$

The last expression is used to express l_{10} and l_{20} in terms of experimentally determined values:

$$l_{10}=\frac{\varepsilon_0\varepsilon}{C_{HF}(U_b)}P_{HF}\tanh\left(\frac{eU_b}{2kT}\right), \tag{36}$$

$$l_{20}=\frac{\varepsilon_0\varepsilon}{C_{HF}(U_b)}\left[1-P_{HF}\tanh\left(\frac{eU_b}{2kT}\right)\right]. \tag{37}$$

It can be seen that Eqs. (34) and (35) connect the density of BSs at the Fermi quasilevel with experimentally determined values; i.e., they are the relations that we are seeking. When $eU_b\gg kT$, we find from Eqs. (33)–(37) the relation

$$N(F_s)=\frac{C_{HF}(U_b)}{e^2}\frac{P_{HF}-\varphi-(1-2\varphi)P_{dc}}{P_{dc}(P_{HF}-\varphi)(1-\varphi-P_{HF})}, \tag{38}$$

where $\varphi=C_{HF}(U_b)[C_{HF}^{-1}(0)-C_0^{-1}]/2$. The position of the Fermi quasilevel at the grain boundary can be expressed in terms of the steady-state current density: $F_s=E_c(0)-kT\ln(2ev_0N_c\theta_0/j_{dc})$ when $eU_b\gg kT$ [see Eq. (17) when $\gamma\ll 1$]. The numerical value of parameter θ_0 can be determined by studying the static conductivity.

It is also possible to obtain from Eq. (30) the following relation for the cross section for capture of an electron at a BS level:

$$S_n=\frac{e^2\theta_0(1-2\varphi)P_{dc}[P_{HF}-\varphi-(1-2\varphi)P_{dc}]}{2kT[(1-2\varphi)C(0,U_b)-C_{HF}(U_b)](P_{HF}-\varphi)}, \tag{39}$$

where $C(0,U_b)$ is the capacitance of the grain boundary when $\omega\tau\ll 1$ and $\omega\tau_v\ll 1$.

The accuracy of Eqs. (38) and (39) can be estimated using the results of a numerical calculation of j_{dc}, $G(\omega,U_b)$ and $C(\omega,U_b)$ given above. Such an estimate shows that, when $U_b<3$ V, neglecting the charge exchange of the deep traps in the bulk of the grains results in an appreciable error in determining $N(F_s)$ and S_n. When $U_b>3$ V, this error is negligible; i.e., it is possible to set $P_{HF}=kTG_{HF}(U_b)/(ej_{dc})$, $\varphi=0$ in Eqs. (38) and (39).

CONCLUSIONS

In this paper I developed the most complete theory of the static and dynamic conductivity of polycrystalline semiconductors, which takes into account not only the features of charge transfer through the grain boundaries but also the influence on this process of deep traps in the bulk of the grains. The application of this theory to the spectroscopy of intergrain BSs gives extremely simple relations which connect the density of the BSs at the Fermi quasilevel and the cross section for capture of the majority carriers at the BS levels with the measured static and dynamic characteristics of the conductivity.

[1] J. Y. W. Seto, J. Appl. Phys. **46**, 5247 (1975).
[2] C. H. Seager and T. G. Castner, J. Appl. Phys. **49**, 3879 (1978).
[3] G. E. Pike and C. H. Seager, J. Appl. Phys. **50**, 3414 (1979).
[4] E. I. Gol'dman and A. G. Zhdan, Fiz. Tekh. Poluprovodn. **10**, 1839 (1976) [Sov. Phys. Semicond. **10**, 1098 (1976)].
[5] E. I. Gol'dman, A. G. Zhdan, and V. N. Nemenushchiĭ, Fiz. Tekh. Poluprovodn. **12**, 833 (1978) [Sov. Phys. Semicond. **12**, 491 (1978)].
[6] N. C. C. Lu, L. Gergberg, C. Y. Lu, and J. D. Meindl, IEEE Trans. Electron Devices **ED-30**, 137 (1983).
[7] G. C. McGonigal, D. J. S. Thomson, J. G. Shaw, and H. C. Gard, Phys. Rev. B **28**, 5908 (1983).
[8] S. N. Singh, R. Kishore, and P. K. Singh, J. Appl. Phys. **57**, 2793 (1985).
[9] C. H. Seager and G. E. Pike, Appl. Phys. Lett. **37**, 747 (1980).
[10] G. E. Pike, Phys. Rev. B **30**, 795 (1984).
[11] J. Werner and H. Strunk, J. Phys. C **1**, 89 (1982).
[12] G. Blatter and F. Greuter, Phys. Rev. B **33**, 3952 (1987).
[13] K. M. Doshchanov, Fiz. Tekh. Poluprovodn. **28**, 692 (1994) [Semiconductors **28**, 412 (1994)].
[14] K. M. Doshchanov, Fiz. Tekh. Poluprovodn. **28**, 1645 (1994) [Semiconductors **28**, 917 (1994)].
[15] A. G. Milnes, *Deep Impurities in Semiconductors* (Wiley, New York, 1973; Mir, Moscow, 1977), p. 44.

Translated by W. J. Manthey

Autosolitons in InSb in a magnetic field

I. K. Kamilov, A. A. Stepurenko, and A. S. Kovalev

Kh. I. Amirkhanov Physics Institute, 367003 Makhachkala, Russia
(Submitted May 26, 1997; accepted for publication December 23, 1997)
Fiz. Tekh. Poluprovodn. **32**, 697–700 (June 1998)

It is shown experimentally that a longitudinal magnetic field of comparatively small magnitude substantially changes the velocity of autosolitons in indium antimonide samples and produces an appreciable redistribution of the electric field of these autosolitons. In this case, the frequency and amplitude of the current oscillations in the external circuit of the sample increases or decreases, depending on the direction of the longitudinal magnetic field. © *1998 American Institute of Physics.* [S1063-7826(98)01306-4]

The theoretical studies of Kerner and Osipov[1–4] have shown that it is possible to use an additional external perturbation to excite thermal-diffusion autosolitons in a heated electron–hole plasma (EHP). In a dense EHP in the presence of an external electric field, autosolitons appear as current sheets directed along the applied electric field,[5,6] whereas an EHP of lower density produces autosolitons in the form of layers of strong electric field which are perpendicular to the current lines.[7–9]

It is shown in Refs. 10–14 that the equilibrium EHP formed in *n*-type GaAs as a result of impact ionization or injection stratifies in an electric field into numerous current filaments and electric-field domains. The results of the detection and experimental study of a traveling hot autosoliton in a homogeneously photogenerated EHP heated by an electric field in *n*-type Ge are presented in Refs. 15 and 16.

It is shown in Refs. 17 and 18 that, in a nonequilibrium EHP obtained in an InSb sample by Joule heating, autosolitons appear in a strong electric field in the form of current sheets and regions of strong electric field. This is in some degree analogous to the experimental results obtained in Refs. 10–12. Since the EHP is nonsymmetric in InSb (for effective hole masses of m_p^* and electron masses of m_e^*, the inequality $m_p^* > m_e^*$ is satisfied), the strong-electric-field regions move in an electric field along the current sheets in the direction of motion of the hot electrons, i.e., from the cathode to the anode, causing current oscillations in the external circuit of the sample. The shape and velocity of the autosolitons are close to those obtained in Refs. 15 and 16. In Ref. 18 it is shown that two main types of oscillations can be distinguished in complex oscillations. Each of these modes is characterized by its own interval of applied voltage. It was found that, in one of them (type I), the frequency of the oscillations decreases and the amplitude increases as the voltage applied to the sample increases; in the other one (type II), the frequency of the oscillations increases smoothly, while the amplitude of the oscillations varies so that its increase changes to a decrease.

The autosolitons in the InSb samples must be rather sensitive to a magnetic field.[19] Since the autosolitons under consideration are localized regions of carrier-concentration gradient and temperature gradient,[17,18] the influence of the magnetic field on them is most likely caused by the Nerst and Ettingshausen thermomagnetic effects.[19]

We studied the behavior of autosolitons in InSb samples in a longitudinal magnetic field. A magnetic field with a strength up to 10^4 A/m was created in the solenoid inside which the sample was placed. The study was carried out on a series of InSb samples of various dimensions, which, at a temperature $T=77$ K, had a carrier concentration of $p=(2-4)\times 10^{12}$ cm^{-3} with a mobility of $\mu \simeq 4000$ cm^2/(V·s). We used an electric-measurement technique like that in Ref. 18. The influence of a longitudinal magnetic field on moving autosolitons was studied. The magnetic field in this case was switched on only when current oscillations appeared in the external circuit of the sample.

Figure 1 shows oscilloscope tracings of the current oscillations of type-I mode (a and b) and the dependences of the frequency (c) and the amplitude (d) of these oscillations with varying applied magnetic field in the interval from 0 to 1500 A/m.

When the direction of the magnetic field coincides with that of the electric field, $\mathbf{H}\uparrow\uparrow\mathbf{E}$, a decrease in the frequency of the current oscillations with increasing magnetic field is observed (curves *1–3* correspond to different amplitudes of the voltage pulses $U_1<U_2<U_3$ at which oscillations that differ in the frequencies and amplitudes appear; the dependence of the frequency and amplitude on magnetic field tracks these values).

When the directions of the magnetic and electric fields are antiparallel (opposite to each other), $\mathbf{H}\downarrow\uparrow\mathbf{E}$, the frequency of the same current oscillations in the sample varies differently (Fig. 1c, curves *1′–3′*). For the smallest value of the initial voltage U_1 (curve *1′*), the frequency of the oscillations initially smoothly decreases with increasing magnetic field, and then passes through three extrema, acquiring a tendency to increase. For a larger initial voltage U_2, (curve *2′*), the frequency of the oscillations increases smoothly with increasing magnetic field and then passes through two extrema, maintaining a tendency to increase. For the largest initial voltage U_3 (curve *3′*), the frequency of the oscillations increases with magnetic field in the entire interval of its variation.

Figure 1d shows the variations ΔI of the amplitude of

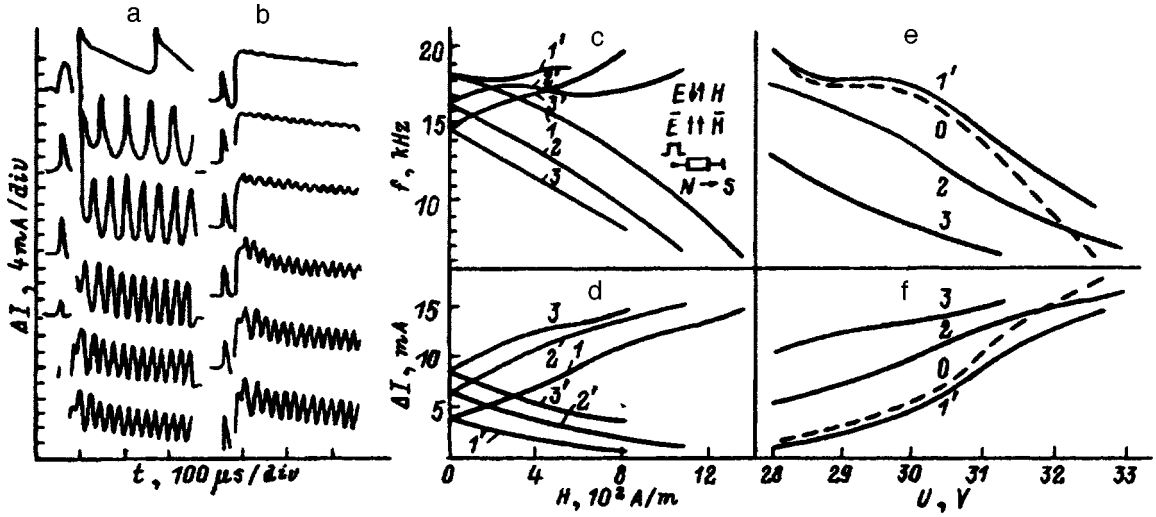

FIG. 1. Current oscillations of the type-I mode in the external circuit of a sample of indium antimonide. (a) and (b) are oscilloscope tracings of the current oscillations for $\mathbf{H}\uparrow\uparrow\mathbf{E}$ and $\mathbf{H}\downarrow\uparrow\mathbf{E}$, respectively. $U_2=30.3$ V; H increases for the oscilloscope tracings from the bottom upward. (c) and (d) show the dependences of the frequency f and amplitude ΔI of the current oscillations on the magnetic field for constant electric field: $U_1=29.5$ V (*1, 1′*), $U_2=30.3$ V (*2, 2′*), $U_3=30.8$ V (*3, 3′*), *1, 2, 3*—$\mathbf{H}\uparrow\uparrow\mathbf{E}$; *1′, 2′, 3′*—$\mathbf{H}\downarrow\uparrow\mathbf{E}$. (e) and (f) show the dependences of the frequency and amplitude of the oscillations on the applied electric field for a constant magnetic field H, A/m: *0*—0, *1′*—136 ($\mathbf{H}\downarrow\uparrow\mathbf{E}$), *2*—544 ($\mathbf{H}\uparrow\uparrow\mathbf{E}$), *3*—1088 ($\mathbf{H}\uparrow\uparrow\mathbf{E}$).

the current oscillations that occur for the same dc voltages $U_1<U_2<U_3$ with increasing magnetic field. The amplitude smoothly increases when $\mathbf{H}\uparrow\uparrow\mathbf{E}$ (curves *1–3*), whereas it smoothly decreases when $\mathbf{H}\downarrow\uparrow\mathbf{E}$ (curves *1′–3′*).

The variation of the frequency and the amplitude of the current oscillations with increasing magnetic field for the case $\mathbf{H}\uparrow\uparrow\mathbf{E}$ are qualitatively similar to the variation of the same parameters with increasing electric field (Figs. 1e and 1f, curves *0, 0*). Figure 1 also shows the dependences of frequency f (Fig. 1e, curves *1′, 2, 3*) and amplitude ΔI of the current oscillations (Fig. 1f, curves *1′, 2, 3*) as the voltage U_1 applied to a sample in a constant magnetic field increases. When $\mathbf{H}\uparrow\uparrow\mathbf{E}$, the decrease of the frequency of the current oscillations occurs at lower U values by comparison with the case $H=0$; i.e., $f_H(U)<f(U)$ (Fig. 1e, curves *0, 2, 3*). When $\mathbf{H}\downarrow\uparrow\mathbf{E}$, the opposite situation $f_H(U)>f(U)$ is observed (Fig. 1f, curves *0, 1′*). The curves of the electric-field dependence of the amplitude of the current oscillations at constant magnetic field are in the reverse order; i.e., $\Delta I_H(U)>\Delta I(U)$ for $\mathbf{H}\uparrow\uparrow\mathbf{E}$ (Fig. 1f, curves *0, 2, 3*) and $\Delta I_H(U)<\Delta I(U)$ for $\mathbf{H}\downarrow\uparrow\mathbf{E}$ (Fig. 1f, curves *0, 1′*).

Figure 2 shows the results of a study of how the magnetic field affects the frequency and the amplitude of the

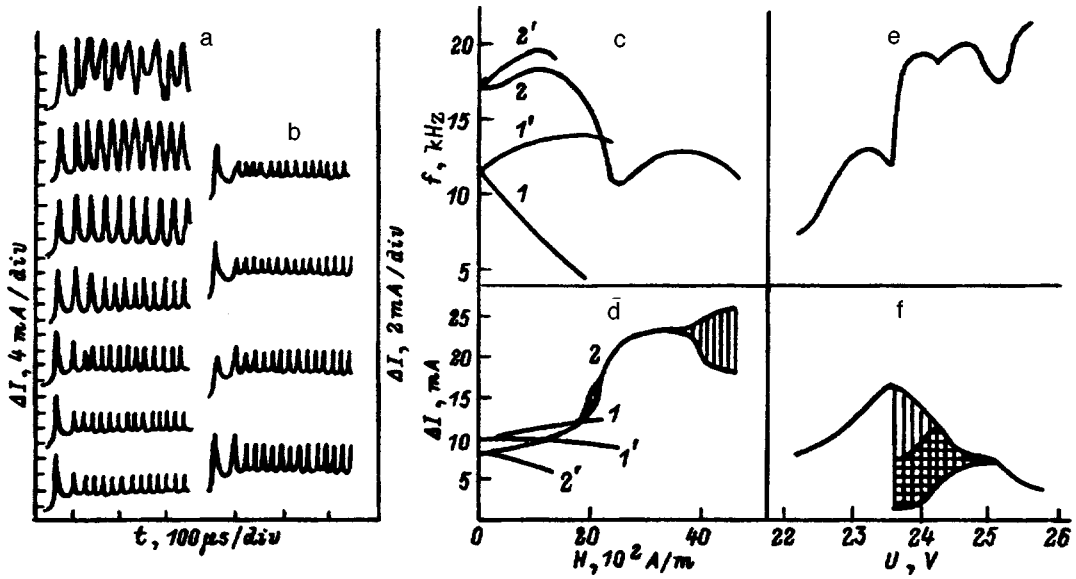

FIG. 2. Current oscillations of the type-II mode in the external circuit of a sample of indium antimonide. (a) and (b) are oscilloscope tracings of the current oscillations for $\mathbf{H}\uparrow\uparrow\mathbf{E}$ and $\mathbf{H}\downarrow\uparrow\mathbf{E}$, respectively; $U_2=25.1$ V; H increases for the oscilloscope tracings from the bottom upward. (c) and (d) show the dependences of the frequency f and the amplitude ΔI of the current oscillations on the magnetic field for a constant electric field: $U_1=22.7$ V (*1, 1′*), $U_2=25.1$ V (*2, 2′*). *1, 2*—$\mathbf{H}\uparrow\uparrow\mathbf{E}$. *1′, 2′*—$\mathbf{H}\downarrow\uparrow\mathbf{E}$. (e) and (f) show the dependences of the frequency and amplitude of the oscillations on the electric field for $H=0$.

current oscillations of type-II mode.[17,18] The behavior of this mode with varying electric field is shown in Figs. 2e and 2f. In this case, this mode undergoes not only bifurcation through period doubling, but also period tripling with increasing electric field applied to the sample. The hatching shows the voltage regions where period doubling and tripling exist and also where their onset occurs. The lines that border these regions show the amplitudes of the current oscillations of these periods. The oscilloscope tracings in Figs. 2a and 2b illustrate the dynamics of the frequency variation and the amplitude of the current oscillations with increasing magnetic field in the interval of H values from 0 to 4800 A/m for $\mathbf{H}\uparrow\uparrow\mathbf{E}$ (Fig. 2a) and for $\mathbf{H}\downarrow\uparrow\mathbf{E}$ (Fig. 2b). The corresponding graphs show that the frequency on the average decreases with increasing magnetic field when $\mathbf{H}\uparrow\uparrow\mathbf{E}$ (Fig. 2c, curves *1* and *2* are for two values of the initial voltage $U_1<U_2$ on the sample). In this case, current oscillations are observed for U_1 in the magnetic-field interval from 0 to 2150 A/m. For the opposite direction of the magnetic field, $\mathbf{H}\downarrow\uparrow\mathbf{E}$, the frequency of the oscillations increases, even though, at the end of the interval, where current oscillations still exist as the magnetic field increases, there is a tendency for the frequency to decrease.

Figure 2d shows the variations of the amplitude of the current oscillations in the sample as the magnetic field varies. At U_1, in a magnetic field $\mathbf{H}\uparrow\uparrow\mathbf{E}$, the amplitude of the current oscillations smoothly increases in the entire interval of magnetic field where oscillations exist (Fig. 2d, curve *1*). At $U_2>U_1$, with an increase of the magnetic field ($\mathbf{H}\uparrow\uparrow\mathbf{E}$), the amplitude of the oscillations increases appreciably (Fig. 2d, curve *2*); when $H=1900$–2200 A/m, the given mode undergoes period-doubling bifurcation. As the field increases further, a transition occurs to regular oscillations; the amplitude of these oscillations increases sublinearly, and then, beginning with $H=3300$ A/m, the mode undergoes the next period-doubling bifurcation.

When U_1 and U_2 in a magnetic field $\mathbf{H}\downarrow\uparrow\mathbf{E}$, the amplitude of the current oscillations of the mode under consideration almost linearly decreases with increasing magnetic field in the existence domain of these oscillations.

The observed phenomena, i.e., the change of the frequency and amplitude of the current oscillations in the external circuit of the sample with decreasing external magnetic field, can be explained by the decisive contribution of thermomagnetic effects. The autosolitons, both in the form of longitudinal current filaments and in the form of transverse current lines of layers of reduced concentration of the charge carriers, are localized regions of increased temperature, with a sharp gradient of the order of $\nabla T=(T_{AS}-T)/\mathcal{L}/2$,where T_{AS} is the temperature in the central region of the autosoliton, T is the temperature at the periphery of the autosoliton, $T_{AS}\simeq 2T$,[20] $l<\mathcal{L}<(Ll)^{1/2}/2$ is the width of the autosoliton,[6] L is the diffusion length of the carriers, l is the cooling length of the carriers, and $\nabla T=2T/\mathcal{L}=2T/l-4T/(Ll)^{1/2}$. For InSb, $T\geqslant 150$ K,[18] $L\simeq 3\times 10^{-3}$ cm, $l\simeq 9\times 10^{-4}$ cm,[21,22] and $\nabla T=(3.3$–$4)\times 10^5$ deg/cm. In a longitudinal magnetic field, the presence of a transverse temperature gradient ∇T of the current filament (the autosoliton) produces a transverse potential difference as a consequence of the Nernst–Ettingshausen effect. The field of the transverse Nernst–Ettingshausen effect is an odd function; i.e., the sign of the transverse potential difference depends on the direction of the magnetic field $E_\perp(H)=-E_\perp(-H)$.[23] Under the action of this potential difference, an autosoliton moving in an external electric field is displaced toward a current filament or away from it. The autosoliton is in the region of the denser and hotter EHP in the first case and in the region of the lower-density and cooler EHP in the second case. In both cases, the relationships of the electron and hole mobilities (μ_e, μ_p) and temperatures (T_e, T_p) change, which changes the phase velocity v_{ph} (of the autosoliton).[7] Numerical calculations were carried out for the velocity of the autosoliton, represented by the expression of Ref. 7. It turned out that the velocity of the autosoliton decreases as it moves into the hotter region of the EHP. Accordingly, the frequency of the current oscillations in the external circuit of the sample will increase in the first case and decrease in the second case.

In the hot, denser region of the EHP, the carrier-concentration deficit in the autosolitons decreases; i.e., the resistance of the autosoliton decreases; consequently, the electric field at the center of the autosoliton decreases. All this has the result that the current jump in the external circuit of the sample decreases as the hot autosoliton moving through the sample breaks down.

In the colder and less dense region of the EHP, the carrier-concentration deficit in the autosoliton increases, and consequently the resistance and accordingly the electric field at the center of the autosoliton increase. As a result, the current jump in the external circuit of the sample increases when the autosoliton breaks down. This explains why the amplitude of the current oscillations in the external circuit of the sample decreases as the autosoliton moves into the hotter and denser region of the EHP and increases as it moves into the colder and less dense region of the EHP.

We have thus experimentally shown that a longitudinal magnetic field with a comparatively small value (up to about 10^4 A/m) substantially changes the velocity of the autosolitons formed in strong heating fields in InSb samples. In this case, the frequency of the current oscillations in the external circuit of the sample decreases, while the amplitude of these oscillations increases with an increasing longitudinal magnetic field that has the same direction as the electric field applied to the sample ($\mathbf{H}\uparrow\uparrow\mathbf{E}$). When the magnetic and electric fields are antiparallel ($\mathbf{H}\downarrow\uparrow\mathbf{E}$), an increase of the frequency of the current oscillations is observed, while the amplitude of these oscillations decreases as the magnetic field increases.

The authors are grateful to V. V. Osipov for his attention to this work and for comments and supplements made by him that improved the quality of this work.

The authors express their gratitude to the Russian Fund for Fundamental Research for supporting this work (Grant 97-02-17623).

[1] B. S. Kerner and V. V. Osipov, Zh. Éksp. Teor. Fiz. **71**, 1542 (1976) [Sov. Phys. JETP **44**, 807 (1976)].
[2] B. S. Kerner and V. V. Osipov, JETP Lett. **41**, 466 (1985).
[3] B. S. Kerner and V. V. Osipov, Usp. Fiz. Nauk **157**, 201 (1989) [Sov. Phys. Usp. **32**, 101 (1989)].

[4] B. S. Kerner and V. V. Osipov, Usp. Fiz. Nauk **160**, 1 (1990).
[5] B. S. Kerner and V. V. Osipov, JETP Lett. **18**, 70 (1973).
[6] B. S. Kerner and V. V. Osipov, Fiz. Tekh. Poluprovodn. **13**, 891 (1979) [Sov. Phys. Semicond. **13**, 523 (1979)].
[7] B. S. Kerner and V. V. Osipov, Fiz. Tverd. Tela (Leningrad) **21**, 2342 (1979) [Sov. Phys. Solid State **21**, 1348 (1979)].
[8] B. S. Kerner and V. V. Osipov, Fiz. Tekh. Poluprovodn. **13**, 721 (1979) [Sov. Phys. Semicond. **13**, 424 (1979)].
[9] A. L. Dubitskiĭ, B. S. Kerner, and V. V. Osipov, Fiz. Tverd. Tela (Leningrad) **28**, 1290 (1986) [Sov. Phys. Solid State **28**, 725 (1986)].
[10] B. S. Kerner and V. F. Sinkevich, JETP Lett. **36**, 436 (1982).
[11] B. S. Kerner, V. V. Osipov, M. T. Romanenko, and V. F. Sinkevich, JETP Lett. **44**, 97 (1986).
[12] V. N. Vashchenko, B. S. Kerner, V. V. Osipov, and V. F. Sinkevich, Fiz. Tekh. Poluprovodn. **23**, 1378 (1989) [Sov. Phys. Semicond. **23**, 857 (1989)].
[13] V. N. Vashchenko, B. S. Kerner, V. V. Osipov, and V. F. Sinkevich, Fiz. Tekh. Poluprovodn. **24**, 1705 (1990) [Sov. Phys. Semicond. **24**, 1065 (1990)].
[14] V. V. Gafiĭchuk, B. S. Kerner, V. V. Osipov, and I. V. Tyslyuk, Fiz. Tverd. Tela (Leningrad) **31**, 46 (1989) [Sov. Phys. Solid State **31**, 25 (1989)].
[15] M. N. Vinoslavskiĭ, Fiz. Tverd. Tela (Leningrad) **31**, 315 (1989) [*sic*].
[16] M. N. Vinoslavskii, B. S. Kerner, V. V. Osipov, and O. G. Sarbey, J. Phys.: Condens. Matter **2**, 2863 (1990).
[17] A. A. Stepurenko, Fiz. Tekh. Poluprovodn. **28**, 403 (1994) [Semiconductors **28**, 243 (1994)].
[18] I. K. Kamilov and A. A. Stepurenko, Phys. Status Solidi B **194**, 643 (1996).
[19] A. K. Zvezdin and V. V. Osipov, Zh. Éksp. Teor. Fiz. **58**, 160 (1970) [Sov. Phys. JETP **31**, 90 (1970)].
[20] V. V. Gafiĭchuk, B. S. Kerner, V. V. Osipov, and A. G. Yuzhanin, Fiz. Tekh. Poluprovodn. **22**, 2051 (1988) [Sov. Phys. Semicond. **22**, 1298 (1988)].
[21] I. A. Baev, Bolg. Fiz. Zh. **7**, 198 (1980).
[22] T. M. Lipshits, A. Ya. Oleinikov, and A. Ya. Shulman, Phys. Status Solidi **14**, 511 (1966).
[23] I. M. Tsidil'kovskiĭ, *Thermomagnetic Effects in Semiconductors*, Academic Press, N.Y. (1962) [Russ. original, Fizmatgiz, Moscow, 1960].

Translated by W. J. Manthey

The effect of a strong electric field on the conductivity of a $MnGaInS_4$: Eu single crystal

O. B. Tagiev, T. Sh. Gashimova, and I. M. Askerov

Physics Institute, Azerbaijan Academy of Sciences, 370143 Baku, Azerbaijan
(Submitted June 19, 1997; accepted for publication December 23, 1997)
Fiz. Tekh. Poluprovodn. **32**, 701–702 (June 1998)

This paper presents the results of a study of the effect of a strong electric field on the electrical properties of $MnGaInS_4$: Eu single crystals. The compound was obtained by the Bridgman method and consists of plane-parallel layered plates. The following parameters are determined on the basis of these studies: concentration of trap levels 10^{13}–10^{14} cm^{-3} and activation energy 0.70–0.50 eV. It is established that the conductivity of $MnGaInS_4$: Eu increases in strong electric fields mainly because the current-carrier concentration increases with electric field. © *1998 American Institute of Physics.* [S1063-7826(98)01406-9]

In this paper we present the results of an experimental study of the effect of a strong magnetic field on the electric properties of single crystals of $MnGaInS_4$: Eu. The compound is obtained by the Bridgman method and is a layered crystal. It has been established that $MnGaInS_4$: Eu crystallizes in the structure of a single-package modification of $ZnIn_2S_4$ with the crystal-lattice parameters $a=3.80$, $c=12.15$ Å, and $z=1$ (the number of formula units in a unit cell), space group $P3m1$.[1,2] Some spectral properties of $MnGaInS_4$ single crystals are given in Ref. 3.

We used In–$MnGaInS_4$: Eu–In samples of sandwich type for the measurements. The I–V characteristics in the temperature interval 280–370 K are shown in Fig. 1. Characteristic sections $I\sim V$, $I\sim V^2$, and $I\sim V^n$ with $n>2$ can be distinguished on the experimental dependences. Such dependences indicate that the main role in current transmission is played by space-charge-limited currents. Moreover, it has been established that the following regularity is satisfied in the dependence of current density j on interelectron spacing L for the quadratic region ($I\sim V^2$): $j\sim L^{-3}$ (Ref. 4). The section of rapid current increase ($I\sim V^n$, $n>2$) can be associated with the maximum filling of traps with a monoenergetic capture level. Therefore, a model that contains one capture level or a system of closely spaced levels is used for the given compound. Since the voltage of the maximum filling of the traps precedes the quadratic section, it can be concluded that the capture levels are located above the Fermi level. The trap concentration[5] that lies within the limits 10^{13}–10^{14} cm^{-3} can be estimated from the voltage corresponding to the maximum filling of the traps.

The I–V characteristics measured at different temperatures can be used to determine the depth of the monoenergetic levels E_t that are associated with the transition voltage V_{1-2} from the ohmic section to the quadratic ($I\sim V^2$) ''trap'' section by the formula[5]

$$V_{1-2}^{-1}\sim\exp[(E_t-E_c)/kT]. \tag{1}$$

The activation energy determined from Fig. 2 equals 0.80 eV. The temperature dependence of voltage V_{1-2} indicates that $MnGaInS_4$: Eu crystals are strongly compensated semiconductors.[5]

Conductivity σ was measured in the temperature interval $T=293$–400 K in strong electric fields up to $F=4\times10^4$ V/cm. It was found that Ohm's law in the test samples is satisfied at fields up to about 5×10^3 V/cm. Beginning with $F\simeq7\times10^3$ V/cm, an increase of σ with increasing electric field is observed.

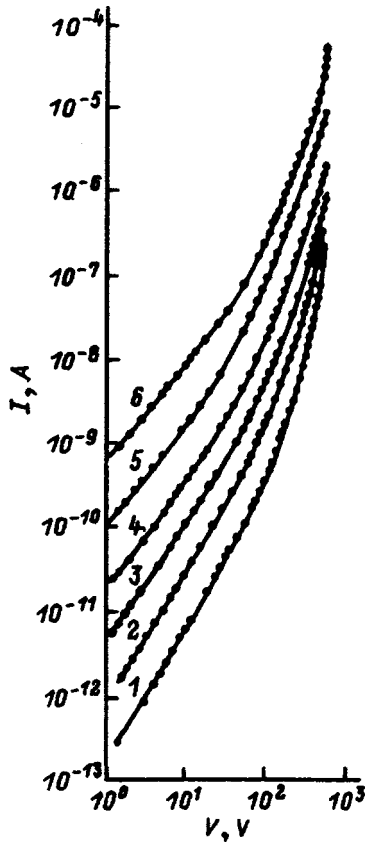

FIG. 1. The I–V characteristics of In–$MnGaInS_4$: Eu–In structures at temperature T, K: *1*—284, *2*—300, *3*—314, *4*—329, *5*—350, *6*—369.

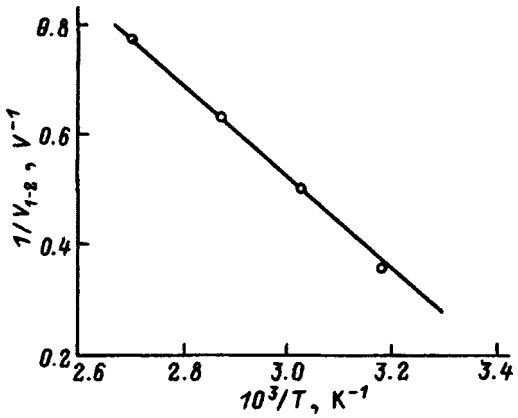

FIG. 2. Temperature dependence of the inverse transition voltage $1/V_{1-2}$.

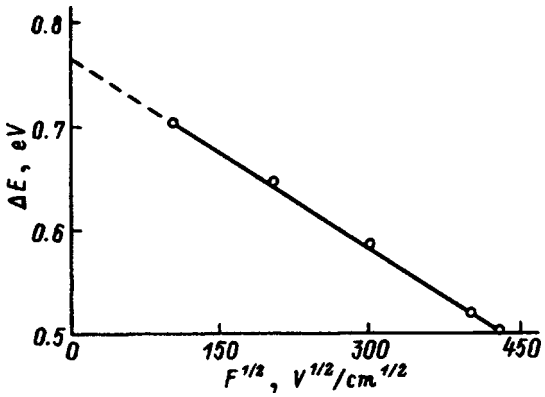

FIG. 3. Conduction activation energy ΔE of a $MnGaInS_4$: Eu single crystal vs the square root of the electric field, $\sqrt{F}$.

It is well known that most semiconductors obey Frenkel's law,[6,7]

$$\sigma=\sigma_0\exp\beta\sqrt{F}, \tag{2}$$

where $\sigma_0=A\exp(-\Delta E_0/2kT)$ is the conductivity in weak fields, and β is the Frenkel coefficient.

Substituting the expression for σ_0 into the Frenkel formula [Eq. (2)], we obtain

$$\sigma=A\exp\left[-\frac{\Delta E_0}{2kT}\right]\exp\beta\sqrt{F}$$

$$=A\exp\left[-\frac{1}{kT}\left(\Delta E_0-2e\sqrt{\frac{eF}{\varepsilon}}\right)\right].$$

If we introduce the notation

$$\Delta E(F)=\Delta E_0-2e\sqrt{eF/\varepsilon}, \tag{3}$$

we obtain

$$\sigma=A\exp[-\Delta E(F)/2kT], \tag{4}$$

where $\Delta E(F)$ is the dependence of the activation energy on the electric field.

The dependence of activation energy ΔE on the square root of the electric field, $\sqrt{F}$, is shown in Fig. 3. It can be seen from the figure that, in accordance with Eq. (3), ΔE linearly decreases with increasing $\sqrt{F}$. The activation energy $\Delta E_0=0.77$ eV in a weak electric field is determined by extrapolating the straight line $\Delta E=f(\sqrt{F})$ to the axis, $\sqrt{F}\to 0$.

The effect of the electric field on the conductivity is thus best expressed by Frenkel's law. An electron associated with a local level is found in a potential well with respect to the conduction band. As pointed out above, the height of the potential well in the presence of a strong electric field is reduced by an amount determined by Eq. (3).

Thus, the agreement of our data with the Frenkel theorem confirms that, in strong electric fields, the increase of the conductivity of $MnGaInS_4$: Eu occurs mainly because the charge-carrier concentration increases with electric field.

[1] E. N. Nagaev, *The Physics of Magnetic Semiconductors* (Nauka, Moscow, 1979).
[2] C. Batistoni, L. Gastaldi, G. Mattogno, M. G. Simeone, and S. Viticoli, Solid State Commun. **61**, No. 1, 43 (1987).
[3] N. N. Niftiev, A. G. Rustamov, and O. B. Tagiev, Fiz. Tekh. Poluprovodn. **27**, 386 (1993) [Semiconductors **27**, 215 (1993)] .
[4] A. G. Milnes, *Deep Impurities in Semiconductors*, (Wiley, New York, 1973; Moscow, 1977).
[5] N. S. Grushko, L. A. Gerasimenko, and T. I. Goglidze, in *The Physics of Semiconductors and Insulators* (Shtiintsa, Kishinev, 1992), p. 83.
[6] Ya. I. Frenkel', Zh. Eksp. Teor. Fiz. **8**, No. 12, 1292 (1938).
[7] B. G. Tagiev, O. B. Tagiev, and N. N. Musaeva, Fiz. Tekh. Poluprovodn. **29**, 1403 (1995) [Semiconductors **29**, 728 (1995)].

Translated by W. J. Manthey

Experimental manifestations of correlated hopping in the temperature dependences of the conductivity of doped CdTe

N. V. Agrinskaya and V. I. Kozub

A. F. Ioffe Physicotechnical Institute, Russian Academy of Sciences, 194021 St. Petersburg, Russia
(Submitted 15 December 1997; accepted for publication 23 December 1997)
Fiz. Tekh. Poluprovodn. **32**, 703–707 (June 1998)

The behavior of hopping transport in the region of the crossover from Mott conduction to conduction among Coulomb-gap states is investigated in doped CdTe crystals. Inconsistencies are discovered in individual parameters (the localization radius and the dielectric constant) estimated from the behavior of the conductivity on different sides of the crossover. These inconsistencies are explained within a simplified model that takes into account the role of assisting hops. © *1998 American Institute of Physics.* [S1063-7826(98)01506-3]

1. INTRODUCTION

Although the presence of a Coulomb gap in the spectrum of the single-particle excitations of disordered semiconductors on the insulator side of the metal-insulator transition is a generally accepted fact and has been confirmed, in particular, by tunneling measurements,[1] the character of Coulomb-gap hopping conduction is still not entirely clear. In particular, the question of whether hopping transport can be described completely on the basis of the single-particle density of states or whether it is completely determined by many-particle effects (correlated hops) has been discussed until now. The problem of correlated hops in the low-temperature conduction of disordered semiconductors was first examined by Pollak in Ref. 2, where it was shown that the current-determining hops can be assisted by hops between surrounding states because of intersite Coulomb interactions. Successive correlations, under which each current-carrying hop is prepared by preliminary hops in the environment, and many-electron hops, in which several electrons hop simultaneously, were considered. The polaron effect, which was subsequently considered by Éfros (see, for example, Ref. 3), should also be included among the many-electron effects. It takes into account the reorganization of the filling of surrounding sites due to Coulomb interactions with the ''current-carrying'' site and relates current transport to polaron hops, which are accompanied by simultaneous restructuring of the ''polaron coat.''

The theory of correlated hops is now being developed rapidly; however, since the analytical treatment of many-particle effects is associated with formidable difficulties, the main results have been obtained within numerical simulations. In particular, we should mention the recent paper by Perez-Garrido,[4] in which it was demonstrated that:

1) many-particle effects have a significant influence on the hopping resistivity with roles being played by both many-electron hops (in which several electrons hop simultaneously) and ''assistance'' (in which the current-carrying hop is preceded by preparation of the environment);

2) the character of the low-temperature dependence of the resistivity is described quite well by the Éfros–Shklovskiĭ law[3]

$$\rho \propto \exp(T_1/T)^{1/2}, \tag{1}$$

but the value of T_1 is appreciably smaller than the value following from an analysis of the single-particle density of states. We note, however, that, as far as we know, there is an analytical proof that (1) also holds for correlated hopping transport only in the case of the polaron effect.

We note that the disparity between the experimentally observed value of T_1 and the value calculated from the formula

$$T_1 = \beta_1/(g_0^{1/3}a)$$

has previously been reported. This fact can serve as indirect experimental confirmation of the role of correlated hops.[5] Here $\beta_1 = 2.8$, $g_0 = \kappa^3/e^6$ is the effective density of states, a is the localization length, and κ is the dielectric constant.

In our opinion, a somewhat different view of the problem of correlated hops as applied to successive correlations can be based on an analysis of fluctuations in the hopping transport regime. As was recently shown theoretically and experimentally,[6–8] hops between sites that are not part of the percolation cluster produce considerable fluctuations in the current because of the fluctuations in the energies of the sites of the percolation cluster caused by them. It follows, in particular, from the estimates in Ref. 8 that the fluctuations of the energies of the sites can be quite considerable. As was noted in Ref. 8, this situation can lead to an influence of the fluctuations on the mean current, suggesting that there are hops simulated by fluctuations. In this case, an electron waits for a favorable fluctuation, which lowers the corresponding activation energy, before completing a hop. This picture is consistent with the concept of ''assisting'' hops.[2] We note, however, that only the case of weak fluctuations, which do not lead to appreciable changes in the mean current, were considered in Refs. 7 and 8.

Thus, the question of the role of correlated hops in hopping conduction among Coulomb-gap states is far from being completely resolved. However, it is natural to expect that

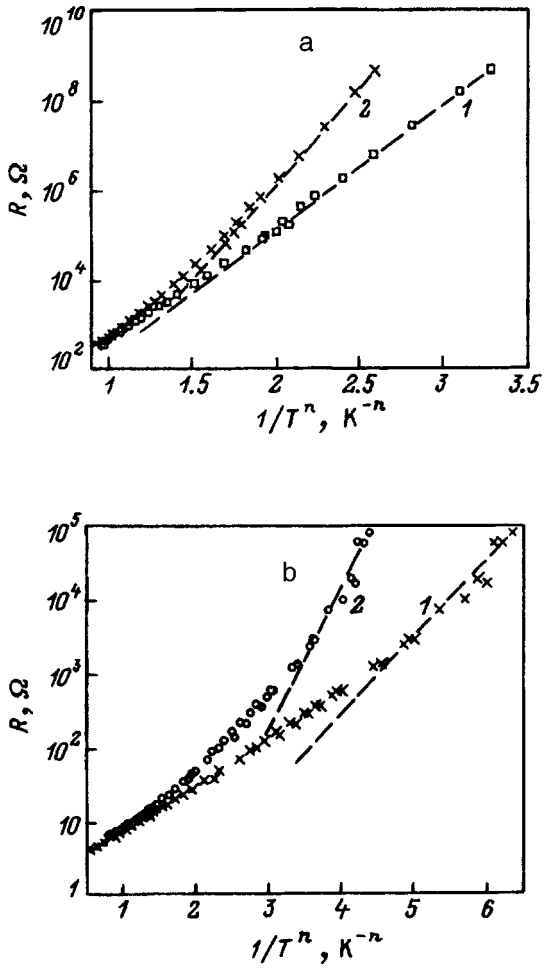

FIG. 1. Temperature dependence of the resistance on different scales: *1* — $(1/T)^{1/2}$, *2* — $(1/T)^{2/5}$; a — sample 1, b — sample 2 (see Tables I and II).

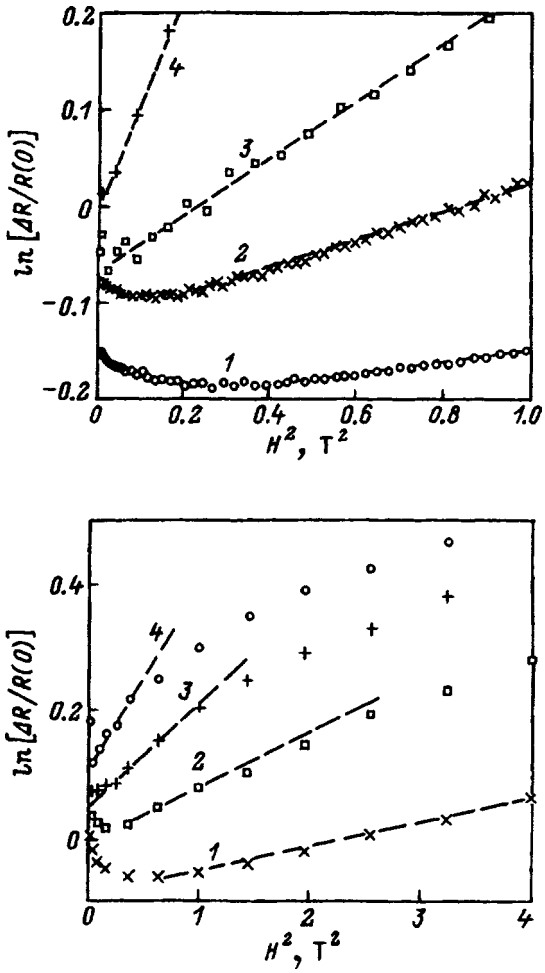

FIG. 2. Dependence of the magnetoresistance on the temperature and the magnetic field: a — sample 1, *T*, K: *1* — 0.6, *2* — 0.4, *3* — 0.3, *4* — 0.15; b — sample 2, *T*, K: *1* — 0.5, *2* — 0.3, *3* — 0.2, *4* — 0.15. The dashed lines show the quadratic positive magnetoresistance segments.

the role of Coulomb correlations is more significant in the Coulomb-gap regime, where Coulomb interactions are the interactions which determine the characteristic energy scale. Therefore, in our opinion, it would be interesting to examine the behavior of hopping transport in the vicinity of the crossover from the Mott law

$$\rho(T) \propto \exp(T_0/T)^{1/4} \tag{2}$$

to the Éfros–Shklovskiĭ law (1). We have accordingly investigated the behavior of the conductivity and magnetoresistance in the vicinity of this crossover for doped and compensated CdTe crystals. The results obtained were analyzed using conclusions which follow from simple model calculations of the fluctuations in the energies of lattice sites.

2. EXPERIMENT

We investigated cadmium telluride crystals doped by shallow donors. In the two samples investigated the donor concentration was approximately the same ($N_d = 5\times10^{17}$ cm^{-3}), but the degree of compensation by intrinsic lattice defects was different: the electron concentration at 300 K was, respectively, 1.2×10^{17} and 8×10^{16} cm^{-3} for the two samples. As can be seen from the temperature dependence of the conductivity (Fig. 1), the temperature ranges for crossover from the Mott law to the Éfros–Shklovskiĭ law for them are different: 0.3−0.4 K for one sample and 0.07−0.1 K for the other sample.

Several regions can be identified on the magnetoresistance curves (Fig. 2): a region of negative magnetoresistance (which is associated with the interference of different tunneling trajectories in the presence of scattering centers[9]) and a region of quadratic positive magnetoresistance (which is associated with compression of the wave functions of centers in a magnetic field). The latter gives way to a smoother magnetic-field dependence of the resistance according to a $\propto H^{2/3}$ law, which is characteristic of the anomalous positive magnetoresistance associated with compression of the wave functions of centers in a magnetic field in the presence of scatterers.[10] The relative contributions of these regions to the overall picture of the magnetoresistance varies strongly as a function of the temperature, especially in the temperature range corresponding to the crossover. For example, the interference contribution is dominant in the region of variable-range-hopping conduction corresponding to the Mott law. Upon passage into the region of conduction among Coulomb-gap states, it decreases sharply, i.e., the region of negative magnetoresistance vanishes. We previously ob-

TABLE I. Principal parameters of the samples.

Sample No.	n_{300}, [a] cm^{-3}	T_0, K	T_1, K	T_c, K	a, Å	a', Å
1	9×10^{16}	2×10^4	43	0.3−0.4	105	170
2	1.2×10^{17}	205	3.5	0.07−0.1	190	315

Note: Here n_{300} is the electron concentration at $T=300$ K obtained from Hall measurements; the values of T_0 and T_1 were obtained from the temperature dependences of the resistivity [see (1) and (2)]; the transition temperature T_c was found experimentally; a is the localization length obtained from the Mott law, and a' is the localization length obtained from the Éfros–Shklovskiĭ law.

served this phenomenon in Ref. 11 and attributed it to either a correlation in the impurity distribution that leads to a decrease in the effective number of scatterers or Coulomb correlations (correlated hops). The region of quadratic positive magnetoresistance narrows significantly with decreasing temperature and is replaced by a region of anomalous positive magnetoresistance (Fig. 2b). In addition, spin effects, which we previously discussed in detail in Ref. 12 and on which we shall not dwell here, can manifest themselves in some samples at low temperatures.

An analysis of the temperature dependences of the conductivity in the regions of the Mott and Éfros–Shklovskiĭ laws allows us to calculate the values of T_0 and T_1 for the two samples, which are presented in Table I. The parameter T_1 was previously defined, and

$$T_0=\beta_0/g(\varepsilon_f)a^3,$$

where $\beta_0=21$ is a numerical coefficient. On the other hand, knowing these parameters, we can obtain the value of the localization length a from the slopes of the quadratic positive magnetoresistance curves by using the expressions

$$B^2=\frac{c^2\hbar^2}{C_0e^2a^4}\left(\frac{T}{T_0}\right)^{3/4}, \tag{3}$$

$$B^2=\frac{c^2\hbar^2}{C_1e^2(a')^4}\left(\frac{T}{T_1}\right)^{3/2}. \tag{4}$$

Expression (3) corresponds to the Mott law and $C_0=1/\alpha_0=0.0025$; expression (4) corresponds to conduction among Coulomb-gap states, and the value $1/\alpha_1=0.0015$ is cited for C_1.[3]

The localization lengths obtained by us are different: a for the Mott law and a' for the Éfros–Shklovskiĭ law. Their values are presented in Table I. The ratio $a'/a\propto T_1^{-3/8}$ is approximately the same for the two samples, being equal to 1.5. To eliminate this discrepancy, T_1 must be increased by a factor of 3.8−3.5, in agreement with the result in Ref. 5. On the other hand, it is known that as the transition is approached, i.e., as $N\to N_c$, not only the localization length a, but also the dielectric constant κ diverge. Fairly close to the transition, the divergence of κ is described by the expression[13]

$$\kappa(N)=\kappa_0+4\pi e^2N(E_F)[a(N)]^2. \tag{5}$$

TABLE II. Sample parameters analyzed.

Sample No.	T_1, [a] K	$T_{1,0}$, K	κ	κ'	κ''
1	43	90	44	120	55
2	3.5	15.5	145	780	176

Note: Here T_1 and $T_{1,0}$ are the values obtained from the experimental temperature dependences of the resistivity plotted on the scales corresponding to the Éfros–Shklovskiĭ law (1) and law (10); κ, κ', and κ'' are the dielectric constants obtained using (5) and (6) with T_1 and $T_{1,0}$, respectively.

Hence, knowing the localization length, we can estimate κ and compare the value obtained to the value calculated from T_1:

$$\kappa'=\beta_1\frac{e^2}{T_1a}. \tag{6}$$

These values are listed in Table II. Considerable disparity is observed between these two parameters, which is strongest for the sample closer to the transition (for this sample the disparity in κ and, consequently, in T_1 is of the order of 7). Hence it follows that the behavior observed by us cannot be described by simply introducing an additional numerical factor, which is identical for all samples, into the estimate of T_1, as was theorized in Ref. 5.

3. DISCUSSION

Thus, although the picture of the temperature dependence of the conductivity and the magnetoresistance is described qualitatively by the familiar models of the crossover from the Mott law to conduction among Coulomb-gap states, a more detailed analysis reveals appreciable quantitative disparities. We shall next try to explain these details using a theory of correlated hops similar to those proposed in Pollak's work.[14] Specifically, we assume that a hop which accounts for the charge transfer (i.e., a hop between sites appearing in the percolation cluster) is ''prepared'' by hops in the immediate environment, which provide for the smallest possible value of the activation energy. It is expected that such behavior is most pertinent to conduction in the Coulomb-gap regime, where the Coulomb energy of the interparticle interactions is of the order of the width of the effective hopping band. In our simplified model we restrict the analysis to the contribution of the ''successive'' correlations (''assistance'') alone and disregard the many-electron hops, in which several electrons hop simultaneously.

For the pair distribution function $f(\mathcal{E},l)$ which describes the ''assisting'' pairs (where $\mathcal{E}$ is the difference between the energies of the sites in a pair, and l is the distance between them), we use the expression[4]

$$f(\mathcal{E},l)=\left(\mathcal{E}+\frac{e^2}{\kappa l}\right)g_0^2,\quad \mathcal{E}+\frac{e^2}{\kappa l}\geqslant\Delta_C,$$

$$f(E,l)=\frac{3\kappa^6}{10\pi^2e^{12}}\left(\mathcal{E}+\frac{e^2}{\kappa l}\right)^5,\quad \mathcal{E}+\frac{e^2}{\kappa l}\leqslant\Delta_C. \tag{7}$$

Here Δ_C is the Coulomb-gap width, and g_0 is the single-particle density of states outside the Coulomb gap. For $l\geqslant r_C$ ($r_C=e^2/\kappa\Delta_C$ is the distance between the sites in an

''intimate'' pair[4]) it can be seen that $\mathcal{E} \ll \Delta_C$ and $f = \text{const}$. We note that this expression disregards the interaction between the ''dipolar'' excitations, while allowance for this interaction[15] leads to some suppression of f at small energies: $f \propto 1/\log(\Delta_C/\mathcal{E})$. However, in view of the weakness of the corresponding dependence, we disregard it in our estimates.

As was noted in Ref. 7, because of the dipolar character of the interaction of the current-carrying sites with the pairs which provide for the energy fluctuations at a site, the main contribution to the fluctuations is made by the nearest pair with the assigned parameters. We note that the assisting pairs must have an activation energy $\mathcal{E}$ that is equal to or less than the activation energy E of a ''current-carrying'' pair (since, otherwise, the assistance effect vanishes); therefore, in our case the constraint corresponds to $\mathcal{E} \leqslant E$. When this is taken into account, the estimate of the minimum distance R from a current-carrying site to an assisting pair has the form

$$\int_0^R d^3R \int d^3l \int_0^E d\mathcal{E} f(\mathcal{E}, l) = 1. \tag{8}$$

It is seen that the main contribution to the integral over l is made by the smallest possible values $l \simeq r_C$, which correspond to intimate pairs. As can easily be seen, for such pairs $R \simeq r_C(\Delta_C/E)^{1/3}$, and, accordingly, the interaction potential of a pair with a site $U \simeq e^2 l/(\kappa R^2)$ is estimated as $U \sim E(\Delta_C/E)^{1/3}$. In other words, the fluctuation caused by an assisting hop can, in fact, exceed the activation energy. We note that pairs with $l > r_C$ can also provide for large fluctuations of the energies of sites up to $l \simeq r$, at which $|U| \simeq E$.

We offer, however, the following remark. As can be seen, the hop in an assisting pair considered here can lead to significant lowering of the energy of the $\langle$assisting pair$\rangle - \langle$current-carrying site$\rangle$ system. Strictly speaking, in this case we cannot refer to the respective hop as a fluctuation relative to the equilibrium state of the $\langle$assisting pair$\rangle - \langle$current-carrying site$\rangle$ system, since it leads to the formation of a deeper state along the energy scale. Within the ''polaron'' picture,[4] the corresponding pairs should be included in the ''polaron coat,'' and thus the hops in such pairs cannot be considered external with respect to the current-carrying excitation (polaron).

At the same time, as we have noted above, the character of the interactions in the many-electron system of a Coulomb glass is still not entirely clear. This refers, in particular, to the consideration of correlations involving a large number of electrons, for example, many-electron interactions in a system of dipolar excitations. In particular, it can be presumed that the establishment of equilibrium in a system of the pairs is faster than the establishment of equilibrium between a specific pair and a current-carrying site. We assume that the picture of ''assisting'' fluctuations is conserved when this is taken into account. Although assisting excitations can, in fact, have a more complicated character than purely dipolar excitations, we also assume that each of them is localized to a considerable extent on a certain pair of sites and can be regarded as a dipolar excitation in the lowest approximation, permitting the use of the simple picture proposed above. Although we are aware of the limitations of the model that we used, we believe that investigating it will be useful, particularly because of the possibility of using analytical estimates.

Taking into account that the ''period'' of the assisting hops is assumed to be much shorter than the characteristic time of a current-carrying hop, we can average the probability W of a current-carrying hop over time, and since the corresponding activation energy vanishes as a consequence of the assisting hops, we find that as a result of the averaging,

$$W \propto \exp\left(-\frac{2r}{a} - \frac{\mathcal{E}}{T}\right), \tag{9}$$

where the ''activation'' term describes the probability of an assisting hop, and r is the distance in the corresponding pair of current-carrying sites. Taking into account that because of assistance, the hops occur in an energy band of width $\simeq |U|$, we have the estimate $r \simeq r_C(\Delta_C/\mathcal{E})^{1/3}$. Using the condition of equality between the ''tunneling'' and activation contributions to the exponent as a condition for connectivity of the percolation cluster and specifying the characteristic energy band $\mathcal{E}$ of the assisting pairs in this manner, we ultimately obtain the following estimate for the resistivity:

$$\log \rho \propto W \propto (T_1'/T)^{2/5}. \tag{10}$$

Here $T_1' \simeq T_{1,0}(T_0/T_{1,0})^{1/4} > T_{1,0}$, where $T_{1,0}$ is the value corresponding to the Efros–Shklovskiĭ law without allowance for the assistance effects.

We note that the variation of the exponent is evidence that the contribution of the assisting hops does not reduce to the renormalization of Δ_C (see Ref. 5), but leads to alteration of the temperature dependence itself. In this respect, the situation considered here differs from the polaron effect. At the same time, the deviation from the law (1) is very small and can hardly be detected to a convincing degree by a simple analysis of the temperature dependence.

Figure 1 shows plots of the temperature dependence of the resistance constructed on the $(T_1'/T)^{2/5}$ scale and on the standard $(T_1/T)^{1/2}$ scale. The values of T_1' obtained from the slopes are significantly greater than the values of T_1 (see Table II), giving larger values of $T_{1,0}$. A calculation of the dielectric constant using the expression $\kappa'' = \beta_1 e^2/(T_{1,0}a)$ gives values that are consistent with the values calculated from Eq. (5) (Table II).

Thus, the consideration of assisting hops within the proposed simplified model leads to more faithful parameters of the samples and improves the agreement between the estimates made on different sides of the crossover. We note that, as follows from a comparison of experimental data with the theory, the slight weakening of the temperature dependence in comparison with (1) predicted by our model permits the achievement of better agreement with experiment than does a simple change in T_1.

This work was supported by the Russian Foundation for Fundamental Research (Grant 97-02-18280) and INTAS (Grant 93-1555-ext).

[1] J. G. Massey and M. Lea, Phys. Rev. Lett. **75**, 4266 (1995).
[2] M. Pollak and M. Ortuno, in *Electron-Electron Interactions in Disordered Systems* (1985).

[3] B. I. Shklovskii and A. L. Efros, *Electronic Properties of Doped Semiconductors* (Elsevier, 1985).
[4] A. Perez-Garrido *et al.*, Phys. Rev. B **55**, R8630 (1997).
[5] A. G. Zabrodskiĭ and A. G. Andreev, JETP Lett. **58**, 809 (1993).
[6] I. Shlimak, Y. Kraftmakher, R. Ussyshkin, and K. Ziberg, Solid State Commun. **93**, 829 (1995).
[7] V. I. Kozub, Solid State Commun. **97**, 843 (1996).
[8] V. I. Kozub and I. Shlimak, in *Proceedings of the 14th International Conference ''Noise in Physical Systems,''* (Leuwen, 1997).
[9] B. I. Shklovskii and B. Z. Spivak, in *Hopping Transport in Solids*, edited by M. Pollak and B. Shklovskii (Elsevier, 1992).
[10] B. I. Shklovskiĭ, Fiz. Tekh. Poluprovodn. **17**, 2055 (1983) [Sov. Phys. Semicond. **17**, 1311 (1983)].
[11] N. V. Agrinskaya, V. I. Kozub, and D. V. Shamshur, Zh. Éksp. Tekh. Fiz. **107**, 2063 (1995) [J. Exp. Theor. Phys. **80**, 1142 (1995)]; N. V. Agrinskaya, V. I. Kozub, Phys. Status Solidi B **205** (1) 11, (1998).
[12] N. V. Agrinskaya, V. I. Kozub, R. Rench, P. Fozoni, and M. D. Li, Zh. Éksp. Teor. Fiz. **111**, 1477 (1997) [J. Exp. Theor. Phys. **84**, 814 (1997)].
[13] T. G. Gastner, in *Hopping Transport in Solids*, M. Pollak and B. Shklovskii [Eds.], Elsevier, (1992).
[14] M. L. Knotek and M. Pollak, Phys. Rev. B **9**, 664 (1974).
[15] S. D. Baranovskiĭ, B. I. Shklovskiĭ, and A. L. Éfros, Zh. Éksp. Teor. Fiz. **78**, 395 (1980) [Sov. Phys. JETP **51**, 199 (1980)].

Translated by P. Shelnitz

Erbium impurity atoms in silicon

V. F. Masterov, F. S. Nasredinov, P. P. Seregin, E. I. Terukov, and M. M. Mezdrogina

St. Petersburg State Technical University, 195251 St. Petersburg, Russia
(Submitted 29 December 1997; accepted for publication 31 December 1997)
Fiz. Tekh. Poluprovodn. **32**, 708–711 (June 1998)

It is shown using ^{169}Er(^{169}Tm) Mössbauer emission spectroscopy that the photoluminescent centers in crystalline erbium-doped silicon are [Er–O] clusters and that the local symmetry of the Er^{3+} ions in these clusters is similar to that in Er_2O_3. The photoluminescent centers in amorphous hydrogenated erbium-doped silicon are clusters, whose local structure also corresponds to erbium oxide. © *1998 American Institute of Physics.* [S1063-7826(98)01606-8]

The discovery of photoluminescence (PL) and electroluminescence at a wavelength of 1.54 μm in crystalline (c-Si) and amorphous hydrogenated silicon (a-Si:H) doped with erbium (c-Si⟨Er⟩ and a-Si⟨Er⟩)[1–4] has opened up prospects for using these materials to fabricate photo- and electroluminescent devices that can be integrated into silicon technology and can operate at the wavelength corresponding to minimum losses and minimum dispersion in fiber-optic communication lines. It has been established that the PL intensity depends on the erbium concentration N(Er) and increases, if oxygen is also introduced as an impurity, and that the oxygen concentration N(O) should be an order of magnitude greater than the erbium concentration.[4,5] According to Adler *et al.*,[6] in samples of c-Si⟨Er⟩ containing 10^{17} cm^{-3} oxygen, the optically active center is a cluster consisting of erbium and oxygen atoms [Er–O], in which the erbium ion is surrounded by six oxygen atoms, the local environment of erbium being close to its environment in Er_2O_3. Lowering the oxygen concentration to 10^{15} cm^{-3} leads to realization of the erbium ion environment characteristic of $ErSi_2$. A similar result is obtained following a low-temperature postimplantation anneal of silicon samples coimplanted with erbium and oxygen ($T_{ann}=400-600$ K),[7] while at $T_{ann}=600-900$ K the clusters have the Er_2O_3 structure; the fraction of clusters with the erbium oxide structure increase with increasing anneal temperature.

A theoretical treatment of the excitation of PL in c-Si ⟨Er⟩ also requires consideration of the emitting [Er–O] cluster, which has the form of a quantum dot with dimensions of the order of 10 Å.[7] Bresler *et al.*[3] believe that the emitting centers in a-Si:H⟨Er⟩ are also [Er–O] clusters, but they did not present any direct evidence to support this claim. We also note that c-Si⟨Er⟩ is characterized by strong PL quenching in the temperature range 77–300 K, while the PL intensity at room temperature is two orders of magnitude higher in a-Si:H⟨Er⟩ than in c-Si⟨Er⟩. This clearly points out a difference in the structure of the emitting centers in the crystalline and amorphous materials or a change in the electronic structure of silicon.[8]

In the present work the states of erbium impurity atoms in c-Si and a-Si:H were investigated by ^{169}Er(^{169}Tm) Mössbauer emission spectroscopy for the purpose of identifying the symmetry of the local environment of the erbium ions in these materials.

EXPERIMENT

The preliminary results were published in Ref. 9. Single-crystal samples of c-Si⟨Er⟩ were obtained by the diffusion doping of c-Si with an oxygen concentration $N(O)\simeq 10^{17}$ or $N(O)\simeq 2\times 10^{19}$ cm^{-3}. The erbium concentration was 5×10^{18} cm^{-3}, and the thickness of the diffusion layer with uniform doping was equal to about 50 μm. Films of a-Si:H ⟨Er⟩ were obtained by the magnetron sputtering of a target of metallic erbium in an atmosphere of silane and argon. The films were sputtered onto an Al substrate, which was at a temperature of 300 °C. The oxygen concentration in all the films investigated was constant and equal to 5×10^{21} cm^{-3}, the hydrogen concentration was between 9 and 11 at. %, and the erbium concentration in the films investigated varied from 10^{19} to 10^{21} cm^{-3}.

Mössbauer sources were produced by irradiating samples of c-Si⟨Er⟩ and a-Si:H⟨Er⟩ in a stream of thermal neutrons with a flux of the order of 5×10^{18} cm^{-2}. The Mössbauer spectra were measured on an industrial SM-2201 spectrometer at 295 K with an absorber in the form of thulium ethylsulfate (the surface density was 5 mg/cm^2 with respect to thulium).

RESULTS AND DISCUSSION

Typical Mössbauer spectra of different Si:Er samples are presented in Figs. 1 and 2. As is seen from the figures, they are the result of the superposition of a quadrupole doublet (spectrum I) and a single line (spectrum II). The ratio between the areas under spectra I and II depends on the type of matrix (amorphous or crystalline), the erbium concentration, and the oxygen concentration. The parameters of the spectra are listed in Table I.

In interpreting the ^{169}Er(^{169}Tm) Mössbauer spectra it should be borne in mind that the ^{168}Er$(n,\gamma)^{169}$Er thermal-neutron capture reaction followed by the β decay of ^{169}Er (see Fig. 3) results in the appearance of the Mössbauer isotope (probe) ^{169}Tm at erbium sites. In the ^{169}Tm Mössbauer spectra there is practically no isomer shift, but the magnitude of the quadrupole splitting is significantly dependent on the

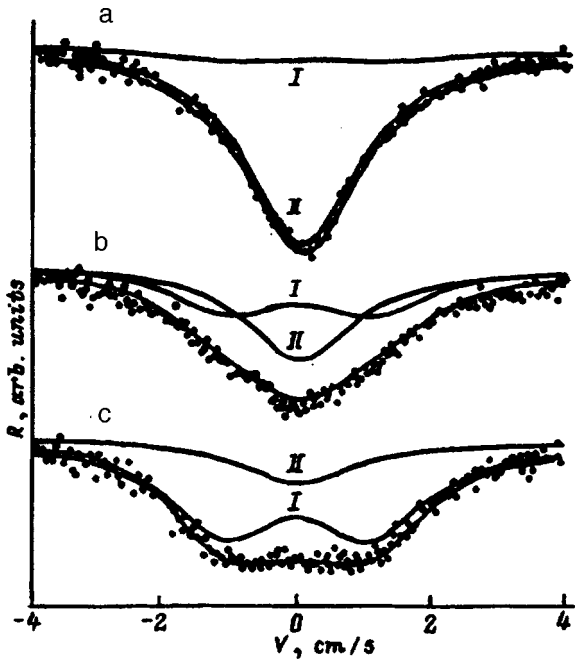

FIG. 1. Mössbauer emission spectra $[R(V)]$ for ^{169}Er(^{169}Tm) in a-Si:H⟨Er⟩ samples at $T=295$ K. Here R is the relative counting rate. Erbium concentration N(Er), 10^{20} cm^{-3}: a — 5, b, c — 1.1. Spectrum c was obtained after the sample was annealed at 800 °C for 2 h in a vacuum. The solid lines show the spectral components of types I and II.

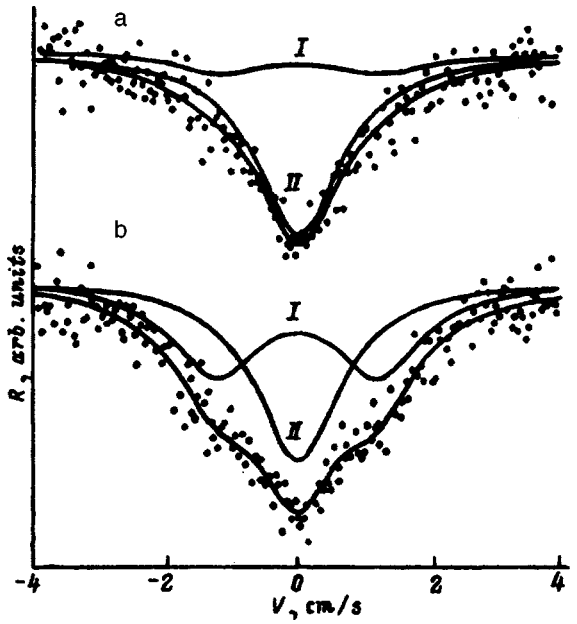

FIG. 2. Mössbauer emission spectra $[R(V)]$ for ^{169}Er(^{169}Tm) in samples of c-Si⟨Er⟩ at $T=295$ K. Oxygen concentration N(O), cm^{-3}: a — 10^{17}, b, — 2×10^{19}. The position of the spectra of types I and II is shown.

symmetry of the local environment of the probe. Thus, ^{169}Er (^{169}Tm) Mössbauer emission spectroscopy provides information on the symmetry of the local environment of the erbium atoms. In particular, as is seen from Figs. 1 and 2, the spectra of the c-Si⟨Er⟩ and a-Si:H⟨Er⟩ samples correspond to two states of the erbium impurity atoms in the structure of the material, spectrum I corresponding to erbium centers with lowered symmetry of the local environment and spectrum II corresponding to erbium centers in an almost regular cubic environment.

The PL spectra of a-Si:H⟨Er⟩ were measured at room temperature. The PL was excited by an argon laser. These spectra display two lines: intrinsic PL of a-Si:H (at $\lambda\simeq1.35$ μm) and PL caused by intercenter $f-f$ transitions in the Er^{3+} ion (at $\lambda\simeq1.54$ μm). Figure 4 presents the dependence of the PL intensity at $\lambda=1.54$ μm on the erbium concentration, from which it is seen that the PL intensity reaches its maximum value when $N(\mathrm{Er})\simeq5\times10^{20}$ cm^{-3}.

Figure 4 also shows the dependence of the fraction P of erbium centers in state I on the erbium concentration

$$P=S(I)/[S(I)+S(II)],$$

where $S(I)$ and $S(II)$ are the areas under Mössbauer spectra I and II, respectively. Data from our work[9] were also used to construct this dependence. Since, as is seen from Fig. 4, the relative intensity of spectrum I increases as the PL intensity increases, just these erbium states are responsible for the PL of the a-Si:H⟨Er⟩ samples. The parameters of spectrum I are close to the parameters of the Mössbauer emission spectrum of $^{169}Er_2O_3$ [$IS=0$, $QS=2.4$ cm/s (Ref. 9)], allowing us to conclude that the PL centers are clusters formed by erbium and oxygen. The fraction of such clusters should increase as the erbium concentration increases in the range N(Er) $<N$(O), since the unit cell of erbium oxide contains 32 erbium atoms and 48 oxygen atoms, and this fraction should decrease as the erbium concentration increases in the range N(Er)$>N$(O). Just this picture is observed in the experi-

TABLE I. Parameters of the ^{169}Er(^{169}Tm) Mössbauer emission spectra.

			Spectrum I			Spectrum II		
Sample	N(Er), cm^{-3}	N(O), cm^{-3}	IS, [a] cm/s	QS,cm/s	W, cm/s	IS, cm/s	W, cm/s	R
c-Si⟨Er⟩	5×10^{18}	10^{17}	0.0	2.5	1.6	0.0	1.6	0.17
c-Si⟨Er⟩	5×10^{18}	2×10^{19}	0.0	2.5	1.6	0.0	1.6	0.17
a-Si:H⟨Er⟩	1.1×10^{20}	4×10^{21}	0.0	2.2	2.0	0.0	2.0	0.48
a-Si:H⟨Er⟩*	1.1×10^{20}	4×10^{21}	0.0	2.2	2.0	0.0	2.0	0.80
a-Si:H⟨Er⟩	6×10^{20}	4×10^{21}	0.0	2.2	2.0	0.0	2.0	0.12

Note: IS — isomer shift, *QS* — quadrupole splitting, *W* — linewidth, *R* — relative intensity of spectrum I.
*This sample was subjected to an anneal at 800 °C for 2 h in a vacuum.

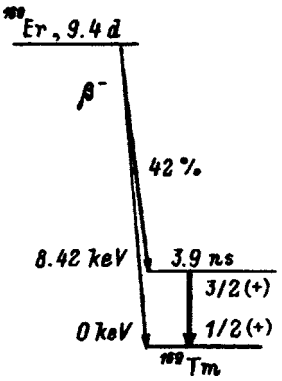

FIG. 3. Diagram showing the formation of the ^{169}Tm Mössbauer level.

ment. Spectrum II should clearly be assigned to erbium ions having only silicon atoms in their environment (by analogy with the environment of erbium in $ErSi_2$).

The spectrum of type I for c-Si⟨Er⟩ should clearly be assigned to the erbium centers responsible for PL, while the spectrum of type II should be assigned to optically inactive centers. We note that the magnitude of the quadrupole splitting in the spectrum of type I is different for crystalline and amorphous silicon (see Table I). This finding should be attributed to the different nature of the clusters formed by erbium and oxygen atoms in c-Si and a-Si:H. In crystalline silicon the [Er–O] cluster has a structure close to the crystal structure of Er_2O_3 (see Refs. 6 and 7), while, according to the magnitude of the quadrupole splitting ($QS=2.2$ cm/s), the structure of the cluster is somewhat different in amorphous silicon. Two points should be noted. First, in the Er_2O_3 crystal lattice there are two sites for erbium atoms with C_2 and C_3 symmetry, which are not resolved in the Mössbauer spectra. Since the quadrupole splitting of the spectrum has contributions from two electric field gradients: a crystalline contribution, which is created by the ions surrounding the Mössbauer atom, and a valence contribution, which is caused by the nonspecific distribution of the charge density of the outer (valence) electrons of the Mössbauer ion itself. As a rule, these contributions have opposite signs. Since the erbium ion has a $4f^{11}$ electronic configuration in both crystalline and amorphous samples and since, according to electron spin resonance investigations, the $4f$ states of rare-earth impurity atoms in semiconductors scarcely hybridize with states of atoms in the environment, the change in the total quadrupole splitting should be attributed to the difference in the local symmetry of the erbium atoms in the [Er–O] clusters in amorphous and crystalline silicon. This is perfectly natural in view of the different structures of the matrices.

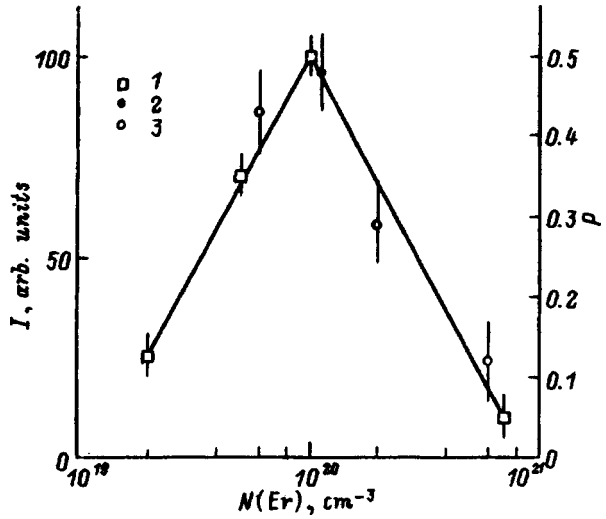

FIG. 4. Dependence of the relative PL intensity at $\lambda=1.54$ μm (points *1*, left-hand scale) and the relative spectral component of type I (points *2* and *3*, right-hand scale) for a-Si:H⟨Er⟩ at $T=295$ K on the erbium concentration N(Er). Points *3* were taken from Ref. 9.

We annealed a sample of a-Si:H⟨Er⟩ with an erbium concentration of 5×10^{20} cm^{-3} at 800 °C for 2 h in a vacuum. The anneal led to the complete removal of hydrogen from the film and crystallization of the latter. According to the data in Ref. 4, the PL intensity at room temperature increases sharply during this process, and, as is seen from a comparison of spectra b and c in Fig. 1, the fraction of erbium centers in state I increases simultaneously (see also Table I). This clearly provides additional evidence of the validity of our hypothesis that state I is responsible for the PL process. We note that the anneal just described is not accompanied by any changes in the parameters of spectrum I; i.e., the change in the structure of the matrix does not lead to a change in the local structure of the erbium atoms in previously formed [Er–O] clusters. This is possible provided a fairly large cluster with dimensions of the order of the lattice constant of erbium oxide forms, i.e., in the model proposed in Ref. 10. The formation of new clusters during a high-temperature anneal apparently takes place already in the amorphous phase. There are two reasons for the increase in the fraction of Er_2O_3 clusters when amorphous silicon crystallizes: first, there is an increase in the concentration of free oxygen, which was previously bound to hydrogen, in the sample, and, second, as was established in Ref. 7, the efficiency of the formation of [Er–O] clusters in crystalline silicon increases as the anneal temperature is increased. A similar effect can also occur in amorphous silicon. We recall that the substrate temperature was equal to 300 °C when the amorphous films were prepared. According to the results in Ref. 7, only clusters with an $ErSi_2$ structure form in crystalline silicon when the postimplantation anneal temperature is 400 °C.

Thus, it has been established as a result of this investigation that the optically active centers in crystalline and amorphous silicon doped with erbium and oxygen are [Er–O] clusters and that the local symmetry of the Er^{3+} ions in these clusters is similar to that in Er_2O_3.

This work was supported in part by INTAS and the Russian Foundation for Fundamental Research (INTAS–RFBR Grant No. 95 0531).

[1] H. Ennen, J. Schneider, G. Pomrenke, and A. Axmann, Appl. Phys. Lett. **43**, 943 (1983).
[2] H. Ennen, G. Pomrenke, A. Axmann, K. Eisele, W. Haydl, and J. Schneider, Appl. Phys. Lett. **46**, 381 (1985).
[3] M. S. Bresler, O. B. Gusev, V. Kh. Kudoyarova, A. N. Kuznetsov, P. E.

Pak, E. I. Terukov, I. N. Yassievich, and B. P. Zaharchenya, Appl. Phys. Lett. **67**, 3599 (1995).
[4] E. I. Terukov, V. Kh. Kudoyarova, M. M. Mezdrogina, V. G. Golubev, A. Sturm, and W. Fuhs, Fiz. Tekh. Poluprovodn. **30**, 820 (1996) [Semiconductors **30**, 440 (1996)].
[5] A. Polman, G. N. van den Hoven, J. S. Custer, J. H. Shin, R. Serna, and P. F. A. Alkemade, J. Appl. Phys. **77**, 1256 (1995).
[6] D. L. Adler, D. C. Jacobson, D. J. Eaglesham, M. A. Marcus, J. L. Benton, J. M. Poate, and P. H. Citrin, Appl. Phys. Lett. **61**, 2181 (1992).
[7] A. Terrasi, G. Franzo, S. Coffa, F. Priolo, F. D'Acapito, and S. Mobilio, Appl. Phys. Lett. **70**, 1712 (1997).
[8] V. F. Masterov and L. G. Gerchikov, Mater. Res. Soc. Symp. Proc. **422**, 227 (1996).
[9] V. F. Masterov, F. S. Nasredinov, P. P. Seregin, V. Kh. Kudoyarova, A. N. Kuznetsov, and E. I. Terukov, Pis'ma Zh. Tekh. Fiz. **22**(23), 25 (1996) [Tech. Phys. Lett. **22** (12), 960 (1996)].

Translated by P. Shelnitz

Oxygen precipitates and the formation of thermal donors in silicon

N. V. Vabishchevich, D. I. Brinkevich, and V. S. Prosolovich

Polotsk State University, 211440 Novopolotsk, Belarus
(Submitted 2 June 1997; accepted for publication 7 June 1997)
Fiz. Tekh. Poluprovodn. **32**, 712–713 (June 1998)

It is established by infrared spectroscopy and Hall measurements that the oxygen precipitates formed during preliminary high-temperature treatment suppress the generation of thermal donors in Si grown either by the Czochralski method or by applying a magnetic field to a melt. Possible mechanisms for the influence of precipitation on the formation of thermal donors are proposed. © *1998 American Institute of Physics.* [S1063-7826(98)01706-2]

It is known that the formation of oxygen-containing thermal donors in Si is influenced to a significant extent by preliminary heat treatment of the crystals. Markevich *et al.*[1,2] showed that even a brief preanneal in the temperature range 530–800 °C leads to a decrease in the concentration of the nucleation centers for these defects. On the other hand, oxygen precipitates, which have a significant influence on the interactions of defects and impurities in the crystal, form in Si during a high-temperature treatment (800–1100 °C).[3] However, the influence of oxygen precipitates on the efficiency of thermal donor generation has not been adequately studied and is an important problem in the practical sense.

In our study we used samples cut from wafers of dislocation-free Si with a resistivity of 20 $\Omega \cdot$cm, which were grown by the Czochralski method (Cz–Si), as well as by applying magnetic fields to a melt (M–Si). The parameters of the samples investigated are presented in Table I. To anneal the thermal donors appearing during growth, all the samples were subjected to a stabilizing heat treatment at 650 °C for 1 h. Some of the samples were subjected to a high-temperature anneal in a hydrogen atmosphere for 5 h at 925 °C (Cz–Si) or 7 h at 1000 °C (M–Si).

The thermal donors were generated in air during a heat treatment lasting up to 50 h at 450 °C. The concentration N_O of oxygen in interstitial positions was determined by IR spectroscopy from the intensity of the absorption band at 1106 cm^{-1}. The carbon content in substitutional positions did not exceed 2×10^{16} cm^{-3} in any of the samples. The Hall effect and the conductivity were measured using standard methods at room temperature.

The high-temperature anneal lowers the efficiency of thermal donor generation only in samples with a high oxygen content (Fig. 1). It is significant that in samples with $N_O < 7\times10^{17}$ cm^{-3} the initial rate of formation and the maximum attainable concentration of thermal donors following the high-temperature anneal described were even somewhat higher than the corresponding values for samples that were cut from the same wafer, but not subjected to preliminary high-temperature heating.

Intense oxygen precipitation took place during the high-temperature anneal in the samples with a high oxygen concentration; the rate of removal of the impurity from interstitial positions increased with N_O. The duration of the high-temperature treatment was chosen so that the concentrations of interstitial oxygen in the samples would be comparable (see Table I, samples *1–3* and *4–5*). This circumstance permitted a detailed examination of the influence of oxygen precipitates on the generation of thermal donors. For example, samples *1–3* and samples *4* and *5* had similar values of N_O following the high-temperature anneal, but the content of oxygen precipitates in them differed significantly. In samples *3* and *5* the dominant portion of the oxygen was found in precipitates ($\sim8.3\times10^{17}$ and $\sim4.8\times10^{17}$ cm^{-3}, respectively). In samples *1*, *2*, and *4* no appreciable removal of atoms of this impurity from interstitial positions was observed during the heating (see Table I), and the concentration of precipitates was close to zero. It is significant (Fig. 2) that in samples *3* and *5*, which contained oxygen precipitates, the efficiency of thermal donor generation was considerably lower than in samples *1*, *2*, and *4*, which did not contain oxygen precipitates. Since these samples had identical thermal histories and did not differ with respect to their content of oxygen in interstitial positions, the following conclusion can be drawn: oxygen precipitates effectively suppress the generation of thermal donors, lowering both the initial rate of formation and the maximum attainable concentration of thermal donors.

It has been theorized[2,4] that the formation of oxygen-containing thermal donors involves the successive addition of definite structural units to thermal donor nucleation centers, which can be electrically inactive complexes consisting of three oxygen atoms. The nature of the mobile particles participating in the formation of thermal donors has not yet been conclusively established. However, it is known that they must include one oxygen atom. It was also previously noted in Ref. 5 that the concentration of the mobile particles does not depend on the thermal history of the crystals and is determined only by the value of N_O.

It has not been ruled out that there are several mechanisms which account for the influence of oxygen precipitates on the generation of thermal donors. For example, it can be asserted *a priori* that prolonged high-temperature treatment accompanied by the intense precipitation of oxygen eliminates the correlated distribution of oxygen atoms and ultimately leads to a decrease in the number of thermal donor

TABLE I. Oxygen concentration N_O in the samples investigated.

Sample	Type of sample [a]	N_O, 10^{17} cm^{-3}	
		Original Si	HTA Si
1	Cz–Si	5.55	5.32
2	Cz–Si	5.37	5.20
3	Cz–Si	13.5	5.21
4	M–Si	7.28	7.15
5	M–Si	12.0	7.20

Note: Cz — Czochralski method, M — melt in a magnetic field, HTA — Si after a high-temperature anneal.

nucleation centers and significant alteration of their accumulation kinetics.[2]

In addition, the introduction of precipitates can lead to the appearance of internal fields of elastic stresses in crystals.

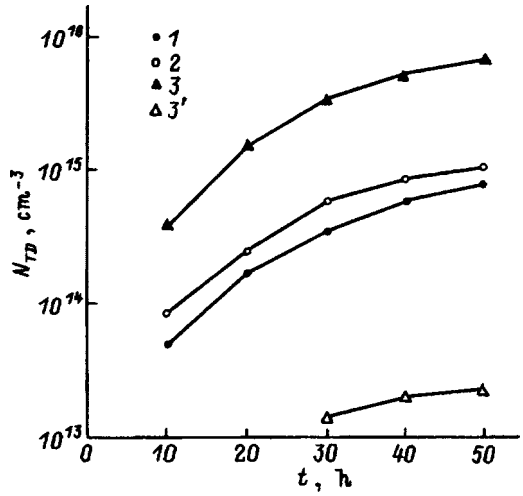

FIG. 1. Kinetic plots of the generation of thermal donors in Cz–Si. The numbers of the curves correspond to the numbers of the samples in Table I. Duration of the high-temperature anneal t, h: *1*, *3* — 0; *1′*, *3′* — 5.

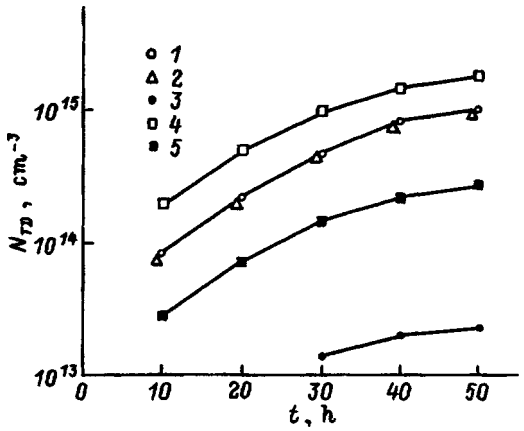

FIG. 2. Kinetic plots of the accumulation of thermal donors in samples that have undergone a high-temperature anneal. The numbers of the curves correspond to the numbers of the samples in Table I. Concentration of oxygen in precipitates N_O^p, cm^{-3}: *1*, *2*, *4* — below 10^{17}; *3*, *5* — above 4×10^{17}.

Such fields can alter the potential well near the nucleation centers and raise the energy barrier to the capture of mobile particles by these centers. However, the ''capture'' of mobile particles by oxygen precipitates, which excludes part of the oxygen atoms from the reactions leading to the formation of thermal donors, is more likely.

[1] V. P. Markevich, L. I. Murin, and A. G. Litvinenko, Fiz. Tekh. Poluprovodn. **21**, 1267 (1987) [Sov. Phys. Semicond. **21**, 767 (1987)].
[2] V. P. Markevich and L. I. Murin, Phys. Status Solidi A **111**, K149 (1989).
[3] K. V. Ravi, *Imperfections and Impurities in Semiconductor Silicon*, Wiley, New York (1981) [Russ. trans., Mir, Moscow (1984)].
[4] D. I. Brinkevich, V. P. Markevich, L. I. Murin, and V. V. Petrov, Fiz. Tekh. Poluprovodn. **26**, 679 (1992) [Sov. Phys. Semicond. **26**, 383 (1992)].
[5] V. P. Markevich and L. I. Murin, Fiz. Tekh. Poluprovodn. **25**, 262 (1991) [Sov. Phys. Semicond. **25**, 158 (1991)].

Translated by P. Shelnitz

Induced photopleochroism of *p*-GaAlAs/*p*–*n*-GaAs structures

A. Berdinobatov, N. Nazarov, and V. M. Sarkisova

Physicotechnical Institute, Turkmenistan Academy of Sciences, 744000 Ashgabad, Turkmenistan

V. Yu. Rud'

St. Petersburg State Technical University, 195251 St. Petersburg, Russia

Yu. V. Rud'

A. F. Ioffe Physicotechnical Institute, Russian Academy of Sciences, 194021 St. Petersburg, Russia
(Submitted 29 October 1997; accepted for publication 3 November 1997)
Fiz. Tekh. Poluprovodn. **32**, 714–717 (June 1998)

The polarization photosensitivity appearing when linearly polarized radiation impinges obliquely on the reception plane coated by the anodic oxide in anodic-oxide/*p*-$Ga_{0.3}Al_{0.7}As$/*p*–*n*-GaAs photoconverter structures is investigated experimentally. It is established that the induced photopleochroism of the structures increases with increasing angle of incidence according to a quadratic law and is determined in the long-wavelength spectral region ($\hbar\omega<1.5$ eV) by optical processes on the air/anodic-oxide interface. The ''dip'' discovered in the spectral dependence of the induced photopleochroism coefficient in the 1.6 to 3-eV range is associated with bleaching, for which a drop in the induced photopleochroism ($\mathcal{P}_I\rightarrow 0$) can serve as a criterion. It is concluded that polarization spectroscopy can be employed for the diagnostics of bleaching in GaAlAs/GaAs photoconverter structures. © *1998 American Institute of Physics.* [S1063-7826(98)01806-7]

1. The discovery and creation of ideal heterojunctions in the GaAlAs/GaAs system in the A. F. Ioffe Physicotechnical Institute led, in their time, to the development of an extensive group of semiconductor devices of a new generation: semiconductor lasers, highly efficient solar photoconverters, etc.[1–7] However, photoconversion has heretofore been investigated in such heterostructures only with respect to natural radiation. In this paper we report the results of the first experimental study of the polarization photosensitivity appearing under the conditions of the oblique incidence of linearly polarized radiation in *p*-GaAlAs/*p*–*n*-GaAs heterostructures coated by an anodic oxide.[8,9]

2. The photoconverter structures were produced by liquid-phase epitaxy from a limited volume of a solution-melt of the Ga-Al-As system on single-crystal GaAs wafers oriented in the (100) crystallographic plane at ~850 °C. The GaAs substrates were doped with tellurium to a free-electron concentration $n_n=(3-5)\times 10^{17}$ cm^{-3} at $T=300$ K. The AlAs content in the wide-gap GaAlAs layers was ~70%. Epitaxial layers with a thickness of 2 μm were doped by introducing Zn and Mg as impurities into the solution-melt to create a free-hole concentration $n_p\simeq 10^{18}$ cm^{-3} at 300 K. Immediately after epitaxy, an oxide film with a thickness of ~1500 Å was formed on the wide-gap surface of the structure during anodic oxidation in an acidic solution.[10] Such a single-layer coating causes bleaching of the wide-gap surface of the structure, permitting significant reduction of the losses due to reflection and the achievement of an efficiency in the GaAlAs/GaAs photoconverters as high as 20–25%.[7,11] Ohmic contacts to the *n*-GaAs substrate and the illuminated *p*-GaAlAs surface were created as a result of the electrochemical deposition of Ni. After the ohmic contacts were deposited, the structures were subjected to heat treatment at 550 °C in a hydrogen atmosphere for ~2 min. The area of the *p*-GaAlAs/*p*–*n*-GaAs structures studied was 10–20 mm^2.

3. A typical stationary current-voltage characteristic of one of the structures studied is presented in Fig. 1 (curve *1*). The linear branch of these structures at bias voltages $U>0.8$ V obeys the relation $U=U_0+R_0\cdot I$. The cutoff voltage $U_0=0.8$ V. This value is faithfully reproduced in the structures obtained and corresponds to the contact potential difference. The residual resistance $R_0=(2-4)\times 10^3$ Ω at 300 K. The maximum current photosensitivity of these structures reaches ~80 mA/W under AM1.5 illumination conditions. The photoconversion efficiency of the structures investigated reaches ~20%.

The spectral dependence of the relative photoconversion quantum efficiency η for a typical structure under illumination by natural radiation along a normal to the plane of the anodic oxide is presented in Fig. 1 (curve *2*). The long-wavelength exponential increase in η is characterized by a slope $S=d(\ln\eta)/d(\hbar\omega)=60-70$ eV^{-1} for different structures, which corresponds to direct interband transitions in the narrow-gap component, and the energetic position of the long-wavelength edge and the deviation from the exponential course at $\hbar\omega>1.41$ eV are in good agreement with the gap width of GaAs.[5] As a rule, all the structures obtained exhibit a spectral dependence of η with a broad-band character. The beginning of an appreciable short-wavelength drop in η is

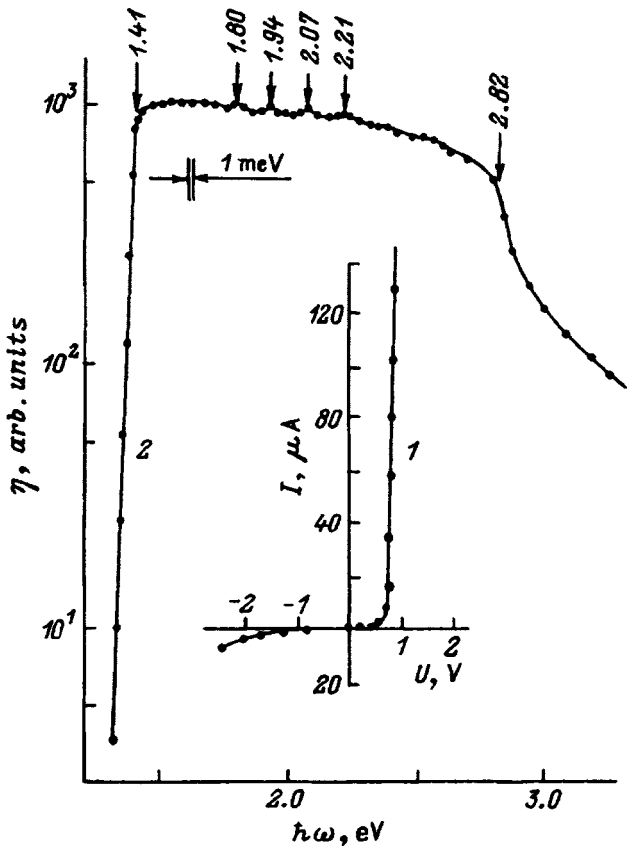

FIG. 1. Stationary current-voltage characteristic (*1*) and spectral dependence of the relative photoconversion quantum efficiency (*2*) of an anodic-oxide/p-$Ga_{0.3}Al_{0.7}As$/$p-n$-GaAs structure under illumination by natural light ($T=300$ K).

observed at photon energies $\hbar\omega > 2.2$ eV, which can be attributed to the onset of interband transitions in the wide-gap layer. The enhancement of the short-wavelength drop in η at $\hbar\omega > 2.8$ eV is apparently attributable to an increase in absorption in the anodic oxide layer. The value of the full width of the spectral dependence of η at half-maximum $\delta_{1/2} = 1.7-1.8$ eV can be cited as a quantitative characteristic of the wide-gap character of the photoconversion. This value was faithfully reproduced for all the structures obtained. Attention should also be focused on the appearance of several equidistant maxima on the spectral dependence of η (Fig. 1), which can be caused by interference of the incident radiation in the anodic oxide layer or in the $Ga_{0.3}Al_{0.7}As$ wide-gap epitaxial layer. The estimate of the refractive index from the formula

$$n = \lambda_m \cdot \lambda_{m-1} / 2d(\lambda_m - \lambda_{m-1}), \tag{1}$$

where λ_m and λ_{m-1} are the wavelengths corresponding to neighboring maxima in the photosensitivity spectrum (Fig. 1), and m is the number of the maximum, allows us to attribute the features observed to interference in the GaAlAs layer.

4. The measurements of the photosensitivity of the anodic-oxide/p-GaAlAs/$p-n$-GaAs structures with illumination along a normal to the plane of the oxide (the angle of incidence $\theta = 0$) by linearly polarized radiation allow us to assume that the short-circuit photocurrent does not depend on the orientation of the electric vector **E** of the light wave relative to the crystallographic axis in the GaAlAs layer and the GaAs substrate. In general, this result is not unexpected and is due to the isotropic properties of the absorbing medium, as well as the absence of any straining of the epitaxial layer as it grows on a substrate with the same type of crystal structure and very similar crystal-lattice parameters. As a result of this feature of GaAs and the solid solution GaAlAs, the natural photopleochroism $\mathcal{P}_N = 0$ when $\theta = 0°$ over the entire photosensitivity region of these structures.

In the case of the oblique incidence of linearly polarized radiation, as θ is increased, the photopleochroism $\mathcal{P}_I$ begins to appear in the structures produced. Its magnitude can be determined from the relation

$$\mathcal{P}_I = \left(\frac{i^p - i^s}{i^p + i^s} \right) \cdot 100\%, \tag{2}$$

where i^p and i^s are the photocurrents for $\mathbf{E} \| \mathrm{PI}$ and $\mathbf{E} \perp \mathrm{PI}$, respectively, and PI denotes the plane of incidence of the linearly polarized radiation. Examples of the dependences of the photocurrents and $\mathcal{P}_I$ on the angle of incidence of the linearly polarized radiation onto the reception plane obtained for several values of the energy of the incident photons for one of the structures investigated are presented in Figs. 2a–2c. The main laws governing the measurements of the photosensitivity of the structures studied in this work reduce to the following. The induced photopleochroism increases with the angle of incidence over the entire photoconversion region according to a quadratic law $\mathcal{P}_I \sim \theta^2$ (Fig. 2, curves *3* and *4*), in agreement with the conclusions in Ref. 8. While the character of the angular dependence of $\mathcal{P}_I(\theta)$ remained unchanged over the entire spectral photosensitivity region, the value at $\theta = \mathrm{const}$ was found to depend on the energy of the incident photons. On the basis of Eq. (2), this can be a consequence of changes in the angular dependences of $i^p(\theta)$ and $i^s(\theta)$ over the spectrum. The results of the investigations of $i^p(\theta)$ and $i^s(\theta)$ performed allow us to conclude that in the long-wavelength spectral photosensitivity region ($\hbar\omega < 1.5$ eV) these dependences correspond to the those expected from an analysis of the optical processes using Fresnel's relations.[12,13] An example of these dependences is presented in Fig. 2a (curves *1* and *2*). In fact, in the case of $\mathbf{E} \| \mathrm{PI}$ polarization, the photocurrent at first increases with the angle of incidence, passes through a maximum near $\theta \simeq 70°$, and begins to decrease sharply at $\theta > 70°$. The ratio $i^p_{70°}/i^p_{0°} = 1.2$, which corresponds to elimination of the losses due to reflection. For an orthogonal wave with $\mathbf{E} \perp \mathrm{PI}$ an increase in $\theta > 0°$ is accompanied by a monotonic decrease in the photocurrent (Fig. 2a, curve *2*).

In the short-wavelength photosensitivity region at $\hbar\omega > 1.5$ eV the law for $i^p(\theta)$ considered above is maintained (Figs. 2b and 2c, curves *1*), while the $i^s(\theta)$ curves become similar to $i^p(\theta)$. This allows us to attribute the present result, as in the case of $i^p(\theta)$, to the elimination of the losses due to reflection for $\mathbf{E} \perp \mathrm{PI}$. This law cannot be explained on the basis of Fresnel's relations,[12,13] but can be a consequence of interference effects. A comparison of the $i^p(\theta)$ and $i^s(\theta)$ curves (Figs. 2b and 2c) also reveals that the $i^p(\theta)$ and $i^s(\theta)$

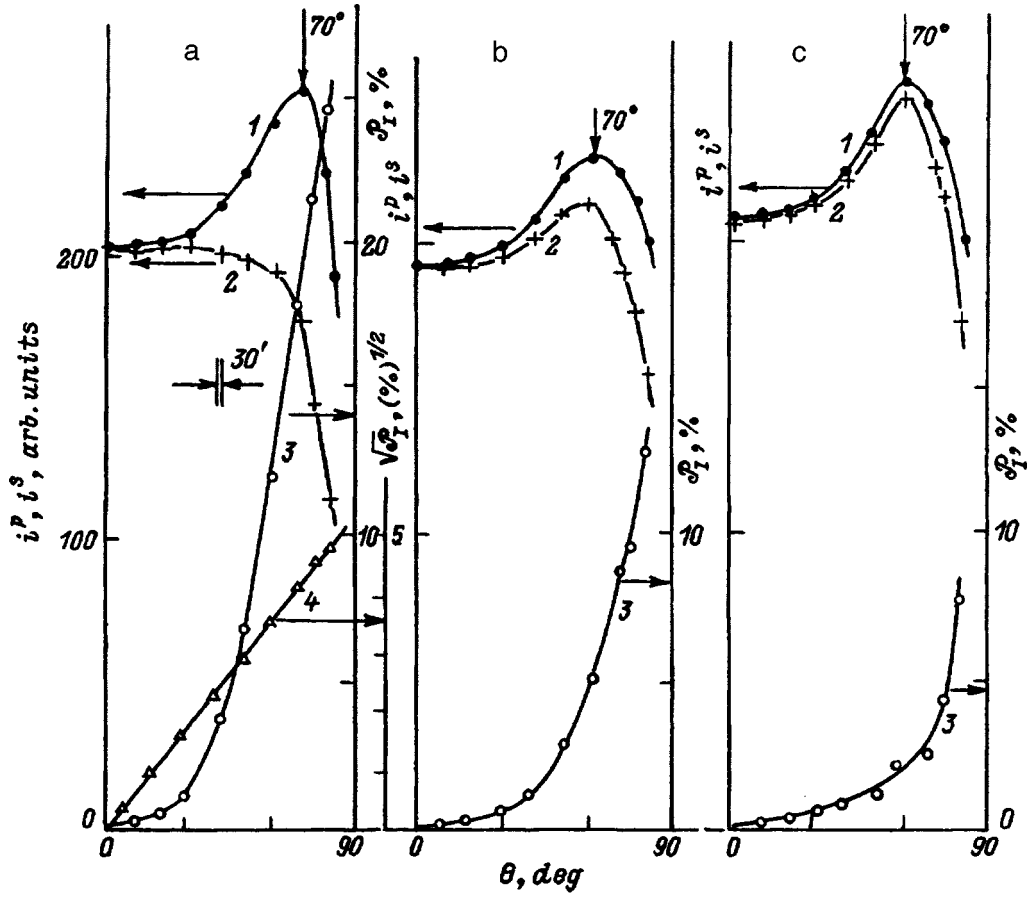

FIG. 2. Dependence of the short-circuit photocurrent (*1* — i^p, *2* — i^s) and the induced photopleochroism (*3*, *4*) of an anodic-oxide/p-$Ga_{0.3}Al_{0.7}As$/$p-n$-GaAs structure on the angle of incidence of linearly polarized radiation onto the plane of the anodic oxide ($T=300$ K, $\hbar\omega$, eV: a — 1.42, b — 1.77, c — 2.07).

curves approach one another with a resultant drop in the value of the induced photopleochroism. Similar laws were previously established in other structures, which also exhibited interference phenomena.[14,15]

The spectral dependence of the induced photopleochroism for one of the anodic-oxide/p-GaAlAs/$p-n$-GaAs structures is presented in Fig. 3. Its characteristic feature is a strong dependence of $\mathcal{P}_I$ on the photon energy. Only in the long-wavelength region ($\hbar\omega \lesssim 1.4$) is the photopleochroism nearly constant, as it is for surface-barrier structures on, for example, GaAs[9] over the entire photosensitivity region. If, according to Ref. 16, the refractive index is estimated from the experimentally obtained value $\mathcal{P}_I \simeq 20-22\%$ (Fig. 3), we obtain $n=1.8$, which coincides with the known value for the anodic oxide on GaAlAs.[10] On this basis the induced photopleochroism of the structures produced in the long-wavelength region can be attributed to optical processes on the air/anodic-oxide boundary. The ''dip'' on the spectral dependence observed in the range of incident photon energies from 1.5 to 3 eV can be associated with bleaching phenomena. This is evidenced by the plots of $i^p(\theta)$ and $i^s(\theta)$ (Figs. 2b and 2c). When the losses due to reflection begin to decrease with increasing angles of incidence for both polarizations, this ultimately leads to the approach of the values ($i^s \rightarrow i^p$), which results in lowering of the induced photopleochroism. As is seen from (2), this effect is strongest under the condition $i^p = i^s$. Therefore, the region of maximum bleaching can easily be determined on the basis of polarization measurements of the photosensitivity of structures with an antireflection coating. It follows from Fig. 3 that maximum bleaching is provided in the structures obtained in the

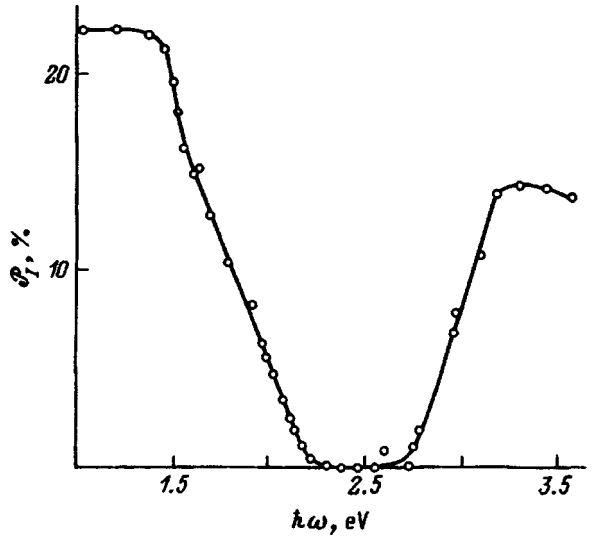

FIG. 3. Spectral dependence of the induced photopleochroism of an anodic-oxide/p-$Ga_{0.3}Al_{0.7}As$/$p-n$-GaAs structure ($T=300$ K, $\theta=75°$).

range from 2.2 to 2.8 eV, where $\mathcal{P}_I = 0$. Clearly, such a quick method for determining the bleaching region can make it possible to correct the conditions for the fabrication of structures in the direction required by a specific practical problem.

In summary, the application of polarization photoelectric spectroscopy to p-GaAlAs/$p-n$-GaAs photoconverter structures permits determination of the magnitude and spectral region for bleaching, opening up new possibilities for diagnostics in industrial processes for fabricating highly efficient photoconverters of solar radiation.

[1] Zh. I. Alfërov, V. M. Andreev, E. L. Portnoĭ, and N. I. Protasov, Fiz. Tekh. Poluprovodn. **3**, 1324 (1969) [Sov. Phys. Semicond. **3**, 1103 (1970)].
[2] Zh. I. Alfërov, V. M. Andreev, N. S. Zimogorova, and D. N. Tret'yakov, Fiz. Tekh. Poluprovodn. **3**, 1633 (1969) [Sov. Phys. Semicond. **3**, 1373 (1970)].
[3] Zh. I. Alfërov, V. M. Andreev, V. I. Korol'kov, S. G. Konnikov, S. Tabarov, and F. M. Tadzhibaev, Fiz. Tekh. Poluprovodn. **12**, 285 (1978) [Sov. Phys. Semicond. **12**, 164 (1978)].
[4] Zh. I. Alfërov and B. V. Tsarenkov, Fiz. Tekh. Poluprovodn. **19**, 2113 (1985) [Sov. Phys. Semicond. **19**, 1303 (1985)].
[5] A. G. Milnes and D. L. Feucht, in *Heterojunctions and Metal–Semiconductor Junctions*, Academic Press, New York (1972) [Russ. trans., Mir, Moscow (1975)].
[6] B. L. Sharma and R. K. Purohit, *Semiconductor Heterojunctions*, Pergamon Press, Oxford (1974) [Russ. trans., Sov. Radio, Moscow (1979)].
[7] A. N. Imenkov, A. A. Stamkulov, T. I. Taurbaev, B. V. Tsarenkov, V. F. Shorin, and Yu. P. Yakovlev, Fiz. Tekh. Poluprovodn. **12**, 948 (1978) [Sov. Phys. Semicond. **12**, 559 (1978)].
[8] Yu. V. Rud' and G. A. Medvedkin, USSR Inventor's Certificate (Patent) No. 671 634; Byull. Izobret., No. 41, 291 (1980).
[9] S. G. Konnikov, D. Melebaev, V. Yu. Rud', and M. Serginov, Pis'ma Zh. Tekh. Fiz. **18** (12), 39 (1992) [Sov. Tech. Phys. Lett. **18** (6), 382 (1992)].
[10] I. N. Sorokin, V. Z. Petrova, Yu. D. Chistyakov, N. R. Aigina, and L. E. Gat'ko, Zarubezh. Elektron. Tekhnol. 14 (209), 64 (1979).
[11] M. M. Koltun, *Solar Cells: Their Optics and Metrology*, Allerton Press, New York (1985).
[12] G. S. Landsberg, *Optics* [in Russian], Nauka, Moscow (1976).
[13] R. M. Azzam and N. M. Bashara, *Ellipsometry and Polarized Light*, North-Holland, Amsterdam (1977) [Russ. trans., Mir, Moscow (1981)].
[14] V. Yu. Rud' and Yu. V. Rud', Fiz. Tekh. Poluprovodn. **31**, 309 (1997) [Semiconductors **31**, 197 (1997)].
[15] V. M. Botnaryuk, A. V. Koval', A. V. Simashkevich, V. A. Shcherban', V. Yu. Rud', and Yu. V. Rud', Fiz. Tekh. Poluprovodn. **31**, 800 (1997) [Semiconductors **31**, 677 (1997)].
[16] G. A. Medvedkin and Yu. V. Rud', Phys. Status Solidi A **67**, 333 (1981).

Translated by P. Shelnitz

Surface mobility and distribution of electrons in the accumulation layer of Ga_2Se_3/GaAs heterostructures

V. F. Antyushin and D. A. Vlasov

Voronezh State Technological Academy, 394017 Voronezh, Russia

I. N. Arsent'ev

A. F. Ioffe Physicotechnical Institute, Russian Academy of Sciences, 194021 St. Petersburg, Russia
(Submitted 28 July 1997; accepted for publication 11 November 1997)
Fiz. Tekh. Poluprovodn. **32**, 718–720 (June 1998)

The dependence of the electron drift mobility in the undepleted conduction channels of Ga_2Se_3/GaAs heterostructures on the surface charge density is measured. The presence of charge coupling in the accumulation layer sufficient for creating electrical (or microelectronic) devices is discovered. © *1998 American Institute of Physics.* [S1063-7826(98)01906-1]

The possibility for the formation of a surface electronic conduction channel modulated by an external electric field in Me/Ga_2Se_3/GaAs(n) structures was demonstrated in Refs. 1 and 2. Under certain conditions the majority-carrier accumulation layer in metal-insulator-semiconductor (MIS) structures is separated from the neutral semiconductor bulk by a depletion region.[3,4] This situation can provide for interelectronic charge coupling in the surface conduction channel. For field-effect transistors or charge-coupled devices based on such structures, an important parameter is the surface drift mobility of the charge carriers. The numerical estimates in Refs. 5–7 show that the specific features of the insulating Ga_2Se_3 layer, i.e., the presence of stoichiometric vacancies in the cation sublattice, do not restrict the mobility of electrons in the GaAs layer, if the vacancies are filled by neutral polarizable impurities. According to the results in Refs. 1 and 2, the number of charged centers in the Ga_2Se_3 layer is negligible (no more than 5×10^{11} cm^{-2}). Such a surface charge density corresponds to a bulk density less than 5×10^{16} cm^{-3} (in the case of a homogeneous distribution), which is many orders of magnitude smaller than the vacancy density. The impurities occupying the vacancies in the cation sublattice are possibly not ionized, just as in bulk crystals of III-VI compounds.[8]

In our study we measured experimentally the surface drift mobility of electrons in Ga_2Se_3/GaAs structures and established the presence of strong charge coupling in the surface electronic conduction channel.

The structures were fabricated from AGCh-25V n-type GaAs of the [111] orientation, side B, with a concentration of majority charge carriers $n_0\simeq(2-4)\times10^{16}$ cm^{-3}. After the GaAs wafer was washed according to the method described in Ref. 9, a layer of Ga_2Se_3 was formed by thermal treatment in hydrogen selenide (H_2Se) vapor with preliminary ventilation of the reaction vessel by hydrogen at a temperature near 800 K. The thickness of the Ga_2Se_3 films was determined from interference reflection spectra and amounted to $h\simeq0.1$ μm. The mobility in the surface electronic channel was measured using the method described in Refs. 4 and 10 with the one difference that the surface conductivity in the peripheral region of the measuring electrode was modulated by capacitive structures with a submicron vacuum gap, whose fabrication technology was described in Ref. 11 (see Fig. 1). Such structures virtually eliminate the influence of substrate-gate leakage currents due to the insulating properties of silicon dioxide and can be used to create a strong electric field on the GaAs surface at small gate voltages and to regulate the surface electronic channel in the peripheral region. The constant-bias sources $\mathcal{E}$ and $\mathcal{E}_g$ control the state of the space-charge layers under the measuring electrode and in the peripheral region, respectively. The test signal generators (G) and the device for measuring the capacitive current (I) we used to record the capacitance of the gate electrode and the Me/Ga_2Se_3/GaAs measuring structure.[1)] Figure 2 presents typical plots of the dependence of the capacitance of the measuring structure on the constant bias applied to the measuring metallic electrode (V_m) for depletion and accumulation voltages on the gate. It is seen that when the peripheral region is depleted, the capacitance of the structure (C) remains less than the geometric capacitance of the insulating Ga_2Se_3 layer (C_0), even if there is an accumulation voltage on the metallic electrode. This indicates the existence of a space-charge depletion layer under the measuring electrode, which separates the accumulation layer from the neutral GaAs bulk. The specific capacitance of the space-charge depletion layer (C_{SC}) under the accumulation layer depends only slightly on the applied voltage. The value $C_{SC}=3.7\times10^{-7}$ F/cm^2 is easily determined from the capacitance saturation level (Fig. 2, curve *1*) and is close to $\varepsilon\varepsilon_0/L$, where L is the Debye screening length in GaAs. If the peripheral region is undepleted, charge coupling is established in the accumulation layer. The capacitance of the depletion region, which is connected in series to the geometric capacitance of the insulator, increases, and the total capacitance of the structure approaches the level of the geometric capacitance (the specific capacitance of the Ga_2Se_3 layer $C_0=1.15\times10^{-7}$ F/cm^2). In a diffusion-drift description of charge transport under the action of a small test signal of

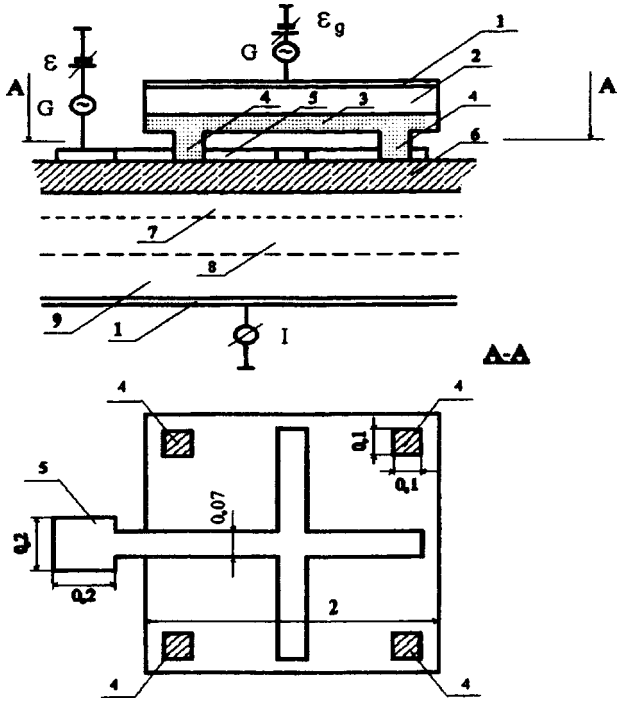

FIG. 1. Schematic representation of the measuring structure: *1* — metallic contacts to silicon and GaAS; *2* — low-resistivity (0.1 Ω·cm) *n*-type silicon; *3* — thick layer (0.05 μm) of silicon dioxide; *4* — silicon dioxide supports; *5* — metallic (Al) measuring electrode; *6* — Ga_2Se_3 layer (0.1 μm); *7* — electron accumulation layer in GaAs; *8* — depletion region in GaAs; *9* — neutral GaAs bulk; *G* — test signal generators; $\mathcal{E}$, $\mathcal{E}_g$ — regulatable constant-bias sources; *I* — device for measuring the capacitive current. The dimensions of the elements in the structure are given in millimeters.

frequency ω in the surface layer, the spatial scale (λ) of the inhomogeneity of the amplitude of the perturbations of the surface charge density in the peripheral region[4] is

$$\lambda \simeq \sqrt{\mu_S Q_S / C_{SC}\omega}, \tag{1}$$

where μ_S and Q_S are the surface mobility and the surface density of the charges in the conduction channel. The area of the peripheral region affected by charge coupling will then be $S' \simeq P\lambda$ (P is the perimeter of the measuring electrode

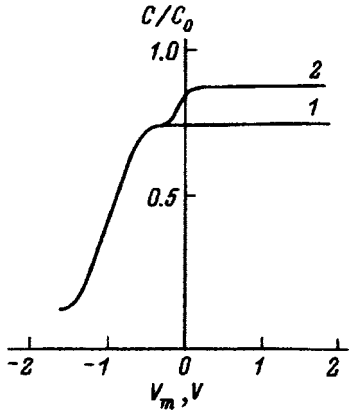

FIG. 2. Capacitance-voltage characteristics of the measurement structure with the depletion (*1*) and accumulation (*2*) voltages on the gate electrode $V_g = \pm 50$ V. The frequency $\omega \simeq 6\times10^4$ Hz, and $T \simeq 300$ K.

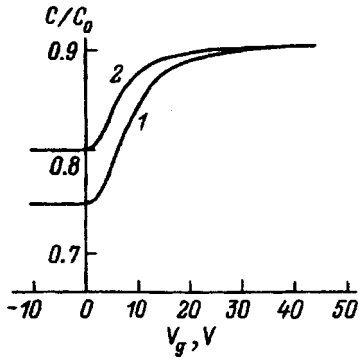

FIG. 3. Dependence of the capacitance of the measuring structure on the voltage across the gate electrode V_g for the accumulation voltage on the measuring electrode $V_m \simeq 1$ V and $\omega = 2\pi\cdot10^4$ Hz. *T*, K: *1* — 300, *2* — 200.

under the gate), and the resultant capacitance of the measuring structure normalized to the geometric capacitance of the insulator is given by the expression

$$\frac{C}{C_0} = \left[1 + \frac{C}{C_{SC}}\left(1 + \frac{P}{S}\sqrt{\frac{\mu_S Q_S}{C_{SC}\omega}}\right)^{-1}\right]^{-1}, \tag{2}$$

where S is the area of the measuring electrode ($P/S \simeq 30$). The relation between Q_S and the gate voltage V_g ($Q_S = C_g V_g$) specifies the dependence of the capacitance of the measuring structure on V_g ($C_g \simeq 1.1\times10^{-9}$ F/cm^2 is the specific capacitance of the gate). The influence of the positive charge in the thin (~0.05 μm) silicon dioxide layer on the state of the Ga_2Se_3/GaAs structure is negligible due to the screening by the low-resistance (with a resistivity of 0.1 Ω·cm) silicon electrode. Having experimental dependences (Fig. 3) and using Eq. (2), we can easily obtain the dependence of the surface mobility μ_S on the surface electron density N_S in the accumulation layer (Fig. 4). The inversely proportional dependence of μ_S on N_S at $N_S > 10^{11}$ cm^{-2} and the weak dependence on the temperature T can be attributed to the scattering of electrons on acoustic phonons. Thus, in a quasi-two-dimensional conduction channel the momentum relaxation time for scattering on acoustic phonons $\tau \sim d(kT)^{-1}$, where d is the effective width of the

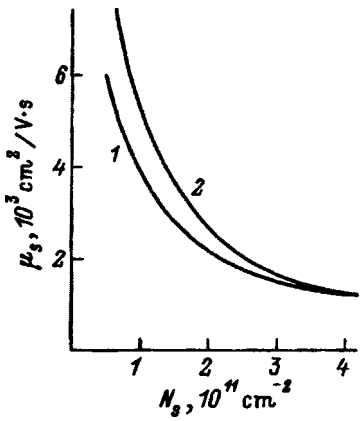

FIG. 4. Dependence of the surface mobility in the accumulation layer of GaAs/Ga_2Se_3 structures on the surface electron density. *T*, K: *1* — 300, *2* — 200.

channel, and k is Boltzmann's constant.[12] For estimates we can assume that the width of the electron accumulation layer is determined by the spatial scale of the nonlinearity of the potential energy of the electrons and that the latter depends on the mean bulk density of the charge across the width of the channel (Q_S/d). We then have $d=\sqrt{\varepsilon\varepsilon_0 kT/e^2(n_0+Q_S/d)}$, and, accordingly,

$$d=\frac{\varepsilon\varepsilon_0 kT}{e^2 n_0}\left[\frac{N_S}{2n_0}+\sqrt{\left(\frac{N_S}{2n_0}\right)^2+\frac{\varepsilon\varepsilon_0 kT}{e^2 n_0}}\right]^{-1}, \qquad (3)$$

where e is the charge of an electron, ε is the relative dielectric constant, and ε_0 is the permittivity of a vacuum. With consideration of the expression for τ, the dependence (3) accounts for the behavior of the electron mobility in response to changes in their surface concentration. Taking into account the approximate character of the formulas used, we can assume that the dominant mechanism for the surface scattering of electrons (in the temperature range 200−300 K) in Ga_2Se_3/GaAs structures is scattering on acoustic phonons. The values for the surface mobility obtained in the Ga_2Se_3/GaAs structures correspond in order of magnitude to the values obtained in (AlGa)As/GaAs structures with modulation doping, which is employed to suppress Coulomb scattering.[13] Order-of-magnitude differences can be attributed either to the different technologies used to fabricate the structures or the different methods used to measure the mobility. As a whole, the results of this work attest to the suitability of Ga_2Se_3/GaAs structures for creating electrical (or microelectronic) devices with charge coupling in an electron accumulation layer.

[1)]Figure 1 shows only part of the measuring circuit of the T-shaped capacitive bridge used to increase the resolution with respect to the capacitance. A resolution no poorer than 0.5% is easily achieved.

[1] B. I. Sysoev, V. F. Antyushin, and V. D. Strygin, Fiz. Tekh. Poluprovodn. **18**, 1739 (1984) [Sov. Phys. Semicond. **18**, 1089 (1984)].
[2] B. I. Sysoev, V. F. Antyushin, and V. D. Strygin, Poverkhnost' (2) 148 (1986).
[3] E. I. Levin, A. M. Monakhov, and A. A. Rogachev, Fiz. Tekh. Poluprovodn. **22**, 450 (1988) [Sov. Phys. Semicond. **22**, 274 (1988)].
[4] B. I. Sysoev, V. F. Antyushin, and M. M. Kipnis, Fiz. Tekh. Poluprovodn. **25**, 708 (1991) [Sov. Phys. Semicond. **25**, 427 (1991)].
[5] B. I. Sysoev, E. V. Rudnev, and V. F. Antyushin, Fiz. Tekh. Poluprovodn. **22**, 1871 (1988) [Sov. Phys. Semicond. **22**, 1185 (1988)].
[6] B. I. Sysoev, V. F. Antyushin, E. V. Rudnev, and V. D. Strygin, Fiz. Tekh. Poluprovodn. **21**, 1310 (1987) [Sov. Phys. Semicond. **21**, 795 (1987)].
[7] V. F. Antyushin and E. V. Rudnev, in *35 Int. Wissenschaftiches Kolloqvium*, Ilmenau, East Germany (1990) p. 7.
[8] V. M. Koshkin, Doctoral dissertation, Khar'kov (1971).
[9] V. F. Antyushin, T. A. Kuz'menko, and V. D. Strygin, in *Semiconductor Electronics (Bulletin of the Voronezh State Pedagogic Institute, Vol. 239)* [in Russian], Voronezh (1985), p. 11.
[10] V. F. Antyushin and B. I. Sysoev, Fiz. Tekh. Poluprovodn. **22**, 902 (1988) [Sov. Phys. Semicond. **22**, 569 (1988)].
[11] B. I. Sysoev, V. F. Antyushin, A. V. Budanov, and A. V. Asessorov, Poverkhnost' (4), 115 (1993).
[12] S. Kawaji, J. Phys. Soc. Jpn. **27**, 909 (1969).
[13] H. L. Störmer, A. C. Gossard, W. Wiegmann, and K. Baldwin, Appl. Phys. Lett. **39**, 912 (1981).

Translated by P. Shelnitz

The quantum Hall effect in a wide p-$Ge_{1-x}Si_x$/Ge/p-$Ge_{1-x}Si_x$ potential well

Yu. G. Arapov, V. N. Neverov, G. I. Kharus, N. G. Shelushinina, and M. V. Yakunin

Institute of the Physics of Metals, Russian Academy of Sciences, Ural Branch, 620219 Ekaterinburg, Russia

O. A. Kuznetsov

Scientific-Research Institute, Nizhniĭ Novgorod State University, 603600 Nizhniĭ Novgorod, Russia
(Submitted 18 April 1997; accepted for publication 19 November 1997)
Fiz. Tekh. Poluprovodn. **32**, 721–729 (June 1998)

Quantum magnetotransport is investigated in a series of selectively doped p-type $(Ge_{1-x}Si_x/Ge) \times N$ multilayered structures with Ge layer widths from 100 to 250 Å in fields up to 35 T at 1.5–4.2 K. The plots of the magnetic-field dependence of the longitudinal (ρ_{xx}) and Hall (ρ_{xy}) magnetoresistance, as well as the ratio between the oscillation periods in strong and weak fields, vary significantly in samples with wide Ge layers and (or) with a high density of the two-dimensional gas. These features can be attributed to the participation of an additional subband in carrier transport. It follows from calculations of the structure of the Ge valence band under the conditions of size quantization and quantization by a magnetic field (performed in the approximation of an infinite rectangular potential well) that the additional subband can be the second heavy-hole quantum-well subband. Estimates of its population correlate with the experimental manifestations of the participation of the additional subband in galvanomagnetic phenomena. © *1998 American Institute of Physics.* [S1063-7826(98)02006-7]

Investigations of quantum magnetotransport in systems with potential wells of different widths, ranging from small to fairly large values, permit the tracking of the transition from two-dimensional (2D) to three-dimensional conduction in the objects studied. This transition reduces essentially to the populating of upper size-quantized subbands of the potential well. Numerous studies of this kind have been carried out. Among them, we can single out the investigations of parabolic quantum wells with selectively doped barriers in Ref. 1, where it became possible to proceed to very wide potential wells (~1000 Å or more) without destroying the quantum Hall state.

However, these studies have heretofore been carried out mostly in systems with an electronic type of conduction. In this paper we attempt to elucidate possible details of the behavior of a quasi-two-dimensional hole gas in a wide potential well.

The longitudinal (ρ_{xx}) and Hall (ρ_{xy}) magnetoresistance of $Ge/Ge_{1-x}Si_x$ multilayers, which were grown by a gas-transport method and have the structure $\langle$Ge(111) substrate$\rangle$/$\langle$1.8-μm Ge buffer layer$\rangle$/$\langle 0-1.6$-μm $Ge_{1-y}Si_y$ buffer layer$\rangle$/$N\times(Ge/Ge_{1-x}Si_x)$, were investigated. The biaxial mechanical stresses in the Ge layers can be varied by varying the ratio between the Si fraction (y) in the $Ge_{1-y}Si_y$ buffer layer and the fraction in the superlattice (x). In the structures investigated the value of y was equal to approximately 0.07, and the mean fraction of Si in the superlattice was $x=0.04-0.05$. In the superlattice the thicknesses of the Ge and $Ge_{1-x}Si_x$ layers were approximately equal. The central part of the $Ge_{1-x}Si_x$ barriers was doped with boron to a concentration of $\sim 10^{18}$ cm^{-3}, while undoped layers (spacers) with a thickness approximately equal to 1/4 of the thickness of the barrier remained on both sides of each barrier. The number of periods in the superlattice (N) and the technologically assigned thicknesses d of the layers in the samples investigated are listed in Table I. The table also presents the values of the hole Hall conductivity μ obtained in a weak magnetic field and the values of the hole concentration p_s^{QHE} determined from the positions of the minima of $\rho_{xx}(B)$ in a strong magnetic field, as well as the values of the Fermi energy and of δ, i.e., half of the deformation gap. The latter were estimated from the hole concentration and effective mass, which were determined from the period and temperature-induced damping of the oscillations in weak magnetic fields.[2] The shape of a double cross was imparted to the samples by etching. The contacts were formed by thermocompression. The measurements were carried out in constant and pulsed magnetic fields at 1.5–4.2 K.

The plots of the magnetic-field dependence of the Hall resistance of the samples investigated exhibited plateaus of the quantum Hall effect (Fig. 1). After recalculation for a single layer, i.e., after multiplying the measured value of the Hall resistance by N, i.e., the number of superlattice periods, the values corresponding to an integer quantum Hall effect, i.e., $\rho_{xy}=h/ie^2$, where the filling factor i takes integer values, are obtained at the center of each plateau. At strong magnetic fields there are distinct plateaus with $i=1$ and 2 for all the samples investigated. The presence of a plateau with $i=1$ means that, first, all the Ge layers of the multilayered system are identical and participate equally in current transport and that, second, each Ge layer contains only one layer of the two-dimensional hole gas. The latter indicates that the bending of the well bottom is not so great that the gas of free carriers in the well would separate into two isolated layers

TABLE I. Parameters of the test samples.

Sample	Number of superlattice periods N	μ, $cm^2/(V\cdot s)$	p_s^{QHE}, 10^{11} cm^{-2}	Layer thickness d, Å	$\frac{S_H}{S_L}$	E_F-E_1, meV	δ, meV	$p_s d^2$	$\frac{E_F-E_1}{E_2-E_1}$
I	90	14 000	4.9	125	2.2	8.0	10	0.8	0.5
II	27	10 000	2.8	200	2.3	7.0	4	1.1	1.2
III	15	14 000	3.4	200(235)	3.1	7.7	5	1.4(1.9)	1.4
IV	90	15 000	4.8	220	3.4	7.2	10.5	2.3	1.6

Note: The technologically assigned values of the layer thickness d are presented. The value $d=235$ Å for sample III was obtained by fitting the calculation to the experimental data.

concentrated in triangular potential wells next to each of the potential walls of the well. If such separation would occur, there would be twice as many 2D layers of free carriers than layers of Ge in the system, and when the Hall resistance measured directly in the experiment is multiplied by the number of superlattice periods in the sample, for the first plateau on the strong-field side we would have not $\rho_{xy}=25.8$ kΩ$=h/e^2$, but a value two times smaller. The appearance of a plateau with $i=1$ for all the samples removes any uncertainty in the identification of the features observed and allows us to associate each plateau of ρ_{xy} and the corresponding minimum of ρ_{xx} for a magnetic level with a definite ordinal number. Here the manner in which the magnetic levels are grouped into quantum-well subbands does not play any role. Therefore, to assign such numbers, all the magnetic levels must be numbered consecutively, without regard to their affiliation with different quantum-well subbands.

The minima on the measured $\rho_{xx}(B)$ curves describing the magnetic-field dependence of the resistance (Figs. 2 and 3) correspond to the midpoints of the $\rho_{xy}(B)$ plateaus and are arranged periodically with respect to the reciprocal magnetic field $1/B$. However, the periods in strong and weak fields differ. In a strong field, where all the Landau levels are separated from one another by mobility gaps, the positions of the minima and their period in the reciprocal field are determined only by the density of the 2D gas and do not exhibit any dependence on the specific form of the pattern of levels:

$$[\Delta(1/B)]^{-1}=hp_s/e.$$

In a weak field the ordered merging of the levels can cause the period of the oscillations observed to differ and to depend on the relative positions of the levels. In the simplest case, where the Landau levels form a single series of spin-split levels, the ratio between the periods in strong and weak fields equals 2:

$$S_H/S_L=2, \quad S_{H,L}\equiv\Delta M/\Delta(1/B),$$

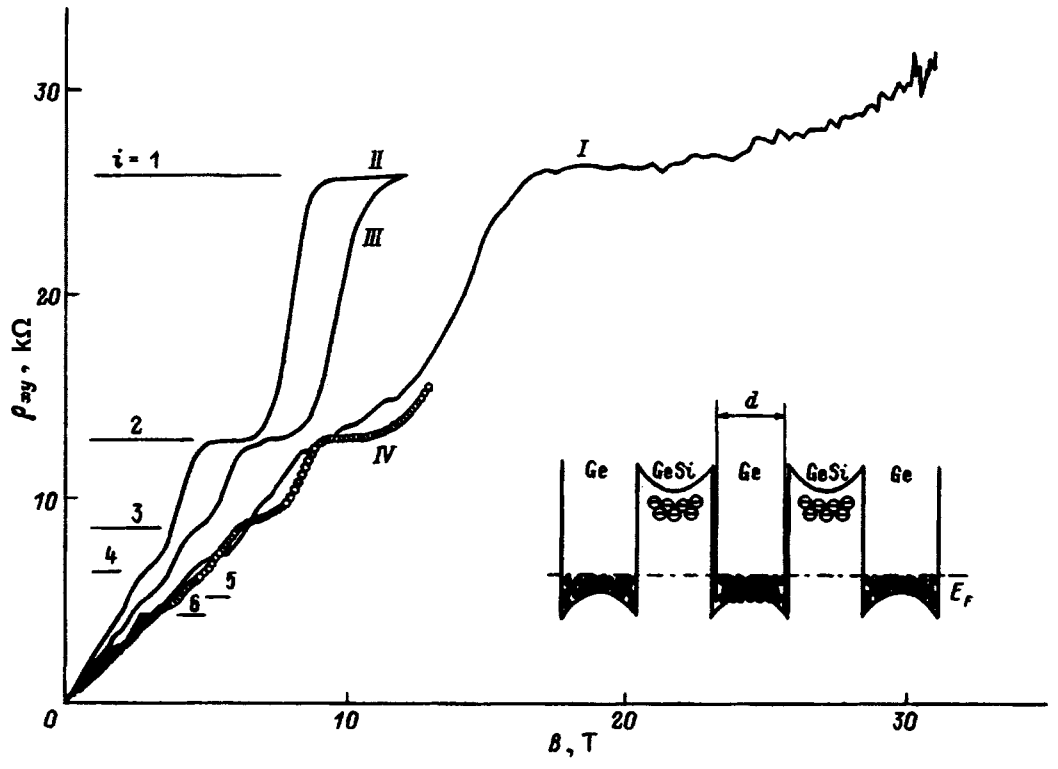

FIG. 1. Dependence of the Hall resistivity ρ_{xy} of samples on the magnetic field B. Inset — energy diagram of the structures investigated and model of the potential well. The Roman numerals on the curves correspond to the numbers of the samples in Table I.

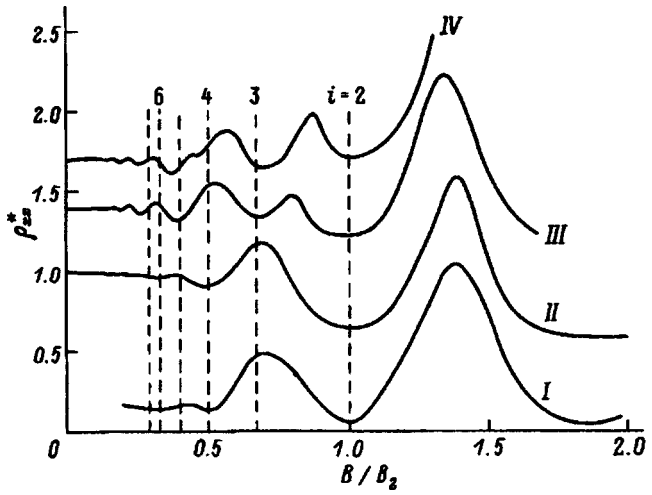

FIG. 2. Magnetic-field dependence of the normalized Hall resistivity ρ^*_{xx}. The Roman numerals on the curves correspond to the numbers of the samples in Table I. The amplitudes of the peaks are normalized relative to the amplitude of the largest peak. The magnetic field B_2 corresponds to the position of the minimum with the number $M=2$.

where M is the number of the minimum when all the minima observed are numbered consecutively with an increment of 1 from strong fields to weak fields. This is due to merging of the spin sublevels and actually means that in a weak field the minima must be numbered with an increment of 2, rather than 1, since twice as many states correspond to an unsplit level. The deviation of this ratio from 2 points to a different pattern of levels. It most probably means that another series of Landau levels, which is associated with another subband located at a deeper position in the band, is superimposed on the principal series. Since the second series corresponds to oscillations separated by larger distances along the field axis, just this series will dominate in weak fields, and the value of S_L corresponding to it will be smaller than $S_H/2$. In the valence band of Ge the second subband can appear either as a result of splitting of the band in an asymmetric potential (two series of levels corresponding to different masses that originate from almost the same point) or when the second quantum-well subband is filled (two similar series originating from different points on the energy axis).

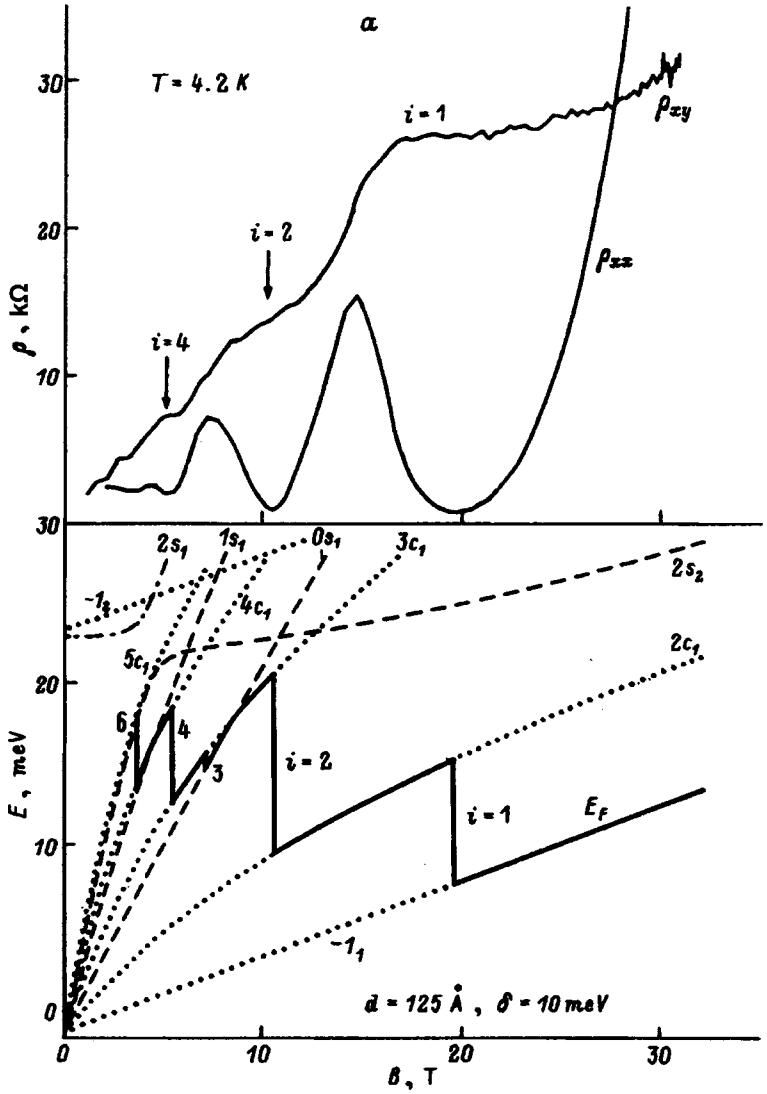

FIG. 3. Magnetic-field dependence of the quantum Hall effect and the magnetoresistance in relation to the calculated pattern of Landau levels for several samples: a — I, b — II, c — III. The energy-level diagrams contain only the lowest levels of the second heavy-hole quantum-well subband. The behavior of the Fermi level is indicated by the thick line. Inset in Fig. 3c — dependence of $\rho_{xx}(B_\perp)$ in oblique fields.

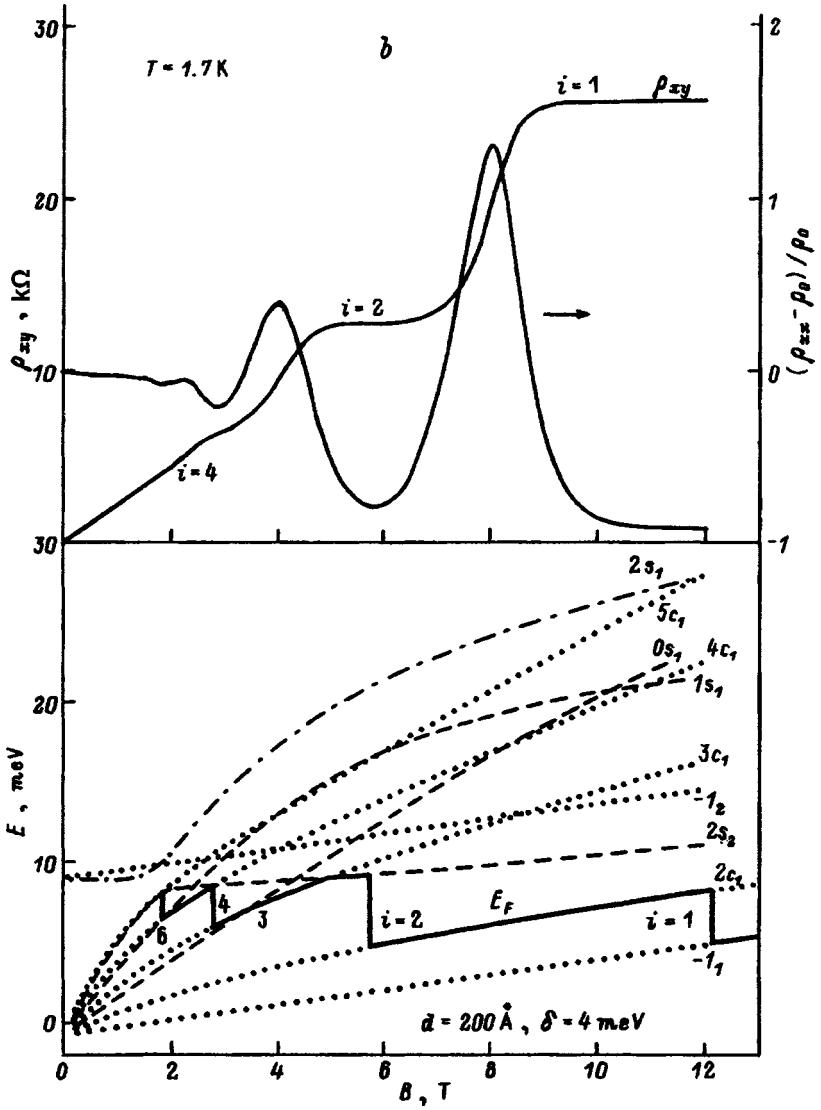

FIG. 3. (Continued).

The oscillations of $\rho_{xx}(B)$ in the quantum wells of p-$Al_{1-x}Ga_x$/GaAs/p-$Al_{1-x}Ga_xAs$ heterostructures were investigated in Ref. 3, and the value $S_H/S_L=2$ was obtained for wells with widths of 50 and 100 Å, but this ratio was equal to 3.3 for a 200-Å well. It was concluded on the basis of this finding that a wide well with a hole density $p_s=5\times10^{11}$ cm^{-2} behaves like two heterojunctions connected in parallel with corresponding asymmetric triangular potential wells and that the deviation of the ratio between the oscillation periods from 2 is attributable to splitting of the valence band in the asymmetric potential. Unfortunately, data on the Hall effect were not presented in that paper.

Among the p-$Ge_{1-x}Si_x$/Ge/p-$Ge_{1-x}Si_x$ samples that we investigated, values of S_H/S_L close to 2 were obtained for two of them (see Table I), and values greater than 3 were obtained for the others. Since all the magnetic levels are resolved in very strong fields, the values of the filling factor determined from the quantum Hall effect can be used here to number the minima of the longitudinal magnetoresistance ρ_{xx}. The minima with such numbers will be physically equivalent in different samples. Such a lack of ambiguity in the identification of the minima of ρ_{xx} at strong magnetic fields permits a graphic illustration of the differences in the values of S_H/S_L for different samples. Figure 4 presents plots of the dependence of the peak number M on the magnetic field B, which characterize the values of $S_{H,L}$. For each sample the field B was recalculated relative to the position of the minimum with $M=i=2$. Such a relative scale of magnetic fields permits elimination of the differences associated with the different densities of the hole gas in the samples. In fact, in Fig. 4 the straight lines practically coincide at strong fields. Conversely, at weak fields the slopes of the straight lines differ appreciably. For the samples with relatively narrow wells the slope of the straight lines corresponding to weak fields is close to 1/2 of the slope of the straight lines corresponding to strong fields. For the samples with wide wells, despite the limited number of experimental points, it is clearly seen that the slope is significantly smaller. It can be concluded on the basis of these data that the Fermi level reached a higher-lying subband in samples III and IV.

If the Fermi level is located above the bend of the well bottom, the influence of the asymmetry of the potential on

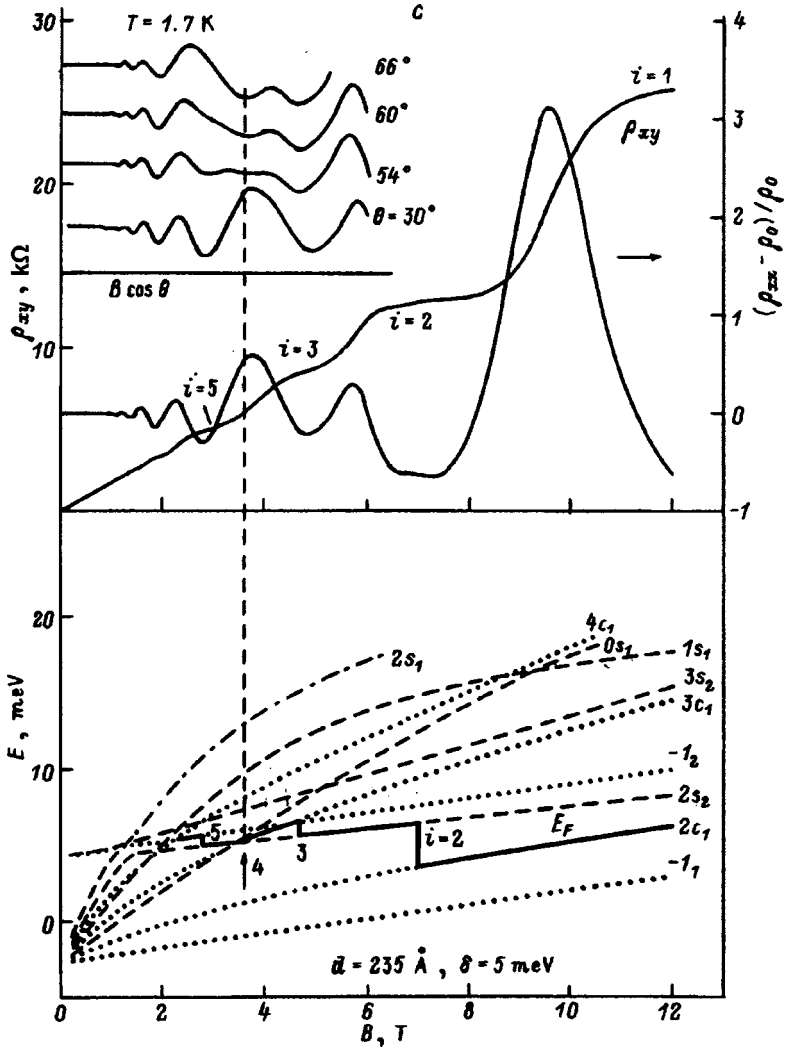

FIG. 3. (Continued).

the hole energy spectrum will be significantly weaker than in the case of a Fermi level lying within the triangular potential wells at the opposite boundaries of the layer. Then it is natural to assume that the new subband manifested in the experimental data is essentially the second quantum-well subband for a symmetric well. We shall obtain approximate estimates of the positions of the quantum-well levels after replacing the real potential well by a rectangular, infinitely deep well of the same width (see the inset in Fig. 1).

According to Ref. 4, the quantum-well levels of the valence band in an infinitely deep rectangular potential well of depth d form two series of levels for heavy and light holes: $E_n^{h,l}=3\pi^2\hbar^2n^2/2m_{h,l}d^2$, $n=1, 2, \ldots$ (the energy axis is directed downward in the valence band). Since the heavy- and light-hole masses in Ge differ by about sevenfold, the first quantum-well level of the light holes is approximately two times higher than the second heavy-hole quantum-well level (this is the situation in the absence of deformation, while in its presence the deformation gap must be added to this difference). Therefore, if the experimental data point to the participation of an additional subband in magnetotransport, it is very likely that it is the second heavy-hole quantum-well subband. Let us assess the conditions for populating it when

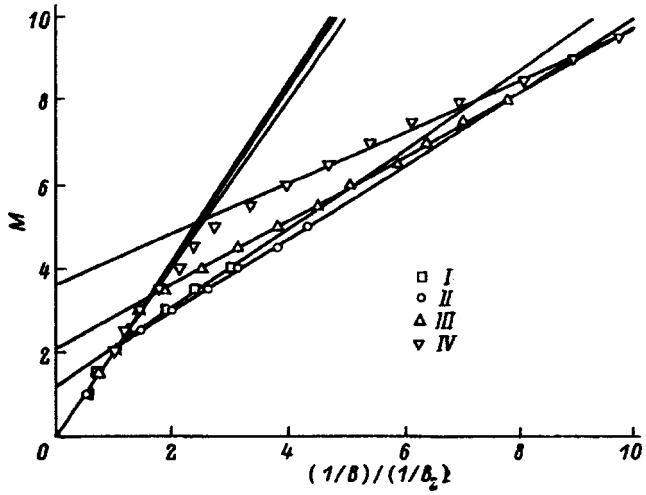

FIG. 4. Diagram characterizing the oscillation periods of ρ_{xx} in strong and weak fields; M — consecutive oscillation numbers. Integer values of M correspond to minima of ρ_{xx}, and half-integer values correspond to maxima. The magnetic fields have been recalculated relative to the position of the minimum with $M=2$ for each sample.

$B=0$. For a simple parabolic isotropic band with a heavy-hole mass $m=m_h$ we obtain

$$(E_F-E_1)/(E_2-E_1)=(\pi\hbar^2 p_s/m)/(3\pi^2\hbar^2/2md^2)\propto p_s d^2.$$

However, we must take into account the complicated form and strong anisotropy of the hole subbands due to spatial confinement in a two-dimensional layer[4] and uniaxial deformation. We performed such estimates for the values of E_F determined in Ref. 2 on the basis of experimental data and obtained[5]

$$m=m_h^{(\mathrm{III})}=\hbar^2(\partial^2E/\partial k^2_{(\mathrm{III})})^{-1}=0.5m_0.$$

As can be seen from Table I, the values of $p_s d^2$ and $(E_F-E_1)/(E_2-E_1)$ and the values of S_H/S_L obtained in our measurements for all the samples investigated increase identically. The ratio S_H/S_L increases dramatically when we go from sample II to sample III. As follows from the remarks made above, such an abrupt increase in this ratio most probably point to the beginning of the populating of the second subband. According to our estimates, the increase in the value of $(E_F-E_1)/(E_2-E_1)$ from 1.2 to 1.4 corresponds to this transition, i.e., the sharp change in the ratio between the oscillation periods S_H/S_L is observed when the Fermi level enters the second heavy-hole subband. Therefore, the hypothesis advanced above regarding the participation of specifically the second heavy-hole quantum-well subband in magnetotransport seems perfectly realistic, and the model of a square well is sufficiently equivalent to the real situation.

While the $\rho_{xy}(B)$ curves for the all the samples are similar at strong magnetic fields and contain plateaus with $i=1$ and 2, the structures of these curves below the plateau with $i=2$ differ strongly (Fig. 1). For samples I and II, the next plateau after the one with $i=2$ in the weak-field direction is the plateau with $i=4$, and other plateaus with even filling factors are dominant. For the other two samples, viz., III and IV, the next plateau after the one with $i=2$ is the plateau with $i=3$, and the plateau with $i=4$ is absent. These differences can be seen more clearly in the structure of the $\rho_{xx}(B)$ curves, whose maxima have amplitudes that correlate with the dimensions of the corresponding plateaus of $\rho_{xy}(B)$, but the monotonic background is almost absent (see Fig. 2). In this figure, as in Fig. 4, the magnetic fields for each sample have been divided by the value of the field at the minimum with $i=2$ to eliminate the differences caused by the differences in the density of the 2D gas. We note that radical differences in the structure of the curves (i.e., the presence or absence of features with definite values of i and the ratio between their amplitudes) are observed specifically in the samples for which a ratio between the oscillation periods $S_H/S_L\neq 2$ was obtained. Therefore, this property, like the ratio S_H/S_L, is most probably associated with populating of the second heavy-hole quantum-well subband.

The pattern of the magnetic levels in the valence band of Ge in the potential well is needed to analyze the magnetotransport in the quantum Hall regime. Detailed self-consistent calculations with consideration of the real profile of the well would be a cumbersome task.[6] It is significantly simpler to perform such calculations within the familiar model of an infinitely deep rectangular well. In that case it can be expected that the simplified calculations will reflect the main features of the real spectrum, since, first, quantum Hall states with $i=1$ are observed for each Ge layer as a whole and, second, the valence-band offset is at least two times greater than the Fermi energy. In Ref. 7 the model of a rectangular well was used to analyze the pattern of hole magnetic levels even in a unilaterally doped heterostructure known to be asymmetric. Quantitative agreement with experiment was obtained for structures with a density of the hole gas of the order of 10^{11} cm^{-2}. In our structures the density of the hole gas was $3-4$ times higher, but the potential wells were symmetric (since the barriers were doped symmetrically from both sides of the well).

The calculation method was described in detail in Refs. 8 and 9. Actually, it is a generalization of the D'yakonov–Khaetskiĭ theory[4] to the case of the presence of a quantizing magnetic field perpendicular to the layer. The magnetic levels were calculated for the Kohn–Luttinger 4×4 Hamiltonian in the isotopic approximation. When the zeroth boundary conditions are imposed on the wave function, the solution for each of the values of the magnetic quantum number $P=0,1,\ldots$ reduces to two independent systems of equations for the symmetric and antisymmetric states, which is reflected in Fig. 3 in the use of the letters s and c in the notation for the levels. A simple analytic solution can be obtained only for the minimum value $P=-1$ as a result of truncation of the Hamiltonian to 1×1:

$$E_n(P=-1)=\pi^2\hbar^2n^2/2m_hd^2 + \hbar eB/m_0[(\gamma_1+\gamma)/2-(3/2)\varkappa]-\delta,$$

where $n=1,2,\ldots$; γ_1, γ, and $\varkappa$ are the Luttinger parameters, and m_0 is the free-electron mass. Each of the systems yields an infinite number of solutions corresponding to different quantum-well subbands. As the levels obtained from one system of equations move with the magnetic field, effects of the repulsion of these levels become apparent, especially at their anticrossing points. The complete notation for a level in Fig. 3 includes the value of P, the letter s or c already mentioned, and an index, which indicates the position of the level in a sequence of levels having identical quantum numbers with increasing energy (to remove any ambiguity, the sequence of levels in very weak fields is indicated). The letter in the notation is omitted for levels with $P=-1$.

The calculations were performed for the parameters of Ge: $\gamma_1=13.4$, $\gamma\equiv(\gamma_2+\gamma_3)/2=5.0$, and $\varkappa=3.4$ (Ref. 5) and various values of the well width and half of the deformation gap δ. The results of the calculations are compared with the experimental curves in Fig. 3. The behavior of the Fermi level as a function of the magnetic field is shown for infinitely narrow Landau levels and a constant total hole concentration. In this case at the field values $B_i=(h/e)(p_s/i)$, where there is complete filling of an integer number of magnetic levels, the Fermi level jumps to the neighboring level. As is seen from Fig. 3, the plots of the magnetic-field dependence of the $2s_2$ and $3s_2$ levels contain a discontinuity. An analysis of the wave functions at strong magnetic fields demonstrates that they belong to the second heavy-hole quantum-well subband and that in the absence of anticrossings with

the corresponding $2s_1$ and $3s_1$ levels they should have reached the position of this quantum-well level when $B \to 0$, as occurs for the -1_2 magnetic level. Levels with different quantum numbers cross without repulsion. As will be seen below, the presence of crossings of the magnetic levels, which become possible because of the superposition of levels of the second subband on levels of the first subband, creates a fundamentally new situation, which is reflected in the experimental results. The higher-lying levels of the second subband are not shown in Fig. 3 to avoid cluttering the figure.

As follows from the calculations, for sample I the Fermi level is found in the first subband over the entire range of fields (Fig. 3a), i.e., all the processes determining the kinetics unfold within one series of Landau levels. This also accounts for the simple structure of the experimental curves and the value of S_H/S_L close to 2. The pattern of levels resembles the pattern for a simple nondegenerate band (Γ_6) in the case of weak spin splitting; therefore, the features with even filling factors dominate.

In sample II the Fermi level partially brushes against the lowest Landau level ($2s_2$) of the second heavy-hole quantum-well subband as it jumps from level to level (Fig. 3b). In weak fields such inclusion of a new subband in magnetotransport is manifested by a small decrease in S_L. However, the relations between the dimensions of the steps on the plot of $E_F(B)$ in strong fields remain the same as in sample I; therefore, the structure of the experimental curves in strong fields remains practically the same as in sample I. This is consistent with the value of $(E_F-E_1)/(E_2-E_1) \gtrsim 1$ obtained for this sample (see Table I), i.e., when the new subband first begins to be populated and strong manifestations of this process are not yet observed experimentally.

The situation is radically different in samples III and IV, where the Fermi level moves along Landau levels of the second subband over a considerable part of the range of magnetic fields investigated (Fig. 3c). The lowest level ($2s_2$) of the second subband runs between the second and third magnetic levels ($2c_1$ and $3c_1$) of the first subband, dividing the gap between them in two. As a result, a situation in which three completely filled Landau levels, rather than two or four, are separated from the next level by a fairly large gap becomes passible [see step 3 on the plot of $E_F(B)$]. For just this reason, a feature corresponding to the filling factor $i=3$ appears on the experimental curves. The step with $i=4$ on the plot of $E_F(B)$ can appear in a field in which the lower (completely filled) and upper (unoccupied) levels cross, but, as a result, the height of this step will be vanishingly small, and the features with $i=4$ will not be displayed on the experimental curves. In our calculations such a situation arises when the well width $d=235$ Å, which exceeds the technologically assigned value $d=200$ Å. The difference between the calculated well width and the technologically assigned value can be attributed to the approximate character of the calculations. In addition, the real width of the Ge layers can differ from the nominal value (such a situation arose, for example, in Ref. 6). Therefore, it is advisable to measure the real width of the Ge layers using transmission electron microscopy. We find it very interesting that the absence of the feature with $i=4$ can be reflected in the calculations only in a narrow range of values of d. In fact, the energy of the quantum-well level in the well should be described approximately by a $1/d^2$ law; therefore, upon a small change in the value of d, the level crossing point moves away from B_4, and the Fermi level must pass through a gap as it moves from level to level at B_4. In other words, the passage of the Fermi level through the level crossing point at B_4 is accidental. Therefore, sample IV with a similar sequence of levels exhibits a the weak feature with $i=4$. The inset in Fig. 3c shows how the feature with $i=4$ reappears in sample III as the magnetic field is rotated by an angle θ relative to a normal to the plane of the layer. Consequently, as the sample is rotated, the level crossing point moves away from $B_4 \cos\theta$ as the sample is rotated.

Thus, we attribute the experimental result that $\rho_{xy}(B)$ and $\rho_{xx}(B)$ curves of totally different form were obtained for samples of the same p-$Ge_{1-x}Si_x$/Ge/p-$Ge_{1-x}Si_x$ system with small differences in the structure, composition, and carrier concentration to the high sensitivity of the experimental results to the relative positions of the Fermi level and the quantum-well subband. Can this conclusion be influenced by the fact that the simplified model of a rectangular potential well was employed in the analysis? One of the principal manifestations of this difference is the disappearance of the features on $\rho_{xx}(B)$ curves corresponding to some values of the filling factor i of the magnetic levels and the appearance of features for other values of i as we move from the samples in the upper rows of Table I to the samples at the bottom. The existing ideas regarding magnetotransport in the quantum Hall regime allow us to attribute this behavior only to the closing or opening of mobility gaps between the corresponding magnetic levels.

1. If the analysis is performed for the series of magnetic levels of only one subband, to explain the significant changes observed, it would be necessary to postulate radical regrouping of the levels in that series. For an ordinary nondegenerate Γ_6 band this would correspond to reversal of the relation between the spin and cyclotron splittings of the levels. It would be even more difficult to account for the presence or absence of individual features, rather than the even or odd series as a whole, as, for example, the absence of the feature with $i=4$ in sample III and its presence in sample IV. Then it would be necessary to assume that only one magnetic level in the series is displaced by an energy of the order of the cyclotron energy upon passage from one sample to another. The increase in the ratio between the oscillation periods from $S_H/S_L=2$ to 3 or more in samples III and IV remains totally inexplicable, since it would then be necessary to assume that the levels of an individually taken series form groups of three. There are too many unfounded assumptions, but we can dispense with them, if we accept that the Fermi level reaches a new subband in samples III and IV.

2. Let us consider an alternative in which we acknowledge the presence of an additional subband, but we assume that its nature is associated with the splitting of the band in the asymmetric potential that appears because of the bending of the well bottom. Here a comparison can be drawn to the results of the detailed self-consistent calculations of mag-

netic levels in Ref. 6 for a potential well known to be asymmetric, which was obtained by unilateral selective doping of the barrier. It follows from these calculations that even for asymmetry of the potential known to be greater than in our case, the splitting of the heavy-hole subband becomes appreciable only at energies greater than about 40 meV, which significantly exceeds the value $E_F=7-8$ meV in our samples. Therefore, we believe that our analysis of the model of a square well permits drawing perfectly realistic conclusions, particularly regarding the decisive influence of the second heavy-hole subband on the experimental results. Of course, the bending of the well bottom causes some changes in the energy differences between the quantum-well levels. However, this leads to quantitative refinements, not to a change in the essence of the phenomena.

In addition, the high sensitivity discovered in our investigations of the experimental results to the structural details of the semiconductor structures investigated under the conditions of a populated second subband could, in turn, be utilized to refine these details. This calls for more exact calculations with consideration of the anisotropy $\gamma_2 \neq \gamma_3$, the finite height of the barriers, the real shape of the well, the finite width of the levels, and other factors.

In conclusion, we note that the participation of the second subband in our experiments is not a reflection of features of the valence band. Since the Fermi level lies significantly below the first light-hole quantum-well subband, a similar manifestation of the participation of the second subband might be expected in the same fields in an ordinary, nondegenerate Γ_6 band with a mass close to the heavy-hole mass. The features of the valence band, which are manifested, in particular, in the calculated spectra by the nonequidistant arrangement and crossings of the magnetic levels of an individual subband, are significant only for relatively fine details in our experimental results. Clearer manifestations of the features of the valence band can be expected either in experiments that permit obtaining high resolution in the narrow ranges of magnetic fields corresponding to anticrossings of levels of different subbands or at populating of the upper subbands high enough that the Fermi level would surpass the gap between the split-off bands of the heavy and light holes (i.e., at large densities of the two-dimensional hole gas or a larger well width).

We thank G. M. Min'kov and A. V. Germanenko for their computer programs.

This work was supported by the Russian Foundation for Fundamental Research (Project No. 95-02-04891) and the Russian Scientific-Technical Program on Nanostructure Physics and Technology (Project No. 95-1005).

[1] K. Ensslin, M. Sundaram, A. Wixforth, J. H. English, and A. C. Gossard, Phys. Rev. B **43**, 9988 (1991).
[2] Yu. G. Arapov, N. A. Gorodilov, O. A. Kuznetsov, V. N. Neverov, L. K. Orlov, R. A. Rubtsova, G. I. Kharus, A. L. Chernov, N. G. Shelushinina, and G. L. Shtrapenin, Fiz. Tekh. Poluprovodn. **27**, 1165 (1993) [Semiconductors **27**, 642 (1993)].
[3] Y. Iye, E. E. Mendez, W. I. Wang, and L. Esaki, Phys. Rev. B **33**, 5754 (1986).
[4] M. I. D'yakonov and A. V. Khaetskiĭ, Zh. Éksp. Teor. Fiz. **82**, 1584 (1982) [Sov. Phys. JETP **55**, 917 (1982)].
[5] J. C. Hensel and K. Suzuki, Phys. Rev. B **9**, 4219 (1974).
[6] R. Winkler, M. Merkler, T. Darnhofer, and U. Rössler, Phys. Rev. B **53**, 10 858 (1996).
[7] S. L. Wong, D. Kinder, R. J. Nicholas, T. E. Whall, and R. Kubiak, Phys. Rev. B **51**, 13 499 (1995).
[8] A. V. Germanenko, G. M. Minkov, E. L. Rumyantsev, and O. E. Rut, Adv. Mater. Opt. Electron. **2**, 57 (1993).
[9] Yu. G. Arapov, N. A. Gorodilov, V. N. Neverov, M. V. Yakunin, A. V. Germanenko, G. M. Min'kov, O. A. Kuznetsov, R. A. Rubtsova, A. L. Chernov, and L. K. Orlov, JETP Lett. **59**, 268 (1994).

Translated by P. Shelnitz

LOW-DIMENSIONAL SYSTEMS

Elimination of the electron-phonon interaction in superlattices in a quantizing magnetic field

O. V. Kibis

Novosibirsk State Technical University, 630092 Novosibirsk, Russia
(Submitted 7 July 1997; accepted for publication 10 September 1997)
Fiz. Tekh. Poluprovodn. **32**, 730–732 (June 1998)

The energy and wave-vector conservation laws impose rigid constraints on the possible electron-phonon interaction processes in a superlattice immersed in a quantizing magnetic field directed along its growth axis. If the width of the Landau subband is smaller than the maximum energy of an acoustic phonon in the superlattice, single-phonon intraband scattering becomes impossible for all electron states in the subband considered. Therefore, the phonon contribution to the electron scattering processes can become negligible in superlattices with a large period in the presence of a quantizing magnetic field. © *1998 American Institute of Physics.* [S1063-7826(98)02106-1]

1. INTRODUCTION

Since the resistance of a conductor is stipulated by the scattering of charge carriers on phonons and crystal-lattice defects, these processes must somehow be suppressed to achieve the nondissipative flow of an electric current in a conductor. While defects can be practically eradicated by using modern technologies for fabricating semiconductor structures, it is considerably more difficult to eliminate scattering on phonons. It was believed for a long time that the phonon scattering mechanism can be suppressed by lowering the temperature of the conductor. Comparatively recent investigations[1] have shown that if it is possible to purposely alter the energy spectrum of the electrons in a crystal using a sufficiently large number of controllable parameters, zero values of the electron-phonon coupling constants can be achieved for some electron states and the interaction of the electrons in these states with phonons can thereby be eliminated. The recently revealed possibility of fabricating artificial crystalline structures with assigned parameters for the energy spectrum of the charge carriers has created a qualitatively different possibility for suppressing the electron-phonon interaction: An idea has been advanced that the parameters of the band structure should be selected in such a way that the energy and wave-vector conservation laws would forbid the scattering of electrons on phonons.[2] As will be seen below, in a superlattice with a fairly narrow conduction band immersed in a quantizing magnetic field directed along its growth axis the conservation laws forbid single-phonon processes involving the intraband scattering of electrons on acoustic phonons and thereby lead to the disappearance of phonon scattering in the first order.

As a model problem, let us preliminarily consider a one-dimensional chain of atoms with a period a. The energy of an electron ε in such a chain is specified in the tight-binding approximation by the relation

$$\varepsilon(k)=\varepsilon_0-2A(a)\cos(ka), \tag{1}$$

where ε_0 is the energy of an electron in an isolated atom, $A(a)$ is the real overlap integral of the atomic wave functions, and k is the wave vector of an electron in the chain of atoms. In a one-dimensional chain of atoms the energy and wave-vector conservation laws for the single-phonon scattering of an electron from state k to state k' have the form

$$\varepsilon(k)\pm\hbar\omega(q)=\varepsilon(k'), \quad k'=k\pm q, \tag{2}$$

where q is the wave vector of the phonon,

$$\omega(q)=\omega_0|\sin(qa/2)| \tag{3}$$

is the frequency of an acoustic phonon, and ω_0 is the maximum frequency of an acoustic phonon in the chain of atoms. After (1) and (3) are substituted into (2), the conservation laws (2) take the form

$$4A(a)\sin[(k\pm q/2)a]\sin(qa/2)=\hbar\omega_0|\sin(qa/2)|, \tag{4}$$

where the plus and minus signs correspond to absorption and emission of the phonon by the electron. If the maximum energy of an acoustic phonon $\tilde{\varepsilon}=\hbar\omega_0$ exceeds the width of the conduction band $\Delta\varepsilon=4A(a)$, Eq. (4) has only the trivial solution $q=\pm 2\pi m/a$ $(m=0,1,2\ldots)$, which corresponds to displacement of the crystal as a single unit and does not alter the interatomic distance a. Thus, the criterion for elimination of the single-phonon intraband mechanism for the scattering of electrons on acoustic phonons has the form

$$\Delta\varepsilon<\tilde{\varepsilon}. \tag{5}$$

Hence it follows that the contribution of the single-phonon processes to the scattering of charge carriers for all the electron states of the band under consideration vanishes in crystalline structures with a narrow conduction band, i.e., a value of $\Delta\varepsilon$ which satisfies the criterion (5). However, when the conduction band is very narrow, the multiphonon processes

can become significant, and they ultimately lead to instability of an electron band state toward the formation of a condenson, i.e., a state of the polaron type, which is created by the interaction of an electron with acoustic phonons.[3–6] The condition under which the multiphonon processes can be disregarded is

$$\Delta\varepsilon \gg \varepsilon_c, \tag{6}$$

where $\varepsilon_c \sim \Xi^2/\lambda a$ (Ξ is the deformation potential constant, and λ is the elastic modulus of the chain of atoms). Finally, in all the foregoing arguments we assumed that there is no interband electron scattering. This assumption corresponds to a phonon energy which is small in comparison to the width ε_g of the gap separating the conduction band from the higher-lying energy bands and is valid at values of the temperature T which satisfy the condition

$$\exp(-\varepsilon_g/T) \ll 1. \tag{7}$$

Thus, simultaneous satisfaction of the criteria (5)–(7) is needed for the complete suppression of electron-phonon scattering in the first order.

It is not difficult to see that the model situation considered by us can be realized in practice in a concrete physical object, viz., a superlattice with a large period immersed in a quantizing magnetic field directed along its growth axis. In fact, in the quantum limit, where electrons fill only the first Landau subband, the quantizing magnetic field ensures the quasi-one-dimensional character of the electron energy spectrum described by (1), and the fact that the superlattice has a large period permits the achievement of a small Landau subband width which satisfies the key criterion for the effect under discussion, i.e., the inequality (5). To analyze the effect in greater detail, we concretize the problem by considering a superlattice formed by δ-doped impurity layers in a semiconductor crystal. In this case the quantity ε_0 in (1) is the energy of an electron in a δ-doped layer, a is the superlattice period, $A(a)$ is the overlap integral of the wave functions of electrons in neighboring δ-doped layers, and k is the wave vector of an electron in the Landau subband directed along the superlattice growth axis. As will be seen from the arguments below, realization of the effect under discussion requires that the superlattice period a significantly exceed the atomic period of the crystal. This ensures that the overlap integral $A(a)$ is small and that the tight-binding approximation, which was used to derive (1), is valid. In the presence of a quantizing magnetic field H, the characteristic electron-phonon interaction energy[4] $\varepsilon_c = 2m(3\Xi^2/16\hbar\pi l_H^2\lambda)^2$ (l_H is the magnetic length, and m is the effective electron mass in the direction of the magnetic field H), and the interband distance ε_g is the distance between neighboring Landau subbands $\hbar\omega_H$, where ω_H is the cyclotron frequency.

Let the δ-doped layers consist of atoms which form shallow impurity levels in the band gap of the semiconductor crystal. The parameters of such impurity atoms are well known[7] and are characterized by the energy of the impurity level $\bar{\varepsilon}$ and the localization length of the impurity wave function $r \sim \sqrt{\hbar^2/2m^*\bar{\varepsilon}}$, where m^* is the effective mass of a charge carrier in the semiconductor crystal. Therefore, when $r \lesssim a$, the overlap integral of the wave functions of neighboring δ-doped layers $A(a) \sim \bar{\varepsilon}\exp(-a/r)$. Thus the Landau subband width $\Delta\varepsilon \sim \bar{\varepsilon}\exp(-a/r)$, and the effective mass in the subband along the superlattice growth axis $m = \hbar^2/A(a)a^2 \sim (\hbar^2/a^2\bar{\varepsilon})\exp(a/r)$. Since the superlattice period significantly exceeds the atomic period of the crystal, the elastic properties of the superlattice are determined mainly by the elastic properties of the original semiconductor crystal, and for this reason $\tilde{\varepsilon} \simeq \hbar c\pi/a$, where c is the speed of sound in the crystal. Taking into account the arguments presented above, we can write the criteria (5)–(7) for a superlattice in a quantizing magnetic field as follows:

$$(\bar{\varepsilon}a/\pi c\hbar)\exp(-a/r) < 1, \tag{8a}$$

$$0.5(3\Xi^2/16a\pi l_H^2\lambda\bar{\varepsilon})^2\exp(2a/r) \ll 1, \tag{8b}$$

$$\exp(-\hbar\omega_H/T) \ll 1. \tag{8c}$$

Clearly, the criterion (8c) for the absence of phonon scattering between Landau subbands is virtually equivalent to the requirement that the magnetic field H be quantizing. In fact, to observe quantization of the energy of electrons in a magnetic field, the thermal spreading of the energy levels must be significantly smaller than the distance between the Landau subbands. As for (8a) and (8b), these criteria can always be satisfied by fabricating a superlattice with a sufficiently large value of the period a. Substituting into (8a)–(8c) the characteristic values for semiconductor materials $c \sim 10^6$ cm/s, $\lambda \sim 10^{11}$ erg/cm^3, $\Xi \sim 10^{-12}$ erg, $r \sim 10^{-6}$ cm, and $\bar{\varepsilon} \sim 10^{-14}$ erg, we find that the criteria for the elimination of phonon scattering (8a)–(8c) can be satisfied in a quantizing magnetic field when $a \sim 10^{-6}$ cm, which corresponds to a width of the superlattice conduction band $\Delta\varepsilon \sim 10^{-3}$ eV.

[1] O. V. Kibis and M. V. Énтin, Fiz. Tekh. Poluprovodn. **28**, 584 (1994) [Semiconductors **28**, 352 (1994)].
[2] O. V. Kibis, in *2nd Russian Conference on Semiconductor Physics. Abstracts* [in Russian], Zelenogorsk (1996) Vol. 2, p. 51.
[3] M. F. Deĭgen and S. I. Pekar, Zh. Éksp. Teor. Fiz. **21**, 803 (1951).
[4] L. S. Kukushkin, JETP Lett. **7**, 194 (1968).
[5] O. V. Kibis and V. S. Shadrin, Fiz. Tekh. Poluprovodn. **21**, 185 (1987) [Sov. Phys. Semicond. **21**, 113 (1987)].
[6] O. V. Kibis, Fiz. Tekh. Poluprovodn. **29**, 125 (1995) [Semiconductors **29**, 66 (1995)].
[7] A. M. Stoneham, *Theory of Defects in Solids: The Electronic Structure of Defects in Insulators and Semiconductors*, Clarendon Press, Oxford (1975) [Russ. trans., Mir, Moscow (1978)].

Translated by P. Shelnitz

Deep states in silicon δ-doped GaAs

V. Ya. Aleshkin,[a] V. M. Danil'tsev, A. V. Murel', O. I. Khrykin, and V. I. Shashkin

Institute of the Physics of Microstructures, Russian Academy of Sciences, 603600 Nizhniĭ Novgorod, Russia
(Submitted July 14, 1997; accepted for publication October 21, 1997)
Fiz. Tekh. Poluprovodn. **32**, 733–738 (June 1998)

The density and electron trapping cross section of deep states in silicon δ-doped GaAs were investigated by means of measurements of the voltage and temperature dependences of the impedance of a Schottky contact to the structure. It was observed that density-of-states tails appear in the band gap when the silicon density in the δ-layer exceeds 6×10^{12} cm^{-2}. In our structures the energy characterizing the penetration depth of a tail was in the range 20–100 meV. The characteristic electron trapping cross section of deep states in δ-layers was of the order of 10^{-17} cm^2. It was shown that saturation of the electron density in the δ-layer with increasing Si density is due to self-compensation of Si. © *1998 American Institute of Physics.* [S1063-7826(98)02206-6]

1. INTRODUCTION

The study of δ-layers started in 1980, when the first structures containing such layers were fabricated.[1] Most experimental and theoretical studies in this field dealt with the investigation of the properties of mobile charge carriers (see the review in Ref. 2) in a δ-layer and the conditions under which very narrow impurity distributions were realized.[3] Since the impurity density in a δ-layer is usually high, deep states in the band gap should exist in it, just as in a strongly doped bulk semiconductor.[4] The importance of investigating these states is obvious, since the frequency dispersion of the conductivity in semiconductor devices with δ-layers (field-effect transistors, photodetectors, and others) can be determined by their charge-transfer times. Saturation of the surface density of current carriers at the level $3\times10^{12}-10^{13}$ cm^{-2} with increasing Si density has been observed in Si δ-layers in GaAs.[5–8] Two mechanisms were proposed in order to explain this phenomenon. In the first one saturation was attributed to self-compensation of Si (some Si atoms occupy Ga sites and become acceptors). In the second mechanism saturation was attributed to filling of DX centers (DX centers sinking below the Fermi level).[9]

In this article we present the results of an experimental study of the density and electron trapping cross sections of deep states in a silicon δ-doped GaAs by means of measurements of the voltage and temperature dependences of the impedance of a Schottky contact to the structure. It was found that density-of-states tails appear in the band gap when the Si density in the δ-layer exceeds 6×10^{12} cm^{-2}. In our structures the energy characterizing the extent of the tails in the band gap varied in the interval 20–100 meV. The characteristic electron trapping cross section of deep states in δ-layers was of the order of 10^{-17} cm^{-2}. It was shown that saturation of the electron density in the δ-layer with increasing Si density is due to self-compensation. A method is proposed for determining the density and electron trapping times of deep states in δ-layers.

2. THEORY

Let us consider the specific (per unit area) weak-signal impedance of a Schottky contact to a structure containing a δ-doped layer. Let the δ-layer lie in the $x=x_1$ plane and the Schottky contact in the $x=0$ plane (see Fig. 1). We assume that before and after the δ-layer the superconductor is uniformly doped with shallow donors with density n, which are completely ionized in the temperature interval of interest to us. Deep states with density $g(\varepsilon)$ are present in the plane of the δ-layer. Let φ_0 be the constant component of the electrical potential at the surface of the semiconductor and $\tilde{\varphi}_0$ be the amplitude of the variable component, varying in time as $\exp i\omega t$; were $\tilde{\varphi}_0 \ll \varphi_0$. We shall denote the amplitudes of all variable quantities by letters with a tilda. We take as the reference point for the potential its value in the bulk of the semiconductor. The impedance of the system can be expressed in terms of the ratio of $\tilde{\varphi}_0$ to its coordinate derivative $\tilde{\varphi}_0'$:

$$z=\frac{4\pi i}{\varkappa\omega}\frac{\tilde{\varphi}_0}{\tilde{\varphi}_0'}=(C+i\omega G)^{-1}, \tag{1}$$

$$C=\frac{\varkappa}{4\pi}\,\mathrm{Re}\left(\frac{\tilde{\varphi}_0'}{\tilde{\varphi}_0}\right), \quad G=\frac{\varkappa\omega}{4\pi}IM\left(\frac{\tilde{\varphi}_0'}{\tilde{\varphi}_0}\right), \tag{2}$$

where $\varkappa$ is the permittivity, and C and G are the capacitance and parallel conductance.

To find z we must solve the Poisson equation

$$\varphi''=\frac{4\pi e}{\varkappa}\left[N_c(T)\Phi_{1/2}\left(\frac{\mu+e\varphi}{T}\right)-n\right], \tag{3}$$

where $N_c(T)$ is the effective density of states in the conduction band, Φ_i is the Fermi integral of index i, T is the temperature in energy units, and μ is the chemical potential measured from the conduction-band bottom in the bulk of the semiconductor. Equation (3) holds everywhere except in the plane $x=x_1$.

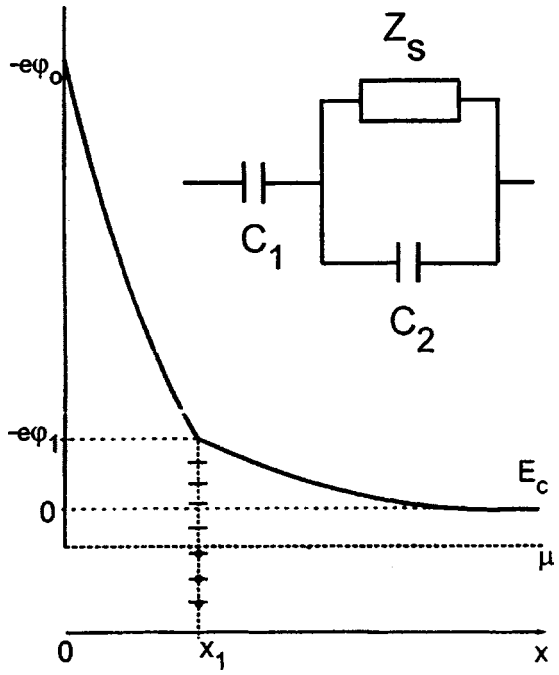

FIG. 1. The band diagram of a Schottky contact to a structure with a δ-layer with high reverse voltages. The inset shows the equivalent circuit.

The electronic states in the δ-layer can be divided into two groups: fast and slow. The electron population of the fast states can follow instantaneously the variation of the potential in time. In the present system the fast states are states in the conduction band, i.e., their energies lie above the conduction-band bottom in the plane $x=x_1$. Since in our samples in the surface density of shallow donors in the δ-layer $N_\delta > 10^{12}$ cm^{-2}, we shall describe the fast states quasiclassically,[2] i.e., we shall employ Eq. (3). The slow states are deep states. We shall assume that the characteristic extents of the electron wave functions of deep states are much smaller than the characteristic scales of variation of the potential, so that the charge density associated with them can be assumed to be proportional to the Dirac δ-function $\delta(x-x_1)$.

Integrating Eq. (3) in the region $x>x_1$ we obtain

$$\varphi' = \pm\sqrt{F(\varphi,0,T)}, \quad \tilde{\varphi}' = \frac{4\pi e}{\varkappa}\frac{N_c\Phi_{1/2}[(\mu+e\varphi)/T]}{\varphi'}\tilde{\varphi}, \quad (4)$$

where

$$F(\varphi_i,\varphi_j,T) = \frac{8\pi}{\varkappa}\left\{N_cT\left[\Phi_{3/2}\left(\frac{\mu+e\varphi_i}{T}\right) - \Phi_{3/2}\left(\frac{\mu+e\varphi_j}{T}\right)\right] - en(\varphi_i-\varphi_j)\right\}.$$

In the relation (4) the plus sign is used if $\varphi(x_1)=\varphi_1<0$ and the minus sign is used if $\varphi_1>0$.

Integrating the Poisson equation near x_1, we find a relation between the derivatives φ' and $\tilde{\varphi}'$ before and after the δ-layer:

$$\varphi'(x_1-0) = \varphi'(x_1+0) + \frac{4\pi\sigma}{\varkappa}, \quad (5)$$

$$\tilde{\varphi}'(x_1-0) = \tilde{\varphi}'(x_1+0) + \frac{4\pi\tilde{\sigma}}{\varkappa}, \quad (6)$$

$$\sigma = eN_\delta + e\int_{-\infty}^{0}\frac{g(\varepsilon)}{1+\exp\left(\dfrac{\mu-\varepsilon+e\varphi_1}{T}\right)}d\varepsilon, \quad (7)$$

where the energy ε is measured from the conduction-band bottom in the plane of the δ-layer, and σ is the surface-charge density in the layer. In deriving Eq. (7) we assumed that the deep states are of donor type; i.e., they are neutral when an electron is present, and they are positively charged when there is no electron. If the deep states are of acceptor type, i.e., they are negatively charged when an electron is present, then N_δ in Eq. (7) must be replaced by the difference

$$N_\delta - \int_{-\infty}^{0} g(\varepsilon)d\varepsilon.$$

To find $\tilde{\sigma}$ we shall examine the variation of the electron population of deep levels lying in the interval from ε to $\varepsilon+d\varepsilon$ under the action of a variable potential $\varphi(x_1,t)$. The variation of the charge density of these states in time is described by the equation[10,11]

$$\dot{\rho}(\varepsilon,t) = \frac{\rho_e[\varepsilon,\varphi(x_1,t)]-\rho(\varepsilon,t)}{\tau(\varepsilon)}, \quad (8)$$

where $\tau(\varepsilon)$ is the lifetime of electrons in deep states and $\rho_e(\varepsilon,\varphi_1)$ is the equilibrium value of $\rho(\varepsilon)$ with fixed φ_1:

$$\rho_e(\varepsilon,\varphi_1) = \frac{eg(\varepsilon)}{1+\exp\left(\dfrac{\mu-\varepsilon+e\varphi_1}{T}\right)}. \quad (9)$$

Since

$$\varphi(x_1,t) = \varphi_1 + \tilde{\varphi}_1 \exp i\omega T, \quad \tilde{\varphi}_1 \ll \varphi_1, T/e,$$

we find the following expression for $\tilde{\sigma}$ from Eqs. (7) and (8):

$$\tilde{\sigma} = -\frac{e^2\tilde{\varphi}_1}{T}\int_{-\infty}^{0}\frac{g(\varepsilon)\exp\left(\dfrac{\mu-\varepsilon+e\varphi_1}{T}\right)}{[1+i\omega\tau(\varepsilon)]\left[1+\exp\left(\dfrac{\mu-\varepsilon+e\varphi_1}{T}\right)\right]^2}d\varepsilon. \quad (10)$$

Let us examine the region $0<x<x_1$. For convenience we introduce the potential φ_2 such that $N_c\Phi_{1/2}(\mu+e\varphi_2/T) \ll n$, $(\varphi_2<0)$ but $\varphi_2>\varphi_0$. We note that the contact potential difference on a Schottky contact to *n*-GaAs is approximately 0.8 V, so that $\varphi_0<-0.8$ V under a reverse bias. The potential φ_2 can be set equal to, for example, $-(\mu+10T)/e$. If $\varphi_1<\varphi_2$, then in the region $0<x<x_1$ the electron charge can be ignored and the Poisson equation becomes

$$\varphi'' = -\frac{4\pi en}{\varkappa}. \quad (11)$$

Integrating Eq. (11), we find

$$\varphi_0=\varphi_1-x_1\left[\varphi(x_1-0)+\frac{2\pi e n x_1}{\varkappa}\right], \tag{12}$$

$$\tilde{\varphi}_0=\tilde{\varphi}_1-x_1\tilde{\varphi}(x_1-0), \tag{13}$$

$$\tilde{\varphi}_0'=\tilde{\varphi}'(x_1-0). \tag{14}$$

Because of they are unwieldy, the results obtained by integrating the Poisson equation in the case $\varphi_1>\varphi_2$ are presented in the *Appendix*. From Eqs. (12)–(14) and (A.4)–(A.6) we find the impedance and potential at the surface as functions of φ_1.

Let us now examine in greater detail the case where $\varphi_1<\varphi_2$, since this is the simplest case. In this case

$$\frac{\tilde{\varphi}_0'}{\tilde{\varphi}_0}=\frac{1}{\tilde{\varphi}_1/\tilde{\varphi}'(x_1-0)-x_1}. \tag{15}$$

It follows from Eq. (15) that the equivalent circuit of the system can be represented as a capacitance $C_1=\varkappa/4\pi x_1$ and an impedance $z_1=-i\omega\varkappa\tilde{\varphi}'(x_1-0)/4\pi\tilde{\varphi}_1$ connected in series. The quantity C_1 corresponds to the capacitance of the GaAs layer from the surface up to the δ-layer. By virtue of Eq. (6) we can represent z_1^{-1} in the form

$$z_1^{-1}=i\omega C_2+z_s^{-1}, \tag{16}$$

where $C_2=-\varkappa\tilde{\varphi}'(x_1+0)/4\pi\tilde{\varphi}_1$ is the capacitance of GaAs after the δ-layer, and z_s is the impedance of the deep states

$$z_s^{-1}=-\frac{i\omega\tilde{\sigma}}{\tilde{\varphi}_1}=\frac{i\omega e^2}{T}\times\int_{-\infty}^{0}\frac{g(\varepsilon)\exp\left(\dfrac{\mu-\varepsilon+e\varphi_1}{T}\right)}{[1+i\omega\tau(\varepsilon)]\left[1+\exp\left(\dfrac{\mu-\varepsilon+e\varphi_1}{T}\right)\right]^2}d\varepsilon. \tag{17}$$

We thus obtain the equivalent circuit shown in the inset in Fig. 1 for our structure. We note that z_s can be represented as an infinite number of *RC* circuits connected in parallel.[12]

From Eqs. (1), (2), and (15)–(17) we obtain

$$\mathrm{Re}\left(\frac{1}{z_s\omega}\right)=\mathrm{Im}\left(\frac{\tilde{\sigma}}{\tilde{\varphi}_1}\right)=\frac{C_1^2G/\omega}{(G/\omega)^2+(C-C_1)^2}, \tag{18}$$

i.e., the real part of z_s^{-1} can be expressed in terms of measurable quantities. We shall now make three additional simplifying assumptions. The first two consist of the requirement that the trapping cross section and density of states vary slowly with energy:

$$|d\ \ln[\sigma_c(\varepsilon)]/d\varepsilon|,\quad |d\ \ln[g(\varepsilon)]/d\varepsilon|\ll T^{-1}.$$

When these requirements hold, the neighborhood of $\varepsilon=\mu+e\varphi_1$ makes the main contribution to the real part of Eq. (17). Then we can set

$$\tau(\varepsilon)=\tau_0\exp(-\varepsilon/T),$$

where

$$1/\tau_0=\sigma_c(\mu+e\varphi_1)v_tN_c$$

and v_t is the thermal velocity of the electrons. The third assumption is the requirement that the condition $\omega\tau_0\ll 1$ be satisfied. Then Eq. (17) can be integrated, and Eq. (18) can be written in the form

$$\mathrm{Im}\left(\frac{\tilde{\sigma}}{\tilde{\varphi}_1}\right)\simeq e^2gU(\gamma)T\ \ln\left[\frac{\omega\tau_0\gamma(-1+\sqrt{1+4/\gamma^2})}{2}\right], \tag{19}$$

where $\gamma=\omega\tau_0\exp[-(\mu+e\varphi_1)/T]$,

$$U(\gamma)=\frac{(\gamma^3-\gamma)\ln\gamma+\pi\gamma^2-(\gamma+\gamma^3)}{(1+\gamma^2)^2}. \tag{20}$$

The function $U(\gamma)$ has a maximum equal to 0.285 at $\gamma=1$. Therefore,

$$\mathrm{Im}\left(\frac{\tilde{\sigma}}{\tilde{\varphi}_1}\right)_{\max}\simeq 0.285e^2g(\mu+e\varphi_1). \tag{21}$$

Thus the maximum of $\mathrm{Im}(\tilde{\sigma}/\tilde{\varphi}_1)$ is determined by the density of states g at the Fermi level. We recall that the argument of the function g is measured from the conduction-band bottom in GaAs in the plane $x=x_1$. The condition for a maximum means that the reciprocal of the electron escape time equals the frequency ω of the external signal for states at the Fermi level.

Using the expression (21), we can propose a method for determining $g(\varepsilon)$. Indeed, changing ω by an amount $\Delta\omega$ at fixed temperature T changes the energy ε corresponding to the maximum of $\mathrm{Im}(\tilde{\sigma}/\tilde{\varphi}_1)$ by the amount $\Delta\varepsilon=T\ln[(\omega+\Delta\omega)/\omega]$. Therefore, $g(\varepsilon)$ can be found by measuring the maximum value of $\mathrm{Im}(\tilde{\sigma}/\tilde{\varphi}_1)$ at different frequencies. However, as long as τ_0 is unknown, the point of origin for ε is undetermined.

We shall now show how τ_0 can be determined from measurements of the frequency dependence of the temperature corresponding to the maximum of $\mathrm{Im}(\tilde{\sigma}/\tilde{\varphi}_1)$ for a fixed external voltage on the Schottky contact. The potential on the semiconductor surface consists of the contact potential difference and the external voltage: $\varphi_0=\varphi_c+\varphi_{\mathrm{ext}}$. The contact potential difference equals the difference of the work functions of the semiconductor and metal. The temperature dependence of the semiconductor work function is determined by the function $\mu(T)$, while the work function of the metal is virtually temperature-independent.[13] For this reason, for a fixed external voltage the temperature dependence of φ_0 is determined by $\mu(T)$. If $|\varphi_0|\gg|\varphi_1|$, then the variation of φ_1 with T is much smaller than that of $\mu(T)$. It can be assumed approximately that φ_1 is temperature-independent. Then σ_c can be determined from measurements of two temperatures T_1 and T_2 corresponding to the maxima of $\mathrm{Im}(\tilde{\sigma}/\tilde{\varphi}_1)$ for two frequencies ω_1 and ω_2, which do not differ too much, such that

$$|T_2-T_1|\ll T_{1,2},\quad \sigma_c(\mu+e\varphi_1)\approx\ \mathrm{const}.$$

Indeed, the condition $\gamma=1$ gives the system of equations

$$\mu(T_1)+e\varphi_1=-T_1\ \ln(\sigma_c v_t N_c/\omega_1), \tag{22}$$

$$\mu(T_2)+e\varphi_1=-T_2\ \ln(\sigma_c v_t N_c/\omega_2). \quad (23)$$

Using the expressions for ν_t and N_c we find from Eqs. (22) and (23)

$$\sigma_c \approx \frac{2\pi\hbar^3\omega_1}{m_c T_1^2} \times \exp\left[\frac{\mu(T_1)-\mu(T_2)+T_2\ \ln(\omega_2 T_1^2/\omega_1 T_2^2)}{T_2-T_1}\right], \quad (24)$$

where m_c is the electron effective mass in the conduction band.

3. EXPERIMENT AND DISCUSSION OF THE RESULTS

Silicon-doped δ-layers in n-GaAs were obtained by the method of organometallic gas-phase epitaxy in a horizontal reactor at atmospheric pressure in the system $Ga(CH_3)_3-AsH_3-SiH_4-H_2$. Growth was conducted on semi-insulating and conducting GaAs substrates disoriented relative to the (100) plane by 3° in the [110] direction. The growth temperature varied in the range 550–700 °C. The Si δ-layer was embedded by interrupting GaAs growth during the introduction of the impurity. The silane flux velocity and the formation time of the δ-layer were varied in order to obtain a different Si density in a layer.

The epitaxial GaAs in which the δ-layers were grown had electron density $n\simeq 10^{15}$ cm^{-3} and Hall mobility 7×10^3 cm^2/(V·s) at 300 K and greater than 3×10^4 cm^2/(V·s) at 77 K. Measurement of the density of deep levels in it by the DLTS method showed the presence of the first electron trap *EL*2 with density not exceeding 10^{14} cm^{-3}. The basic laws of growth and characteristics of δ-layers have been published in Ref. 14 .

Hall measurements at temperatures 300 and 77 K and measurements of the capacitance C and weak-signal parallel conductance G of the Schottky contact at three frequencies 1 MHz, 10 kHz, and 1 kHz in the temperature range 77–360 K were performed in order to study the electrical properties of the δ-doped layers. The Schottky contacts were prepared by depositing 500 μm in diameter aluminum contacts on GaAs.

Figure 2 shows the electron mobility μ_n versus the surface density N_δ of free electrons in the δ-layer. The solid curve shows the dependence obtained in Ref. 5 and the dots and crosses show the results of our measurements. Samples with Si density in the δ-layer exceeding 6×10^{12} cm^{-2} (marked by crosses) possessed a low mobility, which, moreover, also increased as the temperature was raised from 77 to 300 K. In addition, the electron density in them is appreciably lower than the Si density. Density-of-states tails were observed in these samples. We note that saturation or even a decrease of the electron density with increasing Si density in the δ-layers was observed earlier.[5,8,14] Hopping conduction in strongly silicon δ-doped GaAs, i.e., actually a metal–insulator transition, has recently been observed.[15]

Figure 3 shows typical observed dependences of the capacitance C and conductance G of a Schottky contact to structures with Si density in the δ-layer greater than

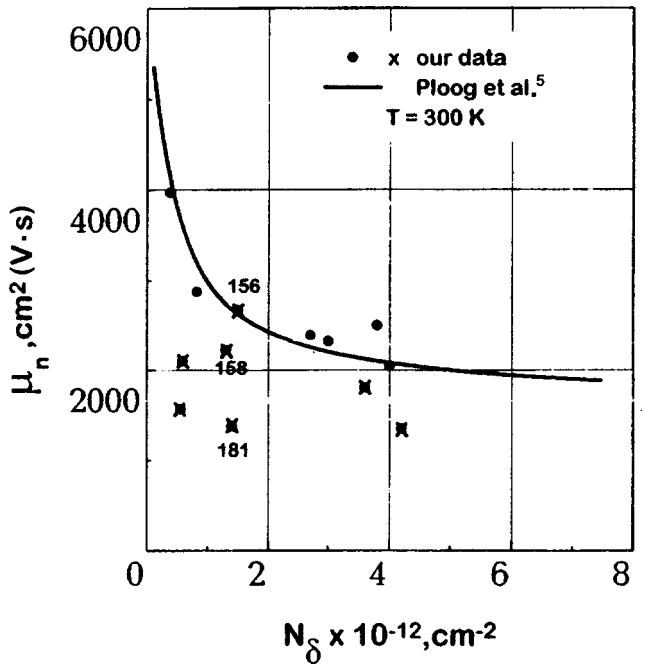

FIG. 2. Mobility μ versus surface electron density N_δ in the δ-layer. The solid curve shows the dependence obtained in Ref. 5 . The crosses show the data for samples with Si density in the δ-layer exceeding 6×10^{12} cm^{-2}. The numbers near the points correspond to the numbers of the samples in Table I.

6×10^{12} cm^{-2} on the applied voltage V. It is clearly evident from the figure that the function $C(V)$ has a characteristic step-like behavior and the curve $G(V)/\omega$ has a sharp asymmetric spike. The results of numerical calculations of these dependences are also presented here. We note that a conductance spike did not occur in structures with Si density in the δ-layer below 6×10^{12} cm^{-2}, and the conductance is at least two orders of magnitude smaller.

Figure 4 shows the observed temperature dependences of the conductance with a fixed external voltage. It is clearly seen that as the applied reverse voltage increases, the con-

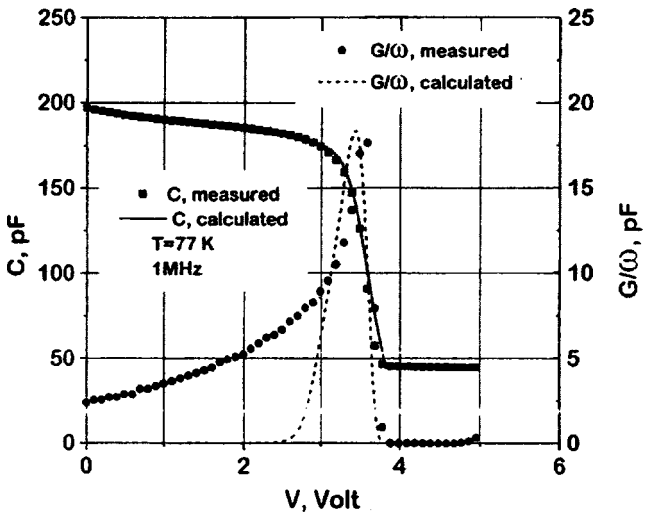

FIG. 3. Capacitance C and conductance G of a Schottky contact to structure No. 158 versus the reverse voltage V at $T=77$ K at frequency 1 MHz.

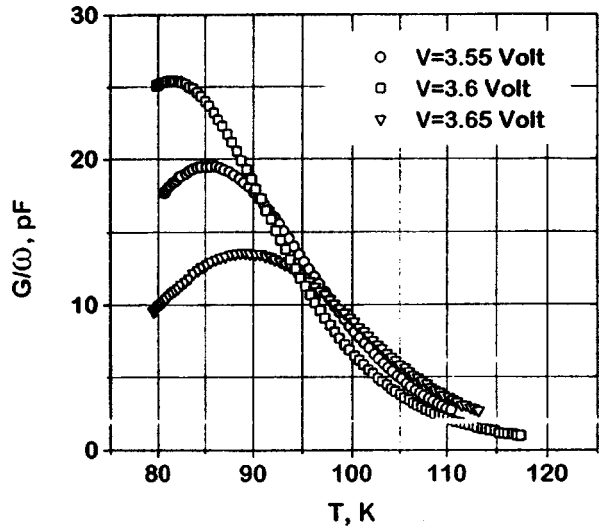

FIG. 4. G/ω of a Schottky contact to structure No. 158 at frequency 1 MHz versus temperature T. The curves were measured for three values of the reverse voltage V.

ductance maxima decrease and shift to higher temperatures. This character of the dependence corresponds to a continuous energy density distribution of deep states. If only one level of deep states were present in the plane of the δ-layer, then only the amplitude of the conductance maximum and not its position would change as the applied reverse voltage increased.[12]

To describe the observed voltage and temperature dependences of the capacitance and conductance we constructed a numerical model on the basis of a theoretical analysis. The calculations showed that if the density of deep states contains a pronounced peak (for example, the density of deep states has a Gaussian spectrum whose maximum is separated from the conduction band edge by an amount greater than the dispersion), then a clearly expressed maximum appears in the computed curves of the capacitance versus the applied voltage. Such maxima were not observed experimentally. On this basis we assume that the density of deep states in our structures decreases monotonically away from the conduction-band bottom into the band gap, i.e., it has the form of tails. For this reason, in the model the energy dependence of the density of deep states was assumed to be exponential $g(\varepsilon)=N_s/\varepsilon_0\exp(\varepsilon/\varepsilon_0)$, where N_s is the surface density of deep states.

Table I shows the parameters of three structures, which were grown at 650 °C and, which differ by the Si densities in the δ-layer. The quantities N_s, ε_0, and σ_c were chosen so as to obtain the best agreement between the experimental and computed voltage and temperature dependences of the capacitance and conductance. We note that the sum of the quantities N_δ and N_s gives the total density of uncompensated donors. DX centers do not change this density; they instead decrease the free-electron density. For this reason, if DX centers were the main reason for saturation of the electron density,[9] then as the Si density in a δ-layer increases, the total number of uncompensated donors in it would also increase. It is evident from the data presented in Table I that as the Si density in the δ-layer increases, not only the surface electron density but also the total density of uncompensated donors in the layer increase. This means that some Si atoms occupy As sites and become acceptors, i.e., self-compensation occurs.

We note as the quantity of Si in a δ-layer increases, the density and depth of deep states increase, while their electron trapping cross sections decrease. We believe that these facts can be explained by a sharp increase in fluctuations in the distribution of Si atoms when the density exceeds 6×10^{12} cm^{-2}. A similar fact has been observed with beryllium δ-doping of GaAs.[16]

This work was supported by the Russian Fund for Fundamental Research under Grants 95-02-05606 and 95-02-05870.

4. APPENDIX

If $\varphi_1>\varphi_2$, then it is convenient to divide the region $0<x<x_1$ into two subregions. The Poisson equation has the form (3) in the region $x_2<x<x_1$ and (11) in the region $0<x<x_2$. In the plane $x=x_2$ the potential $\varphi(x_2)=\varphi_2$. Integrating the Poisson equation in the region $0<x<x_1$ we find

$$\varphi_2'=\sqrt{F(\varphi_2,\varphi_1,T)+(\varphi'(x_1-0))^2}, \tag{A.1}$$

$$\tilde{\varphi}_2'=\frac{4\pi e\tilde{\varphi}_1}{\varkappa\varphi_2'}\left[n-N_c\Phi_{1/2}\left(\frac{\mu+e\varphi_1}{T}\right)\right]+\frac{\varphi(x_1-0)\tilde{\varphi}_1'}{\varphi_2'}, \tag{A.2}$$

$$\varphi_0'=\sqrt{\frac{8\pi en}{\varkappa}(\varphi_2-\varphi_0)+(\varphi'(x_1-0))^2}, \tag{A.3}$$

$$\varphi_0=\varphi_2+(x_s-x_1)\left[\frac{2\pi en(x_1-x_s)}{\varkappa}+\varphi_2'\right], \tag{A.4}$$

$$\varphi_0'=-\frac{4\pi en\tilde{\varphi}_0}{\varkappa\varphi_0'}+\frac{\varphi_2'\tilde{\varphi}_2'}{\varphi_0'}, \tag{A.5}$$

$$\tilde{\varphi}_0=\tilde{x}_s\left[\frac{2\pi en(x_1-x_s)}{\varkappa}+\varphi_2'\right]+(x_1-x_s)\left[\frac{2\pi en\tilde{x}_s}{\varkappa}-\tilde{\varphi}_2'\right], \tag{A.6}$$

TABLE I.

Sample No.	SiH_4, ml/min	Growth time, s	Si density, relative units	μ_n, $\mathrm{cm}^2/(\mathrm{V}\cdot\mathrm{s})$ $T=300$ K	N_δ, 10^{11} cm^{-2} $T=300$ K	μ_n, $\mathrm{cm}^2/(\mathrm{V}\cdot\mathrm{s})$ $T=77$ K	N_δ, 10^{11} cm^{-2} $T=77$ K	N_s, 10^{11} cm^{-2}	ε_0, meV	σ_c, 10^{17} cm^{-2}	x_1, μm
156	20	50	1000	2670	15	2400	20	5	30	0.55	0.15
158	67	10	670	2200	13	2600	18	4	20	1.4	0.12
181	100	120	12000	1300	14	1040	15.6	9	70	0.4	0.43

where

$$x_s = x_1 - x_2 = \int_{\varphi_2}^{\varphi_1} \frac{d\varphi}{\sqrt{F(\varphi,\varphi_1,T)+(\varphi'(x_1-0))^2}}, \quad \text{(A.7)}$$

$$\tilde{x}_s = \frac{\tilde{\varphi}_1}{\varphi'(x_1-0)} + \int_{\varphi_2}^{\varphi_1} \frac{d\varphi}{[F(\varphi,\varphi_1,T)+(\varphi'(x_1-0))^2]^{3/2}} \times \left\{ \frac{4\pi e}{\varkappa} \left[N_c \Phi_{1/2}\left(\frac{\mu + e\varphi_1}{T} \right) - n \right] \times \tilde{\varphi}_1 - \varphi'(x_1-0)\tilde{\varphi}'(x_1-0) \right\}. \quad \text{(A.8)}$$

[a)]Fax: (8312) 675553; e-mail: aleshkin@ipm.sci-nnov.ru

[1] C. E. Wood, G. Metze, J. Berry, and L. F. Eastman, J. Appl. Phys. **51**, 383 (1980).
[2] A. Ya. Shik, Fiz. Tekh. Poluprovodn. **26**, 1161 (1992) [Sov. Phys. Semicond. **26**, 649 (1992)].
[3] E. F. Schubert, J. B. Stark, B. Ullrich, and J. E, Cunningham, Appl. Phys. Lett. **52**, 1508 (1988).
[4] B. I. Shklovskiĭ and A. L. Efros, *Electronic Properties of Doped Semiconductors*, Springer-Verlag, N. Y., 1984 [Russian original, Nauka, Moscow, 1979], Chap. 11, p. 321.
[5] K. Ploog, M. Hauser, and A. Ficher, Appl. Phys. A **45**, 233 (1988).
[6] Y. Yamanchi, T. Makimoto, and Y. Horikoshi, Jpn. J. Appl. Phys. **28**, L1689 (1986).
[7] E. F. Shubert, R. F. Korf, J. M. Kuo, H. S. Luftman, and P. A. Garbinski, Appl. Phys. Lett. **57**, 497 (1990).
[8] H. C. Nutt, R. S. Smith, M. Towers, P. K. Rees, and D. J. James, J. Appl. Phys. **70**, 821 (1991).
[9] A. Zrenner, F. Koch, R. L. Williams, R. A. Stradling, K. Ploog, and G. Weimann, Semicond. Sci. Technol. **3**, 1203 (1988).
[10] W. G. Oldham and S. S. Naik, Solid-State Electron. **15**, 1085 (1972).
[11] C. Ghezzi, Appl. Phys. A **26**, 191 (1982).
[12] V. Ya. Aleshkin, Fiz. Tekh. Poluprovodn. **30**, 2202 (1996) [Semiconductors **30**, 1148 (1996)].
[13] V. L. Bonch-Bruevich and S. G. Kalashnikov, *Semiconductor Physics* [in Russian, Nauka, Moscow, 1990], Chap. 6, p. 214.
[14] V. M. Danil'tsev, I. V. Irin, A. V. Murel', O. I. Khrykin, and V. I. Shashkin, Neorg. Mater. **30**, 1026 (1994).
[15] A. V. Buyanov, P. O. Holtz, W. M. Chen, B. Monemar, T. G. Anderson, and J. Thordson, Appl. Phys. Lett. **68**, 3464 (1996).
[16] B. Johnson, P. M. Koenraad, W. C. van der Vleuten, H. W. M. Saleminh, and J. H. Wolter, Phys. Rev. Lett. **75**, 1606 (1994).

Translated by M. E. Alferieff

Electron-phonon interaction and electron mobility in quantum-well type-II PbTe/PbS structures

V. V. Bondarenko and V. V. Zabudskiĭ

Institute of Semiconductor Physics, Ukrainian National Academy of Sciences, 252028 Kiev, Ukraine

F. F. Sizov

Institute of Semiconductor Physics, Ukrainian National Academy of Sciences, 252028 Kiev, Ukraine

(Submitted July 24, 1997; accepted for publication November 17, 1997)
Fiz. Tekh. Poluprovodn. **32**, 739–742 (June 1998)

Electron mobilities in PbTe layers were calculated, taking into account electron scattering by longitudinal polar optical phonons, for low-dimensional structures — multiple PbTe/PbS quantum wells, which are type-II structures. Comparison with the electron mobilities obtained from Hall coefficient and magnetoresistance investigations in undoped multiple PbTe/PbS quantum wells versus the magnetic field intensity showed good agreement between the computed and experimental results for these structures. © *1998 American Institute of Physics.* [S1063-7826(98)02306-0]

1. INTRODUCTION

The main scattering mechanisms that limit carrier mobility in undoped narrow-gap bulk IV–VI semiconductors and their solid solutions in the temperature range important for practical applications 77–300 K are:[1,2] 1) scattering by polar longitudinal optical (*LO*) phonons, 2) scattering by the deformation potential of acoustic phonons, and 3) scattering due to the disordering of the alloy potential. Of these mechanisms the dominant one for the present group of semiconductors is the interaction of electrons with polar longitudinal optical phonons [$\hbar\omega_{LO}\approx 160$ K[3] (Ref. 3)], which can be accurately calculated without using adjustable parameters. This type of scattering determines the maximum electron and hole mobilities in undoped narrow-gap IV–VI semiconductors in the temperature range $T\geqslant 70$ K.

In low-temperature structures size quantization influences both the energy spectrum of the charge carriers and the spectrum of optical phonons. We have therefore investigated scattering by optical phonons for low-dimensional structures — PbTe/PbS multiple quantum wells (MQWs) — under the assumption that, just as in bulk narrow-gap IV–VI semiconductors, this mechanism of charge-carrier scattering is the main mechanism determining the maximum values of the electron mobilities at temperatures $T>70$ K.

2. THEORY

Optical oscillations in PbTe/PbS quantum wells have been studied in the dielectric continuum model (DCM).[4] In this model the optical phonons in low-dimensional structures decay into bounded *LO* and *TO* modes and surface-like (interfacial) *IF* modes, and the bounded *TO* modes do not contribute to charge-carrier scattering. The polarization fields of the bounded *LO* modes are formed by volume charges and charges at the boundaries of the layers, while the polarization field of the *IF* modes (symmetric *s* and antisymmetric *a* are produced only by surface waves of charges on the interfaces of the layers. For this reason, decreasing the layer thickness *d* in low-dimensional structures will have the effect of increasing the influence of *IF* modes on charge-carrier transport as compared with bounded *LO* modes. In the case where *IF* modes dominate, this decreases the charge-carrier mobilities in the individual layers of a multilayer quantum-well structure, while in the case where the bounded *LO* modes dominate, the mobility increases as *d* decreases. It is therefore important to determine the relative contributions of the bounded *LO* and *IF* modes for interpreting experimental results and for designing devices using low-dimensional structures.

In connection with the large values of the static permittivities ε_s in IV–VI compounds (for example, in PbTe $\varepsilon_s>400$ at $T=300$ K and increases with decreasing temperature because of the softening of the transverse optical mode) the influence of the *IF* modes is effective in these compounds. It should appreciably change the charge-carrier mobilities as compared with the mobility in bulk crystals, especially in thin layers of such structures.

The interaction of electrons with optical phonons in a PbSnTe quantum well and in a three-layer structure PbTe/PbSnTe/PbTe was studied earlier in Refs. 5 and 6, taking into account the nonparabolicity of the band spectrum but in the approximation of infinitely high barriers. In the present article we report the results of an experimental study of the energy spectrum of current carriers in multiple PbTe/PbS quantum wells (see, for example, Ref. 7) in a two-band Kane model, with allowance for the nonparabolicity of the band spectrum and the finite height of the barriers with carriers populating the first two subbands. In this system the offset of the valence bands at $T=77$ K is $\Delta E_v=0.32\pm 0.05$ eV, while the distance between the conduction-band edges in PbTe and PbS is[7] $\Delta E_c\approx 0.4$ eV. Since the conduction-band edge in PbTe lies below the conduction- and valence-band edges in PbS for the layer thicknesses $d>60$ Å being con-

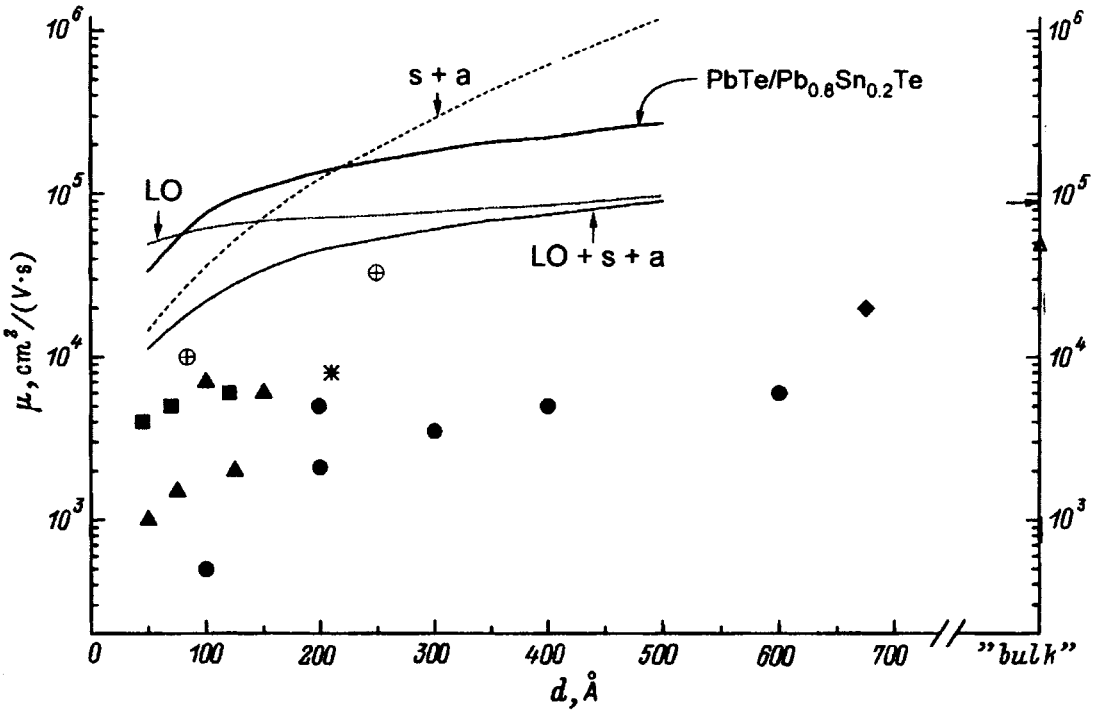

FIG. 1. Computed electron mobilities for scattering by different phonon modes ($LO+s+a$, LO, $s+a$) and experimental ($\oplus$) data on electron mobility for multiple PbTe/PbS wells as a function of the well period at $T=77$ K. The experimental data for PbTe/EuTe ($\blacktriangle$)[14] and PbTe/$Pb_{0.8}Sn_{0.2}$Te ($\blacksquare$) superlattices and PbTe/$Pb_{0.87}Sn_{0.13}$TE ($\blacklozenge$)[15] and PbTe/$Pb_{0.8}Sn_{0.2}$Te (*, $\bullet$)[5,16] quantum wells are also presented. The solid curve at the top refers to calculations of electron mobility in PbTe/$Pb_{0.8}Sn_{0.2}$Te quantum wells on ($LO+s+a$) modes. The symbol Δ on the right-hand ordinate marks the experimental values of the electron mobility in perfect single crystals and ''thick'' ($d\geqslant 3$ μm) epitaxial PbTe quantum wells with electron density of the order of 10^{17} cm^{-3}, where the highest electron mobilities are observed. The arrow on the right-hand ordinate marks the maximum computed values of the electron mobility in PbTe single crystals in the two-band nonparabolic Kane model, with allowance for the scattering of current carriers by longitudinal optical phonons only.

sidered here, the PbTe/PbS structures are type-II structures. It has been shown that these structures possess semimetallic conductivity for layer thicknesses[7] $d\geqslant 60$ Å. Longitudinal transport is realized by electrons in PbTe layers and holes in PbS layers. The electron mobility in the PbTe layers is several times higher than the hole mobility in the PbS layers.

An expression for the scattering rates of an electron with the emission ($-$) and adsorption ($+$) of one phonon can be obtained[5] by applying the Fermi rule to the structures studied:

$$W(i,f)=\sum_{\alpha}\frac{2\pi}{\hbar}|\langle f|\hat{H}_{\alpha}|i\rangle|^2\delta(-\varepsilon_f+\varepsilon_i\pm\hbar\omega), \qquad (1)$$

where ε_f and ε_i are the total electron energies in the final and initial states. The electron-phonon interaction Hamiltonian is

$$\hat{H}_{\alpha}=\sum_{\mathbf{q}_{\parallel}}\sum_{q_z} e^{i\mathbf{q}_{\parallel}\cdot\boldsymbol{\rho}}\Gamma_j(\mathbf{q}_{\parallel},q_z,z)[\hat{a}_j(\mathbf{q}_{\parallel},q_z)+\hat{a}_j^{+}(-\mathbf{q}_{\parallel},-q_z)], \qquad (2)$$

where $\Gamma_{\alpha}(\mathbf{q}_{\parallel},q_z,z)$ is the coupling function, which describes the interaction of an electron with an α mode of optical lattice vibrations. The form of this function is given in Ref. 4 for different phonon modes.

Since the electron-phonon interaction is an inelastic process, a variational method[8] was used to calculate the carrier mobilities. This method was first used for quasi-two-dimensional structures in Refs. 5 and 6 . The computational results for the case of multiple PbTe/PbS quantum wells are shown in Fig. 1. It is evident from the results presented in this figure that on switching from bulk samples to short-period multiple quantum wells and superlattices it is important to take into account the electron scattering by *IF* phonons.

3. EXPERIMENT AND COMPARISON WITH CALCULATIONS

The following parameters of the materials and their band structure were used in the numerical calculations of the electron mobility at $T=77$ K: band gap $E_g(\text{PbTe})=0.21$ eV and $E_g(\text{PbS})=0.31$ eV; static permittivity $\varepsilon_s(\text{PbTe})=650$ and $\varepsilon_s(\text{PbS})=195$; dynamic permittivity $\varepsilon_{\infty}(\text{PbTe})=37$ and $\varepsilon_s(\text{PbS})=19$; longitudinal optical phonon energy $\hbar\omega_l(\text{PbTe})=14.1$ meV and $\hbar\omega_l(\text{PbS})=26.3$ meV; and the transverse optical phonon energy $\hbar\omega_t(\text{PbTe})=3.4$ meV and $\hbar\omega_t(\text{PbS})=8.2$ meV. Here we have presented the experimental data of Refs. 3 and 9 and in some cases we used the Lyddane–Sachs–Teller relation $\varepsilon_s/\varepsilon_{\infty}=(\omega_l\omega_t)^2$.

Type-II PbTe/PbS structures, grown by the hot-wall method on KCl (100) dielectric substrates with PbTe or PbS buffer layers of the order of 10^2-10^3 nm thick, were used to obtain the experimental values of the mobility. The measured values of the PbTe and PbS layer thicknesses in multiple PbTe/PbS quantum wells ranged from 60 to 500 Å.[10] The

anomalously strong dependences of the Hall coefficient observed for such structures, even in weak magnetic fields, attest to the presence of two types of carriers with different signs and make it possible to determine in the multilayer conductivity model the density and mobility of electrons in PbTe layers and holes in PbS layers.[11]

The large difference in the lattice constants of PbTe and PbS ($a_0=6.46$ and 5.94 Å, respectively) in quantum-well PbTe/PbS structures leads to the appearance of a substantial number of misfit dislocations at the interfaces. However, it has been shown[12] that in the system PbTe/PbS the transitional layer where misfit dislocations are concentrated between the layers does not exceed 10–20 Å, while the layers themselves are mechanically unstrained,[12] giving hope that the mobilities in them will be high. Moreover, the temperature at which multiple quantum wells are obtained by the hot-wall method[10] did not exceed $T=350$ °C so as to prevent mixing of the components at the interfaces, since in a PbTe/PbS system mixing does not occur at temperatures $T<400$ °C.[13] The presence of a large number of misfit dislocations at the interfaces likewise prevents mixing in the system PbTe/PbS.[12]

Because of the relatively large barrier heights between individual layers of quantum-well structures PbTe/PbS, the penetration of wave functions into neighboring layers is small[7] and the envelopes of the wave functions are localized in the corresponding layers. The approximation of multiple quantum wells therefore can be used quite effectively for our objects, where for layer thicknesses $d\geqslant 60$ Å the wells essentially do not interact with one another.

As one can see from the figure, the experimental and theoretical results for the electron mobilities agree satisfactorily for PbTe/PbS structures. The good agreement confirms the assumption that the mobilities in the layers in the quantum-well PbTe/PbS structures can indeed be high. This is due to the presence of misfit dislocations only at the interfaces between the layers, the presence of a sharp metallurgical boundary due to the absence of mixing of the constituent components of the PbTe/PbS structure, and localization of the envelopes of the wave functions in the corresponding layers due to the low height of the energy barriers ($\Delta E \geqslant 0.4$ eV).

The mobility calculations performed in this approximation for the case of PbTe/$Pb_{0.2}Sn_{0.8}$Te quantum wells with finite potential barriers ($\Delta E_c=60$ meV) and also presented in the figure give charge-carrier mobilities of the order of $3\times 10^4-10^5$ cm^2/(V·s) for layer thicknesses 50–600 Å. These values are higher than the observed electron mobilities in PbTe/$Pb_{0.2}Sn_{0.8}$Te quantum wells and other IV–VI compounds, indicating that it is necessary to take into account other scattering mechanisms, of which apparently the most noticeable could be scattering by interfacial irregularities, since in the other IV–VI structures, in contrast to PbS/PbTe structures, interdiffusion of the components at the interfaces is substantial. The experimental values of the charge-carrier mobilities in other low-dimensional IV–VI structures (see Fig. 1) is, as a rule, three to five times lower than that observed in bulk crystals of these materials.

In closing, we note that scattering by longitudinal optical phonons is the main mechanism of scattering in multiple PbTe/PbS quantum wells at temperatures $T\geqslant 70$ K. For quantum well widths $d<150$ Å scattering by *IF* modes dominates in both PbTe/PbS and PbTe/$Pb_{0.2}Sn_{0.8}$Te structures. This causes the mobility to decrease with decreasing layer thickness d.

[1] F. F. Sizov, G. V. Lashkarev, M. V. Radchenko, V. B. Orletskiĭ, and E. T. Grigorovich, Fiz. Tekh. Poluprovodn. **10**, 1801 (1976) [Sov. Phys. Semicond. **10**, 1075 (1976)].
[2] V. V. Bondarenko, V. A. Shenderovskiĭ, and V. V. Teterkin, Ukr. Fiz. Zh. **36**, 344 (1991).
[3] A. V. Lyubchenko, E. A. Sal'kov, and F. F. Sizov, *Physical Principles of Semiconductor Infrared Photoelectronics* [in Russian], Naukova Dumka, Kiev, 1984.
[4] L. Wedler and R. Haupt, Phys. Status Solidi B **43**, 487 (1987).
[5] V. V. Bondarenko and F. F. Sizov, Phys. Low-Dimens. Semicond. Struct. **8/9**, 123 (1995).
[6] V. V. Bondarenko and F. F. Sizov, Neorg. Mater. **33**, 224 (1997).
[7] F. F. Sizov, V. V. Zabudsky, and J. V. Gumenjuk–Sichevskaya, Phys. Low-Dimens. Semicond. Struct. **3**, 81 (1996).
[8] P. N. Gorleĭ and V. A. Shenderovskiĭ, *Variational Method in Kinetic Theory* [in Russian], Naukova Dumka, Kiev, 1992.
[9] Yu. I. Ravich, B. A. Efimova, and I. A. Smirnov, *Methods of Investigation of Semiconductors in Application to Lead Chalcogenides* [in Russian], Nauka, Moscow, 1968.
[10] V. V. Golovin, J. V. Gumenjuk–Sichevskaya, J. Kulumbetov, F. F. Sizov, V. V. Tetyorkin, and V. V. Zabudsky, Phys. Low-Dimens. Semicond. Struct. **6**, 19 (1994).
[11] V. V. Zabudsky, F. F. Sizov, and V. V. Tetyorkin, Modell. Simul. Mater. Sci. Eng. **3**, 575 (1995).
[12] S. S. Borisova, I. F. Mikhaĭlov, L. S. Palatnik, and A. Yu. Sipatov, Kristallografiya **34**, 716 (1989) [Sov. Phys. Crystallogr. **34**, 426 (1989)].
[13] A. Kh. Abrikosov and L. E. Shelimova, *Semiconductor Materials Based on IV–VI Compounds* [in Russian], Nauka, Moscow, 1970.
[14] F. Ishida, S. Matsuura, H. Fujiyasu, H. Ebe, and K. Shinohara, Superlattices Microstruct. **2**, 575 (1986).
[15] G. Bauer, Surf. Sci. **168**, 462 (1986).
[16] S. V. Plyatsko, Yu. S. Gromovoj, G. E. Kostyunin, F. F. Sizov, and V. P. Klad'ko, Thin Solid Films **218**, 151 (1992).

Translated by M. E. Alferieff

PHYSICS OF SEMICONDUCTOR DEVICES

Degradation of MOS tunnel structures at high current density

I. V. Grekhov, A. F. Shulekin, and M. I. Veksler

A. F. Ioffe Physicotechnical Institute, Russian Academy of Sciences, 194021 St. Petersburg, Russia
(Submitted July 17, 1997; accepted for publication July 29, 1997)
Fiz. Tekh. Poluprovodn. **32**, 743–747 (June 1998)

The stability of tunneling-thin (2–3 nm) SiO_2 films during prolonged flow of high-density currents (10^2-10^3 A/cm^2) was investigated. A sharp increase in the charge which a tunneling MOS structure is capable of transmitting without degradation on switching from Fowler–Nordheim injection to direct tunneling (10^3 C/cm^2 and 10^7 C/cm^2, respectively) was observed. The degradation of SiO_2 films was investigated using Al/SiO_2/n-Si/p^+-Si thyristor structures with a positive bias on the semiconductor, i.e., with reverse bias of the MOS structure. The use of these devices accounted for the uniformity of the current distribution over the area and made it possible to monitor the state of the insulator layer by measuring the device gain in the phototransistor mode. © *1998 American Institute of Physics.* [S1063-7826(98)02406-5]

1. INTRODUCTION

The interest which has developed in MIS structures with tunneling-thin ($\simeq 1.5-3$ nm) silicon dioxide (SiO_2) films is due to the fact that the thickness of the subgate insulator in field-effect transistors is now at the tunneling level[1–5] and, moreover, it is becoming clear that tunneling SiO_2 layers can now be used as the subgate insulator to improve substantially the basic device parameters.[6] The possibility of using tunneling MOS structures in this manner makes their applications more realistic in other fields, in particular, as efficient charge-carrier injectors in Si in transistors and thyristors with a tunneling MOS emitter, especially since a substantial amount of data has now been accumulated in this field.[7–14]

The indicated applications of tunneling MOS structures presume that the latter operate in a reverse-biased mode with a quite high current density (up to 10^3 A/cm^2 when used as an injector[8,11–13]). This makes it important to investigate the ''stability'' of a tunneling-thin oxide against a current, since systematic investigations of the degradation of tunneling MOS structures during charge transport (which has been studied extensively for a long time for thicker ($\geqslant 3$ nm) SiO_2 films[3–5]) have not yet been undertaken. The existing data on the degration of tunneling structures are extremely limited: They cover only the current range below 1 A/cm^2 (Refs. 6 and 15) and almost exclusively the direct-bias regime of MIS structures.[1,15]

In the present work we endeavor to determine the ''stability'' of tunneling MIS structures, i.e., the maximum transmitted charge that does not give rise to degradation, as well as the physical reasons determining the magnitude of this charge at high current densities (10^2-10^3 A/cm^2) and under a reverse bias.

2. FACTORS DETERMINING THE DEGRADATION OF MOS STRUCTURES WITH ''THICK'' AND TUNNELING-THIN INSULATORS DURING CURRENT FLOW

A substantial volume of data has been accumulated on relatively thick (>4 nm) SiO_2 films carrying a current.[1–5] In such structures appreciable currents start to flow only in fields of the order of 10^7 V/cm in the insulator. Under Fowler–Nordheim injection conditions electrons (holes) enter the allowed band of the oxide by tunneling through a triangular barrier (see, for example, Figs. 1a) and are then transported along it. Such transport is dangerous from the standpoint of degradation because energy relaxation of these electrons directly into the oxide layer is possible (band–band carrier recombination as well as recombination through levels in the band gap of SiO_2). Large amounts of energy can be instantaneously released in the process of such relaxation, and this is accompanied by the generation of new defects.

In contradistinction of what we have described above, in MOS structures with a thinner SiO_2 layer (<3 nm) appreciable charge transfer starts in substantially weaker fields in the insulator (for example, 10^6 V/cm), where the predominant mechanism of charge transfer is direct tunneling (Fig. 1b). As a result of this circumstance, right up to a definite voltage corresponding to a transformation of the tunneling barrier from trapezoidal to triangular, current flow is not accompanied by the appearance of injected carriers in an allowed band of the insulator.

For this reason, for tunneling structures it can be expected that, in the first place, there will be a substantial increase in ''stability'' against current flow (quantitatively characterized by the total transported charge giving rise to degradation) as well as a catastrophic decrease of this stability with a definite voltage on the oxide corresponding to a transition to Fowler–Nordheim injection. This feature of MOS structures with direct bias was observed in Ref. 1 for

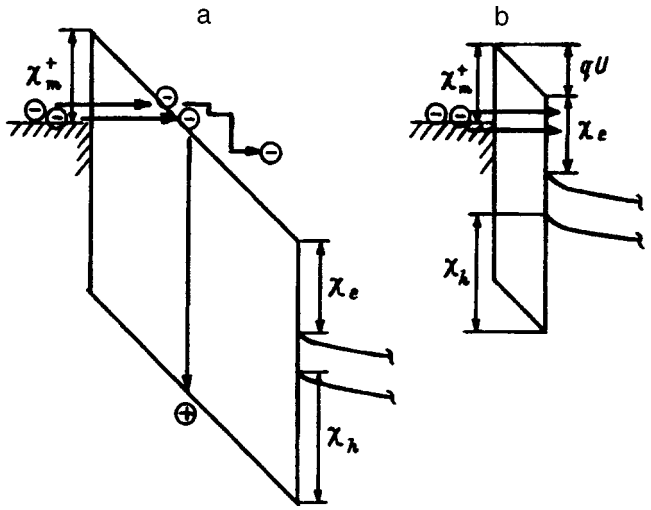

FIG. 1. Charge transport in MOS structures with a SiO_2 layer: a — Thick layer; b — tunneling-thin layer.

samples with an insulator layer with a relatively large thickness of 3–4 nm (the change in the charge transport mechanism occurred at current density $10^{-2}-10^{-4}$ A/cm^2).

As far as functioning of a tunneling device in the direct tunneling regime is concerned, in the complete absence of electron-trapping levels in the band gap of the oxide (no possibility of energy relaxation with a substantial energy release), the ''service life'' of the device is unlimited. Indeed, in Ref. 15 it was observed that the critical charge giving rise to degradation of a tunneling MOS structure is very large ($>10^6$ C/cm^2); tests were performed with current densities <1 A/cm^2.

3. FORMULATION OF AN EXPERIMENT ON THE INVESTIGATION OF THE DEGRADATION OF TUNNELING MOS STRUCTURES. SAMPLE PREPARATION

The structures Al/⟨tunneling-thin SiO_2⟩/n-Si/p^+-Si (Fig. 2a) with a positive bias on the semiconductor were investigated in the experiment.

In this case the structure consists of a thyristor with a tunneling MOS emitter on ''top,'' an induced p base (inversion layer at the oxide/Si boundary), Si volume playing the role of a n base, and a p^+ emitter at the ''bottom.'' The current-voltage characteristic of such a structure is S-shaped (Fig. 2b). The device can operate in the active mode (regime of relatively low currents) and it can also switch into a self-maintaining on state with a uniform current distribution over the area.[12] The on state is maintained, first, by the standard ''thyristor'' positive feedback[10,16] and, secondly, by *Auger ionization* of the Si atoms[8,12] by *hot* electrons injected from the metal into the semiconductor by a tunneling MIS junction.

In the preswitching regimes the current through a structure is determined by the delivery of majority carriers into the thyristor base (especially, into the inversion p base) as well as by intensification of the ''top'' (tunneling MOS section) and ''bottom'' transistors. A thyristor in this regime can be controlled by supplying a base current and by illuminating the structure. Degradation of the SiO_2 layer sharply decreases the gain of the tunneling MOS transistor (because of an increase in hole leakage from the inversion layer into the metal); i.e., the current through the device in the active regime depends strongly on the state of the tunneling oxide.

The devices (Fig. 2a) were fabricated on the basis of an epitaxial structure: p-type substrate with resistivity $\rho=0.005$ $\Omega\cdot$cm with a 9-μm-thick epitaxial n layer ($\rho=0.3$ $\Omega\cdot$cm); the total wafer thickness is 300 μm. The tunneling-thin oxide was grown by thermal oxidation in dry oxygen at $T=700$ °C; the SiO_2 film was about 2.5 nm thick. The diameter of ''top'' aluminum electrode was equal to 400 μm. During the measurements the required thermal contact with a copper radiator was provided by a layer of liquid eutectic alloy In–Ga, located between the backside of the substrate and the radiator.

4. EXPERIMENTAL RESULTS

The measurements consisted of putting the device into the ''on'' state, which corresponds to a uniform current dis-

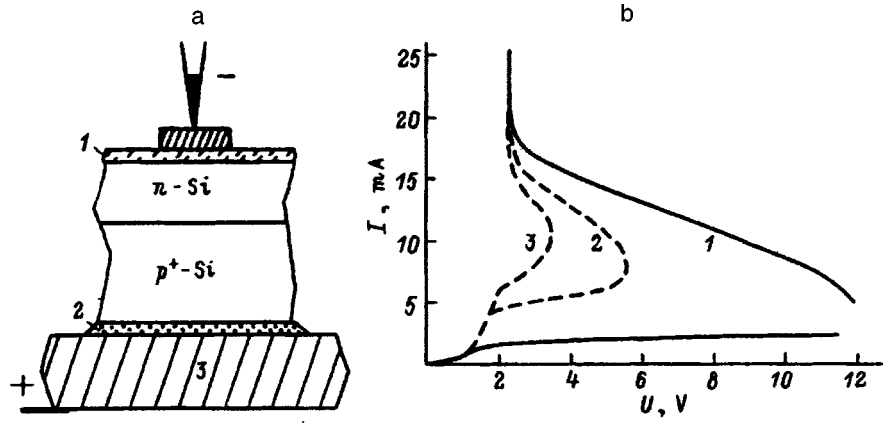

FIG. 2. Schematic diagram of the Al/SiO_2/n-Si/p^+-Si thyristor structure used for studying the stability of tunneling-thin SiO_2 films (a) and typical current-voltage characteristics (IVC) of such a structure (with SiO_2 thickness $t=2.5$ nm) in the relatively low current density range (b). a: *1* — tunneling-thin oxide, *2* — In–Ga liquid alloy, *3* — Cu cold duct. b — IVC: *1* — in the dark; *2, 3* — with different intensities of external illumination. Device area 1.26×10^{-3} cm^2.

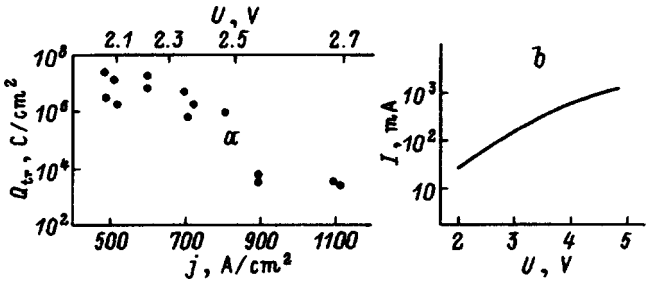

FIG. 3. a — Charge Q_{tr} transmitted through a tunneling-thin SiO_2 layer prior to degradation as a function of current density j (bottom scale) and as a function of the estimated voltage U across the insulator (top scale). b — Current-voltage characteristic of the experimental structure in the ''on'' state with high current density.

tribution, and holding it in this state for a prolonged period of time — right up to the onset of degradation of SiO_2. In the course of the tests the voltage and the current through the device were periodically decreased briefly and the gain in the active regime with a fixed applied voltage and intensity of external illumination was monitored. In addition, the change in the properties of the structure could be judged according to the change in the parameters of the *S*-shaped thyristor current-voltage characteristic (IVC). For definiteness it was assumed that ''degradation'' consists of an appreciable decrease in the gain of the structure in the phototransistor mode (approximately by 10%).

The range of currents through a sample with degradation time from several seconds up to tens of hours ranged from 0.5 to 1.5 A (the current density ranged from 4×10^2 to 1.3×10^3 A/cm^2), while the typical voltage drop across the device was equal to 3–4 V.

Estimates of the possible current-induced heating of the sample showed that because of the small size of the top electrode, the temperature difference ΔT between the most highly heated region of the sample (near the SiO/SiO_2 interface) and the radiator does not exceed $\Delta T=60[\mathrm{K/A}]I_0$, where I_0 is the current (in A) through the sample. This shows that the thermal phenomena were not responsible for the degradation of the structures.

The main experimental result is the demonstration of the high stability of tunneling-thin (2–3 nm) oxide against the flow of a high-density current (up to 10^3 A/cm^3) in the direct-tunneling regime. The critical transported charge giving rise to degradation of the SiO_2 film is much larger than in the Fowler–Nordheim injection regime (Fig. 3).

For example, in the case of a current with density $j=500$ A/cm^2 the degradation became appreciable (the gain decreased and the parameters of the *S*-shaped IVC changed somewhat) only after approximately 40 h of operation, which corresponds to a transported charge of the order of $5\times10^7-10^8$ C/cm^2. This is much greater (by approximately 4 orders of magnitude) than for ''thick'' MOS structures (Fowler–Nordheim injection regime), for which the transported charge leading to complete degradation of the structure is approximately 10^3 C/cm^2 with oxide thickness of about 4 nm.[3–5] No appreciable manifestations of degradation were observed when the structures were tested for 40 h at current density 350 A/cm^2.

The devices degraded much more rapidly when the current density was increased to 700–1000 A/cm^2, and at 1200 A/cm^2 they could operate for only a few seconds. The charge transported before device degradation was of the order of 10^3 C/cm^2 with a large variance from one device to another.

We underscore that Joule heating did not play an appreciable role in any regime.

5. INTERPRETATION OF THE EXPERIMENTAL RESULTS

As one can see from the data presented, the assumption that the stability of MOS structures against current flow in principle increases on switching from Fowler-Nordheim injection to direct tunneling is confirmed experimentally. Indeed, the charge transferred without degradation of the structure increases radically (by four orders of magnitude), while the decrease in stability to the level of thick MOS structures (with a definite current density $j\simeq1000$ A/cm^2) is a consequence of a transition to charge transport by the Fowler–Nordheim mechanism. The transition from high to low stability occurs in a rather narrow interval of current densities (Fig. 3a).

This is completely understandable, since for any parameters of the tunneling system the fraction of the Fowler–Nordheim component j_{FN} in the total current j_{tot} through SiO_2 increases sharply from 0 to 1 when the tunneling barrier transforms from trapezoidal to triangular. This can be verified by calculating this fraction as a function of the voltage U on the insulator (Fig. 4a).

We shall employ the following expression for the tunneling-current density[17]

$$j=\frac{4\pi m_e^* q}{h^3}\int\frac{dE}{1+\exp[(E-E_{Fm})/kT]}\int_0^E\theta(E_z)dE_z, \tag{1}$$

where E is the total energy of the electron, E_z is the energy of the electron motion in the direction of tunneling, $\theta(E_z)$ is the tunneling probability,[7,11] m_e^* is the effective electron mass in the plane of the Si/SiO_2 interface [$m_e^*\simeq2.1m_0$ (Ref. 16)]. The energy E is measured from the conduction-band bottom E_{co} (Fig. 4b). The integration limits should be taken as $0\leqslant E\leqslant\chi_e$, where χ_e is the conduction-band offset at the Si/SiO_2 interface, to calculate the direct tunneling current, while χ_e and χ_e+qU should be used for the Fowler–Nordheim current. Figure 4a shows an example of the results of such a calculation, from which it follows that the fraction j_{FN} of the Fowler–Nordheim current in the total current j_{tot} increases from 0 to 1 as the voltage across SiO_2 is varied over an approximately 0.4-V range.

For practical applications it is of interest to know, besides the current densities, the electric field $\mathcal{E}$ in tunneling-thin SiO_2 in the regimes investigated. In the experimental reverse-biased structures (Fig. 4b), in addition to the voltage drop U across the insulator, there is also an appreciable drop

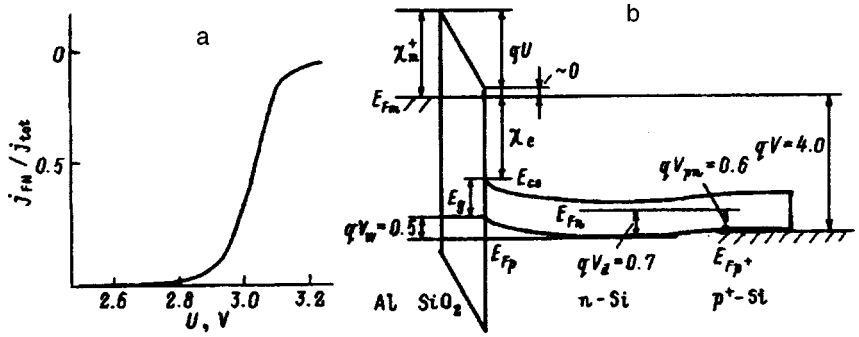

FIG. 4. a — Computed fraction of the Fowler–Nordheim current component j_{FN} in the total current j_{tot} as a function of the voltage U across the insulator. Computational parameters: Electron mass in SiO_2 $m_i=0.5m_0$, $\chi_e=\chi_m^+=3$ eV, SiO_2 thickness — 3 nm; b — energy band diagram of the experimental structure in the ''on'' state; the numerical values of the potential differences are given in eV. Here E_{Fm} is the Fermi level in the metal, E_{Fp} is the Fermi quasilevel for holes in the inversion layer, E_{Fn} is the Fermi level in the bulk of the n material, E_{Fp}^+ is the Fermi level in the p^+ substrate.

in the voltage across the inversion layer, V_w, across the space-charge layer in the n region, V_d, and across the p^+–n junction, V_{pn}:

$$\chi_m^+ - qU - \chi_e - E_g - qV_w + qV_d + qV_{pn} + qV = 0, \qquad (2)$$

where χ_m^+ is the barrier height at the metal–insulator boundary (Fig. 4b). Therefore, knowing the voltage V across the entire structure it is possible to estimate U (or $\mathcal{E}$, if the theory of a transistor with a tunneling MOS emitter is used[13,14]).

For the most interesting regime $V=V_c$, corresponding to a transition to fast degradation (from experiment $V_c\simeq 4$ V), the voltage $V_d\simeq 0.7$ V, since in the ''on'' state (in which the measurements are performed) the excess of holes which enter the Si/SiO_2 interface is ejected into the volume of n-Si.[7,8,11,13] The typical depth qV_w of the quantum well formed at the Si/SiO_2 boundary equals about 0.58 eV in the experimental regimes.[13,14] The band gap in Si is $E_g=1.1$ eV, while the characteristic voltage drop across the p–n junction under these conditions is essentially equal to $V_{pn}=0.6$ V. If it is assumed (as is the case, for example, in Ref. 11) that $\chi_m^+\approx\chi_e$ (Fig. 4b), then the relation (2) gives $U=U_0\simeq 2.5$ V (the field in the insulator is $\mathcal{E}\simeq 10^7$ V/cm). Under our assumptions, the quantity U_0 is identical to the barrier heights χ_m^+ and χ_e; i.e., these values can be estimated to be $\chi_m^+\simeq\chi_e\simeq 2.5$ eV from the experiment performed.

The values of U presented in Fig. 3a were calculated similarly on the basis of the models of Refs. 11 , 13 , and 14. The fact that the barrier heights χ_m^+ and χ_e are less than approximately 3.1 eV (Ref. 16) (Fowler–Nordheim injection starts at a voltage $U\lesssim 3.1$ eV across the insulator) should not be surprising: The band offsets at the Si/SiO_2 heterojunction in tunneling structures can be much less than in the case of ''thick'' layers.[11,18]

Apparently, there is one more factor which accounts for even greater stability to the thin oxide in the Fowler–Nordheim injection regime (as compared with thick MOS structures). The point here is that the oxide always contains a positive charge, which is concentrated near the Si/SiO_2 interface.[16] This charge promotes recombination of the electrons injected through the centers in SiO_2. From the standpoint of degradation, this is a safer alternative to band–band recombination. In a thick oxide this charge occupies only a small fraction of the volume. In the case of small thicknesses, however, it can occupy the entire volume of SiO_2, and its role thereby increases.

6. CONCLUSIONS

Let us summarize the results.

It has been demonstrated experimentally that the characteristic charge that can be transmitted through a tunneling MOS structure without a degradation of the structure in the case of direct tunneling is several orders of magnitude greater than in the Fowler–Nordheim regime: 10^7 C/cm^2 and 10^3-10^4 C/cm^2, respectively. The latter value is identical to the corresponding value for ''thick'' MOS structures. The transition from high to low stability occurs in a rather narrow range of voltages across the oxide. For the structures investigated the change in the charge transport mechanism occurs at current densities 500–800 A/cm^2.

A new method has been proposed for investigating the ''stability'' of tunneling-thin (1.5–3 nm) SiO_2 films, assuming the use of thyristor structures with a tunneling MOS emitter. This gives a uniform charge distribution and facilitates monitoring of the oxide degradation.

We wish to express our gratitude to the Multidisciplinary Science and Technology Program ''Physics of solid-state nanostructures'' for their support. M. I. Veksler thanks the Competitive Center for the Fundamental Natural Sciences (GRACENAS, St. Petersburg) for support under the grant ''Research projects.'' We also thank O. V. Voĭtsyshenko for assistance in the preparation of the samples.

[1] M. Depas, B. Vermeire, P. W. Mertens, M. Meeuris, and M. M. Heyns, Semicond. Sci. Technol. **10**, 753 (1995).
[2] M. Depas, T. Nigam, and M. M. Heyns, IEEE Trans. Electron Devices **ED-43**, 1449 (1996).
[3] D. J. DiMaria, Appl. Phys. Lett. **68**, 3004 (1996).
[4] D. J. DiMaria, E. Cartier, and D. Arnold, J. Appl. Phys. **79**, 3367 (1993).
[5] D. J. DiMaria, D. Arnold, and E. Cartier, Appl. Phys. Lett. **61**, 2329 (1992).
[6] H. S. Momose, M. Ono, T. Yoshitomi, T. Ohguro, A. Nakamura, M. Saito, and H. Iwai, IEEE Trans. Electron Devices **ED-43**, 1233 (1996).
[7] J. G. Simons and G. W. Taylor, Solid-State Electron. **29**, 287 (1986).
[8] I. V. Grekhov, A. F. Shulekin, and N. I. Vexler, Solid-State Electron. **38**, N 3, 1533 (1995).
[9] T. Yoshimoto and K. Suzuki, Jpn. J. Appl. Phys. **32**, L180 (1993).

[10] W. K. Choi and A. E. Owen, J. Appl. Phys. **68**, 6447 (1990).
[11] K. M. Chu and D. L. Pulfrey, IEEE Trans. Electron Devices **ED-35**, 188 (1988).
[12] S. V. Belov, I. V. Grekhov, A. F. Shulekin, and M. I. Vexler, Thin Solid Films **294**, 281 (1997).
[13] E. V. Ostroumova and A. A. Rogachev, Fiz. Tekh. Poluprovodn. **28**, 1411 (1994) [Semiconductors **28**, 793 (1994)].
[14] M. I. Vexler, IEEE Trans. Electron Devices **ED-42**, 656 (1995).
[15] K. R. Farmer, M. O. Andersson, and O. Engstrom, Appl. Phys. Lett. **58**, 2666 (1991).
[16] S. Sze, *Physics of Semiconductor Devices*, Wiley, N. Y. [Russian translation, Mir, Moscow, 1984, Vol. 1].
[17] W. A. Harrison, Phys. Rev. **123**, 85 (1961).
[18] L. A. Kasprzak, R. B. Laibowitz, and M. Ohring, J. Appl. Phys. **48**, 4281 (1977).

Translated by M. E. Alferieff

On the temperature and field dependences of the effective surface mobility in MIS structures

V. A. Gergel', M. V. Timofeev, and A. P. Zelenyĭ

Institute of Radioengineering and Electronics, Russian Academy of Sciences, 141120 Fryazino, Russia
(Submitted January 13, 1998; accepted for publication January 15, 1998)
Fiz. Tekh. Poluprovodn. **32**, 748–751 (June 1998)

A physical model establishing a relation between the surface density of the free electronic charge in an inversion layer and the surface density of stationary (localized) electrons trapped in surface states at a semiconductor–insulator interface is constructed. It is established that at moderately low temperatures this relation is close to a direct proportionality. The presence of surface states, which localize some of the surface electronic charge, is manifested as a decrease in the effective electron mobility in the channel of a MIS transistor. The well-known decrease of the surface mobility with increasing transverse electric field is attributed to field-induced variations in the position of the percolation level that separates bound electronic states from free states. © *1998 American Institute of Physics.* [S1063-7826(98)02506-X]

In Refs. 1 and 2 the question of the relation between localized surface electronic charge (trapped surface states) and the surface density of free (delocalized) electrons in the semiconductor in a MIS structure with different inversion levels, determined, as is well known,[5] by the temperature and magnitude of the applied voltage, was investigated in detail in a development of a previously proposed theory of fluctuation surface states of the semiconductor–insulator interface.[3,4] It was discovered that there exists a rather wide temperature range where the localized (Q_l) and delocalized (free) (Q_d) electronic charges, which increase with the applied voltage, are virtually directly proportional to one another, $Q_l(V) \approx \alpha(T) Q_d(V)$. It was established that the limits of this temperature range are determined by the inequality

$$\Delta/2 < T < 2\Delta, \tag{1}$$

where

$$\Delta = \frac{e^2}{\varepsilon_s + \varepsilon_i}(4\pi\sigma)^{1/2}$$

is the characteristic magnitude of the fluctuations in the electrostatic energy in the skin layer of the semiconductor of a MIS structure which arise as a result of the spatial fluctuations in the density of charged centers in the insulator (built-in charge density). It should be underscored that for typical values of the effective surface density of the built-in charge $\sigma \equiv \sigma_+ + \sigma_- \approx 10^{12}$ cm^{-2} the characteristic energy of the fluctuations is $\Delta \approx 0.025$ eV ≈ 300 K. Therefore, the range (1) encompasses several hundreds of degrees near room temperature, where, as is well known, most experimental data on the electric properties of MIS structures and the corresponding electronic phenomena are concentrated. It should be underscored that the dependence $Q_l = \alpha Q_d$ established in Refs. 1 and 2 is of fundamental importance for a correct understanding of the nature of the surface electrical conductivity in MIS structures and transistors, since it gives a simple and convincing explanation of its main feature: the fact that the surface carrier mobility μ_s is several times lower than the values of the standard bulk mobility μ_v of a semiconductor and that it has a markedly different temperature dependence.[6] Since upon taking into account the bound surface states the total surface electron density Q decomposes into two parts, a free part $Q_d = [1/(1+\alpha)]Q$ and a bound part $Q_l = [\alpha/(1+\alpha)]Q$, the effective surface mobility is $1+\alpha$ times lower than its true value determined by the corresponding scattering mechanisms.

Our further investigations showed that proportionality of the free and bound charges is not a specific property of the model of fluctuation surface states that was studied in Refs. 1 and 2 , but rather it must occur in virtually any situations where the bound and free states are not separated from one another by an energy gap but rather are separated only by a so-called percolation level[7] — the energy below which the electronic states are localized (bound) and above which they are delocalized (free). To prove this more general assertion, we shall examine a very simple model of a MIS structure in which we shall consider only the resulting energy spectrum of the bound surface states without being concerned with the physical nature of their appearance. This formulation of the problem, which is much simpler than in Refs. 1 and 2, will enable us, in addition to giving a clearer physical picture of the results, to make substantial progress in determining the temperature dependence of the effective surface mobility and to investigate the question of its dependence on the voltage or transverse field at the semiconductor–insulator interface.

For subsequent quantitative analysis we shall employ, first and foremost, very simple relations[6] for the charges and the surface potential in the inversion regime of a MIS structure:

$$V = \varphi + \frac{d}{\varepsilon_i \varepsilon_0}\left\{\left[2\varepsilon_i \varepsilon_0 qN\left(\varphi + T\exp\frac{\varphi - 2\varphi_B}{T}\right)\right]^{1/2} + qQ_l\right\}. \tag{2}$$

The corresponding band diagram is shown in Fig. 1. In Eq.

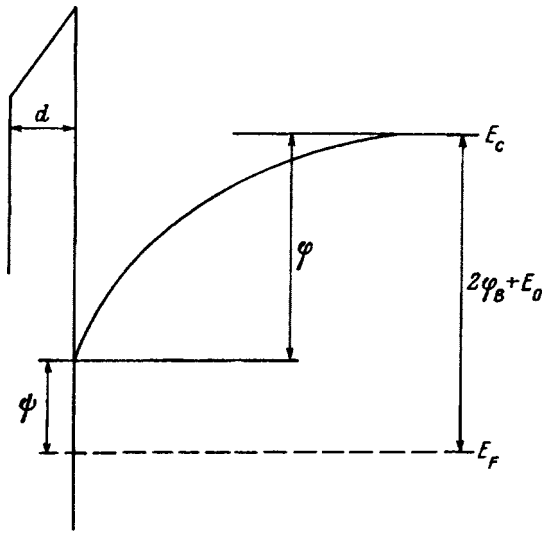

FIG. 1. Band diagram of the surface layer of the semiconductor MIS structure in a deep inversion regime.

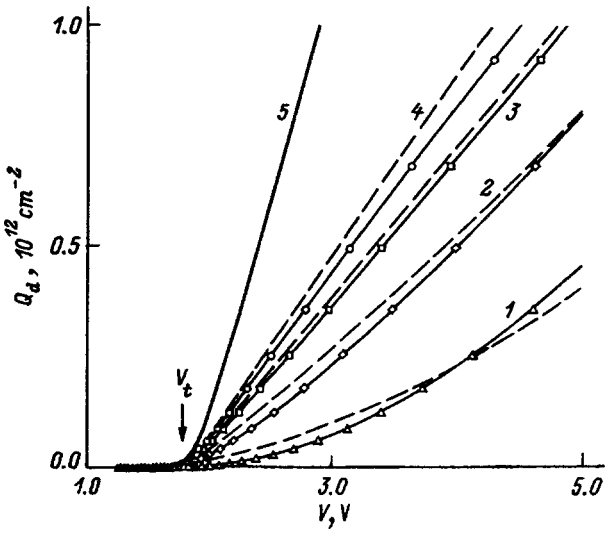

FIG. 2. Free charge density of a MIS structure with (*1*)–(*4*) and without (*5*) surface states: calculation for an exponential spectrum (*5*) (solid lines) and a step spectrum (8) (dashed lines) of surface states. E_{ch}, eV: *1* — 0.003, *2* — 0.013, *3* — 0.026, *4* — 0.052.

(2) $V>0$ is the voltage on the structure (minus the flat-band voltage) and φ is the surface potential (voltage on the semiconductor). The second term in Eq. (2) is the voltage drop in the insulator layer. Here the square root corresponds to the total charge of the acceptors in the depleted layer (N is the acceptor density) and the charge of mobile delocalized electrons in the inversion layer

$$qQ_d=q\left(\frac{2\varepsilon\varepsilon_0 N}{q}\right)^{1/2}\left[\sqrt{\varphi+T\exp\frac{\varphi-2\varphi_B}{T}}-\sqrt{\varphi}\right], \quad (3)$$

while the charge due to the localized electrons can be expressed in the conventional manner in terms of the density of surface states $N_{ss}(E)$

$$qQ_l=d\int_0^\infty dEN_{ss}(E)/\left(1+\exp\frac{-\varphi-E+2\varphi_B+E_0}{T}\right). \quad (4)$$

In Eqs. (3) and (4) E is the energy of the states, measured from the conduction-band edge into the band gap of the semiconductor, $2\varphi_B=2T\ln(N/n_i)$ is the characteristic potential of the onset of deep inversion, $E_0=T\ln(N_c/N)$, where $N_c=2(mT/2\pi\hbar^2)^2\approx10^{19}$ cm^{-3} is the effective density of states in the conduction band of the semiconductor.

Using the relations (2)–(4) presented above, we shall now calculate the dependence of the mobile charge Q_d on the voltage V for the case of surface states with an exponential energy spectrum:[3]

$$N_{ss}(E)=Q_0E_{ch}^{-1}\exp(-E/E_{ch}), \quad (5)$$

where Q_0 is the so-called total density of states, and E_{ch} is the characteristic energy scale of the distribution. The computational results for $T=300$ K, $Q_0=10^{13}$ cm^{-2}, $N=10^{17}$ cm^{-3}, $d=2\times10^{-6}$ cm and certain typical values of the attenuation rate E_{ch} are presented in Fig. 2, where the curve of charge accumulation in the ideal situation (no surface states, $Q_0=0$) is also shown for comparison.

Analyzing the plots presented here, it should be noticed first that the threshold voltage V_t is virtually identical for all curves and therefore does not depend on the attenuation rate E_{ch} and the value of Q_0 itself. The quasilinearity of these curves for $V>V_t$ indicates the desired proportionality of the bound and free surface charges.

Of course, the numerical results can also be represented in the form of the dependences $Q_l(Q_d)$ and $\mu_s=\mu_v Q_d(Q_d+Q_l)^{-1}$, which are directly of interest to us. However, it is desirable to simplify the computational procedure at this point, which, it seems to us, will also make it easier to understand the physics of the results obtained. We will accordingly disregard in Eq. (3), as is conventionally done for the deep-inversion regime, the change in the charge density Q_1 of the depleted layer; i.e., we shall assume that

$$Q_1=\left(\frac{2\varepsilon\varepsilon_0 N\varphi}{q}\right)^{1/2}\approx2\left(\frac{\varepsilon\varepsilon_0 N\varphi_B}{q}\right)^{1/2}=\text{const}.$$

After this simplification of Eq. (3) we can explicitly express in terms of the electron density Q_d the Boltzmann exponential appearing there

$$\exp\left(\frac{\varphi-2\varphi_B-E_0}{T}\right)=\frac{qQ_d(Q_d+2Q_1)}{2\varepsilon\varepsilon_0N_c(T)T}, \quad (6)$$

and then obtain, substituting the expression (6) into Eq. (4), an explicit relation between the localized and delocalized charges

$$Q_l=\int_0^\infty dEN_{ss}(E)/\left[1+\frac{2\varepsilon\varepsilon_0N_c(T)T}{qQ_d(Q_d+2Q_1)\exp(-E/T)}\right]. \quad (7)$$

The results of a numerical integration of Eq. (7) with the distribution function (5) with the parameters $Q_0=10^{13}$ cm^{-2} and $E_{ch}=0.026$ eV in the interval of characteristic temperatures 0.009–0.045 eV (100–500 K) are presented in Fig. 3. With the exception of the curve corresponding to the lowest

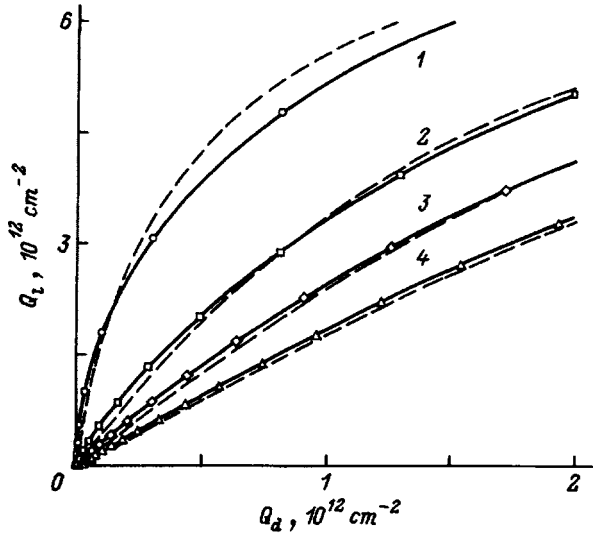

FIG. 3. Relation between localized and free charges: calculation for an exponential spectrum of (5) (solid lines) and a step spectrum (8) (dashed lines) surface states. kT eV: *1* — 0.008, *2* — 0.018, *3* — 0.026, *4* — 0.036.

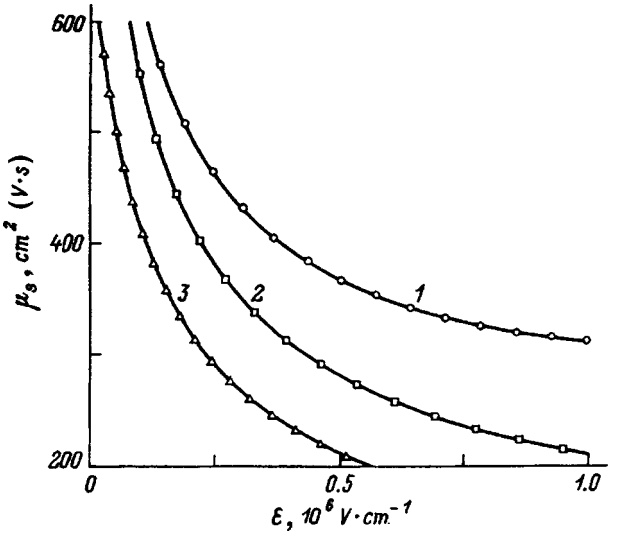

FIG. 4. Field dependence of the effective surface mobility. T, K: *1* — 200, *2* — 300, *3* — 400.

temperature, they demonstrate a quasilinear behavior with an average slope α, which decreases with increasing temperature.

To determine how strongly the results presented above depend on the form of the energy spectrum of the surface states we performed similar calculations after replacement of the exponential distribution (5) by a step distribution

$$N_{ss}(E)=Q_0\frac{1}{2E_{\rm ch}}\begin{cases}1, & E<2E_{\rm ch},\\ 0, & E>2E_{\rm ch}.\end{cases} \tag{8}$$

The corresponding results, represented by the dashed lines in Figs. 2 and 3, attest to the fact that the character of the charge accumulation and the relationship between the free and bound surface electronic charges which we are studying do not depend too strongly on the form of the spectrum of the states, and that they are determined mainly by the total density and the average energy of the distribution.

Finally, let us consider the most interesting part of our investigation. We shall estimate the effect of the intrinsic electric field on the relation between the localized and free surface charges. We start from the intuitively obvious idea that the transverse electric field in the semiconductor part of the MIS structure at the boundary with the insulator, which presses electrons to the surface, will lead to additional localization of previously delocalized electronic states and a corresponding decrease in the density of free states. In other words, the transverse electric field $\mathcal{E}$, which produces an additional asymmetry of the potential well in the boundary part of the semiconductor, gives rise to a corresponding shift of the percolation level $\Delta E=\zeta(\mathcal{E})$, where ζ is the corresponding characteristic transverse lateral percolation length. We cannot give an exact analytical expression for ζ, but it is natural to assume that it should be of the order of several tens of angstroms, just as the quantum localization length $(\hbar^2/mq\mathbf{E})^{1/3}$ of electrons in the inversion layer. We shall treat the exact value of ζ as an adjustable parameter in our theoretical model. Taking into account this energy shift of the percolation level that separates the free and bound states, the right-hand side of the relation (6) must be multiplied by $\exp[q\zeta(Q_1+Q_d)/\varepsilon\varepsilon_0 T]$ and correspondingly the lower limit of integration in the resulting Eq. (7) must be replaced by $[-q\zeta(Q_1+Q_d)/\varepsilon\varepsilon_0]$. Then, for example, for the stepped spectrum (8), where the integration in Eq. (7) can be performed analytically, we obtain the following expression after simple manipulations:

$$Q_l=Q_0\frac{T}{2E_{\rm ch}}\ln\left\{\left[Q_d(Q_d+2Q_1)\times\exp\left(\frac{2E_{\rm ch}+q\zeta(Q_1+Q_d)/\varepsilon\varepsilon_0}{T}\right)+\frac{2\varepsilon\varepsilon_0 N_c(T)T}{q}\right]\Big/\left[Q_d(Q_d+2Q_1)+\frac{2\varepsilon\varepsilon_0 N_c(T)T}{q}\right]\right\}. \tag{9}$$

Proceeding from this expression, we calculated the effective surface mobility of the inversion layer $\mu_s=\mu_v[Q_d/(Q_d+Q_l)]$ for a series of temperatures $T=200$, 300, and 400 K for the following values of the numerical parameters: $\zeta=2\times10^{-7}$ cm, $Q_0=10^{13}$ cm^{-2}, $N=10^{15}$ cm^{-3}, and $E_{\rm ch}=0.026$ eV. We used in this case for the volume mobility the standard relation $\mu_v=1500(T/300)^{-2/3}$ cm^2/(V·s). The corresponding results are presented in Fig. 4 in the conventional form (the mobility as a function of the total electric field in the oxide part of the structure $q(Q_1+Q_l+Q_d)/\varepsilon\varepsilon_0$). They are very close to the corresponding experimental dependences[6] and show, just as the experimental curves, a mobility drop with increasing transverse field or voltage on the structure. According to the model which was developed, this drop is due to an increase in the density of bound states with increasing field due to the corresponding shift of the percolation level.

In conclusion, let us formulate the main result of this study: The main reason why the surface mobility in the inversion layers is lower than the bulk mobility of the material

is trapping of the carriers of the inversion layer in comparatively shallow surface states whose energy spectrum adjoins an allowed band. The characteristic decrease of the surface mobility with increasing field is due to the relative increase in the density of bound states, which can be characterized by a corresponding shift of the percolation level — the energy separating localized and delocalized electronic states of the semiconductor–insulator boundary.

In a future we shall propose, on the basis of the results obtained here, a new physical approach to constructing two-dimensional programs for modeling MIS transistors, where, we believe, the conventionally employed hypothetical dependence of the mobility on the transverse coordinate should be eliminated by introducing instead into the boundary condition for the Poisson equation a localized surface electronic charge, which is functionally related to the surface electron density and to the electric field.

[1] V. Gergel' and G. Shpatakovskaya, Zh. Éksp. Teor. Fiz. **102**, 640 (1992) [Sov. Phys. JETP **75**, 342 (1992)].
[2] V. Gergel' and G. Shpatakovskaya, Fiz. Tekh. Poluprovodn. **27**, 923 (1993) [Semiconductors **27**, 500 (1993)].
[3] V. Gergel' and R. Suris, Zh. Éksp. Teor. Fiz. **84**, 719 (1983) [Sov. Phys. JETP **57**, 415 (1983)].
[4] V. Gergel', Fiz. Tekh. Poluprovodn. **17**, 637 (1983) [Sov. Phys. Semicond. **17**, 398 (1983)].
[5] S. Sze, *Physics of Semiconductor Devices*, Wiley, N. Y. [Russian translation, Mir, Moscow, 1984].
[6] A. Sabnis and J. Clemens, in *IEEE Tech. Dig. Int. Electron. Dev. Meet.* (1979) p. 18.
[7] B. Shklovskiĭ and A. Efros, *Electronic Properties of Doped Semiconductors*, Springer-Verlag, N. Y., 1984 [Russian original, Nauka, Moscow, 1979].

Translated by M. E. Alferieff

Subthreshold characteristics of electrostatically controlled transistors and thyristors III. Buried gate

A. S. Kyuregyan

V. I. Lenin All-Russia Electrical Engineering Institute, 111250 Moscow, Russia
(Submitted September 23, 1997; accepted for publication October 15, 1997)
Fiz. Tekh. Poluprovodn. **32**, 752–758 (June 1998)

A rigorous analytical theory of the blocking state of electrostatically controlled thyristors and transistors (ECTs) and a buried gate of arbitrary shape is constructed. The problems of the distribution of the potential in the base, the height of the barrier for electrons, and the current-voltage characteristics in the subthreshold region are solved in quadratures by the method of conformal mappings. It is shown that the subthreshold current j_d for ECTs with an undoped and lightly doped base depends on the gate potential U_g and the drain potential U_d as $\ln j_d \propto -U_g(g-U_d/U_g)^{3/2}$, irrespective of the type of conduction, where g is the blocking factor. If the base is strongly doped with acceptors, then $\ln j_d \propto -(gU_g-U_d)^2$, but for electrostatically controlled transistors with a heavily doped n-type base the problem is impossible to solve analytically. As an example, the variant of a deep buried quasielliptical gate, which corresponds to the configurations of real devices, is studied. Simple formulas for g and the parameters of the current-voltage characteristics as a function of the dimensions of the ECT cell, base doping, and gate voltage are obtained in limiting cases. © *1998 American Institute of Physics.* [S1063-7826(98)02606-4]

1. INTRODUCTION

A rigorous analytical theory of subthreshold characteristics of electrostatically controlled transistors and thyristors (ECTs), where the minimum gate–source distance δ is negligible compared to all other dimensions of the device, has recently been developed.[1,2] This assumption made it possible to reduce the problem of calculating the potential distribution $\varphi(x,y)$ in the space-charge region (SCR) to the well-known Dirichlet problem for a strip[3] and to obtain comparatively simple formulas for subthreshold IVCs and the blocking factor of ECTs with a planar gate of arbitrary shape. However, an important class of ECTs with a buried gate,[4] where δ is usually comparable to the gate width and greater than the distance between them, remained inaccessible in this theory. Determining the subthreshold characteristics of such devices is the subject of this study.

2. POTENTIAL DISTRIBUTION AND BARRIER PARAMETERS IN THE GENERAL CASE

We shall seek the potential distribution $\varphi(x,y)$ in the SCR under the same assumptions as in Refs. 1 and 2 but for an ECT the cross section of one of its cells in the complex plane $z=x+iy$ is shown schematically in Fig. 1a. The function $\varphi_0(x,y)$ determined by the equation

$$\varphi(x,y)=\varphi_0(x,y)-V_s y^2/s^2, \tag{1}$$

is a solution of the Laplace equation with boundary conditions at the electrodes

$$\varphi_0(x,0)=0, \tag{2}$$

$$\varphi_0(x,y)=-U_g+V_s y_g^2(x)/s^2 \tag{3}$$

with

$$2mL+l<x<2(m+1)L-l \quad \text{and} \quad y=y_g^2(x),$$

$$\varphi_0(x,w)=U_d+V_w, \tag{4}$$

where $s=(H-h)$ is the gate thickness, $V_s=qns^2/2\varepsilon\varepsilon_0$, the function $y=y_g^2(x)$ describes the position of the gate boundary, and the remaining notation is defined in Refs. 1 and 2. Moreover, as a result of the translational symmetry of the ECT, the following relation evidently must hold:

$$\frac{\partial\varphi(\pm L,y)}{\partial x}=\frac{\partial\varphi_0(\pm L,y)}{\partial x}=0 \tag{5}$$

for $0<y<h$ and $H<y<w$, i.e., in the source–gate and gate–drain gaps (see Fig. 1a). This means that the harmonic function $\varphi_0(x,y)$ is a solution of not only the Dirichlet problem for a multiply-connected SCR of the ECT but also the so-called[3] mixed boundary-value problem (2)–(5) for a single simply-connected cell. A method, described for example, in Ref. 3 , for solving such a problem consists of the following. Let the function $T(z)$ realize a conformal transformation of the ECT cell into the upper half-plane of the $t=\theta+i\tau$ plane in a manner so that its boundary is transformed into the real axis $\tau=0$, while the points $z=\pm L$, $z=\pm L+ih$, $z=\pm L+iH$, and $z=\pm L+iw$ are transformed into the points $t=\pm\alpha$, $t=\pm\beta$, $t=\pm\gamma$, and $t=\pm 1$, respectively (Fig. 1b). If the function $\varphi_1(\theta,\tau)$ is harmonically conjugate to $\varphi_0(\theta,\tau)$, then

$$\Phi(t)=\varphi_1(\theta,\tau)+i\varphi_0(\theta,\tau) \quad \text{and} \quad \mathbf{E}(t)=d\Phi(t)/dt$$

are analytic functions in the upper half-plane, and the boundary values of $\mathbf{E}(t)$ on the $\tau=0$ axis, which follow from Eqs. (2)–(5) and the Cauchy–Riemann conditions, have the form

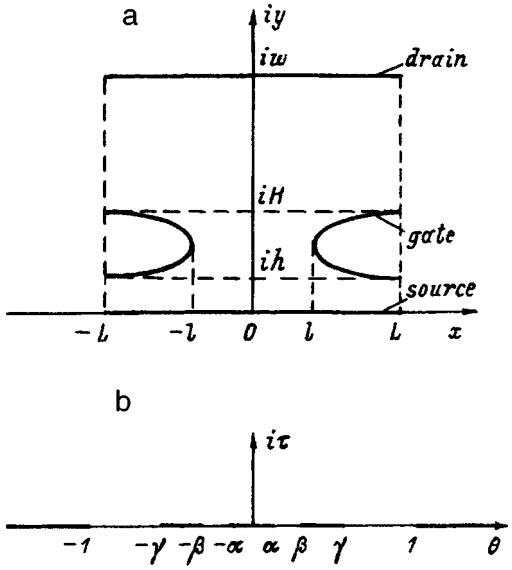

FIG. 1. a — Model of an electrically controlled transistor cell (ECT) with a buried gate, used for calculating the potential distribution in the plane $z=x+iy=Z(t)$; b — ECT cell in the plane $t=\theta+i\tau=T(z)$.

$$\mathrm{Re}\ \mathbf{E}(t)=\frac{\partial\varphi_0}{\partial\tau}=0 \quad \text{for } \alpha<|\theta|<\beta \ \text{ and } \ \gamma<|\theta|<1, \tag{6}$$

$$\mathrm{Im}\ \mathbf{E}(t)=\frac{\partial\varphi_0}{\partial\theta}=\begin{cases}0 & \text{for } |\theta|<\alpha \ \text{ and } \ |\theta|>1;\\ \dfrac{V_s}{s^2}\dfrac{dy_g^2[x(\theta,0)]}{d\theta} & \text{for } \beta<|\theta|<\gamma.\end{cases} \tag{7}$$

The solution $\mathbf{E}(t)$ of the boundary-value problem (6) and (7), unbounded at $t=\pm\alpha,\ \pm\beta,\ \pm\gamma$, and ±1 but integrable, can be represented in the form

$$\mathbf{E}(t)=\frac{1}{\sqrt{G(t)}}\left\{\frac{2V_s}{\pi s^2}\left[\int_{-\gamma}^{-\beta}\frac{dy_g^2}{d\theta'}\sqrt{G(\theta')}\,\frac{d\theta'}{\theta-t}+\int_{\beta}^{\gamma}\frac{dy_g^2}{d\theta'}\sqrt{G(\theta')}\,\frac{d\theta'}{\theta-t}\right]-(v_0+v_1t+v_2t^2+v_3t^3)+E(\infty)\right\}, \tag{8}$$

where

$$G(t)=(\alpha^2-t^2)(\beta^2-t^2)(\gamma^2-t^2)(1-t^2)$$

and the branch $\sqrt{G(\theta)}$ of interest is positive on the segment $|\theta|<\alpha$ of the real axis; v_i are integration constants. This solution was obtained exactly in the same way as the well-known Keldysh–Sedov formula, containing the function $G(t)$ of a different (asymmetric) form and therefore much less convenient for further use in our case, which is symmetric relative to the $\theta=0$ axis. As a result of this symmetry $v_1=v_3=0$, while the function $dy_g^2/d\theta$ must be odd. Moreover, since the complex field $\mathbf{E}(t)$ must evidently approach zero at infinity, Eq. (8) can be simplified

$$\mathbf{E}(t)=\frac{-1}{\sqrt{G(t)}}[v_0+v_2t^2+V_s\chi(t)], \tag{9}$$

where

$$\chi(t)=\frac{2}{\pi}\int_{\beta}^{\gamma}\frac{dy^2(\theta',0)}{d\theta'}\,\frac{\theta'\sqrt{G(\theta')}}{\theta'^2-t^2}\,\frac{d\theta'}{s^2}.$$

The solution $\varphi_0(\theta,\tau)$ of the boundary-value problem (2)–(5) follows directly from the definitions of $\mathbf{E}(t)$ and $\Phi(t)$:

$$\varphi_0(\theta,\tau)=\mathrm{Im}\int_0^{\tau}\mathbf{E}(t)dt. \tag{10}$$

Substituting the expressions (9) and (10) into the relation (1), we obtain the desired potential distribution along the source axis as a function of τ:

$$\varphi(0,\tau)=-v_0P(\tau)+v_2Q(\tau)-V_s\left[\frac{y^2(\tau)}{s^2}+R(\tau)\right], \tag{11}$$

where

$$P(\tau)=\int_0^{\tau}\frac{d\tau'}{\sqrt{G(i\tau')}}, \quad Q(\tau)=\int_0^{\tau}\frac{\tau'^2d\tau'}{\sqrt{G(i\tau')}},$$

$$R(\tau)=\int_0^{\tau}\frac{\chi(i\tau')d\tau'}{\sqrt{G(i\tau')}}.$$

The constants v_0 and v_2 can be found using Eq. (10) and the boundary conditions following for $\varphi_0(\theta,\tau)$ in the t plane from Eqs. (2)–(4):

$$v_0=\frac{Q_{0\infty}(U_g-V_h-V_sR_{\alpha\beta})-Q_{\alpha\beta}(U_d+V_w+V_sR_{0\infty})}{P_{\alpha\beta}Q_{0\infty}+Q_{\alpha\beta}P_{0\infty}}, \tag{12}$$

$$v_2=\frac{P_{0\infty}(U_g-V_h-V_sR_{\alpha\beta})+P_{\alpha\beta}(U_d+V_w+V_sR_{0\infty})}{P_{\alpha\beta}Q_{0\infty}+Q_{\alpha\beta}P_{0\infty}}. \tag{13}$$

The quantities appearing in Eqs. (12) and (13) are determined by the equalities

$$P_{0\infty}=P(\infty), \quad Q_{0\infty}=Q(\infty), \quad R_{0\infty}=R(\infty)$$

$$P_{\alpha\beta}=\int_{\alpha}^{\beta}\frac{d\theta}{\sqrt{|G(\theta)|}}, \quad Q_{\alpha\beta}=\int_{\alpha}^{\beta}\frac{\theta^2d\theta}{\sqrt{|G(\theta)|}},$$

$$R_{\alpha\beta}=\int_{\alpha}^{\beta}\frac{|\chi(\theta)|d\theta}{\sqrt{|G(\theta)|}}$$

and are related with one another by the relations

$$P_{0\infty}=P_{\alpha\beta}-P_{\gamma1}, \quad Q_{0\infty}=-Q_{\alpha\beta}+Q_{\gamma1},$$

$$R_{0\infty}=R_{\alpha\beta}+R_{\gamma1}-(H+h)/s, \tag{14}$$

where $P_{\gamma1}$, $Q_{\gamma1}$, and $R_{\gamma1}$ differ from $P_{\alpha\beta}$, $Q_{\alpha\beta}$, and $R_{\alpha\beta}$, respectively, only by the integration limits.

Equations (9)–(13) give the complete solution of the problem of the potential distribution, if the parameters α, β, and γ of the conformal mapping $T(z)$ are known and if the SCR fills the entire base of the device, i.e., $w=d$. In the

opposite case (which it makes sense to study when the base is doped with donors[1,5]) $w<d$ and the position of the SCR boundary, next to the drain, must be determined from the condition $\nabla\varphi(x,w)=0$. This is easy to do since in the cases of practical interest the relation

$$w-H\geqslant 2L \tag{15}$$

is satisfied with a wide margin. As a result, for any shape of the gate[2]

$$\gamma\leqslant 4\ \exp\left(-\frac{\pi}{2}\frac{w-H}{L}\right)\ll 1.$$

It can be shown that the real boundary of the SCR deviates from the plane $y=w$ by a negligible amount of the order of $\gamma^2 w$, and w is determined by the equation

$$2V_L\frac{w}{L}=\frac{\pi}{2}v_2. \tag{16}$$

Substituting into Eq. (16) the base thickness d for w gives an equation for the drain potential $U_{d\,\min}$, which distinguishes these two cases.

3. PARAMETERS OF THE SADDLE POINT AND THE BLOCKING FACTOR

In a ECT with an undoped base the saddle point is located at

$$\tau=\tilde{\tau}=\sqrt{\frac{v_0}{v_2}}=\sqrt{\frac{Q_{0\infty}U_g-Q_{\alpha\beta}U_d}{P_{0\infty}U_g+P_{\alpha\beta}U_d}}, \tag{17}$$

and the minimum value of the potential is

$$\varphi(\tilde{\tau})=\tilde{\varphi}=-v_2[\tilde{\tau}^{\,2}P(\tilde{\tau})-Q(\tilde{\tau})]. \tag{18}$$

Since $\tau^2P(\tau)>Q(\tau)$ for $\tau>0$, the condition $\tilde{\varphi}=0$ determining the threshold voltage can be satisfied only if $\tilde{\tau}=0$. It thus follows from Eqs. (12) and (17) that the blocking factor

$$g=g_0\equiv\frac{Q_{0\infty}}{Q_{\alpha\beta}}. \tag{19}$$

Near the threshold, where

$$g_0-\frac{U_d}{U_g}\ll\alpha^2\frac{g_0P_{\alpha\beta}+P_{0\infty}}{Q_{\alpha\beta}},$$

the right-hand side of Eq. (18) can be expanded in a series in powers of $\tilde{\tau}$, which gives

$$\tilde{\varphi}=-kU_g\left(g-\frac{U_d}{U_g}\right)^{3/2}, \tag{20}$$

where $k=\dfrac{2\sqrt{Q_{\alpha\beta}}}{3\alpha\beta\gamma}(g_0P_{\alpha\beta}+P_{0\infty})^{-3/2}$.

If $N\neq 0$, while the coordinate $\tilde{\tau}$ of the saddle point can be calculated analytically only if $\tilde{\tau}^{\,2}\ll\alpha^2$, so that the expansion of the right-hand side of Eq. (11) in powers of τ can be limited to terms proportional to $\tau^{\,3}$, and since as a result of the symmetry principle (in this case — relative to the real axis) for the conformal mapping $Z(t)$ the expansion of the function $y(0,\tau)$ contains only terms with odd powers of τ, we obtain

$$\tilde{\varphi}=\varphi_0\left(\frac{\tilde{\tau}}{\tau_0}\right)^2\left(4\frac{\tilde{\tau}}{\tau_0}-3\right), \tag{21}$$

$$\xi=\sqrt{1-\frac{\tau_0}{2\tilde{\tau}}}, \tag{22}$$

$$\tilde{\tau}=\frac{1}{2}\left(\tau_0+\sqrt{\tau_0^2+\tau_1^2\frac{U_0-U_d}{U_g}}\right), \tag{23}$$

where

$$\varphi_0=-\frac{A\tau_0^3U_g}{6\alpha\beta\gamma Q_{\alpha\beta}},\quad U_0\equiv g_NU_g,$$

$$\tau_0=\frac{Q_{\alpha\beta}}{A}\frac{qN}{\varepsilon\varepsilon_0U_g}\alpha\beta\gamma\left[\frac{dy(0,0)}{d\tau}\right]^2,$$

$$\tau_1^2=\frac{Q_{\alpha\beta}}{A(g_0P_{\alpha\beta}+P_{0\infty})},$$

$$A=1-\frac{V_h}{U_g}-\frac{V_s}{U_g}(R_{\alpha\beta}-\chi_1P_{\alpha\beta}-\chi_\beta Q_{\alpha\beta}),$$

$$\chi_n=\frac{2}{\pi}\int_\beta^\gamma\frac{dy^2(\theta,0)}{d\theta}\frac{\sqrt{|G(\theta)|}}{\theta'}\frac{d\theta}{x^2},$$

$$g_N=g_0\left[1-\frac{V_n}{U_g}-\frac{V_s}{U_g}(R_{\alpha\beta}-\chi_1P_{\alpha\beta})\right]-\frac{V_w}{U_g}-\frac{V_s}{U_g}(R_{0\infty}-\chi_1P_{0\infty}). \tag{24}$$

If the base of the ECT is doped so lightly that $\tau_0^2\ll\alpha^2$, then there exists a range of values of the drain potential determined by the inequalities

$$\tau_0^2\ll\tau_1^2\frac{U_0-U_d}{U_g}\ll\alpha_0^2, \tag{25}$$

for which Eq. (21) holds and can be put into the form (20) with $g=g_N$ and $k=\dfrac{2}{3\alpha\beta\gamma}\sqrt{\dfrac{Q_{\alpha\beta}}{A}}\,(P_{0\infty}+g_0P_{\alpha\beta})^{-3/2}$, while the blocking factor is g_N. The latter assertion, which holds for a p-type base with arbitrary doping, is justified for a n-type base only because the quantity $\eta\equiv\dfrac{U_1-U_0}{U_0}$, where U_1 is the drain potential for which $\tilde{\varphi}=0$ in accordance with Eq. (21), is small.[1,2] In our case

$$\eta=\frac{3U_g}{16U_0}\frac{\tau_0^2}{\tau_1^2}\leqslant\frac{3\tau_0^2}{8\alpha^2}, \tag{26}$$

so that $\eta\ll 1$ only for $\tau_0^2\ll a^2$. If the thickness of the n-base is so large that $U_d<U_{d\,\min}$, then when calculating g from Eq. (24) the value

$$w=w_0\equiv\frac{\pi}{4}L\frac{U_g-V_h-V_s(R_{\alpha\beta}-\chi_1P_{\alpha\beta})}{Q_{\alpha\beta}V_L}, \tag{27}$$

obtained from Eqs. (12), (13), and (16) with $U_d=U_0$, must be substituted on the right-hand side.

The situation changes qualitatively in the case of a heavily doped base, so that $\tau_0^2 \geqslant \alpha^2$. The region of applicability of a relation of the type (20) vanishes. However, if the base is doped with acceptors (i.e., $N=N_A<0$ and $\tau_0<0$), then close to the threshold, where

$$U_0-U_d \ll 4U_g\frac{\alpha|\tau_0|}{\tau_1^2}, \tag{28}$$

the condition $\tilde{\tau}^2 \ll \alpha^2$ still holds, it follows from Eq. (23) that

$$\tilde{\tau}=\frac{\tau_1^2}{|\tau_0|}\frac{U_0-U_d}{4U_g} \ll |\tau_0| \tag{29}$$

and Eq. (21) assumes the form

$$\tilde{\varphi}=-\frac{(U_0-U_d)^2}{V_A}, \tag{30}$$

where $V_A=32\,\frac{qN_A}{\varepsilon\varepsilon_0}\,[\alpha\beta\gamma(dy(0,0)/d\tau)(P_{0\infty}+g_0P_{\alpha\beta})]^2$, and the region of applicability of (30) expands as N_A increases. However, if the base is doped with donors ($N=N_D>0$ and $\tau_0>0$), then $\tilde{\tau}^2>\tau_0^2 \geqslant \alpha^2$ and the expansion employed in the derivation of Eqs. (21)–(23) is incorrect. Moreover, the barrier $q\tilde{\varphi}=q\varphi_0$, which remain when $U_d=U_0$, can still be so high that the electron current through it is negligible. On the other hand, as noted in Refs. 1 and 2 , for $U_d>U_0$ a potential well filled with electrons, which compensate for the donor charge close to the saddle point, forms near the source. For this reason, our approximation in which the base is completely depleted breaks down near threshold and it is impossible to calculate analytically the I–V characteristic of an ECT with a *n* base.

4. BURIED OVAL-SHAPED GATE

The general but complicated formulas obtained above greatly simplify if the inequalities between α, β, γ, and 1, which determine the function $G(t)$, are satisfied. The number of possible variants is too large for us to analyze all of them. For this reason, as a concrete example of the application of the general theory we shall consider only one characteristic case, where $\alpha \ll \beta$ and $\gamma \ll 1$. Disregarding terms of order α^2/β^2 and γ^2 compared to 1, we obtain

$$P_{\alpha\beta}=\frac{1}{\beta\gamma}\,\ln\frac{4\beta\gamma}{\alpha\sqrt{\gamma^2-\beta^2}}, \quad P_{0\infty}=\frac{1}{\beta\gamma}\,\ln\frac{4\beta\gamma}{\alpha(\gamma+\beta)}, \tag{31}$$

$$Q_{\alpha\beta}=\tanh^{-1}\frac{\beta}{\gamma}, \quad Q_{0\infty}=\ln\frac{4}{\gamma+\beta}, \tag{32}$$

$$(R_{\alpha\beta}-\chi_1P_{\alpha\beta})=\Phi_{22}\left(\frac{\gamma}{\beta}\right)+2\frac{h}{s}\Phi_{12}\left(\frac{\gamma}{\beta}\right), \tag{33}$$

$$(R_{0\infty}-\chi_0P_{0\infty})=\Phi_{22}\left(\frac{\gamma}{\beta}\right)-\Phi_{20}\left(\frac{\gamma}{\beta}\right)+2\frac{h}{s}\left[\Phi_{12}\left(\frac{\gamma}{\beta}\right)-\Phi_{10}\left(\frac{\gamma}{\beta}\right)\right], \tag{34}$$

$$\chi_3=\left(\frac{\gamma}{\beta}+\frac{\beta}{\gamma}\right)\Phi_{22}\left(\frac{\gamma}{\beta}\right)-2\Phi_{24}\left(\frac{\gamma}{\beta}\right), \tag{35}$$

$$\Phi_{nm}(a)=\frac{2}{\pi}a^{m/2}\int_1^a\left[\frac{y(\beta x,0)-h}{H-h}\right]^n\frac{x^{1-m}dx}{\sqrt{(x^2-1)(a^2-x^2)}}. \tag{36}$$

For a gate whose cross section is an oval, the mapping of the half-plane Im $t>0$ on the SCR of the ECT cell can be represented in the form

$$Z(t)=\int_0^t[C_1(\lambda^2-t^2)+C_2\sqrt{(\beta^2-t^2)(\gamma^2-t^2)}]\frac{dt}{\sqrt{G(t)}}, \tag{37}$$

where both roots in the integrand are positive on the segment $|\theta|<\alpha$ of the real axis. The constants C_1, C_2, α, β, γ, and λ must be determined from the condition that the points match under the mapping (see Sec. 2). In our case we obtain

$$\alpha=\exp\left\{-\frac{\pi}{2L}\left[w-\frac{s}{\mu}\ln(\cosh\,\mu)\right]\right\}\left(\frac{2}{\cosh\,\mu}\right)^2, \tag{38}$$

$$\beta=\exp\left\{-\mu-\frac{\pi}{2L}\left[w_{gd}-\frac{s}{2\mu}\ln(\cosh\,\mu)\right]\right\}\frac{2}{\cosh\,\mu}, \tag{39}$$

$$\gamma=\beta\,\exp 2\mu, \tag{40}$$

$$\frac{dy(0,0)}{d\tau}=\frac{2L}{\pi\alpha}, \tag{41}$$

where $w_{gd}=(w-H+h/2)$ is the distance from the center of the gate to the drain, and the parameter μ is the solution of the equation

$$\tanh\,\mu=\sin\frac{2\pi(L-l)\mu}{4L\mu-\pi s}. \tag{42}$$

It is evident from Eqs. (38)–(40) that the inequalities employed in the present section are satisfied, and that the width $2L$ of the cell is less than the gate–source distance h and the gate–drain distance $w-H$. The gate boundary can be described by the parametric equations

$$x(\theta,0)=L-\frac{L-l}{2}\left[\arcsin\left(\frac{\gamma-\beta}{\gamma+\beta}\right)\right]^{-1}\times\left[\arcsin\frac{(\gamma^2+\beta^2)\theta^2-2\beta^2\gamma^2}{(\gamma^2-\beta^2)\theta^2}+\arcsin\frac{\gamma^2+\beta^2-2\theta^2}{\gamma^2-\beta^2}\right], \tag{43}$$

$$y(\theta,0)=h+s\frac{\ln\,\theta/\beta}{\ln\,\gamma/\beta}. \tag{44}$$

An analysis of these equations shows that right up to values $\gamma/\beta \leqslant 100$ this oval differs by no more than 5% from an ellipse with semiaxes $(L-l)$ and $s/2$. Substituting the expression (44) into Eq. (36) makes it possible to calculate the functions $\Phi_{nm}(a)$ by numerical integration, whose results are shown in Fig. 2.

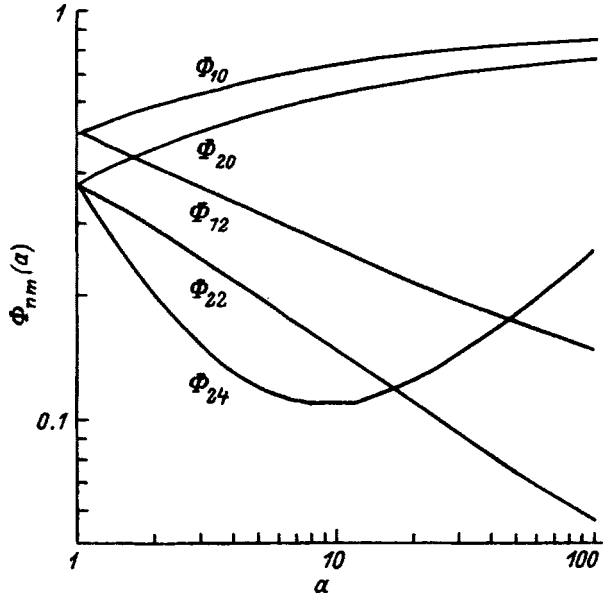

FIG. 2. Computed functions $\Phi_{nm}(a)$ for a deep buried oval gate.

Using the results of the numerical solution of Eq. (42), which are presented in Fig. 3, we can calculate the subthreshold characteristics of the ECT for any ratios of the gate dimensions if $2L<h$, $(d-H)$. A purely analytical calculation is possible in a number of limiting cases.

If $s \ll \min(l, L-l)$, then the gate has the form of a thin horizontal plate and

$$\mu = \tanh^{-1}\left(\sin\frac{\pi}{2}\frac{L-l}{L}\right). \tag{45}$$

For $(L-l) \ll \min(s,L)$ the gate has the form of a thin vertical plate and

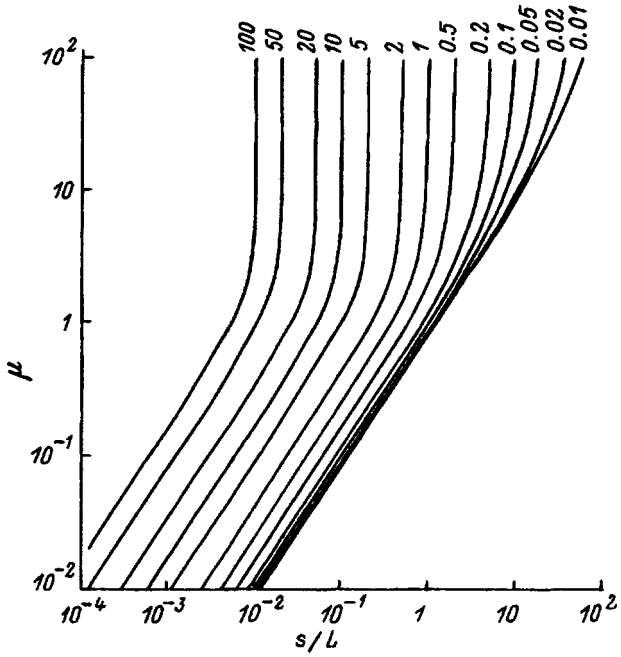

FIG. 3. Computed curves of μ versus s/L for an oval gate. The numbers on the curves are the values of the parameter $(L-l)/s$.

$$\mu = \frac{\pi}{4}\frac{s}{L}. \tag{46}$$

For $(L-l+s/2) \ll L$ the perimeter of the cross section of the gate is small compared with the period of the ECT cell and

$$\mu = \frac{\pi}{2}\frac{s+2(L-l)}{2L}. \tag{47}$$

If the gate is round, then $s=2(L-l)$ and for $s \ll L$

$$\mu = \frac{\pi}{2}\frac{s}{L}. \tag{48}$$

This limiting case was studied earlier in a development of the theory of electronic tubes; the well-known formula for the gain of a flat vacuum triode with a thin grid[6]

$$g_0 = \frac{\pi d_{gd}/L - \ln(\cosh \pi s/2L)}{\ln(\coth \pi s/2L)} \approx \frac{\pi d_{gd}}{L \ln(2L/\pi s)} \tag{49}$$

is obtained by substituting the expressions (48) and (38)–(40) into Eqs. (32) and (19).

Finally, for $l \cosh(\pi s/4l) \gg \max(l, L-l)$, so that $\gamma \gg \beta$, and μ is determined by the equality

$$\mu = \frac{\pi}{4}\frac{s}{l}. \tag{50}$$

We shall study this limiting case in detail, since, in the first place, the blocking factor is large (this is important for practical applications) and, in the second place, the formulas from the preceding section simplify substantially because of the inequality $\gamma \gg \beta$. Indeed, using the data of Fig. 2, it is easy to show that for $\gamma \gg \beta$ all terms in the final formulas containing the factor V_s are negligible, since ordinarily $V_s < U_g$. In addition, it follows from Eq. (31) that $P_{0\infty} \leqslant P_{\alpha\beta} \leqslant g_0 P_{\alpha\beta}$. Taking this circumstances into account, it can be shown that

$$\varphi_0 = -\frac{4}{3}\left(\frac{2}{\pi}\right)^6 \frac{V_L^3}{(U_g - V_h)^2}\left(\frac{\beta}{\alpha}\right)^4, \tag{51}$$

$$\frac{\tau_0}{\alpha} = \frac{8}{\pi^2}\frac{V_L}{U_g - V_h}\left(\frac{\beta}{\alpha}\right)^2, \tag{52}$$

$$\frac{\tau_0}{\tau_1} = \frac{8}{\pi^2}\frac{V_L}{\sqrt{U_g(U_g - V_h)}}\frac{\beta}{\alpha}\sqrt{g_0 \ln\left(4\frac{\beta}{\alpha}\right)}, \tag{53}$$

$$k = \frac{2\beta}{3\alpha}\frac{V_L}{\sqrt{U_g - V_h}}\left[g_0 \ln\left(4\frac{\beta}{\alpha}\right)\right]^{-3/2}, \tag{54}$$

$$V_A = \frac{2^8}{\pi^2}V_L\left[g_0 \ln\left(4\frac{\beta}{\alpha}\right)\right]^2, \tag{55}$$

$$\frac{\beta}{\alpha} = \frac{1}{4}\exp\left(\frac{\pi h}{2L} + \frac{l}{L}\ln 2\right), \tag{56}$$

$$g_N = g_0\left(1 - \frac{V_h}{U_g}\right) - \frac{V_w}{U_g}, \tag{57}$$

$$g_0=\frac{\pi}{2}\frac{w-H}{L}\exp\left(\frac{\pi s}{2l}\right), \tag{58}$$

and the ''threshold'' thickness of the SCR is $w=\min(w_0,d)$, where

$$w_0=\frac{\pi}{4}L\frac{U_g-V_h}{U_g}\exp\left(\frac{\pi s}{2l}\right). \tag{59}$$

The applicability condition (25) for Eq. (20) becomes

$$1\ll\left[\frac{\alpha}{\beta}\frac{U_g-V_h}{V_l\ln(4\beta/\alpha)}\right]^2\frac{U_0-U_d}{U_0}\ll\left(\frac{U_g-U_h}{V_L}\right)^2\left(\frac{\alpha}{\beta}\right)^4 \tag{25a}$$

and can be satisfied only if

$$V_L^2\ll(U_g-V_h)^2\left(\frac{\alpha}{\beta}\right)^4. \tag{60}$$

This inequality is necessary in order that $\eta\ll 1$ and the blocking factor of an ECT with a *n*-type base be determined by Eq. (57). The presence of the small factor $(\alpha/\beta)^4$ on the right-hand side of Eq. (60) distinguishes this condition from the similar condition for the case of contiguous gate and source,[2] and it has the effect that the subthreshold IVC and g can be calculated analytically only if the n base of the ECT with a deep buried gate is very lightly doped. On the other hand, the region of applicability of the quadratic law (30) is greatly expanded for an ECT with a *p*-type base: This law should be observed when

$$\frac{U_0-U_d}{U_0}\ll\frac{32}{\pi^2}\frac{g_0V_L}{U_0}\ln\left(4\frac{\beta}{\alpha}\right)\leqslant\frac{16}{\pi}\frac{V_L}{U_g-V_h}\frac{h}{L}, \tag{28a}$$

which holds all the better, the deeper the gate and the heavier the doping are.

5. CONCLUSIONS

Our methods of the theory of functions of complex variables made it possible to solve, for the first time, the problem of subthreshold I–V characteristics of ECTs in quadratures for gates of arbitrary shape. In all cases the exponent in the exponential in the formula

$$J_s=qN_sD_n\xi\exp\left(-\frac{|q\tilde{\varphi}|}{kT}\right)$$

for the current density of the drain is a nonlinear function of the electrode potentials because of the fact that the saddle point of the barrier approaches the source as the ratio U_d/U_g increases. Close to the source either the 3/2 law [Eq. (20)] should be observed, if the base of the ECT is sufficiently lightly doped, or the quadratic law [Eq. (30)] should be observed, if the base is heavily doped, and the types of conduction in the base and gate are the same. All parameters of the subthreshold IVCs, including the blocking factor, can be calculated as soon as the conformal mapping of the upper half-plane onto the cross section of the SCR of a unit cell of the ECT is known. These results are absolutely rigorous to the extent that:

the completely depleted SCR approximation is applicable;

the penetration of the SCR into the source and gate can be neglected; and,

the boundary condition (5) is satisfied in the source–gate gap, i.e., the normal field $E_\perp=0$.

The latter assumption is justified, strictly speaking, only for the above-studied ECTs with a buried gate. However, all results are equally applicable in the case of contiguous gate and source (i.e., for $\alpha=\beta$), since the conditions at the ''absent'' section of the boundary do not influence at all the distribution of the potential. For this reason, in the limit $\alpha\to\beta$ all formulas in this paper should be identical to the corresponding results from Ref. 2 , as simple but very cumbersome calculations confirm. In all other cases it is necessary to solve the boundary-value problem inside the SCR as well as above the ECT surface with interfacial values of $E_\perp$, which are not known *a priori*. This can be done, for example, by a method similar to the method employed in the present paper. The functions $E_\perp(\theta)$ in the interval $\alpha<\theta<\beta$ will have to be determined by solving a singular integral equation, following from the standard conditions on the interface of insulators. The results of this very complicated program could quantitatively differ substantially from the results presented above. It is obvious, however, that the character of the potential well in the SCR and its evolution under a variation of the voltages on the electrodes cannot change. For this reason, qualitatively, all the results obtained by us are completely general.

I thank T. T. Mnatsakanov and S. N. Yurkov for a discussion of this work.

This work was supported by the Russian Fund for Fundamental Research under Project No. 95-02-05767 and the INTAS fund under Project No. 94-0417.

[1] A. S. Kyuregyan and S. P. Yurkov, Fiz. Tekh. Poluprovodn. **32**, 249 (1998) [Semiconductors **32**, 225 (1998)].
[2] A. S. Kyuregyan, Fiz. Tekh. Poluprovodn. **32**, 497 (1998) [Semiconductors **32**, 446 (1998)].
[3] M. A. Lavrent'ev and B. V. Shabat, *Methods of the Theory of Functions of a Complex Variable* [in Russian] (Nauka, Moscow, 1987).
[4] B. J. Baliga, *Modern Power Devices* (Singapore, 1987), p. 132.
[5] A. V. Gorbatyuk and I. V. Grekhov, Fiz. Tekh. Poluprovodn. **15**, 1353 (1981) [Sov. Phys. Semicond. **15**, 781 (1981)].
[6] K. R. Spangenberg, *Vacuum Tubes* (McGraw-Hill Book Co., N. Y., 1949), p. 134.

Translated by M. E. Alferieff